RL920

MICROMACHINED HIGH FREQUENCY TRANSMISSION LINES ON THIN DIELECTRIC MEMBRANES

(Thesis)

Thomas McCrea Weller

May, 1995

MICROMACHINED HIGH FREQUENCY TRANSMISSION LINES ON THIN DIELECTRIC MEMBRANES

by

Thomas McCrea Weller

A dissertation submitted in partial fulfillment
of the requirements for the degree of
Doctor of Philosophy
(Electrical Engineering)
in The University of Michigan
1995

Doctoral Committee:

Professor Linda P. B. Katehi, Chairperson
Assistant Professor Carlos H. Mastrangelo
Associate Professor Gabriel M. Rebeiz
Associate Professor Kim A. Winick
Dr. William R. McGrath (Technical Group Supervisor,
Jet Propulsion Laboratory)

To my mother, Marion Gayleen Weller, and in memory of my father, Richard Albert Weller; both builders of fine homes.

ABSTRACT

MICROMACHINED HIGH FREQUENCY TRANSMISSION LINES ON THIN DIELECTRIC MEMBRANES

by

Thomas McCrea Weller

Chairperson: Linda P. B. Katehi

This thesis represents a detailed investigation of high-frequency transmission lines which are supported by thin-film dielectric membranes. The associated fabrication techniques rely on established silicon micromachining technology to realize new architectures for high-performance microwave and millimeter wave circuits. In the majority of the material, attention is directed towards the characterization, fabrication, and measurement of a transmission line which has been named the microshield line. This is a quasi-planar geometry with a signal line and ground planes which are patterned on the thin membrane, and a lower shielding cavity which is realized by micromachining the silicon substrate. It is demonstrated that the microshield line offers significant advantages in comparison to conventional planar lines such as coplanar waveguide (CPW), in terms of attenuation, parasitic radiation, broadband operation, and overall circuit performance.

Two of the chapters in the thesis are devoted to theoretical characterization of coplanar waveguide-type discontinuities, such as the microshield configuration. One method is a full-wave integral equation technique which has been used to analyze many of the circuits and antennas involved in this research. A more computationally efficient, but much less general, quasi-TEM analysis of coupled slot configurations is also presented. This method was developed in order to characterize new filter arrangements which combine distributed element tuning stubs with lumped element overlay capacitors.

After describing the theoretical foundation, specific applications of the membrane-supported lines are considered. This includes several millimeter wave components such as transitions to conventional CPW, new geometries for compact tuning stubs, low-pass and band-pass filters, and the distributed/lumped element configurations mentioned above. To demonstrate the potential for high-performance submillimeter wave microshield circuits, the design, measurement, and performance of a 250 GHz planar bandpass filter are presented. A membrane-supported microstrip geometry is also investigated in order to realize a very low loss, Ka-band Wilkinson power divider/combiner. Finally, a study of new CPW-fed, single and double folded-slot antennas is described. These uniplanar designs exhibit very wide impedance bandwidths and well-shaped beam patterns.

The thesis concludes by discussing some possible future directions for this work. Included in the appendices are general guidelines on the fabrication process used in this research and on the measurement of microshield circuits.

ACKNOWLEDGEMENTS

I sincerely thank my advisor, Professor Linda Katehi, for her guidance throughout the past five years and her selfless contributions to my personal and professional growth. Her technical insight never ceases to amaze me, and it is rivaled only by her energy, understanding, and uniquely genuine character.

Many others also deserve recognition for their substantial contributions to my research. Sincere thanks are due to Professor Gabriel Rebeiz, whose original work pioneered the membrane-supported transmission lines which are the primary subject of this thesis. As a teacher and as participant in various projects of mine, his expertise added greatly to my graduate education. I am indebted to Dr. Nihad Dib for his patient tutelage concerning theoretical techniques, for his interesting conversation, and for always letting me in his door to ask questions. I also thank Dr. Martin Herman, who has provided a great deal of enthusiasm and assistance during the last two years. Finally, I greatly appreciate the contributions made by the members of my Doctoral Committee in reviewing this dissertation and participating in the oral defense. Special thanks to Dr. William McGrath for traveling in from California to attend the defense, and for his instruction and pleasant cooperation in our previous collaborative efforts.

I would also like to thank several people for their friendship and unconditional willingness to share both wisdom and experience, i.e. tribal knowledge. Drs. Walid Ali-Ahmad and Steven Gearhart were excellent sources for clean-room guidance. On

numerous occasions, the help and cooperation of Mrs. Rhonda Franklin Drayton has been invaluable. For all things lab-related, Mr. Steve Robertson, Mr. George Ponchak, Mr. Thomas Budka, Mr. Chen-Yu Chi, Mr. Sanjay Raman, and Mr. Heng-Ju Cheng have all been of tremendous help. Finally, back in the far corner of our 15-person, 1-phone suite, much was gained from conversations with Dr. Andrew Engel, Jr., Mr. Daniel Ross, and Dr. Kazem Sabetfakhri.

For continuous financial support since 1990, I thank the NASA Center for Space Terahertz Technology, the Jet Propulsion Laboratory, and the Office of Naval Research. I also thank Drs. Katehi, Rebeiz and Fawwaz Ulaby for their efforts in providing truly remarkable laboratory facilities.

Most importantly, I wish to express my deep gratitude to my family. For the love and support they have never failed to provide, I thank my mother, Gayleen, my brother Rick and his wife Debi, my sister Liz and her husband Frank, my sister Kimmy, and my parents-in-law Kenneth and Francis Ohlrich. As the most incredible person I have ever met, whom I am lucky enough to have as a best friend and a partner in marriage, Lisa Weller will receive my thanks for an eternity.

PREFACE

This thesis represents a detailed investigation of high frequency transmission lines which are supported by thin-film dielectric membranes. The associated fabrication techniques rely on established silicon micromachining technology and are used to realize new architectures for high performance microwave and millimeter wave circuits. In the majority of the presented material, attention is directed towards the characterization, fabrication, and measurement of a transmission line which has been named the microshield line. This is a quasi-planar geometry with a signal line and ground planes which are patterned on the thin membrane, and a lower shielding cavity which is realized by micromachining the silicon substrate. It is demonstrated that the microshield line offers significant advantages in comparison to conventional planar lines such as coplanar waveguide (CPW), in terms of attenuation, parasitic radiation, broadband operation, and overall circuit performance.

Two of the chapters in the thesis are devoted to theoretical methods for characterizing discontinuities in coplanar waveguide-type lines, such as the microshield configuration. One approach is a full-wave integral equation technique which has been used to analyze many of the circuits and antennas associated with this research. A more computationally efficient, but much less general quasi-TEM analysis of coupled slot geometries is also presented. This method was developed in order to characterize new filter arrangements which combine distributed element tuning stubs with lumped element overlay capacitors.

After describing the theoretical foundation, specific applications of the membrane-supported lines are considered. This includes several millimeter wave components such as transitions to conventional CPW lines, new geometries for compact tuning stubs, low-pass and band-pass filters, and the distributed/lumped element configurations mentioned above. In order to demonstrate the potential for submillimeter wave operation, the microshield line was employed in the design of a 250 GHz planar band-pass filter. The performance of the circuit was characterized using quasi-optical techniques, and represents the first experimental validation of a planar filter at this frequency. A membrane-supported microstrip architecture is also investigated in the development of a very low loss Ka-band Wilkinson power divider/combiner. The final study concerns new CPW-fed, single and double folded-slot antennas which exhibit very wide impedance bandwidths and well-shaped beam patterns.

To conclude, some possible future directions for this work are discussed and general guidelines on the fabrication steps and the measurement of microshield circuits are outlined.

TABLE OF CONTENTS

LIST OF FIGURES

Figure

LIST OF TABLES

LIST OF APPENDICES

Appendix

CHAPTER I

INTRODUCTION

1.1 Motivation

In recent years, powerful methods for theoretical characterization were combined with sophisticated solid state processing techniques to greatly enhance both the understanding and capability of planar transmission lines. This work has produced a steady stream of research developments that lead to the realization of high performance microwave components and the ability to accurately predict their behavior. By far the most common of the planar lines are microstrip and coplanar waveguide transmission line (CPW), which are illustrated in Figure 1.1. These two geometries are widely used because their properties are well understood and because they provide the advantages of MMIC (monolithic microwave integrated circuit) compatibility, small size, and low cost. Despite the desirable characteristics, however, there exist potentially significant limitations to the use of these conventional types of lines at millimeter wave frequencies and above. The primary problems are attenuation, dispersion and multi-mode propagation, all of which arise due to the underlying high permittivity substrate.

An obvious solution to these problems is to remove the substrate beneath the conducting lines, and this objective was the motivation behind the work contained

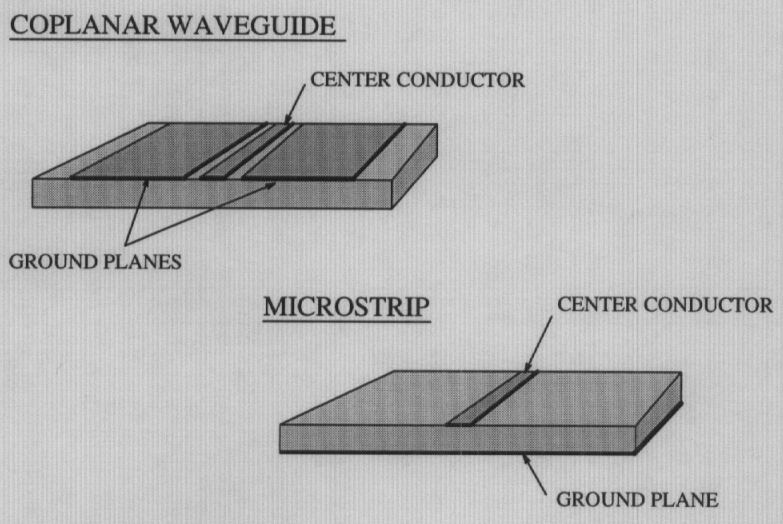

Figure 1.1: Coplanar waveguide and microstrip planar transmission lines.

herein. In order to meet this goal, techniques for silicon micromachining, originally developed for solid state sensors and micro electro-mechanical systems (MEMs), have been utilized to fabricate transmission lines supported by thin dielectric membranes. The use of such membranes for RF applications was originally demonstrated by Rebeiz et. al [1, 2], where they were used to support planar antenna elements. By extending their use to micromachined, membrane-supported transmission lines, all the advantages of the conventional lines are retained, in addition to gaining the potential for superior high frequency performance.

1.2 Membrane-Supported Transmission Lines

The concept of utilizing a thin dielectric membrane to support a high frequency transmission line was first presented in 1991 by Dib et. al [3]. In this work it was demonstrated that the radiation loss from certain membrane-supported discontinuities is lower than that exhibited by conventional coplanar waveguide. Furthermore, since the conducting lines are surrounded by a nearly homogeneous air dielectric,

this approach makes available the benefits of broad-band single mode operation, zero dielectric loss, and essentially zero dispersion. Membrane-supported lines are thus suitable for operation well into the submillimeter wave frequency range, unlike standard planar implementations. The new lines also provide an important alternative to metallic waveguide for very high frequency applications; depending on the particular system configuration, planar lines may simplify circuit design (e.g. filters) and antenna integration.

The main body of research contained in this thesis centers upon the study of the two membrane-supported architectures shown in Figure 1.2. One of these lines is similar to coplanar waveguide, except that the substrate is replaced by an air-filled metallic shielding cavity; this configuration is called the microshield line. The second line is simply a microstrip line with an air substrate. Common to both designs is the dielectric membrane, which is 1.5 μm thick and comprised of an $SiO_2/Si_3N_4/SiO_2$ tri-layer; the thicknesses are approximately 7500Å, 3500Å and 4500Å, respectively. This composite is designed to be under slight tensile stress, such that it remains rigid and flat when the silicon substrate is removed.

Of central importance in the fabrication of these lines is the use of silicon micromachining techniques. Using dielectric or metal masking layers, the high resistivity silicon wafer is selectively etched to create three-dimensional features such as the shielding sidewalls, and to expose the free-standing membrane. Micromachining is similarly used to realize silicon-based shadow masks which are necessary for the backside metalization of the microshield line (see App. C), and possibly for upper shielding cavities which are integrated into a separate wafer. The remaining process steps rely on standard solid state technology including photolithography and thin-film deposition, in common with the fabrication of conventional MMIC components.

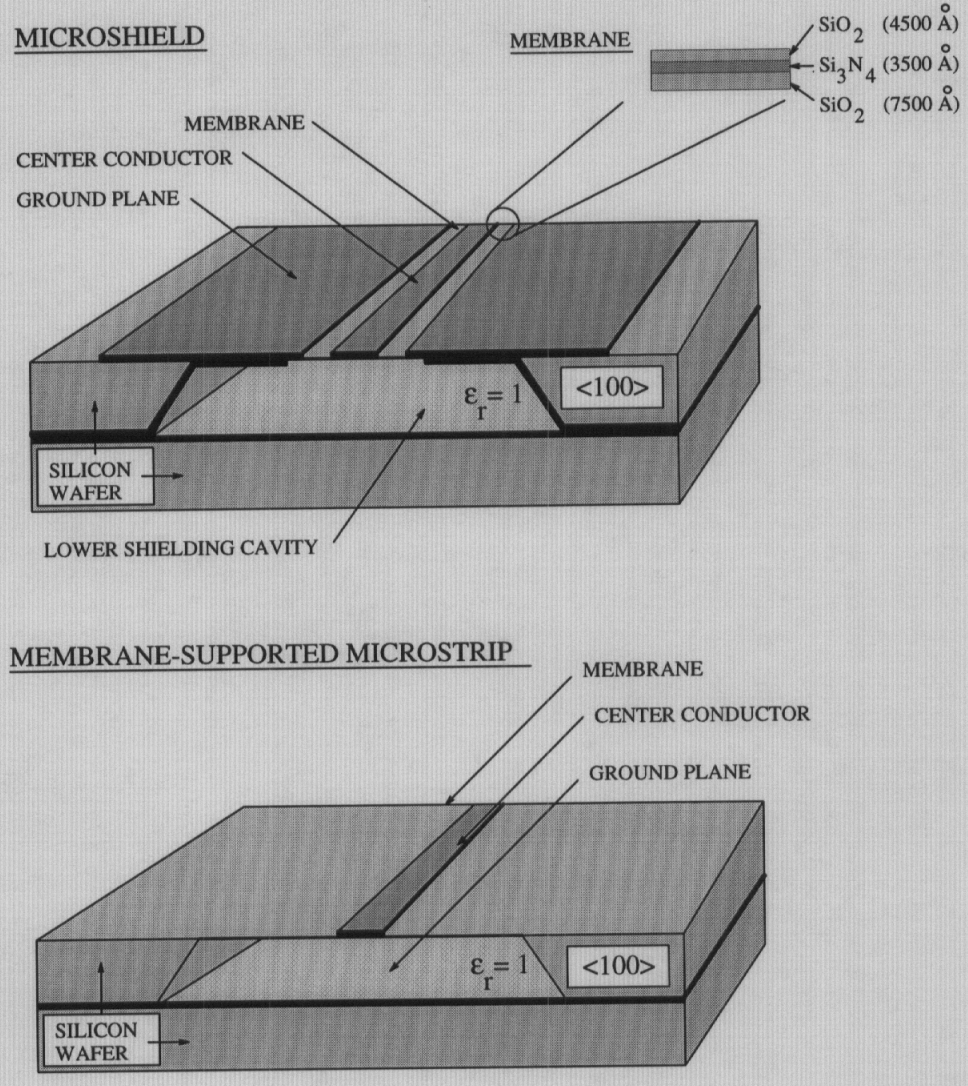

Figure 1.2: Membrane-supported transmission line structures.

Since the introduction of microshield in 1991, research on membrane-supported passive circuits has been conducted by this author and others, such as Chi [4] and Robertson [5]. In addition, the application of micromachining techniques to realize self-packaged CPW [6] and rectangular waveguide [7] has been successfully demonstrated. These works represent only a fraction of the impact that micromachining can have on the field of RF circuit design.

1.3 Overview of Thesis

The significance of membrane-supported transmission lines, and the microshield line in particular, derives primarily from the hypothesis that they offer better performance than do conventional planar lines. As proof of this, Chapter II is devoted to the exposition of the basic electrical characteristics of microshield, in comparison to coplanar waveguide printed on high permittivity substrates (e.g. silicon or GaAs). This distinction of the substrate is of interest because the micromachined geometries are especially well-suited for millimeter and submillimeter wave applications, in which monolithic fabrication techniques are predominant. The main topics of Chapter II are attenuation, single mode operation, parasitic radiation, and the performance of certain discontinuities. In each category, the microshield line is shown to be superior to substrate-supported coplanar waveguide.

The remaining chapters center on the theoretical methods used to characterize microshield circuits, and on the demonstration of various transitions, stubs, filters and antennas. Also included are examples of circuits which are developed using the membrane-supported microstrip geometry.

1.3.1 Theoretical Methods

Many of the microshield circuits examined in this work were characterized using a full-wave analysis that is based on the space domain integral equation (SDIE) technique. The SDIE approach is a well-established method for solving high frequency, planar transmission line problems. It requires a knowledge of the Green's function for the given geometry, which in turn mandates that the regions surrounding the transmission line be canonical in nature. An advantage of using Green's functions is that current or field quantities are only needed to satisfy boundary conditions at surface discontinuities, such as the slots in the metalization of a coplanar waveguide. The number of unknowns, and likewise the computer memory requirements, are minimized in this way since the entire circuit volume is not subdivided. Furthermore, a variety of practical circuit implementations can be accurately modeled as being non-shielded or partially shielded with rectangular boxes, leading to relatively straight-forward Green's function derivations. The specific formulation utilized here is developed in Chapter III.

Methods based on differential equations, such as the finite element method (FEM) or the finite difference time domain method (FDTD), require that the entire three-dimensional geometry be subdivided. Consequently, the differential techniques demand greater computer storage than the SDIE approach, but also enable the analysis of very general structures. Of course, as computational technology continues to accelerate, memory requirement becomes less of a hindrance. Also, using FDTD, broad band frequency characterization is accomplished using a Fourier transform of the time domain results. Despite the potential of the differential techniques, however, the SDIE approach remains a competitive solution for accurate, full-wave circuit characterization.

A second method has been developed in order to predict the performance of various CPW-type tuning stubs. It relies on the assumption of quasi-TEM propagation within the circuit element, and minimal influence from the parasitics which exist at discontinuities. For the geometries of interest, these conditions are satisfied to a high degree simply by following standard design principles; primarily, that line widths should be minimized to maintain single-mode operation. A tremendous advantage of this method over the full-wave techniques is that the required computation time is reduced by an order of magnitude. Furthermore, the capability exists to analyze distributed stubs which contain integrated lumped elements, an approach which has been explored herein to achieve compact, narrow-band components. The formulation utilizes a two-dimensional spectral domain approach in combination with a coupled line analysis, as presented in Chapter IV. The accuracy of the technique is demonstrated in comparisons with experimental data and results from the SDIE analysis, for frequencies up to 40 GHz.

1.3.2 Demonstrated Results

Given the novelty of the micromachined transmission line approach, a significant part of this research centered on experimental investigation of circuit performance. At a basic level, the attenuation due to conductor loss and the influence of the membrane on the effective guide wavelength were studied (see Chapters II and VII). More complex geometries were also characterized, as presented in Chapter V. Part of this work involved the study of transitions between microshield and conventional coplanar waveguide on silicon, resulting in a simple approach for designing electrically short, broad band transitions with greater than 18 dB return loss. The balance of the chapter is directed at the characterization of different tuning stub and filter

implementations, completed in close correlation with the theoretical work previously described. Notable developments in this area include new configurations for compact series stubs which are 60% shorter than conventional designs, and hybrid elements which incorporate thin-film capacitors into distributed element tuning stubs.

The chapters that follow present some additional areas in which the micromachining techniques have been applied. In Chapter VI, a quasi-optical measurement approach is used to characterize the first planar 250 GHz band-pass filter. The filter is a microshield-based design with a 58% bandwidth and a passband insertion loss of approximately 1.5 dB at 250 GHz. The development of a Wilkinson power divider/combiner using the membrane-supported microstrip line comprises the material in Chapter VII. This circuit exhibits about half the loss which is typical of designs implemented in conventional microstrip, and was eventually demonstrated in a 0.8 Watt, Ka-band solid state power amplifier. Finally, a study of single and double folded-slot antennas on semi-infinite substrates is presented in Chapter VIII. The double folded-slot is a CPW-fed, uniplanar geometry which has a very broad impedance bandwidth and good beam-shaping characteristics.

In order to complete the link between theoretical and experimental characterization, details pertaining to the fabrication and measurement of membrane-supported circuits are provided in Appendices C and D, respectively.

CHAPTER II

CHARACTERISTICS OF THE MICROSHIELD TRANSMISSION LINE

2.1 Introduction

A sound justification of any new technology generally relies on a demonstration of the advantages to be gained with respect to current competing technologies. It is therefore requisite to present some fundamental performance characteristics of the microshield transmission line. In so doing, the microshield line is contrasted with conventional, substrate-supported coplanar waveguide on a basic level, and those areas in which microshield has the distinct advantage are emphasized. The characteristics to be examined include the effective dielectric constant, attenuation, and the parasitics associated with various discontinuities. Through these comparisons it will be seen that, in addition to its significant potential for mm-wave and sub-mm wave application, the microshield line can also provide enhanced performance relative to conventional CPW at lower microwave frequencies.

2.2 Effective Dielectric Constant

Successful circuit design and analysis depend on a knowledge of the substrate permittivity. It may not be immediately obvious, however, that this is an important

concern with the microshield line since greater than 99% of the substrate is air. Ironically, the fact that the supporting membrane is so thin becomes one of the more problematic aspects of modeling the microshield line as compared to conventional coplanar lines.

To understand this, first consider the difficulty in attempting an analysis of the exact geometry. Since the membrane is only as thick as the metalization itself, and is comprised of three separate layers with different permittivities (see Chapter I), a complete model would need to account for each thin layer and finite metalization thickness. Although the necessary Green's function for this problem can be derived, the accuracy of treating the very thin layers is a concern. In fact, even two-dimensional spectral domain moment method codes (see Chapter IV) were found to be unsatisfactory in this respect. An alternative approach which is used in this work is to approximate the membrane and air substrate layers using a single, uniform material with a dielectric constant greater than 1 (Figure 2.1). This approach is computationally efficient and is suitable in many instances, but it can also significantly underestimate the dependence of the *effective* dielectric constant, ϵ_{re}, on the line geometry. With the uniform substrate model, the effective dielectric constant changes slowly as the slot width and center conductor width change, since the substrate is relatively thick compared to the line size. As shown in the following plots, however, ϵ_{re} can vary by up to 18% as the line width doubles (e.g. Figure 2.6). It can therefore take on different values at different locations in the same circuit, and this is the source of the potential modeling complications.

The physical explanation for the variation in ϵ_{re} is that a geometry-dependent fraction of the fields get trapped within the membrane itself. As the center conductor or slot width increase, there is less confinement in the slots, and thus a greater fraction

of the fields exist on either side the membrane; this leads to a decrease in the effective dielectric constant. As shown in Figure 2.2, the measured ϵ_{re} changes from 1.15 to 1.08 as the slot width is increased from 25 to 55 μm, representing an increase of 3% in the guided wavelength. In contrast, the uniform substrate model results in an ϵ_{re} which is very closely approximated by

$$\epsilon_{re} = \frac{\epsilon_{ru} + 1}{2} \tag{2.1}$$

assuming an air superstrate, where ϵ_{ru} is the value used as the relative permittivity of the uniform material layer. In this case, separate values of $\epsilon_{ru} = 1.3$ and $\epsilon_{ru} = 1.16$ would be necessary to accurately analyze the two line geometries specified in Figure 2.2, illustrating the limitation of this model.

For design and analysis purposes, it is therefore useful to have available data on the dependence of ϵ_{re} over a range of geometrical parameters. To this end, conformal mapping programs [8] have been used to generate the curves shown in Figures 2.3-2.6, applying a collection of measured data as reference points. From these calculations it was found that the membrane could be treated as a single layer of $\epsilon_r = 7$ material, which is a reasonable value since the relative permittivity of the oxide layers is 4 and that of the nitride layer is 7.5. Also, the effects of the lower shielding cavity have been neglected, which is a valid approximation when the aspect ratio, $S/(S+2W)$, is greater than 0.3 and the cavity sidewalls are removed from the middle of the center conductor by approximately $S+2W$. From these ϵ_{re} values, the relative permittivity to be used for the membrane-air combination layer, ϵ_{ru}, can be found by rearranging Eqn. 2.1. By examining the curves on an expanded x-axis, it could also be found that ϵ_{re} becomes independent of the aspect ratio when the substrate (membrane) thickness is approximately $(S + 2W)/3$, and converges to $(\epsilon_r + 1)/2 = 4$ when the thickness is approximately $S + 2W$.

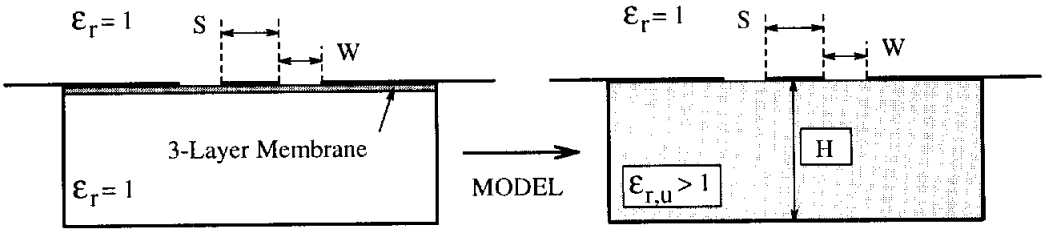

Figure 2.1: Cross-section of the microshield geometry, and the uniform substrate model which is used to approximate the effects of the thin membrane layer.

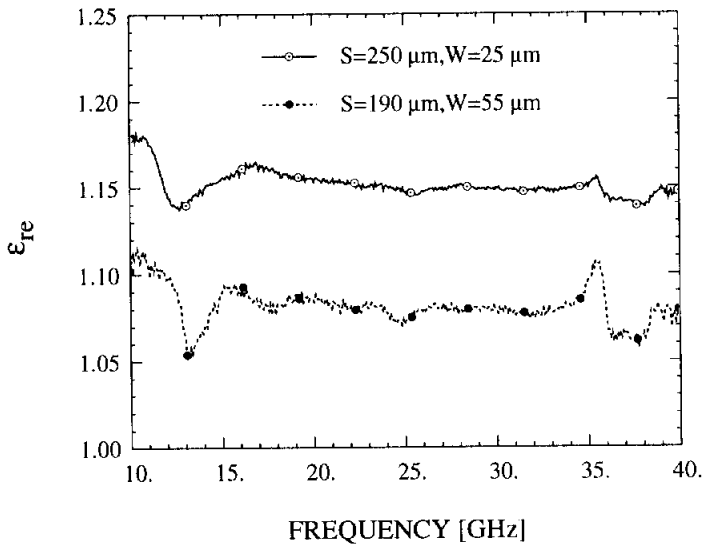

Figure 2.2: Measured effective dielectric constant, ϵ_{re}, on two microshield lines with different aspect ratios. The cavity height (H) is 350 μm.

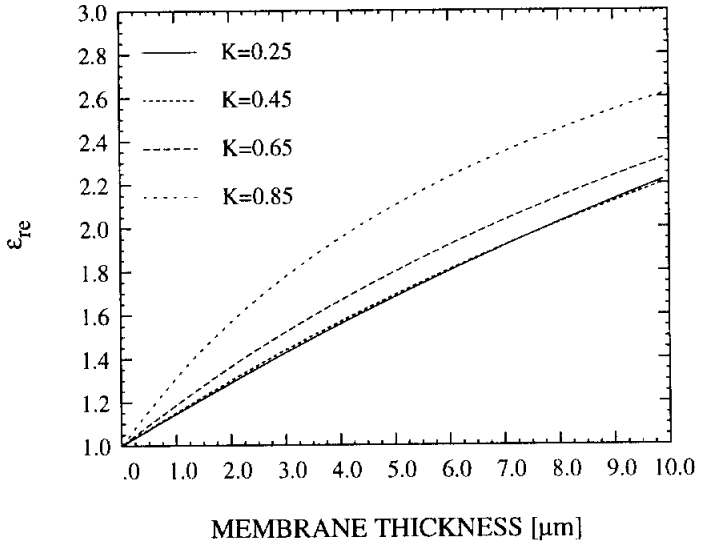

Figure 2.3: Effective dielectric constant versus membrane thickness for different aspect ratios, $K = S/(S + 2W)$, where $S + 2W = 100$ μm.

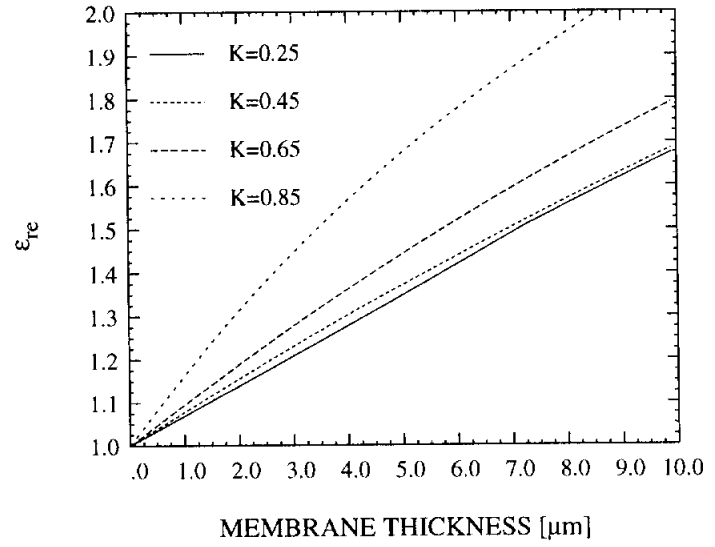

Figure 2.4: Effective dielectric constant versus membrane thickness for different aspect ratios, $K = S/(S + 2W)$, where $S + 2W = 200$ μm.

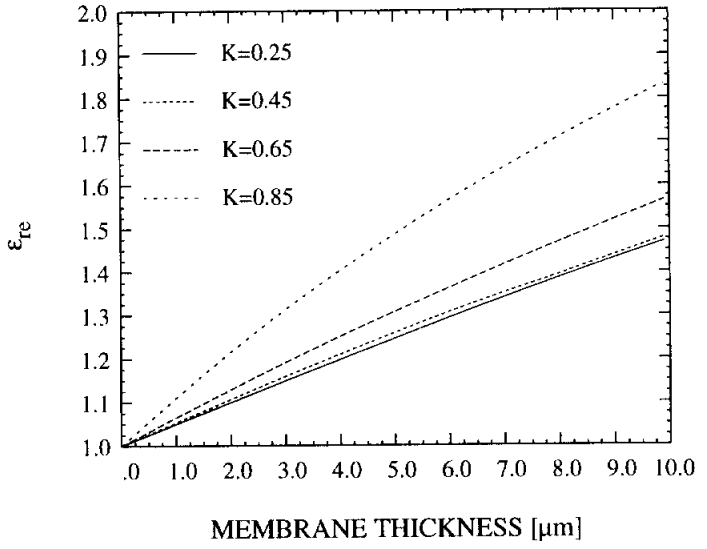

Figure 2.5: Effective dielectric constant versus membrane thickness for different aspect ratios, $K = S/(S + 2W)$, where $S + 2W = 300$ μm.

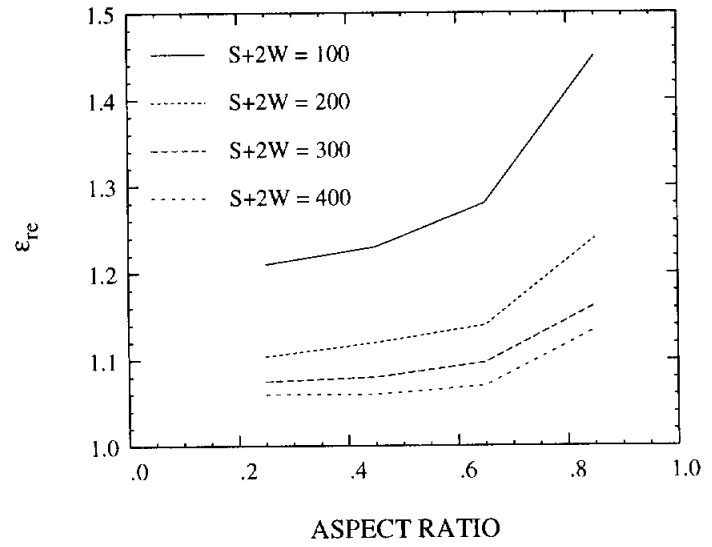

Figure 2.6: Effective dielectric constant versus aspect ratio for different line widths, where the membrane thickness is 1.5 μm.

The values which have been presented for ϵ_{re} can also be used to find the characteristic impedance for the microshield line. In cases where the lower shielding cavity is sufficiently large relative to the line dimensions, conformal mapping programs for conventional coplanar waveguide can be used along with an appropriate ϵ_{ru} (from Eqn. 2.1) to provide very accurate impedance values. Alternatively, the values found in [9] can be scaled by $(1/\sqrt{\epsilon_{re}})$, since an effective dielectric constant of 1 has been assumed in those calculations.

2.3 Attenuation

The attenuation characteristics of the microshield line have been investigated by comparing measured data on different microshield geometries against experimental and theoretical results for coplanar waveguide [10, 11, 12, 13]. At low frequencies, the two types of lines are expected to perform equally well, since dielectric and radiative losses are relatively small and attenuation is therefore dominated by conductor loss. At higher frequencies, however, the microshield line gains an increasing advantage since it has essentially zero dielectric loss and does not radiate energy into the substrate, unlike a conventional CPW line. This characteristic has been verified by electro-optic sampling experiments, which provided attenuation data on membrane-supported lines up to 1000 GHz [14].

The comparison between microshield and CPW attenuation is shown in Figure 2.7. The CPW curves were chosen either because the dimensions are similar to the microshield lines (curves C,F,G) or to illustrate the increased attenuation that results from reducing the line geometry (curve D vs. E). All pertinent geometrical parameters for the CPW and microshield examples are given in the table beneath the figure, and it is noted that the conductor thickness is only about 2 skin depths

at 25 GHz for all but two cases[1].

Some aspects of the information shown in Figure 2.7 deserve comment. The first point is that the results for the microshield lines are consistent with the CPW loss behavior outlined in [15] by Jackson; namely, for a constant ground plane separation, an aspect ratio $S/(S+2W)$ of 0.83 (curve A) gives much higher loss than an aspect ratio of 0.63 (curve B). A second point relates to a comparison between the CPW and microshield data in terms of loss per electrical length, as the wavelength in the air dielectric is about 2.5 times longer than in GaAs and about 1.5 times longer than in quartz. The *calculated* loss for CPW in points F and G is about 0.1 dB/λ_g lower than the *measured* loss in curve A for the microshield line, which has identical center conductor and slot widths. These differences may be explained by measurement errors or inaccuracies in the theoretical model. Finally, it is important to point out that the maximum line dimensions $(S+2W)$ for which quasi-TEM propagation is maintained scale inversely with the permittivity of the substrate. From [10], the line size must be less than approximately $\lambda_g/10$, such that at 50 GHz a GaAs CPW line and a microshield line are limited to widths of about 170 μm and 600 μm, respectively. At 100 GHz, the allowable dimensions drop to 85 μm and 300 μm, respectively. Therefore, in designing for low loss mm-wave transmission lines, significantly wider microshield geometries can be used to minimize the attenuation.

The results presented here confirm that the microshield line is free from unexpected or excessive conductor-loss mechanisms, and has performance which is comparable to conventional substrate-supported coplanar waveguide at lower frequencies. Furthermore, the absence of dielectric-related loss and the ability to maintain non-dispersive, single-mode propagation over a very broad bandwidth lead to low

[1]The technique used in [12] assumes zero conductor thickness.

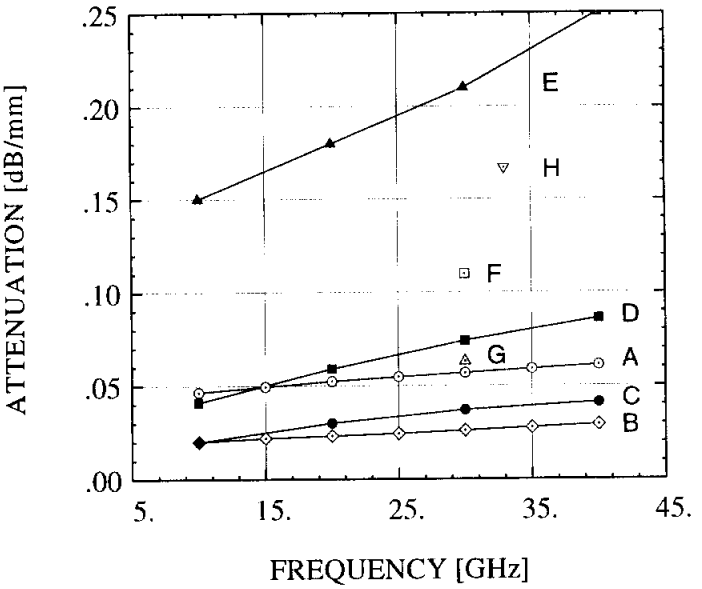

Curve	Line	ϵ_r	Substr	S	W	H	t	Z_O Ω	Data	Ref.
A	μshield	1.0	Air	250	25	355	1.2	75	Meas	[11]
B	μshield	1.0	Air	190	55	355	1.2	100	Meas	[11]
C	CPW	12.8	GaAs	232	84	100	-	50	Calc	[12]
D	CPW	12.8	GaAs	69	28	100	-	50	Calc	[12]
E	CPW	12.9	GaAs	88	16	500	1.0	30	Meas	[13]
F	CPW	12.9	GaAs	250	25	500	1.0	30	Calc	[10]
G	CPW	4.0	Quartz	250	25	250	1.0	50	Calc	[10]
H	GCPW	11.7	Si	50	125	355	1.2	73	Meas	[11]

Figure 2.7: Attenuation for microshield and coplanar waveguide lines. S is the center conductor width, W the slot width, H the substrate height, and t the metal thickness (in μm). The width of the lower shielding cavity for the microshield lines is 1800 microns.

attenuation well into the millimeter-wave frequencies.

2.4 Advantages of a Low Permittivity Substrate

There are several potential advantages of the nearly homogeneous air-dielectric substrate of the microshield line. These include the absence of substrate moding problems, which in turn reduces dispersion and losses due to parasitic radiation. Another advantage is the improved electrical performance of discontinuities such as shorts, opens, steps and bends. As a result of these characteristics, the design process is simplified since less circuit tuning or compensation is necessary, and fabrication steps such as via-holes and substrate thinning are not required. Some examples of the possible performance improvements over conventional substrate-supported coplanar waveguide are given in the following sections.

2.4.1 Dispersion and Parasitic Modes

The term *dispersion* refers to the distortion of a signal that results when different frequency components propagate at different phase velocities. The phenomenon arises in any single-conductor waveguide, or on a non-TEM planar transmission line. For example, longitudinal field components must exist in two-conductor lines which have lossy dielectrics or conductors, leading to a frequency-dependent phase velocity. In low-loss materials, however, the transverse field components are much larger than the longitudinal components, so that these effects may often be neglected. Another cause of dispersion is the presence of inhomogeneous dielectric layers in the propagation medium, since a true transverse electric-magnetic wave can only exist in a homogeneous environment. Therefore, planar lines with different substrate and superstrate layers will always have modes with non-zero longitudinal fields. In addition,

the phase velocities of the "even" and "odd" modes in a coplanar-waveguide type line can exhibit very different frequency behavior [16]. This limits the bandwidth of circuits such as directional couplers, which depend on a fixed phase relationship between the two modes. Overall, dispersion can degrade the performance of broad-band communications systems since it results in a smearing out of the signal, and corrective measures must be used to compensate for the effects. The advantage of the microshield line in this respect is that there is essentially no dispersion, due to the nearly homogeneous air-dielectric. Furthermore, it has been demonstrated that the even and odd mode propagation velocities are much closer on a membrane-supported line than on GaAs [14].

While dispersion is a concern primarily in broad-band systems, the problem of unwanted propagation modes affects even single frequency applications. A large volume of work has been done to understand the moding behavior in microstrip, slot line, coplanar strips, coplanar waveguide and various related configurations, testifying to the significance of the issue. Specifically for CPW, excellent discussions are presented in [17, 18, 19, 20, 21, 22]. At the fundamental level, it is shown that the substrate thickness and ground plane width must be large relative to the line width (S+2W) to ensure propagation of the odd (desired) CPW-mode [17]. As a minimum, since practical considerations limit the use of very wide ground planes, S+2W must be small relative to the dielectric wavelength [18]. This in turn results in increased conductor loss, as seen in Section 2.3. If these conditions are not met, radiation loss and dispersion may arise due to a variety of different mechanisms. The existence of a lower ground plane, or the metal base plate of a circuit housing, presents ample opportunity for parallel plate mode propagation and the associated resonant phenomena [19]. Approaches used to alleviate these moding difficulties are to employ

multiple substrate layers [20] or to use via-holes to equalize ground potentials, at the expense of increased fabrication complexity. Another form of parasitic modes are the TE and TM surface wave modes which are an inevitable consequence of dielectric interfaces or grounded dielectrics. On high permittivity substrates such as GaAs, silicon, or alumina, leakage from these modes generally starts to occur when the substrate thickness becomes greater than $\lambda_o/10$, where λ_o is the free-space wavelength [21, 22, 23]. If thin substrates are then used to avoid the surface wave modes, line widths must be reduced correspondingly to avoid dispersion. Following all the above arguments to their conclusion, it is clearly discerned that the membrane supported architectures provide the most natural solution to low-loss, broad band, single mode operation. For the microshield line, the only significant mechanism for higher order modes is in the shielding cavity, which must be kept smaller than $\lambda_o/2$ in both dimensions. However, this presents little difficulty due to the capabilities of the micromachining process.

2.4.2 Parasitic Radiation

In the design of compact high-frequency circuits, a critical issue concerns parasitic radiation from the various components and the cross-talk that results. This limits how closely spaced the components can be, and may also necessitate the use of special shielding [6] and/or substrate modifications [20] to prevent excessive performance degradation. The microshield line is particularly desirable in this respect, since the level of parasitic radiation can be significantly lower than that of coplanar lines on high permittivity substrates such as gallium arsenide or silicon. To illustrate, the theoretical performance of a compact open-end tuning stub (Figure 2.8) is shown in Figures 2.9 and 2.10 for semi-infinite substrates of ϵ_r=1.4 and ϵ_r=13, respectively.

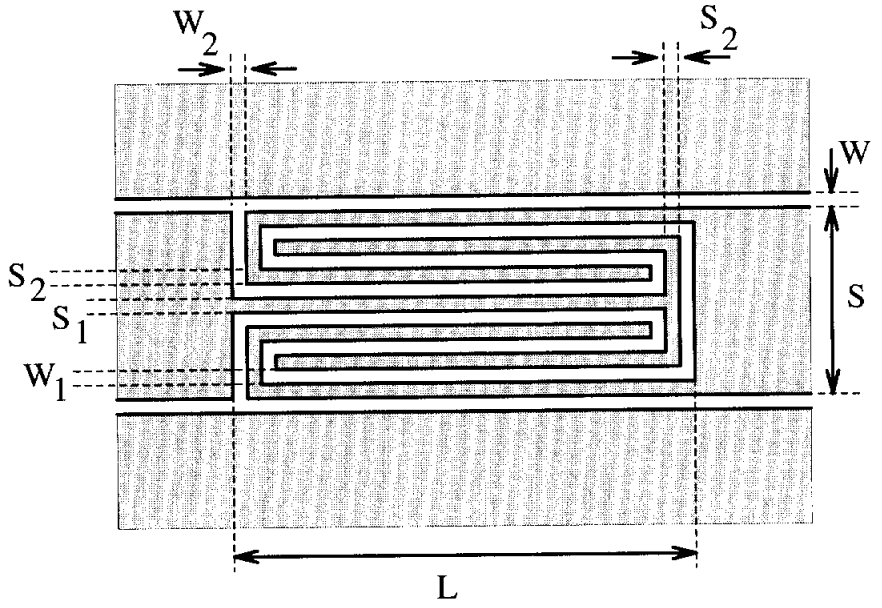

Figure 2.8: Compact open-end stub which is analyzed on semi-infinite substrates with ϵ_r=1.4 (S=260, W=20, S_1=S_2=W_1=W_2=20, L=1140 μm) and ϵ_r=13 (S=130, W=80, S_1=S_2=W_1=W_2=10, L=550 μm).

Both circuits are open to free-space on top. The performance of the stub on the low permittivity substrate is much better than that on the GaAs substrate, and in fact is nearly unchanged when the circuit is fully enclosed in a shielding cavity. At 50 GHz, this circuit loses less than 7% of the power due to radiation, where the loss is defined as $\sqrt{1-|S_{11}|^2-|S_{21}|^2}$. Recall that conductor loss is not taken into account in the full-wave analysis (see Chapter III). In contrast, the stub with the GaAs substrate has considerable radiation loss and its useful frequency range is limited to about 25 GHz, where 15% of the power is already being lost. Significant improvement in this performance is obtained with the use of a lower shielding cavity, verifying that the power loss is through the substrate.

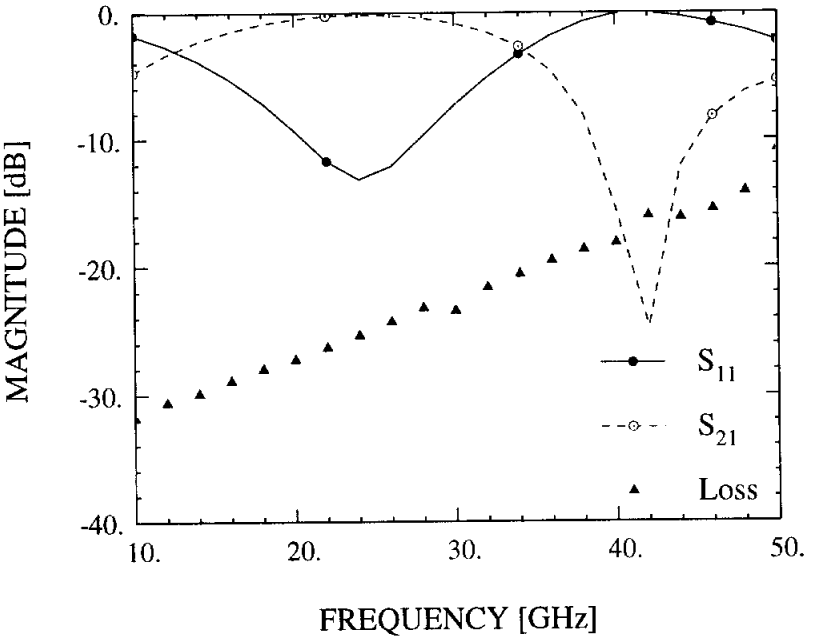

Figure 2.9: Theoretical performance of the stub shown in Figure 2.8 on a dielectric half-space of ϵ_r=1.4.

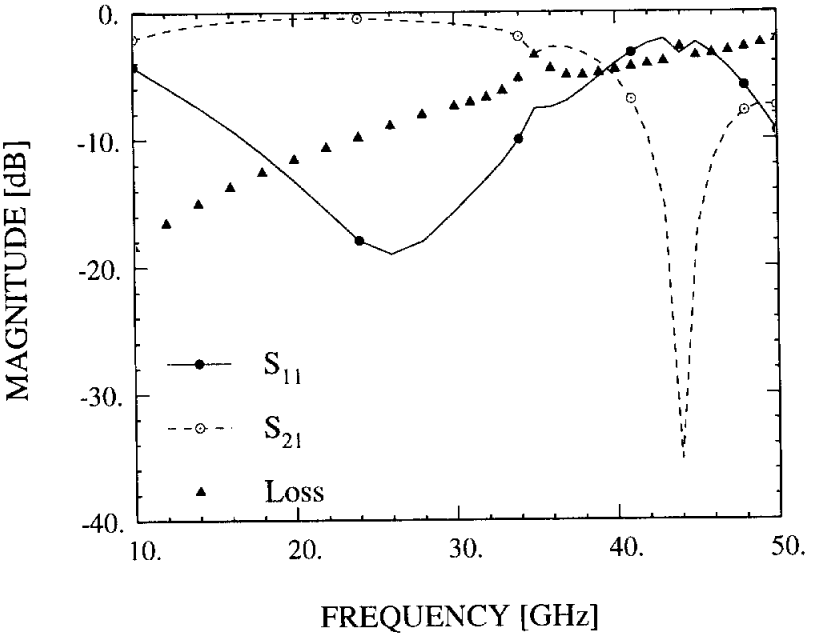

Figure 2.10: Theoretical performance of the stub shown in Figure 2.8 on a dielectric half-space of ϵ_r=13.

2.4.3 Short- and Open-End Discontinuities

The exact electrical length of short-end and open-end discontinuities must be known to accurately predict the frequency response of tuning stubs for narrow-band applications. In order to study the influence of the substrate, the effective length extension [2], ΔL_{sc}, of a grounded coplanar short-end on substrates with ϵ_r=1.25 and ϵ_r=12.9 (GaAs) is shown in Figures 2.11 and 2.12. The plots contain theoretical results from the full-wave analysis described in Chapter III, and from an expression by Getsinger which is applicable for quasi-TEM lines printed on an infinitely-thick dielectric [24]. In Figure 2.11, all lines have S=W=100 μm with substrate thicknesses of 350 and 700 μm, while in Figure 2.12, all lines have a characteristic impedance around 65 Ω. Since the end-effect is completely inductive for pure-TEM operation, the *physical* size of the length extension is nearly independent of the dielectric constant. The shorter wavelength in the GaAs substrate, however, makes the extension become longer electrically. A similar argument can be made regarding the performance of coplanar open-ends. Under the quasi-TEM conditions, the physical length of the effective length extension, ΔL_{oc}, is roughly independent of ϵ_r, for small values of ΔL_{oc}. Again, this results in an increased electrical length when the substrate dielectric constant is higher, and these end effects can become significant since ΔL_{oc} is typically at least twice as large as ΔL_{sc} [25]. Thus, the air-filled environment of the microshield geometry offers the optimum conditions for making circuit performance less susceptible to this type of frequency dependent behavior.

[2]The effective length extension, ΔL_{sc}, is the position at which an ideal short circuit would result in the same impedance seen at the physical end of the line.

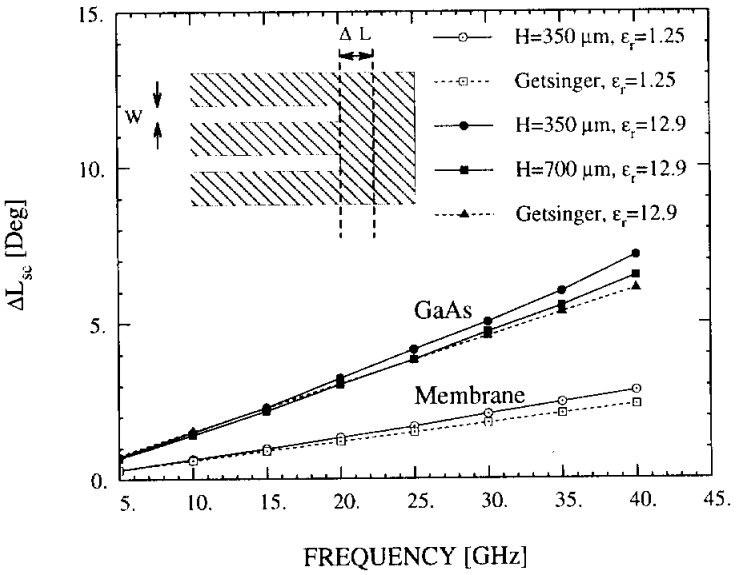

Figure 2.11: Effective length extension (in degrees) for a short-end discontinuity on lines with equal aspect ratios of $S/(S+2W)$=0.33. The characteristic impedance for the lines are 135 Ω (ϵ_r=1.25) and 55 Ω (ϵ_r=12.9). The line parameters are S=100 μm, W=100 μm and the substrate height H is given in the legend.

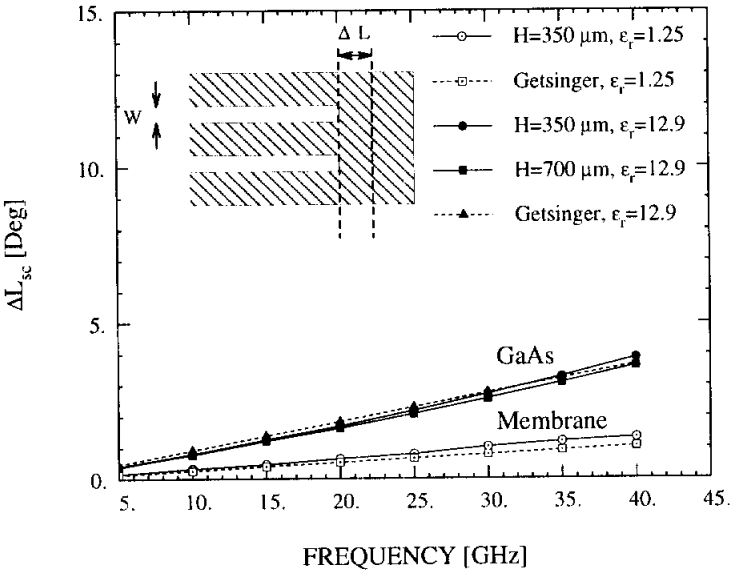

Figure 2.12: Effective length extension (in degrees) for a short-end discontinuity on lines with equal characteristic impedance (65 Ω). The parameters are S=165 μm, W=10 μm for the line with ϵ_r=1.25, and S=40 μm, W=67 μm for the line with ϵ_r=12.9. The substrate height H is given in the legend.

2.4.4 Right-Angle Bend

A very common circuit 'element' in millimeter-wave systems is the right-angle bend. This structure gains significance with increasing frequency due to the parasitic capacitance and inductance which are associated with the abrupt change in the field orientation. These problems, combined with the mode-conversion which can also occur, cause incident power to be reflected back from the discontinuity. In microstrip form, the typical means of improving the return loss is to miter the outside corners of the signal line [26]. This approach is less effective for coplanar waveguide [27], however, and alternative approaches such as air-bridges and dielectric overlays are adopted [28]. Both of these techniques are meant to offset the effects of different electrical path lengths along the two slots. The air-bridges are placed very near to the bend in order to equalize the potential on the outer ground planes, while the overlays lower the phase velocity of the wave in the inside slot relative to that in the outer slot. Without this type of compensation, the asymmetry of the CPW right-angle bend will lead to excitation of the unwanted slot-line (even) mode.

Many of the problems inherent to bends which are printed using conventional CPW line can be minimized with the microshield geometry. The absence of the high dielectric constant material has two important effects: it leads to a reduction in the parasitic capacitance and, for a fixed physical size, it reduces the difference in electrical path lengths through the two slots. In order to demonstrate the potential improvement, a comparison between the measured performance of a 75Ω microshield line bend and a 50Ω CPW line bend on GaAs [27] is shown in Figure 2.13. The microshield bend has an S_{11} which is at least 8 dB lower over the 10-40 GHz band. Although data for a CPW bend similar to the microshield design could not be found, the comparison is justified since the small dimensions of the CPW bend result in an

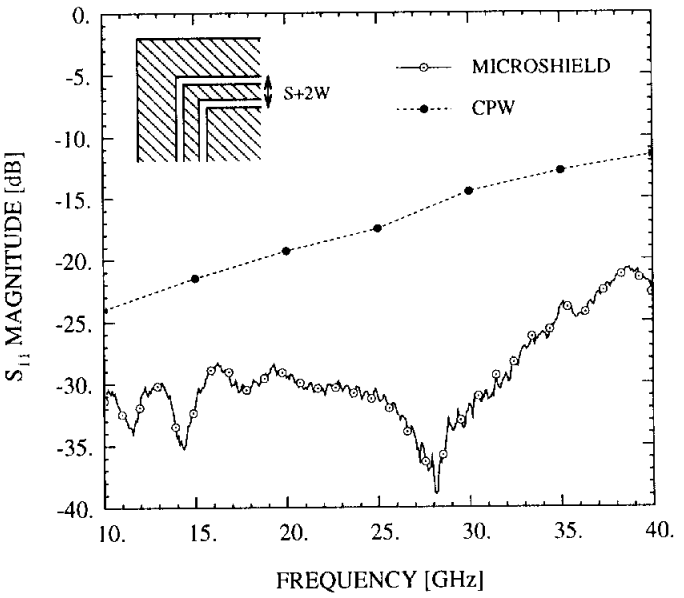

Figure 2.13: Measured performance of right-angle bends fabricated using a microshield line and a CPW line on GaAs. The CPW bend has S=39, W=24, H=90 and uses 2 μm-high air-bridges on each side of the bend [27]. The microshield line has S=250, W=25 and H=350. All dimensions are in microns.

electrical path length difference through the slots which is less than half that in the microshield bend. Measurements were also made with the lower ground plane of the microshield line removed by mounting the circuit on a Styrofoam block. This configuration forfeited the advantage of ground plane equalization through the shielding cavity, however the S_{11} remained below -20 dB. The effects of the slot-line mode must therefore be relatively small, which implies that simplifications in circuit design and fabrication are possible. Specifically, individual components may not need separate shielding cavities or air-bridges to maintain high performance operation.

2.5 Conclusions

This chapter has presented a comprehensive study of some fundamental properties of the microshield line. Its most prominent characteristic is the nearly homo-

geneous air-dielectric, which distinguishes it from conventional substrate-supported coplanar waveguide, and allows operating frequencies to be pushed well into the sub-mm wave regime. It also offers significant benefits at lower microwave frequencies, including reduced attenuation and parasitic radiation, and improved performance for discontinuities such as right-angle bends, as compared to standard CPW. These characteristics combine to make the microshield line a strong candidate for high performance monolithic applications.

CHAPTER III

FULL-WAVE ANALYSIS OF CPW-TYPE DISCONTINUITIES

3.1 Introduction

An accurate space domain integral equation (SDIE) technique for the theoretical characterization of three-dimensional, coplanar waveguide-type discontinuities is presented in this chapter. The approach proceeds the work by Dib [9], where the main theoretical deviations lie in the applicable Green's functions. The method uses a full-wave analysis to solve for the electric field distribution in the slots of the metalization, and inherently accounts for all mutual coupling mechanisms. Circuit parameters, such as the impedance or scattering parameters, are extracted by applying a transmission line analysis to the standing waves which are setup in the CPW feedlines connected at the input/output ports. With regard to the geometries, the circuits may be partially or completely shielded configurations with single substrate layers, such as the microshield designs shown in Figure 1.2. Similar methods for multilayer substrates and superstrates are described in [9, 29].

In this work, the following simplifying assumptions are made:

1. Metalization layers are infinitely thin and perfectly conducting.

2. Ground planes are of infinite extent.

3. Dielectric materials are loss-free.

4. Shielding cavities are rectangular.

Although these assumptions represent approximations to actual physical configurations, there generally is not significant error introduced by their use. Common thin-film fabrication techniques for microwave and mm-wave applications utilize low-loss metals (e.g. gold) which are applied in layers ranging in thickness from about 0.5 μm to 3 μm, much less than $\frac{1}{100}^{th}$ of a wavelength. Also, the ground planes on CPW-type circuits are typically designed to be wide enough that non-ideal effects, which might arise from finite ground planes, can be avoided. Finally, with the exception of lines such as the MIS (metal-insulator-substrate) line, most circuits are designed using low-loss substrates such as semi-insulating GaAs, high-resistivity silicon, alumina, or air (in the case of the microshield line). For these applications, dielectric losses remain essentially a second-order effect for operating frequencies into the millimeter-wave regime. In contrast, conductor losses often contribute to noticeable discrepancies between theoretical and experimental data, even when low-loss metals are employed. Although small differences occur in the propagation constant [30], the dominant effect is manifested as a decrease in the magnitude of the scattering parameters. Incorporating conductor loss into this analysis, however, would require significant modifications and the computational efficiency would suffer.

In the following sections, the complete theoretical method is presented in the order of application. First, the magnetic field integral equation will be derived, along with the necessary Green's functions. Next, the method of moments solution is outlined and the resulting admittance matrix elements are evaluated in detail. Finally, the excitation of the numerical system and the general method for network

parameter extraction is presented. For the remainder of this work, the assumed time dependence $e^{j\omega t}$ is suppressed for simplicity.

3.2 Space Domain Integral Equation

The integral equation to be derived in this section is based on enforcing the continuity of the tangential electric and magnetic fields across the openings in the circuit metalization. To this end, consider the cross-section shown in Figure 3.1. Using the equivalence principle [31], this geometry is separated into isolated half-spaces by placing fictitious metal surfaces in the slot openings, S_{eq}, and the original fields are maintained by imposing equivalent current sources just above and below each side of the boundary. The equivalent sources must satisfy the following:

$$\begin{aligned} \vec{J}_{eq} &= \hat{n} \times \vec{H} \\ \vec{M}_{eq} &= \vec{E} \times \hat{n} \end{aligned} \tag{3.1}$$

where $\hat{n}$ is the outward unit normal and $\vec{E}$ and $\vec{H}$ are the original fields over the surface, $S_o + S_{eq}$. Outside the fictitious planes which were introduced, the tangential electric field is zero. Also, using reciprocity, it can be shown that an electric current just above a perfect electric conductor will not radiate. Based on these two facts, the only equivalent current of interest is $\vec{M}_{eq}$ above and below the surfaces S_{eq}. Furthermore, in order to satisfy continuity of the tangential electric field across S_{eq}, we simply require that:

$$\vec{M}_{eq,1} = -\vec{M}_{eq,2} = \vec{M}_{eq} \tag{3.2}$$

in the absence of any *impressed* magnetic current sources.

The remaining boundary condition that must be satisfied is the continuity of the

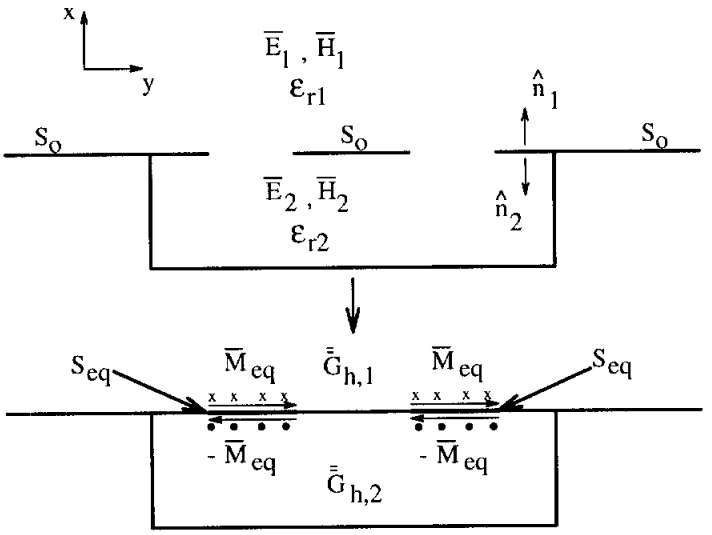

Figure 3.1: Cross-section of a coplanar waveguide line with a lower shielding cavity. The equivalent geometry is shown below, where fictitious metal surfaces and magnetic currents have been introduced into the slot openings.

tangential magnetic field. For this, use is made of the following [31]:

$$\vec{H} = \int\int_{S'} \bar{\bar{G}}_h\left(\vec{r},\vec{r'}\right) \cdot \vec{M}_{eq}\left(\vec{r'}\right) ds' \tag{3.3}$$

where $\bar{\bar{G}}_h$ is the dyadic Green's function for a given region of space and S' defines the surface over which the magnetic current exists. Utilizing Eqns. 3.2 and 3.3, we arrive at the necessary integral equation:

$$\begin{aligned} \vec{J}_s &= \hat{n}_1 \times \left[\vec{H}_1 - \vec{H}_2\right] \\ \vec{J}_s &= \hat{n}_1 \times \int\int_{S'} \left[\bar{\bar{G}}_{h,1} + \bar{\bar{G}}_{h,2}\right] \cdot \vec{M}_{eq}\, ds' \end{aligned} \tag{3.4}$$

For treatment of the general circuit configuration, separate Green's functions are used in regions 1 and 2, and these functions are presented in the following sections. The impressed electric current $\vec{J}_s$ is used as the excitation mechanism, as described in Section 3.3.2.

3.2.1 Green's Function for a Rectangular Cavity

A Green's function is defined as the response of a linear system to an impulse of unit strength. In electromagnetic applications, it is used to describe the fields at any location in space within a given region, due to a point source. For the shielding cavity of a planar line, the region of interest is a rectangular waveguide cavity such as that shown in Figure 3.2. Inside the cavity is a point magnetic current source, $\vec{M}$, given by

$$\vec{M} = (\hat{y} + \hat{z})\delta(x - x')\delta(y - y')\delta(z - z') \tag{3.5}$$

and related to this delta source is a vector potential, $\vec{G}_c$, that satisfies the Helmholtz equation:

$$\nabla^2\vec{G}_c + k^2\vec{G}_c = \epsilon\vec{M} \tag{3.6}$$

where k is the wavenumber in the medium. In the problems considered here, the magnetic current source is confined to the $y-z$ plane, and so it is seen from Eqn. 3.6 that the vector potential will also contain only y and z components. Furthermore, once the proper form of $\vec{G}_c$ is known, the associated electric and magnetic fields are found from the following:

$$\begin{aligned} \vec{H} &= \frac{j}{\omega\epsilon\mu}\left(k^2 + \nabla\nabla\cdot\right)\vec{G}_c \\ \vec{E} &= \frac{1}{\epsilon}\nabla \times \vec{G}_c \end{aligned} \tag{3.7}$$

This methodology is referred to as vector potential theory, and the derivation of Eqns. 3.6 and 3.7 can be found in ([32], Chp. 3).

In order to ascertain the necessary magnetic field dyadic Green's function from these equations, it is recognized that $\vec{H}$ can be expressed as the sum of contributions

from the point sources M_y (through $G_{c,y}$) and M_z (through $G_{c,z}$). The dyadic function can thus be extracted as:

$$\begin{aligned}
\bar{\bar{G}}_c &= \hat{y}\hat{y}G_{c,yy} + \hat{y}\hat{z}G_{c,yz} + \hat{z}\hat{y}G_{c,zy} + \hat{z}\hat{z}G_{c,zz} \\
G_{c,yy} &= \frac{j}{\omega\epsilon\mu}\left(k^2 + \frac{\partial^2}{\partial y^2}\right)G_{c,y} \\
G_{c,yz} &= \frac{j}{\omega\epsilon\mu}\frac{\partial}{\partial y}\frac{\partial}{\partial z}G_{c,z} \\
G_{c,zy} &= \frac{j}{\omega\epsilon\mu}\frac{\partial}{\partial z}\frac{\partial}{\partial y}G_{c,y} \\
G_{c,zz} &= \frac{j}{\omega\epsilon\mu}\left(k^2 + \frac{\partial^2}{\partial z^2}\right)G_{c,z}
\end{aligned} \tag{3.8}$$

It remains to determine the correct form for the vector potential function. Since Eqn. 3.6 can be solved independently for each component y, z, consider first the y-component:

$$\nabla^2 G_{c,y} + k^2 G_{c,y} = \epsilon M_y = \epsilon\delta(x - x')\delta(y - y')\delta(z - z') \tag{3.9}$$

Using the method of separation of variables, two general solutions to the homogeneous (source-free) second-order equation can be written as

$$G_y^{I,II} = A_y^{I,II} R^{I,II}(x) S(y) T(z) \tag{3.10}$$

where $A_y^{I,II}$ are unknown coefficients and the subscript c has been dropped. From the expression for $\vec{E}$ in Eqn. 3.6, and imposing the boundary condition $\hat{n} \times \vec{E} = 0$ on the cavity sidewalls, it is immediately found that the complete set of solutions is:

$$\begin{aligned}
G_y^I &= \sum_m \sum_n A_y^I cos(k_x x) sin(k_y y) cos(k_z z) \\
G_y^{II} &= \sum_m \sum_n A_y^{II} cos(k_x (x - a)) sin(k_y y) cos(k_z z)
\end{aligned} \tag{3.11}$$

where

$$k_y = \frac{m\pi}{b}, \qquad k_z = \frac{n\pi}{c}, \qquad k_x = \sqrt{k^2 - k_y^2 - k_z^2} \tag{3.12}$$

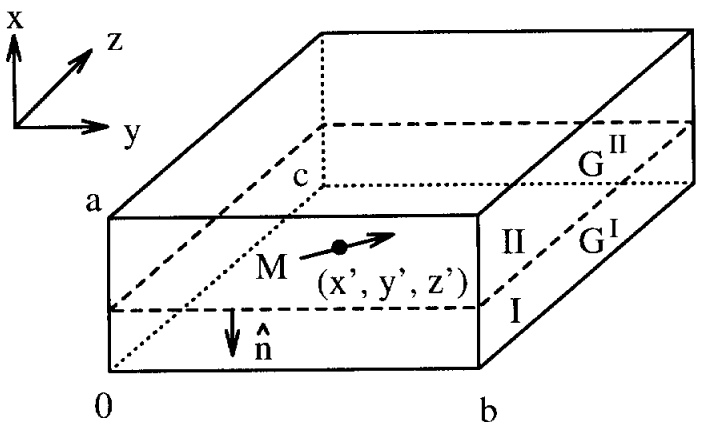

Figure 3.2: Rectangular waveguide cavity with a point source magnetic current, $\vec{M}$. The cavity is separated into two regions about $x = x'$.

In these steps the cavity has been separated into regions for $x \leq x'$ and $x \geq x'$, as depicted in Figure 3.2. As a result, k_x is a function of the separation equation given in Eqn. 3.12 and may become imaginary, in which case the proper root must be chosen to ensure exponential decay away from the source in the x-direction. Furthermore, the existence of only two independent eigenvalues, k_y and k_z, is consistent with the intuitive understanding that the source discontinuity fixes one degree of freedom.

With the homogeneous solution in hand, it is necessary to find the particular solution and thereby determine the unknown coefficients. First, using the argument that the potential must be continuous at $x = x'$ [33], it is required that:

$$A_y^{II} = A_y^I \frac{cos(k_x x')}{cos(k_x(x' - a))} \tag{3.13}$$

We now return to the 2^{nd} order P.D.E, rewriting it as:

$$\left(\frac{\partial^2}{\partial x^2} - k_y^2 - k_z^2 + k^2\right) G_y = \epsilon\delta(x - x')\delta(y - y')\delta(z - z') \tag{3.14}$$

By integrating both sides of 3.14 across the boundary at $x = x' \pm \Delta$, as $\Delta \to 0$, it is

found that

$$\left.\frac{\partial G_y^{II}}{\partial x}\right|_{x=x'} - \left.\frac{\partial G_y^{I}}{\partial x}\right|_{x=x'} = \epsilon\delta(y-y')\delta(z-z') \tag{3.15}$$

$$-\sum_{m,n} A_y^{II} sin(k_x(x'-a))k_x sin(k_y y)cos(k_z z) \; + \sum_{m,n} A_y^{I} k_x sin(k_x x')k_x sin(k_y y)cos(k_z z) = \epsilon\delta(y-y')\delta(z-z') \tag{3.16}$$

Finally, each side of each 3.16 is multiplied by

$$sin\left(\frac{m'\pi}{b}y\right) cos\left(\frac{n'\pi}{c}z\right) \tag{3.17}$$

and integrated from $y = 0, b$ and $z = 0, c$. For $m = m'$ and $n = n'$, orthogonality of the trigonometric functions leads to:

$$A_y^I = \frac{\epsilon cos(k_x(x'-a))sin(k_y y')cos(k_z z')}{k_x sin(k_x a)\, b\, c\, \tau_m \tau_n}$$

$$\tau_i = \begin{cases} 1 & \text{i} = 0 \\ \frac{1}{2} & \text{i} > 0 \end{cases} \tag{3.18}$$

The potential $G_{c,y}$ is completely defined through Eqns. 3.11, 3.13 and 3.18. Also, the solution for $G_{c,z}$ can be immediately found by interchanging the y, y' and z, z' dependence in $G_{c,y}$.

The dyadic Green's functions components of Eqn. 3.8 can now be expressed in their final form. By considering that the fields will always be evaluated at $x = x' = 0$ (bottom wall of cavity) or at $x = x' = a$ (top wall of cavity) for the problems of interest here, it becomes necessary to utilize only one set of equations, since the potential functions from Regions I and II are continuous at the separation boundary. Arbitrarily choosing the potentials from Region I, the following expressions are obtained:

$$G_{c,yy} = \sum_{m=0}^{\infty}\sum_{n=0}^{\infty} \frac{j}{\omega\epsilon\mu}\left(k^2 - k_y^2\right) A_y^I cos(k_x x)sin(k_y y)cos(k_z z)$$

$$
\begin{aligned}
G_{c,yz} &= \sum_{m=0}^{\infty}\sum_{n=0}^{\infty}\frac{-j}{\omega\epsilon\mu}k_y k_z A_z^I cos(k_x x)sin(k_y y)cos(k_z z) \\
G_{c,zy} &= \sum_{m=0}^{\infty}\sum_{n=0}^{\infty}\frac{-j}{\omega\epsilon\mu}k_y k_z A_y^I cos(k_x x)cos(k_y y)sin(k_z z) \\
G_{c,zz} &= \sum_{m=0}^{\infty}\sum_{n=0}^{\infty}\frac{j}{\omega\epsilon\mu}\left(k^2 - k_z^2\right)A_z^I cos(k_x x)cos(k_y y)sin(k_z z) \\
A_y^I &= \frac{\epsilon cos(k_x(x'-a))sin(k_y y')cos(k_z z')}{k_x sin(k_x a)\, b\, c\, \tau_m \tau_n} \\
A_z^I &= \frac{\epsilon cos(k_x(x'-a))cos(k_y y')sin(k_z z')}{k_x sin(k_x a)\, b\, c\, \tau_m \tau_n}
\end{aligned}
\tag{3.19}
$$

A final comment regarding the separation about $x = x'$ is of interest. In treating the infinitely long waveguide problem, it is necessary to utilize exponential functions and enforce the radiation condition along the direction of propagation. This dictates that the separation must also be taken along the waveguide axis, since the step equivalent to Eqn. 3.17 can only be applied in the cross-section. In contrast, the boundary conditions inside a rectangular cavity are satisfied using trigonometric functions in all three dimensions. This being the case, there are no obstacles to applying the method used here for separation about any plane, which is analogous to stating that alternative *mode sets* can be used to describe the fields [31]. If possible, however, it is convenient to choose the separation such that the partial derivative of the vector potential in this direction will not be computed. As shown by Eqn. 3.16, the derivative is discontinuous at the source point, and thus additional care must be taken to evaluate field components which are functions of this term ([34], App. B). For the particular problem being considered here, with magnetic fields which are driven by magnetic currents in the same $(y-z)$ plane, the separation is chosen to be normal to this plane and the discontinuity is thus avoided (refer to Eqn. 3.8).

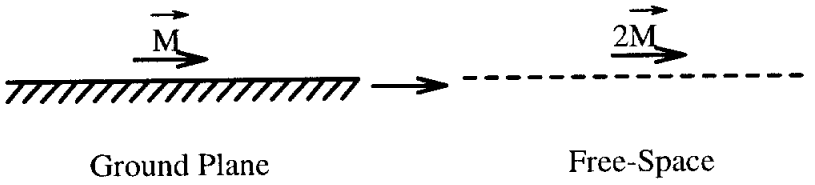

Figure 3.3: Magnetic current source located above a ground plane in a dielectric half-space, and the equivalent problem for the upper half-space with the ground plane removed.

3.2.2 Green's Function for a Dielectric Half-Space

The Green's function associated with a magnetic current source that is located just above an infinite ground plane, and immersed in a homogeneous dielectric half-space, is easily found by invoking the equivalence principle. As illustrated in Figure 3.3, the situation in the upper half-space is equivalent to one in which the current source is doubled in strength and the ground plane is removed, and one for which the free-space Green's function G_o applies.

A derivation of the necessary dyadic Green's function components can be carried out using the vector potential method from Section 3.2.1 ([33], Chp. 1). To start, the scalar Helmholtz equation is written using spherical components in the following form:

$$\nabla^2 G_o(\tilde{r}) + k^2 G_o(\tilde{r}) = \epsilon\delta(\vec{r} - \vec{r'}) \tag{3.20}$$

where $\tilde{r} = |\vec{r} - \vec{r'}|$ represents the distance between the observation and source points. The solution to 3.20 must satisfy the radiation condition, $G_o \to 0$ as $\tilde{r} \to \infty$, and thus an exponential function is the obvious choice. Furthermore, it can be shown by direct differentiation that

$$\nabla^2 \left(\frac{e^{-jk\tilde{r}}}{\tilde{r}} \right) = e^{-jk\tilde{r}} \nabla^2 \left(\frac{1}{\tilde{r}} \right) - \frac{k^2}{\tilde{r}} e^{-jk\tilde{r}} \tag{3.21}$$

Rearranging this equation yields

$$\nabla^2\left(\frac{e^{-jk\tilde{r}}}{\tilde{r}}\right)+k^2\frac{e^{-jk\tilde{r}}}{\tilde{r}} \;=\; e^{-jk\tilde{r}}\nabla^2\left(\frac{1}{\tilde{r}}\right) \tag{3.22}$$

Since $\nabla^2(1/\tilde{r})$ is equal to zero except at $\tilde{r}=0$ (sifting property), the exponential term on the right-hand side can be dropped since it equals unity at this non-zero point. Thus, by comparing 3.20 and 3.22, a solution for G_o can be written as

$$G_o \;=\; C\frac{e^{-jk\tilde{r}}}{\tilde{r}} \tag{3.23}$$

where C must be used to account for the difference in source functions $\epsilon\delta(\vec{r}-\vec{r'})$ and $\nabla^2(1/\tilde{r})$, in 3.20 and 3.22, respectively. To determine C, the following relations are utilized:

$$\begin{aligned} \int_V\left(\nabla^2+k^2\right)C\tfrac{e^{-jk\tilde{r}}}{\tilde{r}}\,dV &= \int_V \epsilon\delta(\vec{r}-\vec{r'})\,dV \;=\; \epsilon \\ \int_V\left(\nabla^2+k^2\right)\tfrac{e^{-jk\tilde{r}}}{\tilde{r}}\,dV &= \int_V\nabla^2\left(\tfrac{1}{\tilde{r}}\right)\,dV \;=\; -4\pi \end{aligned} \tag{3.24}$$

showing that

$$C \;=\; -\frac{\epsilon}{4\pi} \tag{3.25}$$

The first relation in Eqn. 3.24 comes from a defining property of the Dirac delta function, i.e. the normalization property. The second relation is derived in ([33], p. 45), and along with the sifting property cited above, demonstrates that $-\nabla^2(1/4\pi\tilde{r})$ possesses the same properties as a delta function.

As the final step, the components of the dyadic Green's function are found as in Section 3.2.1:

$$\begin{aligned} \bar{\bar{G}}_o &= \hat{y}\hat{y}G_o+\hat{y}\hat{z}G_o+\hat{z}\hat{y}G_o+\hat{z}\hat{z}G_o \\ G_{o,yy} &= \frac{j}{\omega\epsilon\mu}\left(k^2+\frac{\partial^2}{\partial y^2}\right)2G_o \\ G_{o,yz} &= \frac{j}{\omega\epsilon\mu}\frac{\partial}{\partial y}\frac{\partial}{\partial z}2G_o \end{aligned}$$

$$G_{o,zy} = \frac{j}{\omega\epsilon\mu}\frac{\partial}{\partial z}\frac{\partial}{\partial y}2G_o$$
$$G_{o,zz} = \frac{j}{\omega\epsilon\mu}\left(k^2 + \frac{\partial^2}{\partial z^2}\right)2G_o \tag{3.26}$$

A factor of two has been included here to account for the necessary doubling of the magnetic current.

3.3 Method of Moments

The method of moments [35] is a numerical technique which is useful for solving inverse problems of the form

$$L(f) = g \tag{3.27}$$

where L is a known linear (integral) operator, g is a known excitation, and f is the unknown system response. The method proceeds by first approximating f as a linear combination of N terms, each of which consists of a known *expansion* or *basis* function with an associated unknown coefficient. Substituting this approximation into Eqn. 3.27 results in a linear equation with N unknowns,

$$\sum_{n=1}^{N} c_n L(f_n^a) = h + \Delta h \tag{3.28}$$

where c_n and f_n^a are the coefficients and expansion functions, respectively. The term Δh is the inherent residual error that is introduced by the approximation to f. Depending on the application, entire domain or subdomain basis functions may be used, signifying whether f_n^a is non-zero throughout the domain of f or, more commonly, only in a specific cell.

As Eqn. 3.28 is an under-determined system, some set of N linearly independent equations are necessary to resolve the unknown coefficients. For this, N independent *weighting* or *testing* functions are first utilized: $\{w_m\} = w_1, ..., w_N$. In addition, an

inner product such as the following is defined:

$$< w, g > \;=\; \int\int (w \cdot g)\, ds \tag{3.29}$$

The necessary system of equations can now be generated by forming inner-products between the set of testing functions and each side of Eqn. 3.28. This technique, known as the method of weighted residuals, enforces the boundary conditions in an average sense over the entire surface. In this way, the residual Δh also approaches zero in an average sense, rather than being forced to zero at each point. The resulting system can then be written as

$$\sum_{n=1}^{N} c_n \left\langle L(f_n^a), w_m \right\rangle = \left\langle h, w_m \right\rangle \qquad \text{m=1,...,N} \tag{3.30}$$

After assembling 3.30 into matrix form, the solution is obtained as follows:

$$[c_n] \;=\; \left[\langle L(f_n^a), w_m \rangle\right]^{-1} \left[\langle h, w_m \rangle\right] \tag{3.31}$$

The matrix inversion is performed using a suitable technique such as LU decomposition with back substitution.

The linear system of interest for this research is that described by Eqn. 3.4. In accordance with the method just described, a suitable expansion of the unknown magnetic current distribution is necessary. First, the slot apertures are subdivided into small rectangles as shown in Figure 3.4. The current expansion is then defined as:

$$\vec{M}_{eq}(y', z') \;=\; \hat{y} \sum_{i=1}^{N_y} \sum_{j=1}^{N_z+1} V_{y,ij} f_i(y') g_j(z') + \hat{z} \sum_{p=1}^{N_z} \sum_{q=1}^{N_y+1} V_{z,pq} f_p(z') g_q(y') \tag{3.32}$$

where $V_{y,z}$ are the unknown amplitude coefficients and the primed coordinates are reserved for the source designation. The basis functions, f and g, are chosen to have

a piecewise sinusoidal variation in the direction of the current, and constant variation in the transverse direction. These are defined as follows:

$$
\begin{aligned}
f_n(\zeta') &= \begin{cases} \frac{sin(k_m\,(\zeta'-\zeta_{n-1}))}{sin(k_m\,l_n)} & \text{if } \zeta_{n-1} < \zeta' < \zeta_n \\ \frac{sin(k_m\,(\zeta_{n+1}-\zeta'))}{sin(k_m\,l_{n+1})} & \text{if } \zeta_n < \zeta' < \zeta_{n+1} \\ 0 & \text{elsewhere} \end{cases} \\
g_n(\xi') &= \begin{cases} 1 & \text{if } \xi_{n-1} < \xi' < \xi_n \\ 0 & \text{elsewhere} \end{cases} \\
l_n &= |\zeta_n - \zeta_{n-1}| \\
l_{n+1} &= |\zeta_{n+1} - \zeta_n|
\end{aligned}
\tag{3.33}
$$

where k_m is a scaling parameter which is set equal to the wavenumber in the region with the highest permittivity. As discussed in [36], an offset is used between the y and z current components in order to enforce the proper edge conditions and to allow each current element to generate cross-polarized fields on its own subsection.

The current expansion is then substituted into Eqn. 3.4, and inner-products are formed as defined in Eqn. 3.29 using weighting functions which are identical to the basis functions (Galerkin's technique). These steps result in the following system of equations:

$$
\begin{pmatrix} [Y_{1,yy} + Y_{2,yy}] & [Y_{1,yz} + Y_{2,yz}] \\ [Y_{1,zy} + Y_{2,zy}] & [Y_{1,zz} + Y_{2,zz}] \end{pmatrix} \begin{pmatrix} [V_y] \\ [V_z] \end{pmatrix} = \begin{pmatrix} [I_z] \\ [I_y] \end{pmatrix} \tag{3.34}
$$

where $[V_{y,z}]$ are coefficient vectors for the current expansion functions and $[I_{y,z}]$ are vectors of weighted integrals of $J_{y,z}$ over a subsection (see Section 3.3.2). The $[Y_{t,\zeta\xi}]$ terms represent blocks of the admittance matrix, with subscript $t = 1, 2$ used to distinguish between contributions from the lower and upper half-space (see Figure 3.1).

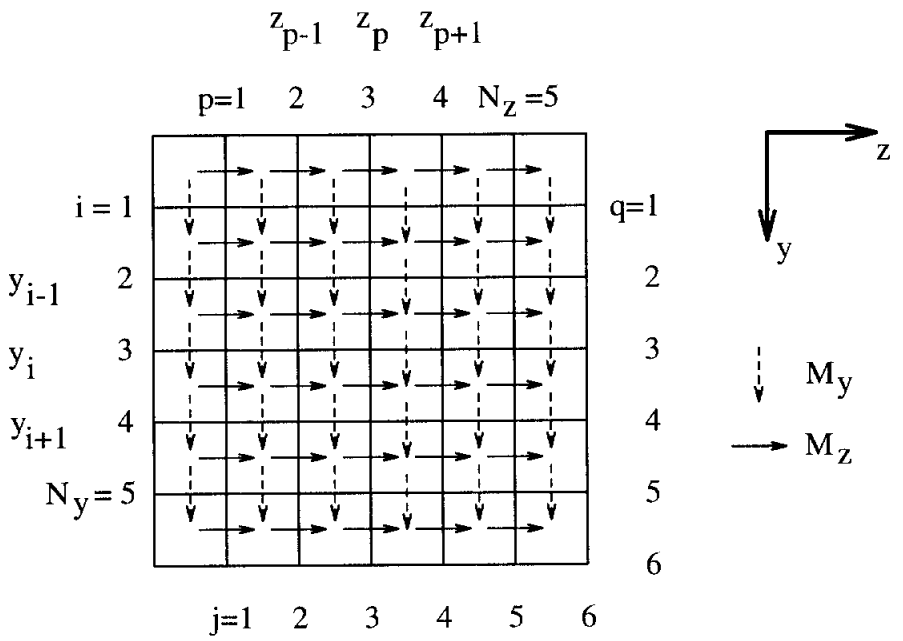

Figure 3.4: Example showing the subdivision of a slot surface into rectangular cells and the basis function distribution used to model the equivalent magnetic current (refer to Eqn. 3.33).

These elements are defined as follows:

$$\begin{aligned}
Y_{t,yy}(k,l/i,j) &= \int_S \int_{S'} f_k(y) g_l(z)\, G_{t,yy}\, f_i(y') g_j(z')\, ds'\, ds \\
Y_{t,yz}(k,l/p,q) &= \int_S \int_{S'} f_k(y) g_l(z)\, G_{t,yz}\, f_p(z') g_q(y')\, ds'\, ds \\
Y_{t,zy}(r,s/i,j) &= \int_S \int_{S'} f_r(z) g_s(y)\, G_{t,zy}\, f_i(y') g_j(z')\, ds'\, ds \\
Y_{t,zz}(r,s/p,q) &= \int_S \int_{S'} f_r(z) g_s(y)\, G_{t,zz}\, f_p(z') g_q(y')\, ds'\, ds
\end{aligned} \tag{3.35}$$

3.3.1 Admittance Elements

Rectangular Cavity

Recalling that the fields are evaluated at $x = x' = 0$ or a, the admittance terms which pertain to the rectangular cavity Green's function are found to be:

$$\begin{aligned}
Y_{yy}(k,l/i,j) &= \sum_{m=0}^{M_{max}} \sum_{n=0}^{N_{max}} \frac{j}{\omega\mu}(k^2 - k_y^2) \frac{I_{S,i}(y') I_{C,j}(z') I_{S,k}(y) I_{C,l}(z)}{k_x tan(k_x a) bc \tau_m \tau_n} \\
Y_{yz}(k,l/p,q) &= \sum_{m=0}^{M_{max}} \sum_{n=0}^{N_{max}} \frac{-j}{\omega\mu} k_y k_z \frac{I_{S,k}(y) I_{C,l}(z) I_{S,p}(z') I_{C,q}(y')}{k_x tan(k_x a) bc \tau_m \tau_n} \\
Y_{zy}(r,s/i,j) &= \sum_{m=0}^{M_{max}} \sum_{n=0}^{N_{max}} \frac{-j}{\omega\mu} k_z k_y \frac{I_{S,i}(y') I_{C,j}(z') I_{S,r}(z) I_{C,s}(y)}{k_x tan(k_x a) bc \tau_m \tau_n} \\
Y_{zz}(r,s/p,q) &= \sum_{m=0}^{M_{max}} \sum_{n=0}^{N_{max}} \frac{j}{\omega\mu}(k^2 - k_z^2) \frac{I_{S,p}(z') I_{C,q}(y') I_{S,r}(z) I_{C,s}(y)}{k_x tan(k_x a) bc \tau_m \tau_n}
\end{aligned} \tag{3.36}$$

where $I_{C,S}$ are the space-domain integrals which result from the application of Galerkin's method:

$$\begin{aligned}
I_{C,i}(\xi) &= \int_{\xi_{i-1}}^{\xi_i} cos(k_\xi(\xi - \xi_b))\, d\xi \\
&= \begin{cases} (\xi_i - \xi_{i-1}) & k_\xi = 0 \\ \dfrac{2sin\left(k_\xi \frac{\xi_i - \xi_{i-1}}{2}\right) cos\left(k_\xi\left(\frac{\xi_{i-1}+\xi_i}{2} - \xi_b\right)\right)}{k_\xi} & k_\xi > 0 \end{cases} \\
I_{S,i}(\zeta) &= \left(\int_{\zeta_{i-1}}^{\zeta_i} \frac{sin(k_m(\zeta - \zeta_{i-1}))}{sin(k_m l_i)} + \int_{\zeta_i}^{\zeta_{i+1}} \frac{sin(k_m(\zeta_{i+1} - \zeta))}{sin(k_m l_{i+1})} \right) sin(k_\zeta(\zeta - \zeta_b))\, d\zeta
\end{aligned} \tag{3.37}$$

$$= \begin{cases} sin(k_\zeta(\zeta_i - \zeta_b))\frac{k_m}{k_m^2 - k_\zeta^2}\left[\frac{cos(k_\zeta l_i) - cos(k_m l_i)}{sin(k_m l_i)} + \frac{cos(k_\zeta l_{i+1}) - cos(k_m l_{i+1})}{sin(k_m l_{i+1})}\right] \\ \\ +cos(k_\zeta(\zeta_i - \zeta_b))\frac{1}{k_m^2 - k_\zeta^2}\left[\frac{k_\zeta sin(k_m l_i) - k_m sin(k_\zeta l_i)}{sin(k_m l_i)} - \frac{k_\zeta sin(k_m l_{i+1}) - k_m sin(k_\zeta l_{i+1})}{sin(k_m l_{i+1})}\right] \end{cases} \tag{3.38}$$

In Eqns. 3.38, ξ_b and ζ_b denote the coordinates at the lower edge of the cavity in a given dimension, and are assumed to be non-zero for generality. Also, the expressions have been written in a form such that the position dependent factors may be separated out for computational convenience.

Dielectric Half-Space

While analytical solutions are obtained for the admittance terms corresponding to the cavity Green's function, numerical techniques must be used for the dielectric half-space. Beginning with the $y-y$ component of the admittance matrix, it is found from Eqns. 3.23, 3.24, 3.26, and 3.35, that:

$$Y_{yy}(k, l/i, j) = \frac{-j}{2\pi\omega\mu}\int_S f_k(y)g_l(z)\int_{S'} f_i(y')g_j(z')\left(k^2 + \frac{\partial^2}{\partial y^2}\right)\frac{e^{-jk\tilde{r}}}{\tilde{r}}\,ds'\,ds \tag{3.39}$$

where $\tilde{r} = |\vec{r} - \vec{r'}|$. As shown in [37], it is possible to transfer the partial derivatives from the exponential function onto the basis and testing functions using the following fundamental theorem of calculus:

$$\int_a^b v\,du = uv|_a^b - \int_a^b u\,dv \tag{3.40}$$

Noting that the basis functions are identically zero at their respective endpoints, and that

$$\frac{\partial}{\partial y}\frac{e^{-jk\tilde{r}}}{\tilde{r}} = -\frac{\partial}{\partial y'}\frac{e^{-jk\tilde{r}}}{\tilde{r}} \tag{3.41}$$

it is then possible to rewrite Eqn. 3.39 in the following form:

$$\begin{aligned} Y_{yy}(k,l/i,j) &= \frac{-j\omega\epsilon}{2\pi}\left[A_{yy}-B_{yy}\right] \\ A_{yy} &= \int_S f_k(y)g_l(z)\int_{S'} f_i(y')g_j(z')\frac{e^{-jk\tilde{r}}}{\tilde{r}}ds'\,ds \\ B_{yy} &= \frac{1}{k^2}\int_S \dot{f}_k(y)g_l(z)\int_{S'} \dot{f}_i(y')g_j(z')\frac{e^{-jk\tilde{r}}}{\tilde{r}}ds'\,ds \end{aligned} \tag{3.42}$$

where $\dot{f}(y/y')$ denotes the derivative of f with respect to y/y'.

The matter of greatest interest in evaluating 3.42 is the $(1/\tilde{r})$ singularity which exists when the testing and expansion functions overlap, i.e. the self-cell. A variety of analytic and approximate numerical solutions for this type of problem have been published [38, 39, 40], as it is widespread in theoretical electromagnetics. However, a method specifically geared toward use with piecewise sinusoidal (PWS) basis functions seems not to have been previously presented. In the remaining steps of this derivation, therefore, the separation and evaluation of the singularity is the primary focus.

For computational purposes, Y_{yy} will be written as the summation of four subcontributions. Each of these terms represents the interaction between the two functions which comprise the sinusoidal dependence of the expansion and test functions. From Eqn. 3.33, the two parts of the PWS can be denoted as ($f_{y'a}$, $a = 1,2$) for the expansion function, and (f_{yb}, $b = 1,2$) for the test function. With these definitions, and by applying the technique of adding and subtracting the singularity, Eqn. 3.42 can be rewritten as:

$$Y_{yy}(k,l/i,j) = \frac{j\omega\epsilon}{4\pi}\sum_{a=1}^{2}\sum_{b=1}^{2}\frac{(-1)^{a+b}(\Upsilon_{ab}+\Psi_{ab})}{sin(k_m l_{i-1+a})sin(k_m l_{k-1+b})} \tag{3.43}$$

where

$$F_{ab} = F^{\theta}_{ab} + F^{\phi}_{ab} = \left(\frac{k_m^2}{k^2}+1\right)cos(k_m y' + \theta_{ab}) + \left(\frac{k_m^2}{k^2}-1\right)cos(k_m y' + \phi_{ab})$$

$$\Upsilon_{ab} = \int_S \int_{S'} \left(F_{ab}^{\theta} + F_{ab}^{\phi}\right) \left[\frac{cos(k\tilde{r}) - 1}{\tilde{r}} - \frac{jsin(k\tilde{r})}{\tilde{r}}\right] ds'\, ds$$
$$\Psi_{ab} = \int_S \int_{S'} \left(F_{ab}^{\theta} + F_{ab}^{\phi}\right) \left[\frac{1}{\tilde{r}}\right] ds'\, ds \qquad (3.44)$$

and a, b = 1,2. The variables θ_{ab} and ϕ_{ab} are independent of the source coordinates y' and z', and are given by:

$$\theta_{ab} = k_m(y - y_{i+(-1)^a} - y_{k+(-1)^b}) \qquad \phi_{11} = -k_m(y - y_{i+(-1)^a} + y_{k+(-1)^b}) \qquad (3.45)$$

In Eqn. 3.44, the integration is over the respective subdomains of the expansion and test functions, and the transverse (pulse function) dependence is assumed.

The integrals denoted by Υ_{ab} are well-behaved in the limit as $\tilde{r} \rightarrow 0$, and are easy to compute numerically. The Ψ_{ab} integrals are singular, however, thus requiring some form of analytical evaluation. Since a closed-form solution to 3.44 cannot be found directly, a second order expansion of the cosine functions has been used to cast Ψ_{ab} into the following approximation:

$$\Psi_{ab}^{\theta} \approx \left(\frac{k_m^2}{k^2} + 1\right) \int_S \int_{S'} \left(\frac{(1 - \theta_{ab}^2/2) - y' k_m \theta_{ab} - (y' k_m)^2/2}{\tilde{r}}\right) ds'\, ds \qquad (3.46)$$

A similar expression for Ψ_{ab}^{ϕ} is easily found.

Even for a relatively large cell size of $\lambda_g/15$, Eqn. 3.46 introduces less than 0.3% error. Furthermore, using relations from ([41], p. 271), a closed form solution for the interior integral may now be obtained:

$$\Psi_{ab}^{\theta} \approx \left(\frac{k_m^2}{k^2} + 1\right) \int_S (I_1(y,z) + I_2(y,z) + I_3(y,z))\, ds \qquad (3.47)$$

where

$$I_1(y,z) = \left(1 - \frac{(\theta_{ab} + y k_m)^2}{2}\right) \{\tilde{y} \ln(\tilde{z} + \tilde{r}) + \tilde{z} \ln(\tilde{y} + \tilde{r})\} \Big|_{\tilde{y}} \Big|_{\tilde{z}}$$

$$
\begin{aligned}
I_2(y,z) &= \left(\frac{k_m\,(\theta_{ab}+yk_m)}{2}\right)\left\{\tilde{z}\,\tilde{r}+\tilde{y}^2\ln(\tilde{z}+\tilde{r})\right\}\Big|_{\tilde{y}}\Big|_{\tilde{z}} \\
I_3(y,z) &= -\left(\frac{k_m^2}{2}\right)\left\{\frac{\tilde{y}\,\tilde{z}\,\tilde{r}}{6}+\frac{\tilde{y}^3\ln(\tilde{z}+\tilde{r})}{3}-\frac{\tilde{z}^3\ln(\tilde{y}+\tilde{r})}{6}\right\}\Big|_{\tilde{y}}\Big|_{\tilde{z}} \\
\tilde{y} &= y-y' \\
\tilde{z} &= z-z' \\
\tilde{r} &= \sqrt{\tilde{y}^2+\tilde{z}^2}, \qquad x=x'
\end{aligned} \tag{3.48}
$$

The integration over the observation coordinates can now be handled using numerical techniques, and the components of Y_{zz} are derived from these expressions by interchanging y and y' with z and z', respectively. In this research, Gauss quadrature using two-point Gauss-Legendre formulas was utilized for the numerical integration.

The evaluation of the cross-polarization admittance elements, Y_{yz} and Y_{zy}, is conducted in a similar manner. The Y_{yz} term can be written as

$$
Y_{yz}(k,l/p,q) = \frac{-j}{2\pi\omega\mu}\int_S f_k(y)g_l(z)\int_{S'} f_p(z')g_q(y')\frac{\partial}{\partial y}\frac{\partial}{\partial z}\frac{e^{-jk\tilde{r}}}{\tilde{r}}\,ds'\,ds \tag{3.49}
$$

After transferring the partial derivatives onto the basis and testing functions Eqn. 3.49 takes the following form:

$$
Y_{yz}(k,l/p,q) = \frac{j\omega\epsilon}{2\pi k^2}\int_S \dot{f}_k(y)g_l(z)\int_{S'}\dot{f}_p(z')g_q(y')\frac{e^{-jk\tilde{r}}}{\tilde{r}}ds'\,ds \tag{3.50}
$$

At this point, the notation of expressing Y_{yz} as the sum of four sub-contributions is again utilized. In this case, however, the order of integration is rearranged as shown below:

$$
Y_{yz}(k,l/p,q) = \frac{j\omega\epsilon}{2\pi}\frac{k_m^2}{k^2}\sum_{a=1}^{2}\sum_{b=1}^{2}\frac{(-1)^{a+b}(\Phi_{ab}+\Theta_{ab})}{sin(k_m l_{p-1+a})sin(k_m l_{k-1+b})} \tag{3.51}
$$

$$
\Phi_{ab} = \int dy\int dz'\,cos(k_m y-\psi_{ab})cos(k_m z'-\nu_{ab})\int dz\int dy'\left(\frac{cos(k\tilde{r})-1}{\tilde{r}}-\frac{jsin(k\tilde{r})}{\tilde{r}}\right)
$$

$$\Theta_{ab} = \int dy \int dz' \cos(k_m y - \psi_{ab}) \cos(k_m z' - \nu_{ab}) \int dz \int dy' \left(\frac{1}{\tilde{r}}\right) \tag{3.52}$$

where

$$\begin{aligned} \psi_{11} &= k_m y_{k-1} & \nu_{11} &= k_m z_{p-1} \\ \psi_{12} &= k_m y_{k-1} & \nu_{12} &= k_m z_{p+1} \\ \psi_{21} &= k_m y_{k+1} & \nu_{21} &= k_m z_{p-1} \\ \psi_{22} &= k_m y_{k+1} & \nu_{22} &= k_m z_{p+1} \end{aligned} \tag{3.53}$$

Although the technique used to evaluate Ψ_{ab} could also be used for Θ_{ab}, an analytical solution for the singularity can in this case be found directly. Due to the change in the order of integration, the interior integral can be evaluated as follows:

$$\begin{aligned} \int dz \int dy' \frac{1}{\tilde{r}} &= \tilde{y} ln(\tilde{z} + \tilde{r}) + \tilde{z} ln(\tilde{y} + \tilde{r})\big|_{y'}\big|_{z} \\ \tilde{y} &= y' - y \\ \tilde{z} &= z - z' \\ \tilde{r} &= \sqrt{\tilde{y}^2 + \tilde{z}^2}, \qquad x = x' \end{aligned} \tag{3.54}$$

As before, the remaining integrals may be computed numerically, and the components of Y_{zy} are obtained from these expressions by interchanging y and y' with z and z', respectively.

3.3.2 Excitation Vector

The model used here for the excitation mechanism is that of ideal electric current sources, as in [9]. Each source is non-zero at only a single node, and this node is typically chosen to be approximately 1.5 λ_g away from the discontinuity being

studied. The number of sources is equal to the number of individual slots which comprise the "feedlines" that are attached to the discontinuity, i.e. for a CPW or coupled slot-type configuration, two sources are required for a 1-port circuit, and four sources are used for a 2-port circuit.

Assuming the feedlines lie along the z-axis, the functional form of $\vec{J}_s$ at nodes n_1, n_2 for a 1-port excitation can be written as follows:

$$\vec{J}_s = \hat{y}\left(J_{n1}p(y-y_{c1})\delta(z-z_n) + J_{n2}p(y-y_{c2})\delta(z-z_n)\right) \tag{3.55}$$

for the configuration shown in Figure 3.5. In 3.55, $p(y-y_c)$ is a constant (pulse) function which is centered at y_c and is non-zero only across the width of the slot, and $J_{n1,n2}$ denote the amplitudes of the sources. The phase relationship between the sources is used to differentiate between the CPW ($J_{n1} = -J_{n2}$) and slot-line ($J_{n1} = J_{n2}$) excitations.

With regard to the method of moments solution, Eqn. 3.55 leads to the following value for element number n of the excitation vector:

$$\begin{aligned} I_n &= \int\int J_n\delta(z-z_n)p(y-y_{c,n})f_r(z)g_s(y)\,dy\,dz \\ &= J_n w_n \end{aligned} \tag{3.56}$$

In this expression, f_r and g_s are the piecewise sinusoid and pulse test functions associated with node n, and w_n is the width of the node in the y-direction.

3.4 Network Parameter Extraction

This section outlines the methods used to extract network parameters, such as the impedance or scattering parameters, from the electric field distribution which derives from the method of moments solution. Techniques for 1-port, longitudinally symmetric 2-port, and longitudinally asymmetric 2-port networks will be described.

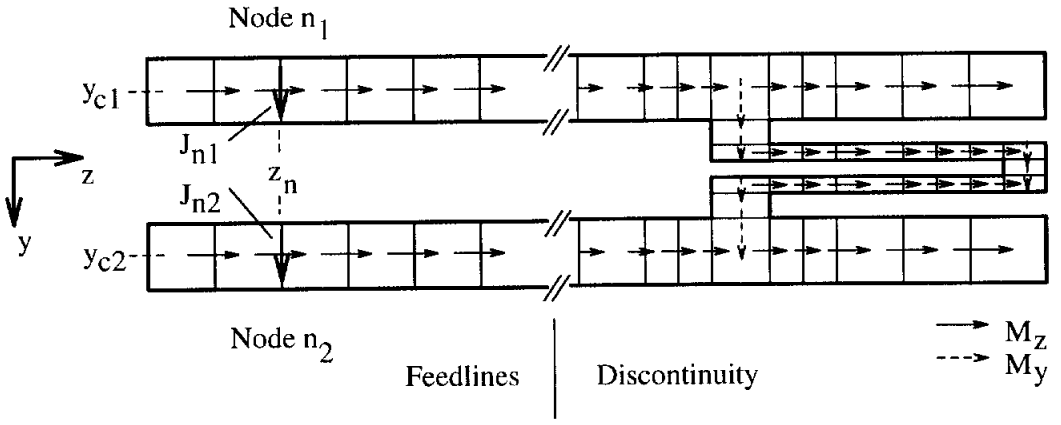

Figure 3.5: Electric current sources for CPW ($J_{n1} = -J_{n2}$) and slot-line ($J_{n1} = J_{n2}$) feedlines. This feed structure is used to characterize 1-port discontinuities such as the circuit shown on the right.

In all cases, the geometries are assumed to possess lateral symmetry such that single mode operation (CPW or slot-line) in the feedlines is maintained. For mixed-mode operation, an extraction technique such as that proposed in [9] may be applied.

The basis of these methods is the determination of the normalized input impedance, z_{in}, at the input/output reference plane of a discontinuity (see Figure 3.6). For this, a cubic-spline interpolation is used to analyze the voltage standing-waveform in the feedlines in order to resolve the values and positions of the minima and maxima [42]. Note that for a given port, either of the two feedlines may be used in the analysis since the E-fields in each slot are either the same (slot-line mode) or 180° out of phase (CPW mode). From these parameters, the guided wavelength (λ_g), standing-wave ratio (swr), and distance from the reference plane to the first voltage maximum (d_{max}) can be calculated. The input impedance is then found as follows:

$$\theta = \frac{4\pi}{\lambda_g} d_{max}$$

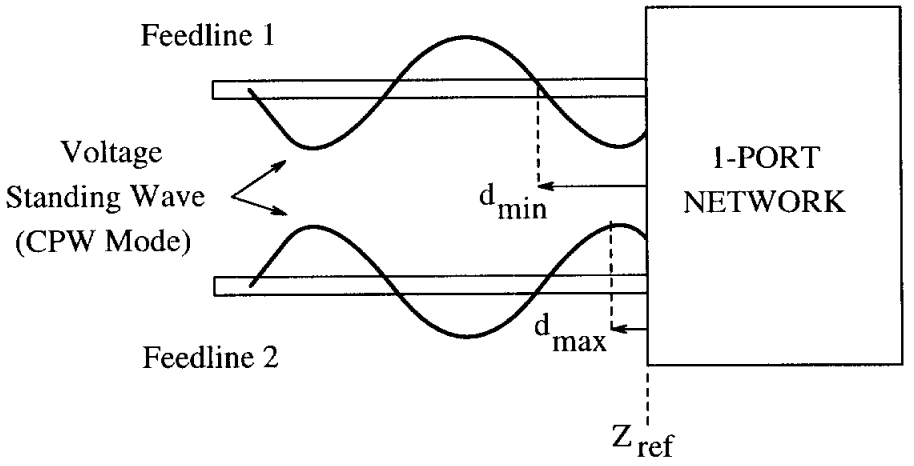

Figure 3.6: Voltage (electric field) standing waveform for a 1-port discontinuity.

$$\begin{aligned} |\Gamma| &= \frac{swr-1}{swr+1} \\ z_{in} &= \frac{1+|\Gamma|e^{j\theta}}{1-|\Gamma|e^{j\theta}} \end{aligned} \tag{3.57}$$

Note that this analysis assumes quasi-TEM propagation in the feedlines, away from the discontinuity.

One-Port Networks

For a one-port network the unknown parameters are the input impedance and the guided wavelength. Other quantities such as the effective dielectric constant, reflection coefficient, or effective line length extension of an open/short circuit can be computed once z_{in} and λ_g are known. This being the case, it is only necessary to use one excitation, such as $J_{n1} = -J_{n2} = 1$ for the CPW mode, and analyze the resulting standing-wave as described in the previous section. The following relations

may then be subsequently applied:

$$\begin{aligned}
&\Gamma_{in} = \tfrac{z_{in}-1}{z_{in}+1} && \text{reflection coefficient} \\
&\epsilon_{re} = \left(\tfrac{\lambda_o}{\lambda_g}\right)^2 && \text{effective dielectric constant} \\
&\Delta l_{sc} = tan^{-1}(-jz_{in})\tfrac{\lambda_g}{2\pi} && \text{short-circuit line length extension} \\
&\Delta l_{oc} = cot^{-1}(jz_{in})\tfrac{\lambda_g}{2\pi} && \text{open-circuit line length extension}
\end{aligned} \tag{3.58}$$

Longitudinally Symmetric Two-Port Networks

A longitudinally symmetric two-port circuit can be characterized by two independent network parameters, such as z_{11} and z_{12}, assuming reciprocity holds. The governing equations for these impedance parameters are:

$$\begin{aligned}
V_1 &= z_{11}I_1 + z_{12}I_2 \\
V_2 &= z_{12}I_1 + z_{11}I_2
\end{aligned} \tag{3.59}$$

where $z_{22} = z_{11}$ and $z_{21} = z_{12}$. In order to determine the two unknowns it is necessary to employ two independent excitations, and utilize the input impedances found for both cases. The typical approach is to use an "even-odd" mode excitation, for which the excitations would be

Port 1	Port 2	
$J_{n1} = -J_{n2} = 1$	$J_{m1} = -J_{m2} = 1$	Even Mode
$J_{n1} = -J_{n2} = 1$	$J_{m1} = -J_{m2} = -1$	Odd Mode

(3.60)

By noting that,

$$\begin{aligned}
z^e_{in,1} &= V^e_1/I^e_1 \\
z^o_{in,1} &= V^o_1/I^o_1
\end{aligned} \tag{3.61}$$

Eqns. 3.59 can be put in the following form:

$$z_{11} = z^e_{in,1} - z_{12}I^e_2/I^e_1$$

$$z_{11} = z^o_{in,1} - z_{12} I^o_2 / I^o_1 \tag{3.62}$$

Finally, since the network is symmetric, $I^e_2/I^e_1 = -I^o_2/I^o_1 = 1$, and 3.62 can be added and subtracted to yield the following

$$\begin{aligned} z_{11} &= (z^e_{in,1} + z^o_{in,1})/2 \\ z_{12} &= (z^e_{in,1} - z^o_{in,1})/2 \end{aligned} \tag{3.63}$$

From the z-parameters, the scattering and y-parameters can be found using standard transformations [43].

Longitudinally Asymmetric Two-Port Networks

For the case of a longitudinally asymmetric circuit there are three independent network parameters, for example z_{11}, z_{22}, and z_{12}. In order to use the z-matrix approach for analysis, therefore, the input impedances from three independent excitations must be found. These excitations could be chosen as follows:

Port 1	Port 2	
$J_{n1} = -J_{n2} = 1$	$J_{m1} = -J_{m2} = 1$	Mode a
$J_{n1} = -J_{n2} = 1$	$J_{m1} = -J_{m2} = -1$	Mode b
$J_{n1} = -J_{n2} = 0$	$J_{m1} = -J_{m2} = 1$	Mode c

(3.64)

A system of three linear equations of the form shown in Eqn. 3.59 is then solved using the port 1 and port 2 input impedances for excitations a, b, and c. The resulting expressions for the network z-parameters are given by [44]:

$$\begin{aligned} z_{11} &= (z^c_{in,1} - z^b_{in,1}) Z^{ca} + (z^a_{in,1} - z^c_{in,1}) Z^{cb} \\ z_{22} &= (z^b_{in,2} - z^c_{in,2}) Z^{ca} + (z^c_{in,2} - z^a_{in,2}) Z^{cb} \\ z_{12} &= \pm (z^a_{in,1} - z_{11}) \left((z^a_{in,2} - z_{22}) / (z^a_{in,1} - z_{11}) \right)^{\frac{1}{2}} \end{aligned}$$

$$
\begin{aligned}
&= (z^a_{in,1} - z_{11})\frac{V^a_1 z^a_{in,2}}{V^a_2 z^a_{in,1}} \\
z_{21} &= z_{12}
\end{aligned}
\tag{3.65}
$$

where

$$
\begin{aligned}
Z^{ca} &= (z^c_{in,1} z^c_{in,2} - z^a_{in,1} z^a_{in,2})/\Delta \\
Z^{cb} &= (z^c_{in,1} z^c_{in,2} - z^b_{in,1} z^b_{in,2})/\Delta \\
\Delta &= (z^c_{in,2} - z^a_{in,2})(z^c_{in,1} - z^b_{in,1}) - (z^c_{in,2} - z^b_{in,2})(z^c_{in,1} - z^a_{in,1})
\end{aligned}
\tag{3.66}
$$

From Eqn. 3.65 it is seen that the relative signs of the voltages at ports 1 and 2 are required in order to determine the phase of z_{12}; these are found directly from the standing waveform analysis.

An alternative method for asymmetric 2-port characterization is the direct S-matrix approach, which has the modest advantage of requiring only two independent excitations. This technique is based on the defining equations,

$$
\begin{aligned}
b_1 &= S_{11} a_1 + S_{12} a_2 \\
b_2 &= S_{21} a_1 + S_{22} a_2
\end{aligned}
\tag{3.67}
$$

where a_i and b_i refer to wave amplitudes traveling toward and away from port i, respectively. The voltage *at the port* is given by:

$$
\begin{aligned}
V_i = V_i^+ + V_i^- &= \sqrt{Z_{o,i}}(a_i + b_i) \\
a_i &= V_i^+ / \sqrt{Z_{o,i}} \\
b_i &= V_i^- / \sqrt{Z_{o,i}} = \Gamma_i V_i^+ / \sqrt{Z_{o,i}}
\end{aligned}
\tag{3.68}
$$

The wave amplitudes may then be determined by considering the expression for the maximum voltage along the feedlines,

$$
V_{max,i} = V_i^+ e^{\mp j\beta_i d_{max,i}}(1 + |\Gamma_i|) \tag{3.69}
$$

where $\beta = 2\pi/\lambda_g$ and d_{max} and Γ are defined as before. The $-/+$ denotes propagation toward or away from the discontinuity, respectively. Using Eqns. 3.68 and 3.69, it can be found that:

$$\begin{aligned} a_i &= \frac{V_{max,i} e^{\mp j\beta_i d_{max,i}}}{\sqrt{Z_{o,i}}(1+|\Gamma_i|)} \\ b_i &= \frac{V_{max,i} e^{\pm j\beta_i d_{max,i}}}{\sqrt{Z_{o,i}}(1+|\Gamma_i|)}|\Gamma_i| \end{aligned} \tag{3.70}$$

Finally, by arbitrarily defining the two excitations as even and odd, the following expressions can be obtained from the linear system composed of two sets of Eqn. 3.67:

$$\begin{aligned} S_{12} &= \left(b_1^o a_1^e - b_1^e a_1^o\right) / \left(a_2^o a_1^e - a_2^e a_1^o\right) \\ S_{21} &= S_{12} \\ S_{11} &= \left(b_1^e - S_{12} a_2^e\right) / a_1^e \\ S_{22} &= \left(b_2^e - S_{21} a_1^e\right) / a_2^e \end{aligned} \tag{3.71}$$

With the direct S-matrix approach the reduced number of required excitations, relative to the z-matrix approach, is a result of finding four independent parameters from each excitation ($a_{1,2}$ and $b_{1,2}$) versus only two ($z_{in,1}$ and $z_{in,2}$).

Finally, in considering the S-parameters of a lossless asymmetric network, it can be shown that S_{11} and S_{22} only vary in phase. If losses are present, however, both the magnitude and phase are generally different. Furthermore, the fractional power loss

$$Loss = \sqrt{1 - |S_{21}|^2 - |S_{11,22}|^2} \tag{3.72}$$

also becomes asymmetric.

3.5 Numerical Issues

In using the SDIE/moment-method technique, attention must be paid to some numerical issues which affect the convergence and accuracy of the results. The two key factors are the rate at which the electric field is sampled (samples/λ_g) and the number of terms which are retained in the Green's function summations (Eqn. 3.19 and 3.36). Both of these topics are addressed in detail in [9, 45] and will therefore be considered only briefly here. The only geometry which will be examined is a 2-port, open-end series stub which is printed in the ground plane (refer to Figure 5.8). The conclusions drawn thus serve as general guidelines, since the convergence characteristics of different configurations can vary, as do the characteristics of the open-end stub with frequency.

The effect of the sampling rate on the scattering parameters of the open-end stub is shown in Figure 3.7. In this case the stub dimensions are the same as those in Figure 5.9, 800x800 modes have been included in the Green's function summations, and the tests have been run at 20 and 28 GHz. The sampling rate refers to the number of basis functions per guide wavelength in the feedlines and inside the circuit element, itself. At 30 samples/λ_g, all four curves are within 0.9% or less of their respective final values.

The same test case has been used in generating the curves shown in Figures 3.8 and 3.9, which illustrate how the solutions converge as the number of modes retained in Eqn. 3.36 increases. The maximum eigenvalue for the y-direction is given by $M_{max}\pi/b$, and that for the z-direction is $N_{max}\pi/c$. In this exercise, the sampling rate was $30/\lambda_g$ and N_{max} (M_{max}) was held at 800 while M_{max} (N_{max}) was varied. The convergence behavior exhibited in these plots is quite different from that shown

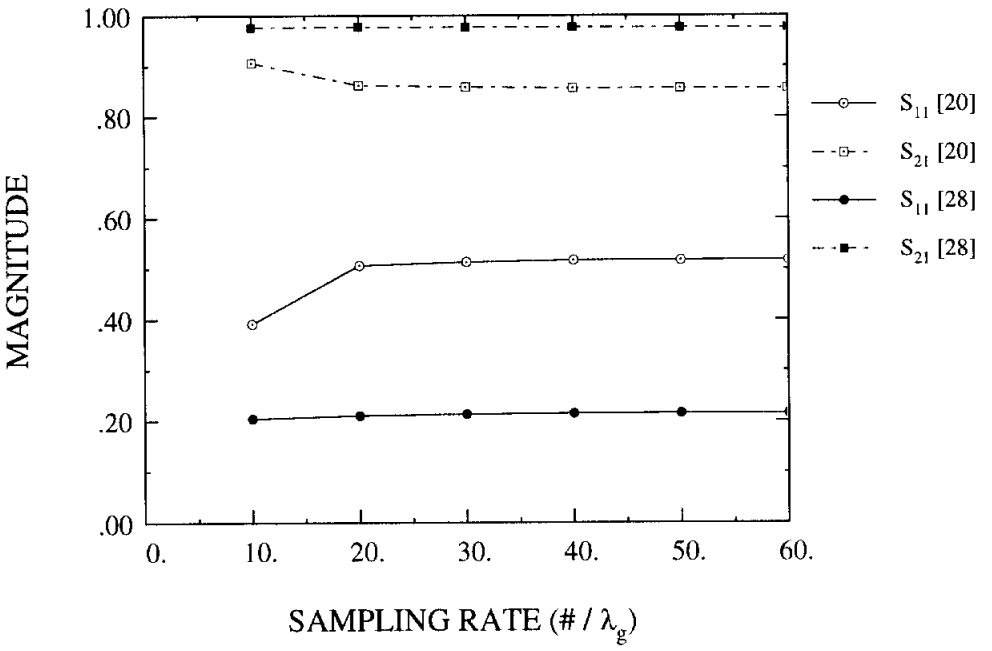

Figure 3.7: Convergence of the SDIE technique versus the electric field sampling rate, at 20 and 28 GHz.

in [9] for a completely shielded circuit on a high permittivity substrate; in the latter case, N_{max} was required to be much greater than M_{max} since the z-dimension of the shielding cavity was much greater than the y-dimension. The differences in this example are that the substrate and superstrate have comparable dielectric constants (1.3 and 1.0, respectively) and the circuit is not shielded on top.

Another issue which is critical for ensuring accurate representation of the field distribution is the placement of the basis functions. In dividing the circuit geometry to create a sampling mesh, it is necessary to force magnetic current (or electric field) elements to be located at all bends and corners. The peak of the basis functions will then correspond with local maxima in the electric field. The maxima exist at these locations since, to a wave propagating in a given direction, a bend in the slot is essentially the same as an increase in the slot width, and likewise an increase in

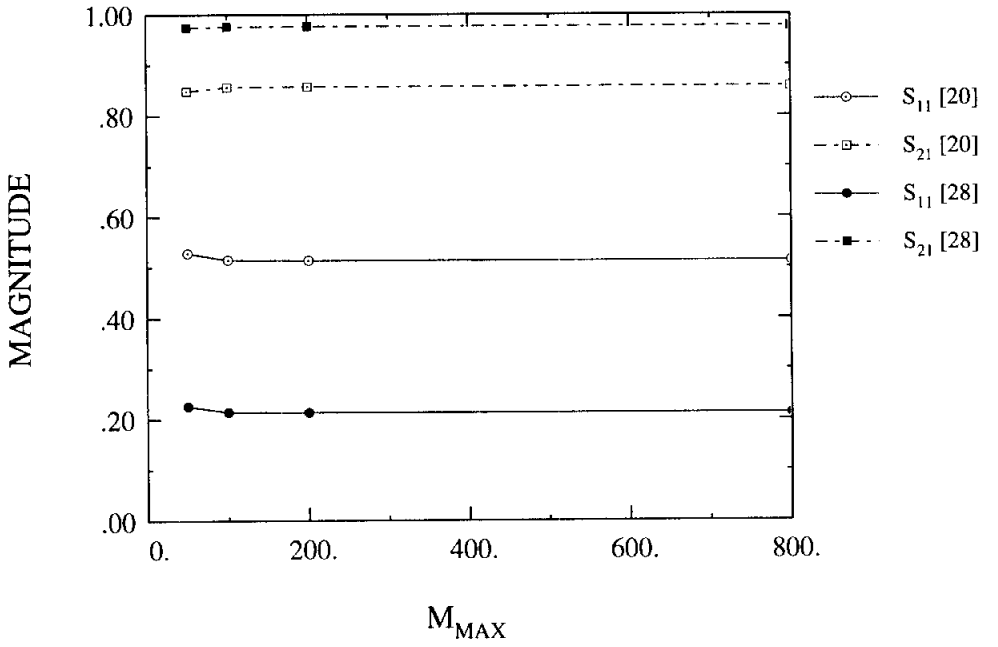

Figure 3.8: Convergence of the SDIE technique versus the maximum eigenvalue for the y-direction, at 20 and 28 GHz.

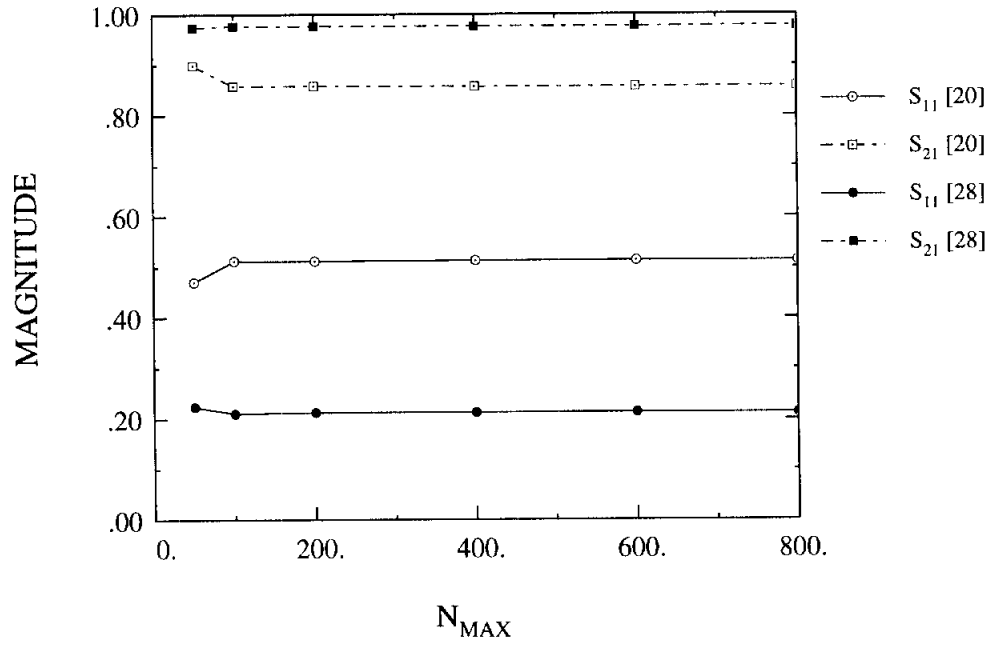

Figure 3.9: Convergence of the SDIE technique versus the maximum eigenvalue for the z-direction, at 20 and 28 GHz.

the characteristic impedance. Note, for example, the placement of the arrows in Figure 3.5 near the discontinuity. To facilitate meeting this prerequisite, a flexible approach for subdividing general circuit configurations has been adopted. The method essentially assigns a different "region" number to separate parts of a circuit, such as the individual arms of the folded stub designs described in Chapter V. Each region may have its own sampling rate, and is connected to neighboring regions using additional magnetic current elements. In this way, samples are automatically positioned at the necessary E-field maxima points. In geometries where the discontinuities occur very close together, forcing elements at these nodes may cause *local* sampling rates to become quite high, particularly at lower frequencies. However, values as high as $750/\lambda_g$ have been reached with no noticeable impact on the numerical stability.

3.6 Conclusion

This chapter has presented the derivation of a full-wave analysis that is based on a space domain integral equation. The technique is suitable for the characterization of CPW-type discontinuities and antennas, and can treat completely shielded or open structures. Included in the presentation was the formulation of the integral equation, the solution by the method of moments, and the extraction of network parameters through analysis of the slot electric field distribution.

CHAPTER IV

QUASI-TEM ANALYSIS OF THREE CENTER CONDUCTOR CPW CIRCUITS

4.1 Introduction

Presented in this chapter is an analysis of coupled lines which are in the form of three center conductor coplanar waveguide. The motivation behind this work was the need to analyze geometries of the type shown in Figure 4.1, which consists of a distributed stub with integrated thin-film capacitors. The full-wave analysis described in Chapter III is capable of accurately characterizing the stub sections, but the treatment of the capacitors is not feasible with this type of integral equation technique. Equally important was the consideration of computational efficiency. Since the geometry in Figure 4.1 represents only one of the possible configurations in this new class of circuits, it was desirable to develop a relatively fast algorithm which could expedite the design process. These factors lead naturally to the use of a method based primarily on quasi-TEM approximations.

The technique which will be described herein treats the geometry as coupled line sections, with lumped element capacitors positioned along their length. A two-dimensional spectral domain moment method is first presented which is utilized to compute the characteristic impedances of the individual slots. Following this, a

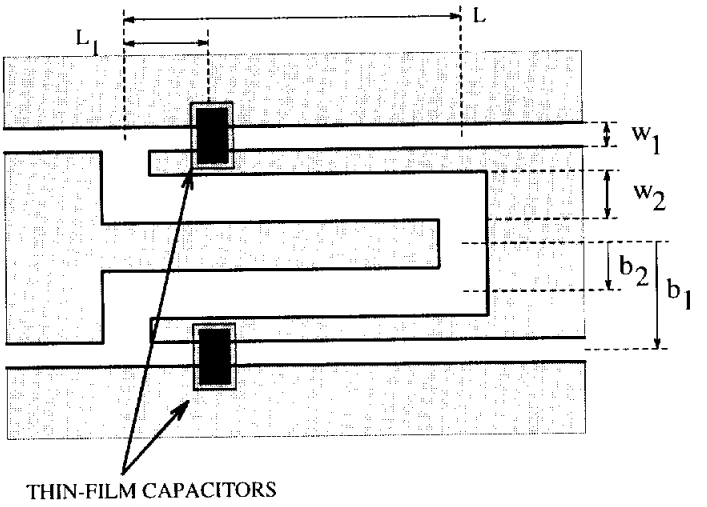

Figure 4.1: Top view of a CPW-type, series open-end stub with three center conductors and integrated thin-film capacitors.

four-port "even/odd" mode analysis is derived for treating the coupled line sections. It will be shown in Chapter V that this is an efficient approach for characterizing open-end and short-end series stubs. Finally, the necessary steps for modeling the lumped elements are presented, along with considerations for the analysis of the dual, coupled strip problem.

4.2 Two-Dimensional Spectral Domain Analysis

The problem of interest is the calculation of the propagation constant and individual slot impedances for cross-sections of the type shown in Figure 4.2. One very popular method which has been used to characterize geometries such as this is conformal mapping [46, 47, 48, 49]. The mapping techniques work extremely well for one and two center conductor geometries with a high degree of symmetry, and have even been extended for the analysis of three center conductor CPW with asymmetric conductor widths [50]. Another possible approach utilizes the point matching method [51], which is based on solving Laplace's equation to find the electrostatic potential

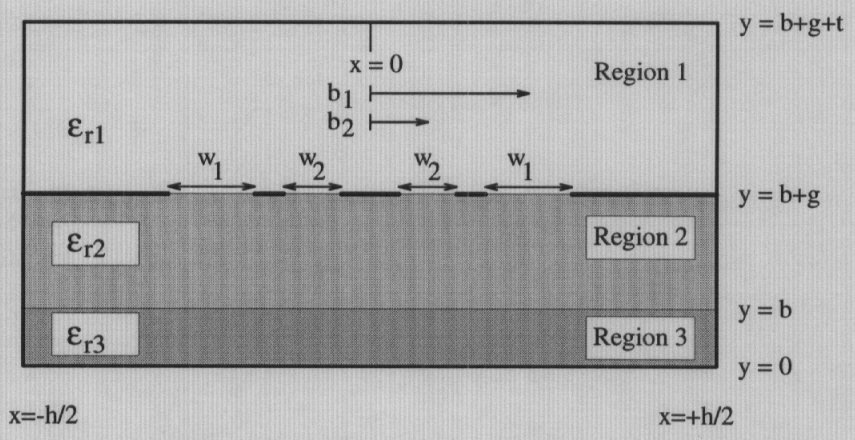

Figure 4.2: Cross-section of a shielded CPW line with three center conductors.

of the system. For this work, though, the method of choice was the two-dimensional spectral domain approach (SDA) [52], due to its full-wave accuracy and flexibility. Computationally, this method is much slower than the conformal mapping techniques, and generally faster than the point matching methods which must subdivide the entire cross-section. It has an advantage over both methods in terms of the ease with which very general structures may be analyzed, however, as for example CPW lines with five or more center conductors [54]. The restrictions associated with the SDA are that the conducting lines must be infinitely thin, and the dielectric layers must be uniform in the x-direction. It is noted that the orientation of the geometry in Figure 4.2 was defined to be consistent with that found in [52], requiring that the x and y directions be interchanged with respect to the notation used in Chapter III.

4.2.1 Spectral Domain Integral Equation

The necessary 2-D integral equation is derived by enforcing boundary conditions on the Fourier transforms of the tangential fields, at all material interfaces. The equation is written in terms of the unknown electric field in the slots, $\vec{E}$, and takes

the following form:

$$\begin{bmatrix} \tilde{Y}_{xx} & \tilde{Y}_{xz} \\ \tilde{Y}_{zx} & \tilde{Y}_{zz} \end{bmatrix} \begin{bmatrix} \tilde{E}_x \\ \tilde{E}_z \end{bmatrix} = \begin{bmatrix} \tilde{J}_x \\ \tilde{J}_z \end{bmatrix} \tag{4.1}$$

where the tilde (˜) represents the Fourier transform of the corresponding quantities, $\tilde{J}$ is the electric current *on the conductors* at y=b+g, and $\tilde{Y}_{\zeta\xi}(\zeta, \xi = x, z)$ are the Green's function admittance matrix elements. The electric current is included here since the Fourier transformation effectively forces the boundary conditions to be satisfied over the range of x.

In order to determine the Green's functions, two basic approaches can be utilized. Using the *general* approach, the fields in all regions are expressed in terms of scalar potentials with unknown coefficients. The spectral domain boundary conditions are then enforced, resulting in a system of equations which can be solved to find the coefficients in terms of the current $\tilde{J}$; the Green's functions fall out when these results are assembled into the form shown in Eqn. 4.1. The disadvantage of this method is that the explicit expressions for $\tilde{Y}$ require increasingly tedious algebraic manipulation as the number of dielectric layers increases. Although this problem can be circumvented if the elements are computed numerically, an alternative method called the *immittance* approach [52] can also simplify the process. Using this method, the fields are decomposed into TM-to-y and TE-to-y components, for which transmission line equivalents are applied to find $\tilde{Y}$. The details of this method are provided in Appendix B. Similar derivations can be found in [34, 53].

In the following sections, attention is directed toward the determination of the propagation constant and slot impedances, through the solution of the integral equation.

4.2.2 Solution of the Integral Equation

In order to solve Eqn. 4.1, the first step is to approximate the electric field using appropriate basis functions with associated unknown coefficients (see Section 3.3). In the most general case, independent basis functions would be used for each slot, and the functions would be non-zero only over that particular slot. The problem can be simplified, however, by enforcing the conditions that the outer ground planes are at the same potential and that the slot fields are laterally symmetric. These conditions are satisfied under the assumptions that a CPW-type excitation is used, versus slot-line mode, and that the circuit geometry is possesses transverse symmetry. This limits the possible modes to the two which are depicted in Figure 4.3, and thus there are only two sets of independent coefficients, one for the outer slot pair and one for the inner slot pair. The E-field expansion functions for slot pairs $i = 1, 2$ are then of the form:

$$\begin{aligned} E_{x,i} &= \sum_{m=1}^{M} c_{i,m} E_{xm,i} \\ E_{z,i} &= \sum_{n=1}^{N} d_{i,n} E_{zn,i} \end{aligned} \tag{4.2}$$

where

$$E_{xm,i} = E_{xm,i^-} + E_{xm,i^+} = \begin{cases} \frac{cos[(m-1)\pi(x+b_i)/w_i]}{\sqrt{1-[2(x+b_i)/w]^2}} + \frac{-cos[(m-1)\pi(x-b_i)/w_i]}{\sqrt{1-[2(x-b_i)/w]^2}}, & \text{m=1,3,...} \\ \frac{sin[(m-1)\pi(x+b_i)/w_i]}{\sqrt{1-[2(x+b_i)/w]^2}} + \frac{sin[(m-1)\pi(x-b_i)/w_i]}{\sqrt{1-[2(x-b_i)/w]^2}}, & \text{m=2,4,...} \end{cases}$$

$$E_{zn,i} = E_{zn,i^-} + E_{zn,i^+} = \begin{cases} \frac{cos[n\pi(x+b_i)/w_i]}{\sqrt{1-[2(x+b_i)/w]^2}} + \frac{cos[n\pi(x-b_i)/w_i]}{\sqrt{1-[2(x-b_i)/w]^2}}, & \text{n=1,3,...} \\ \frac{sin[n\pi(x+b_i)/w_i]}{\sqrt{1-[2(x+b_i)/w]^2}} + \frac{-sin[n\pi(x-b_i)/w_i]}{\sqrt{1-[2(x-b_i)/w]^2}}, & \text{n=2,4,...} \end{cases} \tag{4.3}$$

It is worth noting that in general, a transmission line with N different conductors will support N-1 modes of propagation ([33], p. 251). Thus, taking each ground plane as a separate conductor, the configuration in Figure 4.2 has five conductors,

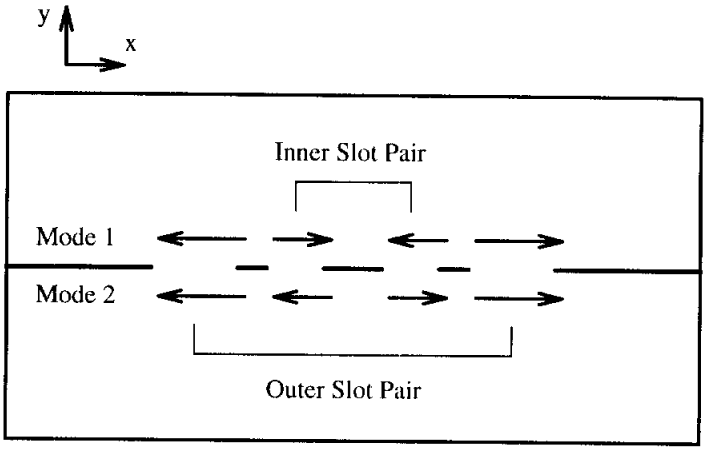

Figure 4.3: Electric field orientation (x-component) for the two possible modes of propagation for the cross-section in Figure 4.2, given a CPW-type excitation and transverse symmetry in the circuit.

and therefore four distinct modes. The restrictions on the excitation and geometric symmetry, however, are equivalent to placing a perfect magnetic conductor at $x = 0$. This reduces the number of conductors to three, and thus limits the number of independent modes to two.

The next step is to take the Fourier transform of the basis functions (see Appendix B), and substitute the resulting spectral domain functions into Eqn. 4.1. Then, applying Galerkin's technique, inner products are computed using test functions which are identical to the basis functions. Since discrete Fourier transforms are appropriate for the completely shielded structure, summations are utilized for the inner products instead of integrals. Also, because the current and electric field exist at complementary locations in space, the reactions between the current and the test functions are zero. This follows from the fact that summations in the spectral domain are directly proportional to integrals in the space domain, as can be shown using Parseval's theorem. As the residual error introduced by the field expansion is

minimized through Galerkin's technique, the following set of equations is obtained:

$$\sum_{\alpha_f=-\alpha_{f,max}}^{\alpha_{f,max}} \left[\tilde{E}_{xk,j}\tilde{Y}_{xx}\left(\sum_{m=1}^{M} c_{1,m}\tilde{E}_{xm,1} + \sum_{m=1}^{M} c_{2,m}\tilde{E}_{xm,2}\right) + \tilde{E}_{xk,j}\tilde{Y}_{xz}\left(\sum_{n=1}^{N} d_{1,n}\tilde{E}_{zn,1} + \sum_{n=1}^{N} d_{2,n}\tilde{E}_{zn,2}\right)\right] = 0 \quad \text{k=1,...,M}$$

$$\sum_{\alpha_f=-\alpha_{f,max}}^{\alpha_{f,max}} \left[\tilde{E}_{zk,j}\tilde{Y}_{zx}\left(\sum_{m=1}^{M} c_{1,m}\tilde{E}_{xm,1} + \sum_{m=1}^{M} c_{2,m}\tilde{E}_{xm,2}\right) + \tilde{E}_{zk,j}\tilde{Y}_{zz}\left(\sum_{n=1}^{N} d_{1,n}\tilde{E}_{zn,1} + \sum_{n=1}^{N} d_{2,n}\tilde{E}_{zn,2}\right)\right] = 0 \quad \text{k=1,...,N} \quad (4.4)$$

for $j = 1, 2$. In these equations, α_f is the Fourier transform variable, which is chosen to be defined as $\alpha_f = 2r\pi/h$, $r = -R_{max}, R_{max}$, where h is specified in Figure 4.2 and R_{max} is typically on the order of one thousand.

To proceed, the set of linear equations in Eqn. 4.4 is assembled into a matrix representation:

$$\begin{bmatrix} K_{1,1} & \cdots & K_{1,M+N} \\ \vdots & & \\ K_{M+N,1} & \cdots & \cdots \end{bmatrix} \begin{bmatrix} c_{1,1} \\ \vdots \\ d_{2,N} \end{bmatrix} = 0 \quad (4.5)$$

Through the admittance elements, the $K_{i,j}$ terms in this equation are functions of the propagation constant, β. A root-seeking algorithm is therefore employed to determine the true value of β, for which the determinant of the K-matrix is zero; this also ensures that the solution is non-trivial. Two convenient techniques for this step are Muller's method and the secant method, using deflation to detect multiple roots.

In order to complete the analysis, the coefficients of the basis functions are computed as the eigenvector of the minimum eigenvalue in Eqn. 4.5 (see Appendix B). This allows the electric field configuration of each slot to be determined and the mode can thus be ascertained. It should be noted that the propagation constants of

the two modes converge to the same value in a homogeneous environment, and are likewise very similar for lines with a low permittivity substrate and no superstrate. As a demonstration, the plots in Figure 4.4 show the absolute value of the determinant $|det(K)|$ as a function of β/k_0, on a typical line with $\epsilon_{r1} = 1$ and $\epsilon_{r2} = \epsilon_{r3} = 1.4$ (see Figure 4.2). Here k_0 is the free-space propagation constant, and $det(K)$ has been normalized to the minimum valued obtained with the root search algorithm. The difference between the two solutions is only 0.2%, and if the substrate layers are changed to $\epsilon_{r2,3} = 13.1$ (GaAs) the difference increases to just 1%. Also, the plots in Figure 4.5 show the corresponding values of the first x-directed electric field coefficient for the inner slot pair, $c_{2,1}$ (normalized to $c_{1,1} = 1$), as a function of β/k_0. It is interesting to observe that the extremum occur very close to the zero crossings of $det(K)$.

4.2.3 Evaluation of the Characteristic Impedance

The final parameter of interest is the characteristic impedance of the individual slots. As is well known, the current or voltage on a non-TEM transmission line cannot be uniquely defined, and thus there exist multiple definitions of the characteristic impedance which may differ in value. Under quasi-TEM operation, however, the longitudinal field components are relatively weak and the different definitions converge to the same value. For slot-type lines, the most convenient expression is:

$$Z_{o,i^-} = \frac{V_{i^-}^2}{2P_{avg,i^-}} \tag{4.6}$$

The subscript i^- indicates that the parameters refer to only one slot of a given slot pair, e.g. the slot centered at $x = -b_i$. The voltage, V_{i^-}, is given by

$$V_{i^-} = -\int_{slot\ i^-} E_{x,i^-}\, dx$$

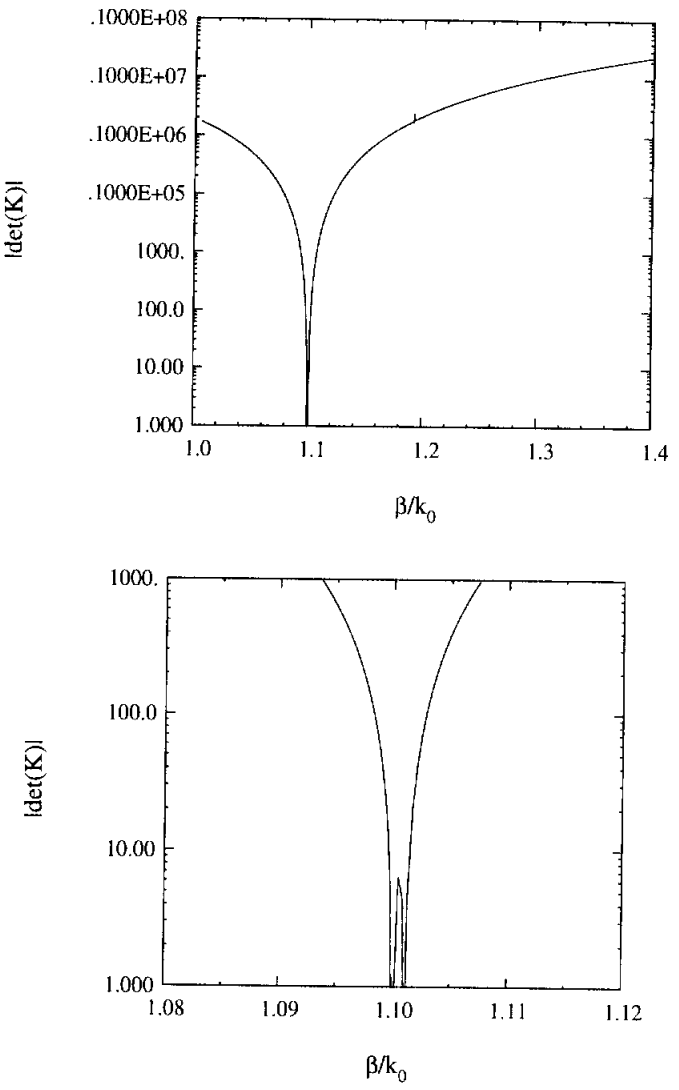

Figure 4.4: An example showing how the determinant of the K-matrix in Eqn. 4.5 varies versus the normalized propagation constant. The lower graph shows the same data on an expanded scale, illustrating the solutions for the two modes of propagation.

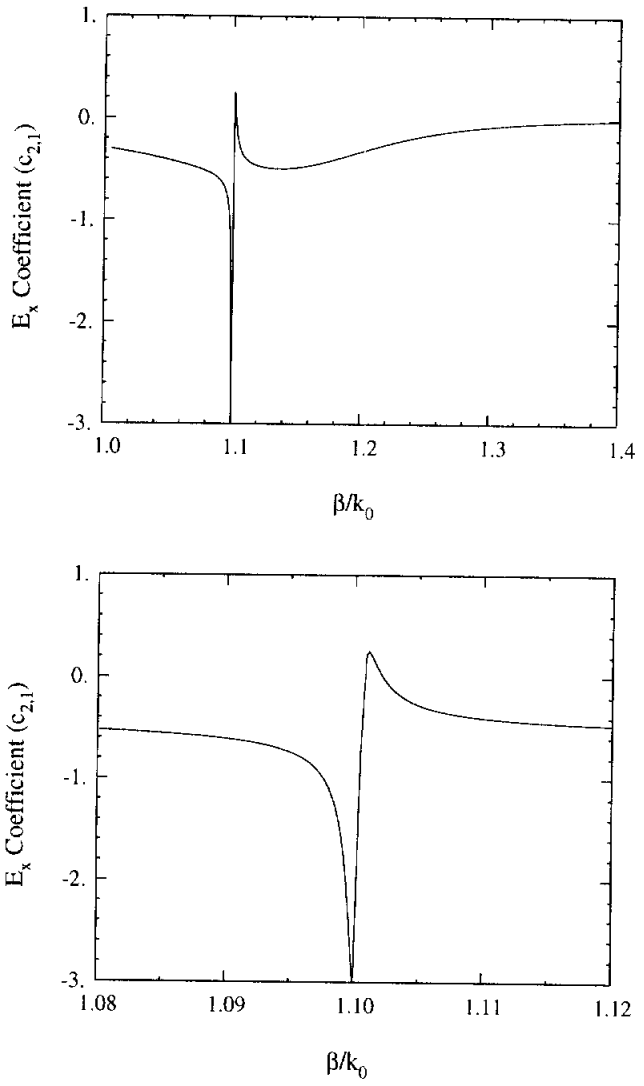

Figure 4.5: An example showing how the first x-directed electric field coefficient for the second slot, $c_{2,1}$, varies versus the normalized propagation constant. The lower graph shows the same data on an expanded scale.

$$= -\sum_m c_{i,m} \frac{\pi w_i}{2} J_o\left(\frac{(m-1)\pi}{2}\right), \quad \text{m=1,3,...M} \tag{4.7}$$

where E_{x,i^-} is equal to the first term on the right-hand side of Eqn. 4.3 and J_o is the zeroth-order Bessel function of the first kind. The quantity P_{avg,i^-} is the time-average power associated with the slot i^-, and can be defined as follows [55]:

$$\begin{aligned} P_{avg,i^-} &= \frac{1}{2}\int_{-h/2}^{+h/2}\int_0^c \vec{E}_T(x,y) \times \vec{H}^*_{i^-}(x,y) \cdot d\vec{s} \\ &= \frac{1}{2h}\sum_{-\alpha_{f,max}}^{\alpha_{f,max}} \int_0^c \left(\tilde{E}_{x,T}(\alpha,y)\tilde{H}^*_{y,i^-}(\alpha,y) - \tilde{E}_{y,T}(\alpha,y)\tilde{H}^*_{x,i^-}(\alpha,y)\right) dy \end{aligned} \tag{4.8}$$

where $c = b + g + t$. In this equation, $\vec{E}_T$ represents the total electric field and $\vec{H}^*_{i^-}$ is the complex conjugate of the magnetic field associated with slot i^-. This form of 4.8 was obtained by using Parseval's theorem to convert from the spatial integration over x to the summation of the Fourier transformed fields. The calculation of these fields, as well as the analytical integration in y, is described in Appendix B.

4.2.4 Convergence

The convergence of the spectral domain analysis is dependent upon the number of basis functions (N,M) and the number of Fourier terms which are retained in the summations (R_{max}). To demonstrate, the plots in Figures 4.6 and 4.7 show the values for the four impedances (two modes and two slots) as a function of R_{max}, for N=M=4 and N=M=6, respectively. The curves are all normalized to the value listed in the legend, which is obtained using R_{max}=4000 and N=M=6. The results are for 20 GHz operation, and correspond to the following geometry (refer to Figure 4.2): b=500, g=350, t=500, h=2000, w_1=60, w_2=30, b_1=100, b_2=35, ϵ_{r1}=1.0, ϵ_{r2}=11.7 and ϵ_{r3}=1.0 (all dimensions in μm). In each case, the solution for the propagation constants, β_1 and β_2, converge to within 0.1% using only 250 Fourier terms; the values are 2.52 and 2.49, respectively. Achieving convergence for the impedance requires

more terms, however, as illustrated in the figures. Here the number of Fourier terms *actually pertains to the calculation of* β, through which the coefficients for the E-field basis functions are eventually found. Once the coefficients are accurately determined, the summations to find the impedance typically converge to within 1.5% using 400 terms. Although no data was known to be available for direct comparison, results from the spectral domain analysis are used with the coupled line technique and compared to experimental and full-wave analysis results in Chapter V.

4.3 Coupled Line Technique

Now that the different mode impedances of the coupled lines (slots) are known, it is necessary to derive expressions which can describe their electrical performance in a circuit application. Therefore, a method for three-dimensional characterization of two asymmetric coupled lines is presented in the following sections. As discussed in Section 4.2.2, the assumptions of a CPW-type excitation and lateral circuit symmetry are equivalent to having a magnetic wall at $x = 0$ in Figure 4.2, such that only one half of the circuit must be analyzed. For this work, the two lines will refer to the two slots on a given side of $x = 0$. Also, for convenience, the two possible modes of propagation will be referred to as "odd" and "even", corresponding to mode 1 and mode 2 in Figure 4.3, respectively. Since the magnitudes of the current and voltage on the two lines are generally different, these definitions do not conform to the conventional usage. The correct anti-phase and in-phase relationship for the odd and even modes does hold, however, making the notation useful in this respect.

The technique which will be used is based on a dual mode analysis that is applicable given quasi-TEM propagation along the lines. It is assumed that the propagation velocities for each mode are the same, which is generally accurate for the edge-coupled

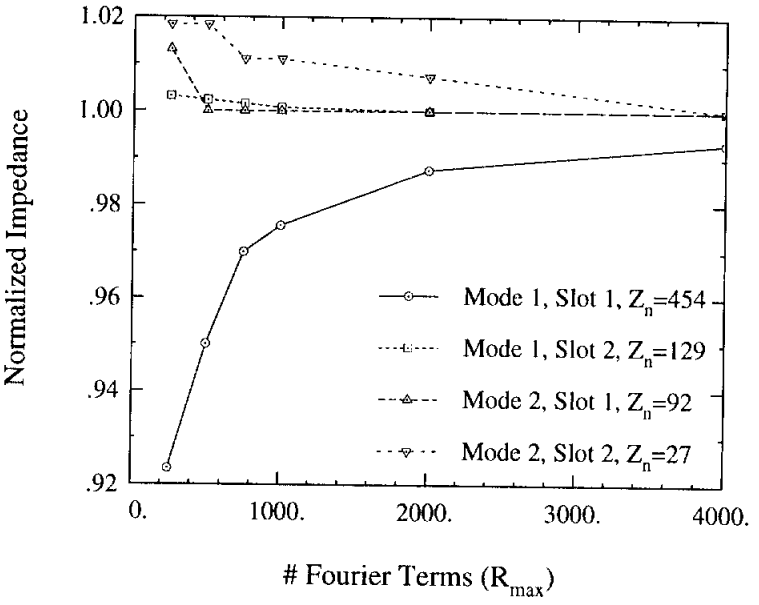

Figure 4.6: Convergence of the spectral domain analysis for N=M=4 (refer to Figure 4.3).

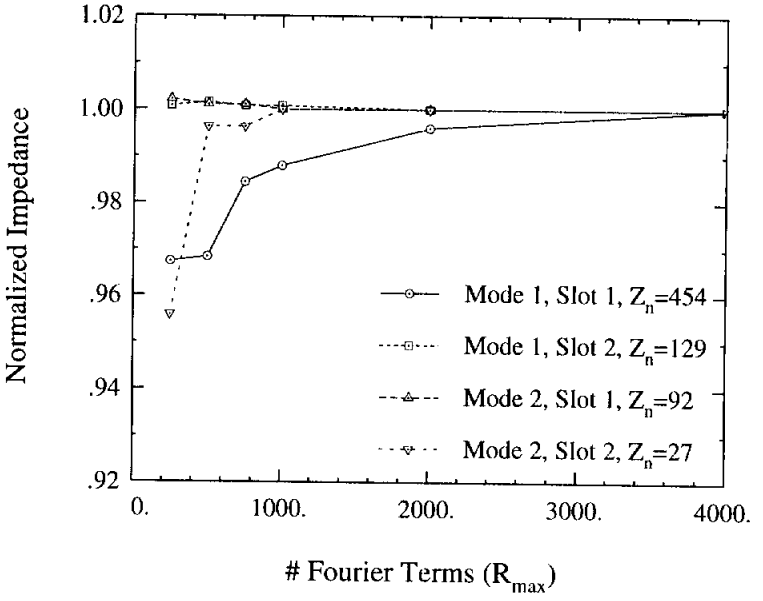

Figure 4.7: Convergence of the spectral domain analysis for N=M=6 (refer to Figure 4.3).

lines considered here, even in an inhomogeneous environment. This approximation breaks down as the permittivity of the substrate increases and the substrate thickness becomes much smaller than the free-space wavelength (see [16] for example). Accounting for different velocities, however, is a straightforward extension of this work.

4.3.1 Derivation of the 4-Port Impedance Matrix

The method applied here to analyze the two coupled lines is based on the use of a 4-port impedance matrix, and can be accomplished following the approach outlined in the classic paper by Jones and Bolljahn [56]. This original work was applicable to symmetric lines in a homogeneous dielectric medium, and the technique was soon expanded for asymmetric lines by Ozaki [57]. Thereafter, considerable attention was directed towards the understanding of non-symmetrical coupled lines in inhomogeneous dielectrics and the possible modes of propagation [58, 59, 60, 61, 62]. In particular, Tripathi [58, 59] presents an excellent analysis that demonstrates how the coupled line characteristics derive from the transmission line equations. For example, from the current-voltage relations it is found that:

$$[z]\,[y]\,[v] \;=\; \gamma^2\,[v] \tag{4.9}$$

where $[z]$ and $[y]$ are the $n \times n$ impedance and admittance matrices, respectively, for an n-coupled line system. The propagation constants squared, γ^2, are seen to be the eigenvalues of the matrix $[z][y]$, and the voltages, $[v]$, are the corresponding eigenvectors. Thus the propagation constant and excitation vectors are found in terms of the self- and mutual-impedances and admittances per unit length of the lines. The mode impedances are subsequently found from these same parameters.

In the derivation presented here, the propagation constants and mode impedances have been found directly from the 2-D analysis. As will be shown below, excitation vectors are also determined using the 2-D results, and thus the self- and mutual-impedances are never explicitly utilized. This is the major difference between the approaches mentioned above and that used in this work.

The physical configuration of the coupled lines is illustrated in Figure 4.8. Following the method in [56], the voltages on each line are determined under the even- and odd-mode current excitations, assuming each current generator has an infinite input impedance. Using equal propagation constants for each mode, the results for the even mode are:

$$\begin{aligned} v_{e1-}(z) &= -jZ_{e1}i_{e1-}\frac{cos(\beta(l-z))}{sin(\beta l)} \\ v_{e2-}(z) &= -jZ_{e2}i_{e2-}\frac{cos(\beta(l-z))}{sin(\beta l)} \\ v_{e1+}(z) &= -jZ_{e1}i_{e1+}\frac{cos(\beta z)}{sin(\beta l)} \\ v_{e2+}(z) &= -jZ_{e2}i_{e2+}\frac{cos(\beta z)}{sin(\beta l)} \end{aligned} \tag{4.10}$$

and for the odd mode:

$$\begin{aligned} v_{o1-}(z) &= -jZ_{o1}i_{o1-}\frac{cos(\beta(l-z))}{sin(\beta l)} \\ v_{o2-}(z) &= -jZ_{o2}i_{o2-}\frac{cos(\beta(l-z))}{sin(\beta l)} \\ v_{o1+}(z) &= -jZ_{o1}i_{o1+}\frac{cos(\beta z)}{sin(\beta l)} \\ v_{o2+}(z) &= -jZ_{o2}i_{o2+}\frac{cos(\beta z)}{sin(\beta l)} \end{aligned} \tag{4.11}$$

where $Z_{e,o}$ are the even and odd mode characteristic impedances of each line, respectively.

There are two distinct differences between the equations put forth in [56] and Eqns. 4.10 and 4.11. The first is the use of different impedances for each line, and

the second difference is in the current generators. With symmetric coupled lines, the relationship between the sources is

$$\begin{aligned} i_{e1-} = i_{e1+} &= i_{e2-} = i_{e2+} \\ i_{o1-} = i_{o1+} &= -i_{o2-} = -i_{o2+} \end{aligned} \tag{4.12}$$

With asymmetric coupled lines, however, these expressions are invalid. To understand this, consider the current-voltage relationships on lines 1 and 2 for the even mode, when the lines are of infinite length:

$$\begin{aligned} V_{e1} &= Z_{e1} i_{e1} \\ V_{e2} &= Z_{e2} i_{e2} \end{aligned} \tag{4.13}$$

Each impedance *and* voltage is known from the 2-D spectral domain analysis (Eqns. 4.6 and 4.7), and in general the two equations above cannot both be satisfied for $i_{e1} = i_{e2}$; the same holds for the odd mode. This is equivalent to stating that only under certain restrictive excitations can the even and odd modes of the asymmetric coupled lines propagate independently. In the general case, an excitation such as $i_{e1} = i_{e2}$ would result in a propagating mode which is a superposition of both modes. However, Eqns. 4.6, 4.7 and 4.13 can be used to determine the necessary "restrictive" relationships:

$$\begin{aligned} \alpha &= \frac{Z_{e1} V_{e2}}{Z_{e2} V_{e1}} \\ \kappa &= -\frac{Z_{o1} V_{o2}}{Z_{o2} V_{o1}} \\ i_{e2} &= \alpha i_{e1} \qquad \text{even mode} \\ i_{o2} &= -\kappa i_{o1} \qquad \text{odd mode} \end{aligned} \tag{4.14}$$

These equations state the relationship that must exist between the currents on each line in order for each mode to propagate independently. The equivalents of α and κ

are defined in terms of the self- and mutual-impedances in [58]. Also, the minus sign has been used in the definition of κ such that the proceeding notation will remain consistent with that in [56].

The analysis continues by first finding the total currents and voltages at each port, as a summation of the individual modal excitations. The currents are given by:

$$\begin{aligned} I_1 &= i_{e1-} + i_{o1-} \\ I_2 &= \alpha i_{e1-} - \kappa i_{o1-} \\ I_3 &= \alpha i_{e1+} - \kappa i_{o1+} \\ I_4 &= i_{e1+} + i_{o1+} \end{aligned} \tag{4.15}$$

and the voltages at each port are

$$\begin{aligned} V_1 &= (v_{e1-} + v_{e1+} + v_{o1-} + v_{o1+})|_{z=0} \\ V_2 &= (v_{e2-} + v_{e2+} + v_{o2-} + v_{o2+})|_{z=0} \\ V_3 &= (v_{e2-} + v_{e2+} + v_{o2-} + v_{o2+})|_{z=l} \\ V_4 &= (v_{e1-} + v_{e1+} + v_{o1-} + v_{o1+})|_{z=l} \end{aligned} \tag{4.16}$$

With some algebraic manipulation, Eqns. 4.10, 4.11, 4.15 and 4.16 can be put into the form of $V = [Z]I$. The elements of the resulting 4-port impedance matrix are:

$$\begin{aligned} Z_{11} = Z_{44} &= -j(\kappa Z_{e1} + \alpha Z_{o1})cot(\theta)/\Delta \\ Z_{22} = Z_{33} &= -j(\alpha Z_{e2} + \kappa Z_{o2})cot(\theta)/\Delta \\ Z_{14} = Z_{41} &= -j(\kappa Z_{e1} + \alpha Z_{o1})csc(\theta)/\Delta \\ Z_{23} = Z_{32} &= -j(\alpha Z_{e2} + \kappa Z_{o2})csc(\theta)/\Delta \\ Z_{12} = Z_{43} &= -j(Z_{e1} - Z_{o1})cot(\theta)/\Delta \end{aligned}$$

$$
\begin{aligned}
Z_{21} = Z_{34} &= -j(Z_{e2} - Z_{o2})\alpha\kappa cot(\theta)/\Delta \\
Z_{13} = Z_{42} &= -j(Z_{e1} - Z_{o1})csc(\theta)/\Delta \\
Z_{31} = Z_{24} &= -j(Z_{e2} - Z_{o2})\alpha\kappa csc(\theta)/\Delta
\end{aligned} \tag{4.17}
$$

where $\theta = \beta l$ and $\Delta = \alpha + \kappa$. It can be observed from Eqns. 4.14 that for symmetric lines, α and κ become equal to one and Eqns. 4.17 then revert to those given by [56].

There are two final points which need to be made regarding this derivation. First, reciprocity requirements must be satisfied for the impedance elements, e.g. $Z_{12} = Z_{21}$, imposing the following necessary condition:

$$
Z_{e1} - Z_{o1} = (Z_{e2} - Z_{o2})\alpha\kappa \tag{4.18}
$$

Second, due to the linear current-voltage relationship, it is easily argued that

$$
\frac{i_{e2}/i_{e1}}{i_{o2}/i_{o1}} = \frac{v_{e2}/v_{e1}}{v_{o2}/v_{o1}} \tag{4.19}
$$

The expression on the left side of this equation is equal to the ratio of α/κ, which can only be equal to the expression on the right side if

$$
\frac{Z_{e1}}{Z_{e2}} = \frac{Z_{o1}}{Z_{o2}} \tag{4.20}
$$

Eqns. 4.24 and 4.20 serve as independent checks of the impedance and voltage parameters which are obtained from the 2-D spectral domain analysis.

4.3.2 Application to Series Tuning Stubs

This section demonstrates how the coupled line technique can be utilized as an efficient tool for the analysis of open- and short-end tuning stubs of the type shown in Figure 4.9. This concept was previously proposed by Getsinger [63], and a similar analysis for interdigitated capacitors was reported in [54]. The accuracy naturally

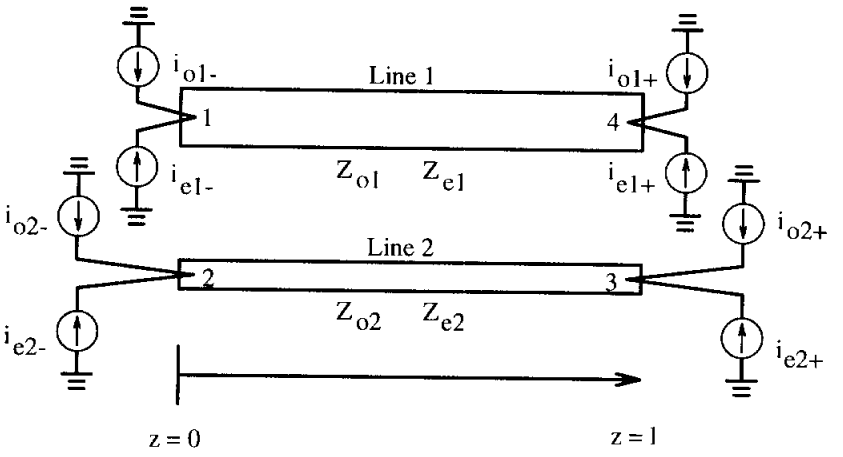

Figure 4.8: Physical configuration of two asymmetric coupled lines and the even and odd mode current excitations.

hinges on the assumption of quasi-TEM operation, but this is not restrictive since properly designed coplanar waveguide circuits generally satisfy this requirement to a high degree.

Once the impedance and voltage parameters for the 4-slot (3 center conductor) geometry have been calculated using the 2-D SDA, the remaining analysis is carried out using simple transmission line theory. The subsequent steps are as follows:

1. Generate the 4-port impedance matrix for a coupled line section of length L (see Figure 4.9). With the open-end stub, an approximate line length extension of $L_{ext} = min(g, (S_1 + 2W_2)/4)$ [25] is included in the overall length to account for the fringing fields at the port 3 discontinuity. The parameter L_{ext} is also denoted in the figure.

2. Add a section of transmission line of length L_2 to port 2. The impedance of this line is difficult to determine, so an approximate value of $Z_{0,s}$ is used. This is the impedance of the (single) feedline slot.

3. Terminate port 3 in an open-circuit or short-circuit, depending on the stub type.

4. Connect ports 1 and 2 in series.

5. Convert the resultant 2-port [Z] matrix to a scattering matrix, [S], using the characteristic impedance of $Z_{0,s}$.

The relations needed for steps 2-4 are included in Appendix A.

As will be demonstrated in Chapter V, this analysis compares extremely well with results from the full-wave technique. Other than requiring that stub geometries be narrow enough to maintain quasi-TEM operation, the only apparent limitation is that the gap widths, g, should be small (see Figure 4.9). Generally, g should be approximately the same size as, or smaller than, the slot width w_2. This ensures that the coupled line analysis will agree with the full-wave results through the first resonance, and usually up to the second resonance, as well. Since there is little compensation for discontinuity effects in the current model, however, the error in the predicted resonant frequency increases to around 4-6% if g becomes much larger than L/15. It is also important to note that for most geometries there is very little frequency dependence in the impedance values, particularly for the microshield implementation. Thus the 2-D SDA analysis can be performed for a single frequency, and the results then used to characterize the stub from DC up to the second resonance. This make the routine extremely efficient and suitable for computer-aided design implementation.

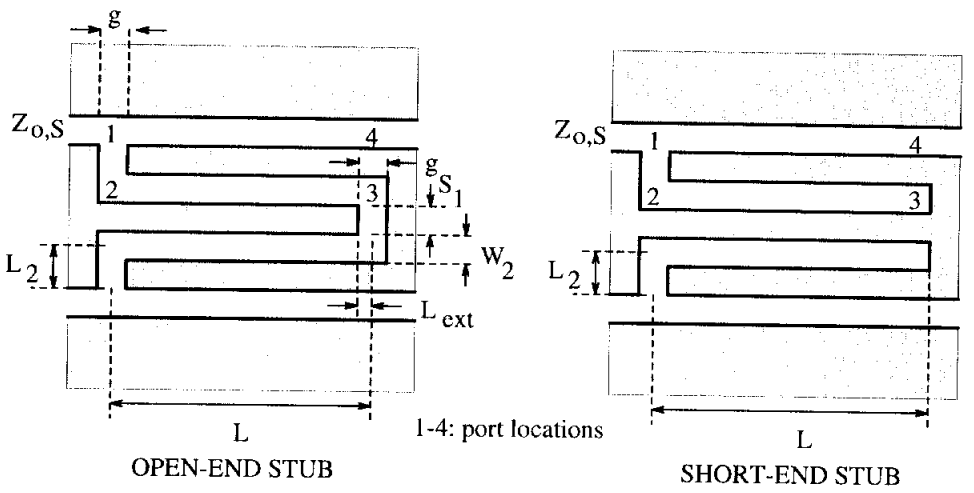

Figure 4.9: Open-end and short-end series tuning stubs.

4.3.3 Application to Dual Geometries

It is a useful exercise to examine how the analysis of two coupled slots can be modified to handle the dual geometry of coupled strips. The transformation proceeds as follows:

1. The first requirement is to substitute the equivalent even- and odd-mode impedances used in the 4-port [Z] matrix, as well as the characteristic impedance of the feedline used to find [S]. As discussed in [63], the required relationship is given by

$$Z_{strip} = \frac{\eta_o^2}{4\epsilon_{re} Z_{slot}} \tag{4.21}$$

where η_o is the free-space impedance (376.7 Ω) and ϵ_{re} is the effective dielectric constant of the surrounding medium. This is simply Babinet's principle, using Booker's extension, applied to circuit duals.

2. The next modification pertains to the definitions of α and κ (see Eqns. 4.14). In either the slot problem or its dual, these parameters are used to relate the

relative magnitudes of the current excitations on the two lines. The difference is that the slot voltages, themselves, are the dual of the strip currents, such that

$$\begin{aligned} \alpha_{strip} &= \left(\frac{V_{e2}}{V_{e1}}\right)_{slot} \\ \kappa_{strip} &= -\left(\frac{V_{o2}}{V_{o1}}\right)_{slot} \end{aligned} \tag{4.22}$$

It can be verified that Eqns. 4.24 and 4.20 still hold under these transformations.

3. The third step relates to a change in the terminations, since a short-end slot becomes an open-end strip and an open-end slot becomes a short-end strip.

4. Finally, the series connection of ports 1 and 2 of the 4-port matrix becomes a shunt connection for the strip lines. This ensures that the dual "short-end" stub will provide the same passband response at the quarter wavelength frequency that the "open-end" slot-type stub provides.

The [S] matrix which results after these changes provides the voltage scattering parameters for the dual strip geometry. This [S] matrix can then be converted back for the coupled slot circuit using the following relations:

$$\begin{aligned} S_{11,slot} &= -S_{11,strip} \\ S_{12,slot} &= S_{12,strip} \\ S_{21,slot} &= S_{21,strip} \\ S_{22,slot} &= -S_{22,strip} \end{aligned} \tag{4.23}$$

where the minus sign accounts for an exchange between current and voltage parameters.

4.3.4 Coupled Lines with Lumped Elements

In this section it is shown how to incorporate the lumped element capacitors, which are illustrated in Figure 4.1, into the analysis. The derivation will arbitrarily be conducted using the dual, strip-line model of the geometry.

From Figure 4.10, it is seen that the overlay capacitors are electrically equivalent to a narrowing of the slots, as both provide a localized increase in the shunt capacitance between the conductors. In the dual problem, this becomes a short section of narrow metal line, which can be recognized as a series *inductor*. Therefore, in order to model the lumped capacitance, C_l, the dual formulation can be used with the following modifications to the 4-port [Z] matrix of the coupled line section:

1. Compute $[Z_a]$ for a coupled line section of length L_1 (see Figure 4.1).

2. Account for the "inductor" connected to port 4 as follows:

$$\begin{aligned} L_{eq} &= \frac{\eta_o^2}{4\epsilon_{re}} C_l \\ Z_{a,44} &\Rightarrow Z_{a,44} + j\omega L_{eq} \end{aligned} \tag{4.24}$$

3. Compute $[Z_b]$ for a coupled line section of length $L - L_1$.

4. Combine $[Z_a]$ and $[Z_b]$ in series (see Appendix A).

4.4 Conclusion

This chapter has presented a method for the quasi-TEM analysis of coplanar waveguide type circuits with three center conductors (4 slots) which may include integrated lumped elements. The computational efficiency of the technique makes it suitable for computer-aided design, and the method could also be extended to analyze circuits with greater numbers of center conductors.

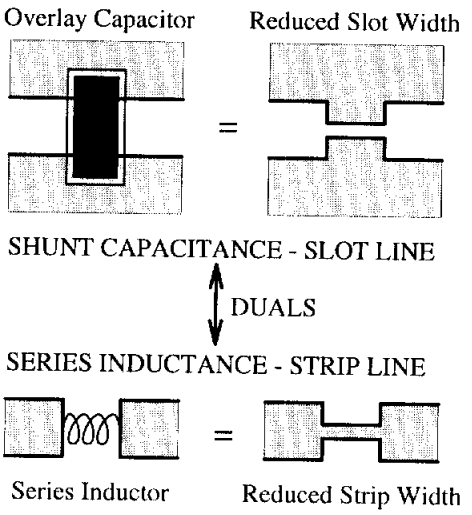

Figure 4.10: Equivalence of an overlay capacitor on a slot-type line to the dual series inductance on a strip-type line.

CHAPTER V

MICROSHIELD CIRCUITS: TRANSITIONS, STUBS, AND FILTERS

5.1 Introduction

An extensive amount of work in the area of microwave passive circuits is related to the design and implementation of filters. The predominant performance objectives are low pass-band insertion loss and high stop-band rejection, and exceptional results have been achieved using designs based on waveguide cavities and dielectric resonators. For example, at X-band, filters have been demonstrated with 2.8% bandwidth, 0.4 dB insertion loss, and 50 dB rejection at $\pm$ 10% of the center frequency [64]. Technologies such as cellular phones and automotive radar, however, demand compact, low cost RF circuitry. These requirements favor the use of planar, monolithic implementations over the waveguide architectures, since they are smaller, less costly to fabricate, and are more easily integrated with active devices and planar antennas. Not surprisingly, the advantages come at the expense of lower performance, since the losses in planar lines are approximately two orders of magnitude greater than in waveguide. This size/cost/performance tradeoff makes the low loss characteristics of the microshield line very important, particularly at millimeter wave frequencies.

In order to investigate the use of microshield-based filters, a number of components have been characterized theoretically and experimentally. These include standard configurations such as transitions from coplanar waveguide, series open- and short-end tuning stubs, and stepped-impedance low-pass filters. The research has also involved the study of new, compact stub and filter designs. In one case, a "folded" stub geometry has been utilized to reduce stub lengths by a factor of approximately 0.42, without significantly altering the electrical characteristics. A second technique is based on the distributed/lumped element configurations which were introduced in Chapter IV. As will be demonstrated, this approach is useful for achieving narrow bandwidth circuits using a limited number of elements.

Unless otherwise mentioned, the microshield circuit examples presented in the following sections have lower shielding cavities which are either 355 or 500 μm high (corresponding to standard thickness silicon wafers) and from 1200 to 1800 μm wide. Specific dimensions are called out only in cases where the cavity size has a noticeable effect on the RF performance.

5.2 Transitions to Coplanar Waveguide

An electrically short, low loss transition between microshield and grounded coplanar waveguide (GCPW) is important for potential applications in which both types of lines could be integrated. This transition constitutes the most direct approach for coupling power into or out of a microshield circuit, as in the example of the microwave probe contact pads described in Appendix D. Quasi-optical (Ch. VI) and waveguide probe [65] techniques are two alternative coupling schemes, but are only appropriate for a narrow range of applications. Beam-lead and flip-chip strategies may eventually become quite useful, however they were not addressed in this work.

Although a rigorous optimization has not been conducted, designs based on a simple matching of quasi-static characteristic impedances have demonstrated very good performance up to 40 GHz. The key factor is to ensure that the field configurations in the GCPW and microshield lines have similar spatial distributions [11]. Specifically, the slots and ground plane spacing should be kept small enough such that the electric field lines are concentrated in the slots, as is typical of conventional CPW. Furthermore, careful design of the substrate-supported line can prevent the angled profile of the silicon sidewall, which results from anisotropic etching, from having a significant effect on the characteristic impedance. Sidewall effects can also be mitigated by tapering the transmission line near the membrane-silicon interface. To demonstrate the transition performance, two of the designs which were tested are shown in Figure 5.1 and their electrical response is given in Figure 5.2. The strong resonances occur at frequencies for which the length of the GCPW sections are multiples of $\lambda_g/2$. Design A has greater than 18 dB return loss across the entire band, and it is expected that a full-wave analysis could lead to even better performance.

5.3 Series Tuning Stubs

Apart from stepped-impedance designs, all stub and filter components considered in this work were based on some form of series tuning stub that is printed in the center conductor. One of the primary reasons is that the parasitic radiation from this type of geometry is generally lower than that of stubs which are printed in the ground plane. Furthermore, the lateral extent of the circuits is minimized by utilizing the center conductor for the stub pattern, allowing smaller lower shielding cavities to be used without affecting the performance. Different variations on the implementation of these stubs are presented in the following sections.

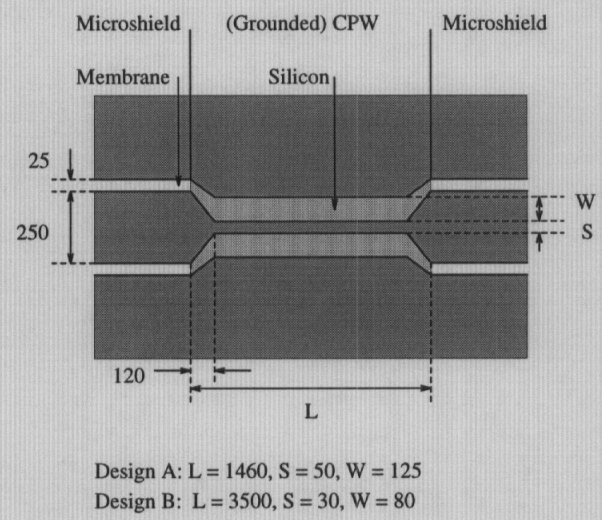

Figure 5.1: Transitions from 75 Ω microshield to 75 Ω grounded CPW, using a 350 μm thick substrate. All listed dimensions are in microns.

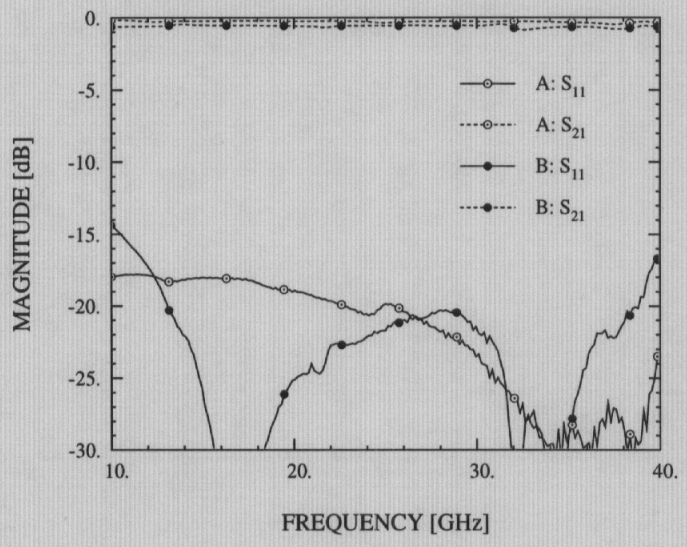

Figure 5.2: Measured scattering parameters for the two transitions shown in Figure 5.1.

5.3.1 Conventional Designs

Short-End Stubs

A conventional short-end series stub in CPW can be realized by deforming the center conductor with two shorted slots which are connected to the center conductor-to-ground plane slots (Figure 5.3). At the resonant frequency, these inner slots are a quarter wavelength long and thus the short circuit at point A is transferred to an open-circuit at point B, resulting in a band-stop response. As reported by several authors [66, 67, 68] this type of stub is useful for circuits such as band-stop filters, pin diode switches and attenuators.

The performance of a design in which L=$\lambda_g/4$ at approximately 30 GHz is shown in Figure 5.4. This plot includes experimental data along with results from the full-wave analysis presented in Chapter III. The shift in the predicted resonant frequency, f_o, is believed to result partly from using an inaccurate value for the effective dielectric constant. Due to fabrication errors, the slot widths in the actual circuit were 3-5 μm smaller than expected, and as discussed in Chapter II, this would cause ϵ_{re} to increase and therefore reduce the resonant frequency. Furthermore, the phase velocity along the stub is certainly somewhat different than it is in the feedlines, due to the 4-slot configuration. This could contribute to the discrepancy in f_o since the estimated ϵ_{re} was taken from measurements of uniform microshield lines.

Another aspect of the data in Figure 5.4 which deserves comment is the radiation loss, $(1 - |S_{11}|^2 - |S_{21}|^2)$; at the first and second resonance, the loss is below -25 dB and -17 dB, respectively. Considerably worse performance is exhibited by short-end stubs which are printed in the ground plane, perpendicular to the transmission line. By bending the stubs to be parallel to the transmission line, however, the

radiation loss then becomes comparable to that of the center conductor stub. This bent geometry is illustrated in Figure 5.5, and the calculated performance assuming two different offsets (S_1) is given in Figure 5.6. It is seen that the loss increases by 2-3 dB by increasing the offset from 75 μm to 150 μm. As the ratio of S_1 to L continues to increase and the stub becomes more perpendicular to the transmission line, the radiation loss increases correspondingly [69].

In addition to being an important performance advantage, the low loss of the center conductor stub also allows for very accurate characterization using the coupled line technique described in Chapter IV. An example of the agreement which can be obtained with the full-wave analysis is shown in Figure 5.7. Depending on the particular geometry, the full-wave results take between 10-30 minutes per frequency point on an IBM RS6000 work-station, whereas the curves shown for the coupled line technique required less than 20 seconds to generate. The speed of this analysis tool is useful for studying the effects such as varying the inner and outer slot widths, which will primarily influence the bandwidth of the circuit. Decreasing the inner slot widths, for instance, increases the series capacitance and causes the 3-dB bandwidth to shrink. This explains why the bandwidth of a microshield stub is a much wider than that of a comparable stub on GaAs (roughly 70% compared to 35%) [66]. Once the S-parameters are known, a circuit simulator can then be utilized to determine an equivalent circuit using the model demonstrated in [9, 66].

Open-End Stubs

The open-end series stub is similar to the short-end stub except that the slots in the center conductor are connected at their ends (Figure 5.8). A band-pass response is thus obtained when the length is equal to $\lambda_g/4$, making these stubs useful as DC

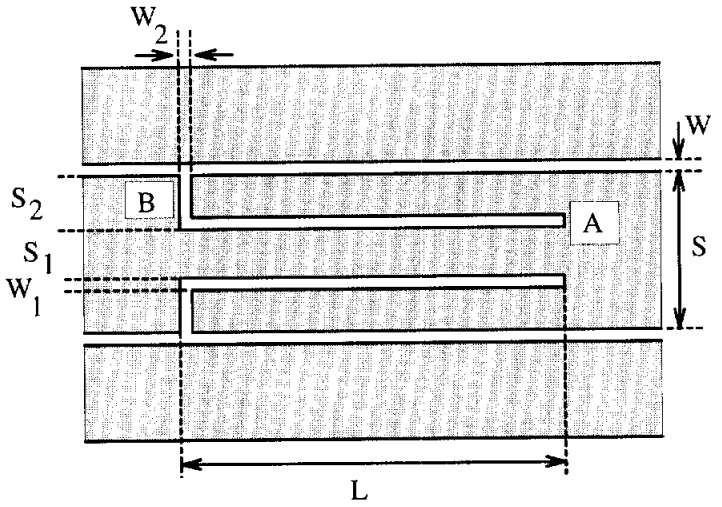

Figure 5.3: A microshield short-end series stub.

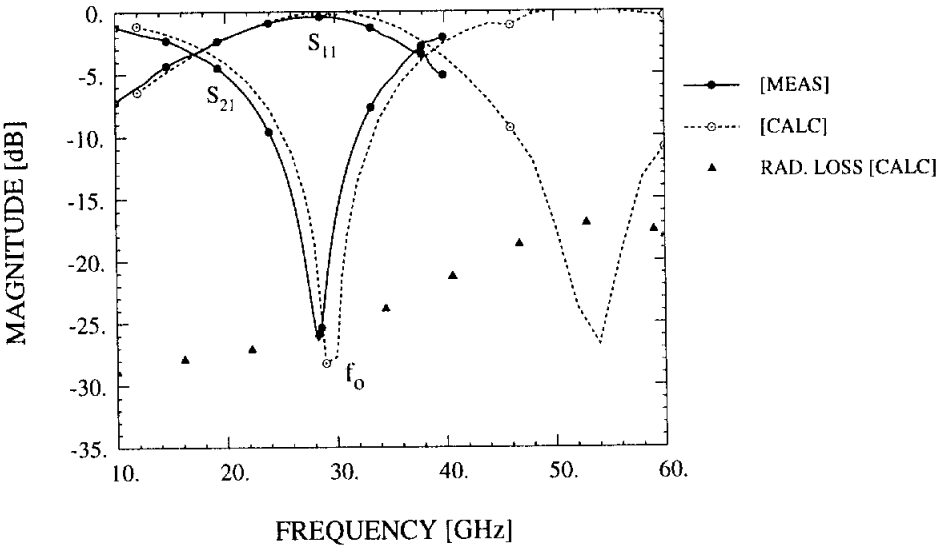

Figure 5.4: Measured and calculated S-parameters for a microshield short-end series stub. The stub dimensions are L=2500, S=250, W=25, S_1=40, S_2=80, W_1=25, and W_2=200 μm.

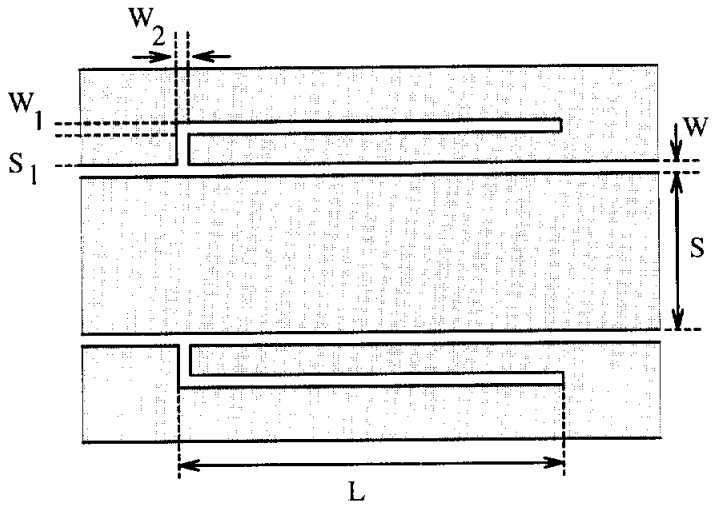

Figure 5.5: A microshield short-end series stub printed in the ground plane.

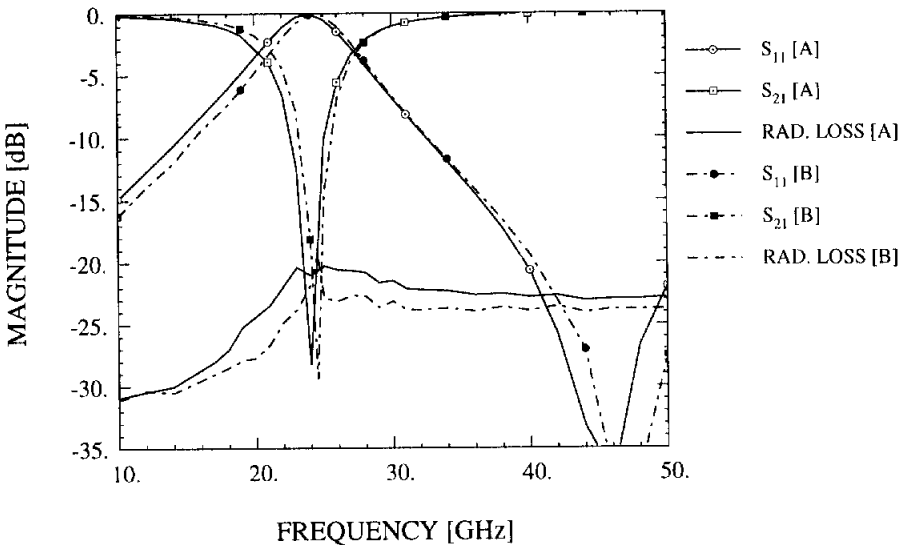

Figure 5.6: Calculated S-parameters for two microshield short-end series stubs printed in the ground plane. For designs A and B, the dimension S_1 is 150 and 75 μm, respectively; the remaining dimensions are L=2720, S=260, W=20, W_1=20, and W_2=20 μm.

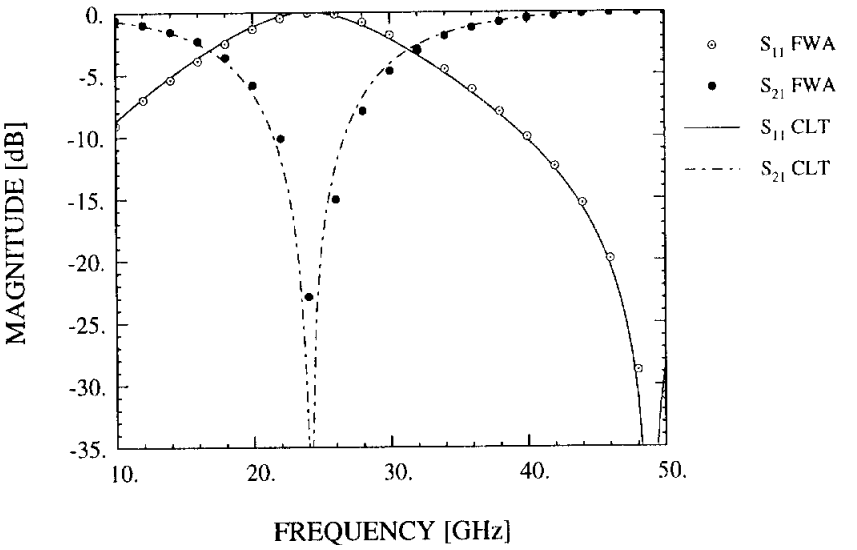

Figure 5.7: Comparison between the results from the full-wave analysis (FWA) and the coupled line technique (CLT). The circuit is a microshield short-end series stub with the following dimensions: L=2720, S=260, W=20, S_1=70, S_2=75, W_1=20, and W_2=20 μm (design S-A from Table5.1).

and LO blocks. They also find application in the design of band-pass filters [70], as will be demonstrated in Section 5.5 and in Chapter VI.

The characteristics of a microshield open-end stub are shown in Figure 5.9, which compares experimental data with results from the full-wave analysis. The radiation loss is below -25 dB through the first resonance and increases to -17 dB when the length is equal to $\lambda_g/2$, in a manner similar to that of the short-end configuration. The discrepancy between the measured and predicted resonant frequency is approximately 3%, and carries the same explanation as that given for the short-end stub. Also, the small structure which is apparent in the measured data near 30 GHz may be explained by inadequate grounding between the upper and lower ground planes. Since the total cavity length (stub plus feedlines) is around $\lambda/2$ at this frequency, poor grounding may result in a noticeable resonance.

Excellent agreement between the full-wave analysis and the coupled line technique is also obtained in characterizing the open-end stub. This is exemplified by the curves in Figure 5.10, in which the values for S_{21} are nearly identical up to the first resonance and the difference in S_{11} is less than 0.5 dB. As with the short-end stub, the accuracy of the coupled line technique makes it useful for analyzing the effects of variations in the stub dimensions. It has been found that an increase in the series capacitance, due to a reduction of the inner slot widths, leads to an increase in the 3-dB bandwidth; this is consistent with the fact that stubs on substrates such as GaAs have larger bandwidths than do comparable microshield geometries. An increase in the shunt capacitance, due to a reduction in the outer slot widths, results in a narrower 3-dB bandwidth. Equivalent circuits can also be determined for the open-end stubs using the model found in [9].

5.3.2 Compact Designs

One of the implications of using a low permittivity substrate, versus a high permittivity substrate such as silicon or GaAs, is that the physical size of a distributed microwave component increases. Compared to a circuit printed on a material with a dielectric constant of ϵ_r, a similar circuit on an air substrate will increase in length by a factor of approximately $\sqrt{(\epsilon_r + 1)/2}$. This can have a significant impact in applications requiring high density layouts, particularly at lower frequencies, and thus a strong interest exists in developing compact geometries.

In order to address this need, attention has been directed towards the miniaturization of the conventional CPW-type series tuning stubs presented in the previous section. The solution considered here involves the concept of a *folded* geometry, in which the stub arms are folded back upon themselves one or two times. Depending

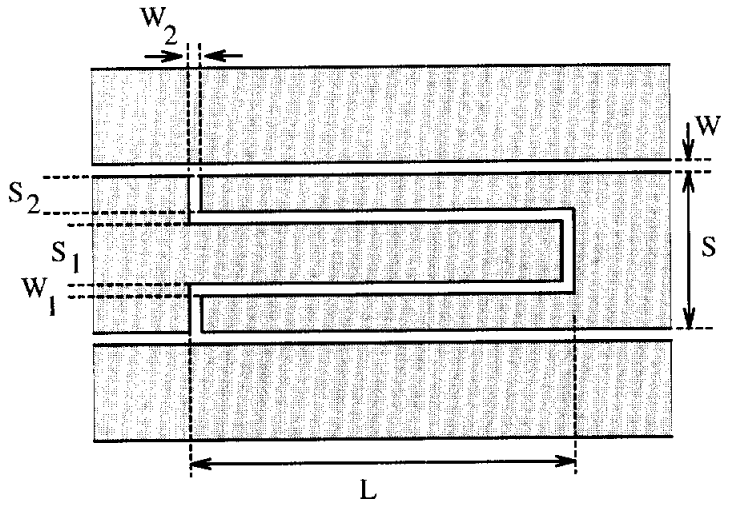

Figure 5.8: A microshield open-end series stub.

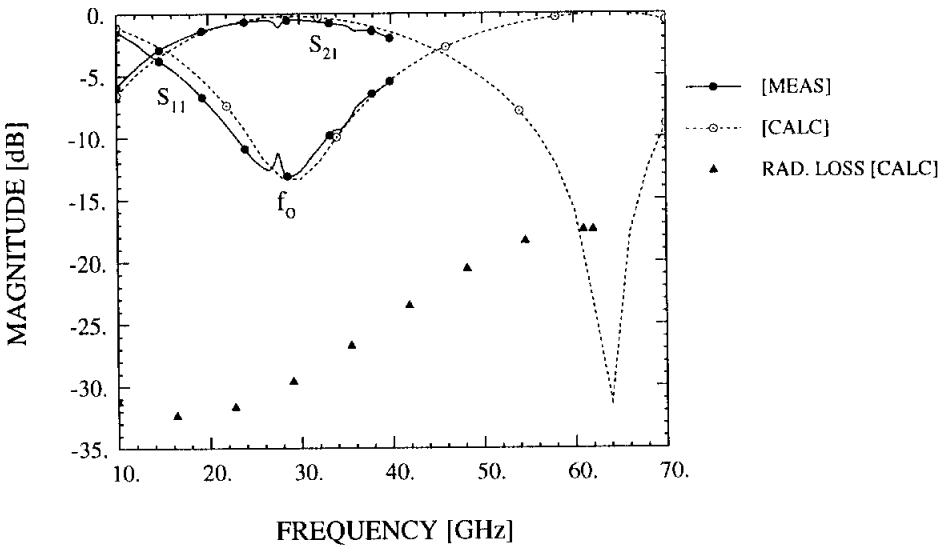

Figure 5.9: Measured and calculated S-parameters for a microshield open-end series stub. The stub dimensions are L=2500, S=250, W=25, S_1=40, S_2=80, W_1=25, and W_2=200 μm.

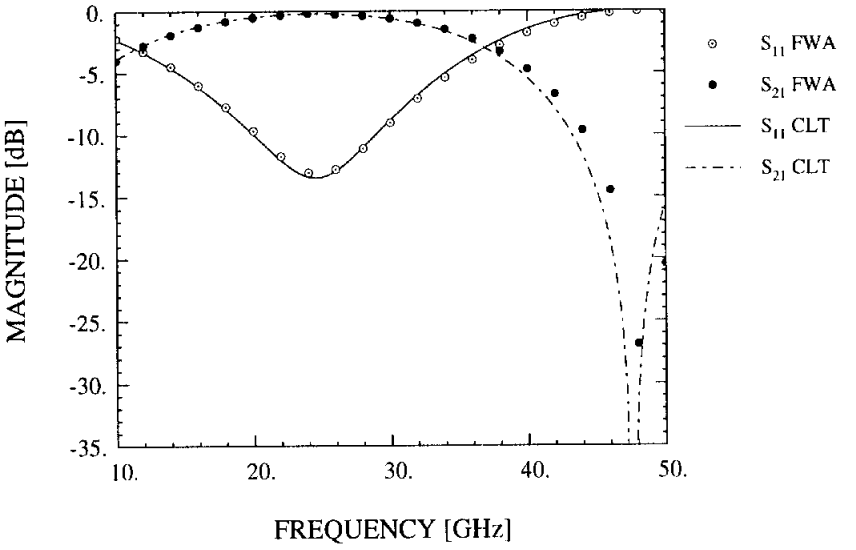

Figure 5.10: Comparison between the results from the full-wave analysis (FWA) and the coupled line technique (CLT). The circuit is a microshield open-end series stub with the following dimensions: L=2720, S=260, W=20, S_1=70, S_2=75, W_1=20, and W_2=20 μm.

on the folding pattern, the effective stub length can be reduced by a factor of up to 2.4, while achieving nearly the same electrical characteristics as a standard design. In this manner the size of a folded microshield stub becomes equivalent to a non-folded CPW stub on a substrate such as GaAs.

Folded Short-End Stubs

The five short-end, folded stub geometries which were studied are illustrated along with the conventional design in Figure 5.11. For the single-folded approach there are two ways of interleaving the fingers, whereas there are three possible arrangements for the double-folded approach. Each pattern yields a unique frequency response, as demonstrated by the examples provided in Table 5.1 and the associated plots in Figures 5.12-5.17. This data contains calculated results which were generated using the full-wave analysis along with experimental results for design S-D. By comparing

these plots to the performance of the conventional design (S-A) shown in Figure 5.7, it is seen that similar behavior is obtained using Design S-D, although it is 2.4 times shorter than S-A at the first band-stop resonance. The other four configurations have somewhat different characteristics and provide varying degrees of miniaturization.

In order to show that the folding technique is also applicable to standard substrate-supported CPW, a design on GaAs is included in Table 5.1 (S-F2). A potential problem with the high permittivity substrate is parasitic radiation, since a relatively wide center conductor is required to accommodate the multi-finger geometry. The performance can be greatly improved, however, by utilizing the micromachining techniques reported by Drayton et al. [6] to integrate a lower shielding cavity. This type of cavity has been assumed in the analysis of design S-F2, the results of which are shown in Figure 5.17. The cavity size in this case was 800 μm wide by 500 μm deep, which was small enough such that a shorter version of the same geometry could be made to operate very well up to at least 35 GHz. At lower frequencies (e.g. below 15 GHz), larger line widths can be used without significant radiation effects, making the shielding cavities unnecessary.

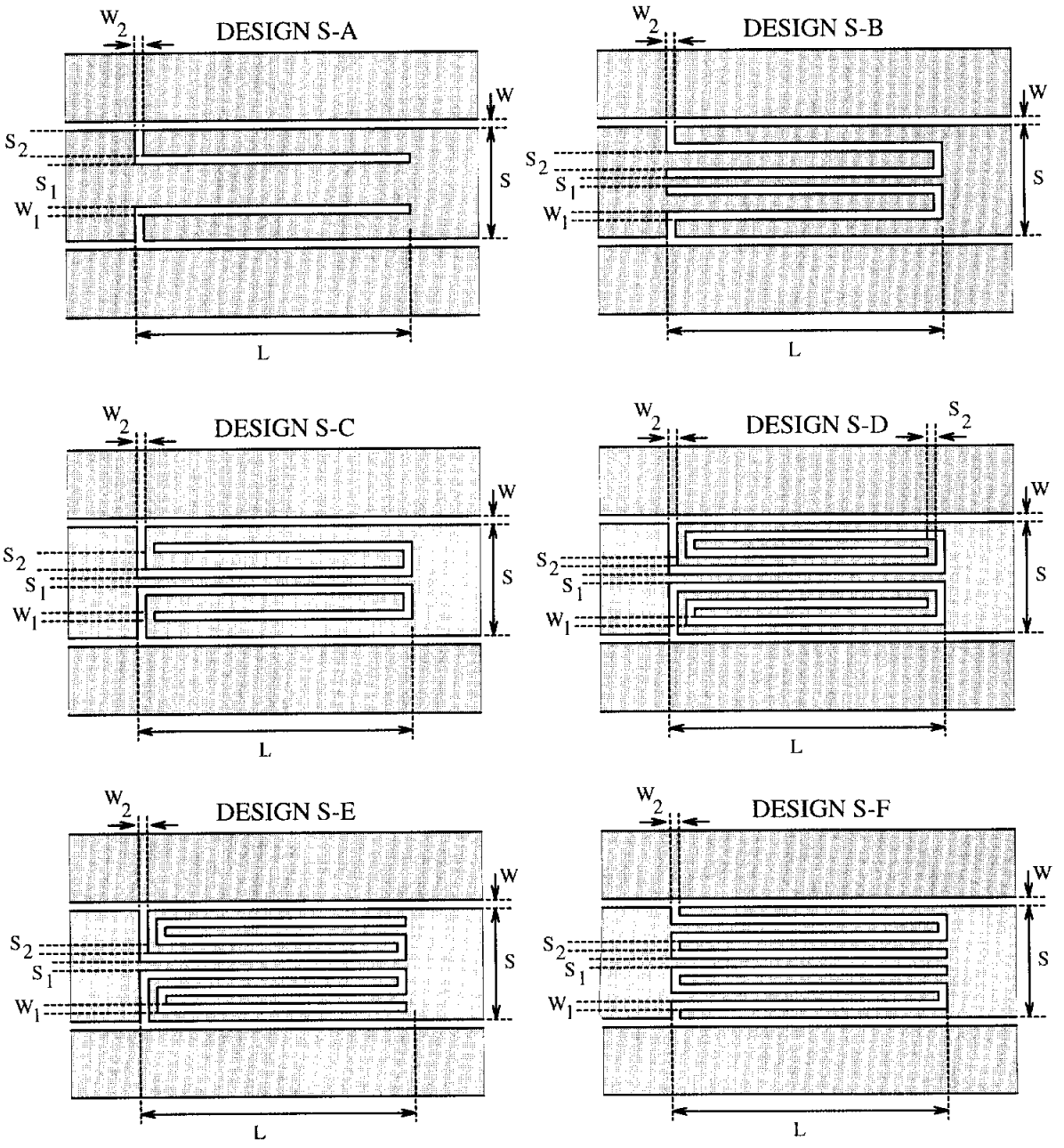

Figure 5.11: Conventional and compact short-end series stub configurations. S_1 refers to the center finger width and S_2 refers to the width of all outer fingers.

Design	S	W	S_1	S_2	W_1	W_2	L	ϵ_r	λ_r/L
S-A	260	20	70	75	20	20	2720	1.4	4.2
S-B	260	20	36	36	20	20	1320	1.4	7.3
S-C	260	20	36	36	20	20	1320	1.4	7.4
S-D	260	20	20	20	20	20	1020	1.4	9.9
S-E	260	20	20	20	20	20	1020	1.4	8.9
S-F1	260	20	20	20	20	20	1020	1.4	9.2
S-F2	130	80	10	10	10	10	720	13.1	9.8

Table 5.1: Parameters for conventional (S-A) and folded short-end stub designs, where λ_r is the guide wavelength at the first band-stop resonance. The dielectric constant of 1.4 was used to simulate the microshield line for the dimensions given in the table. All dimensions are in μm.

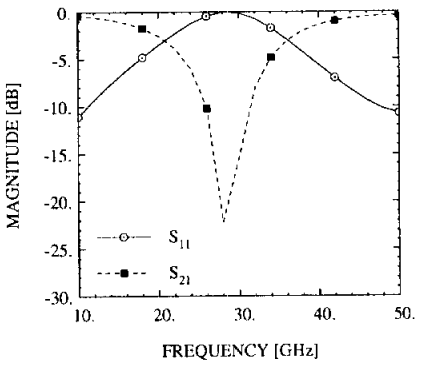

Figure 5.12: Performance of stub S-B.

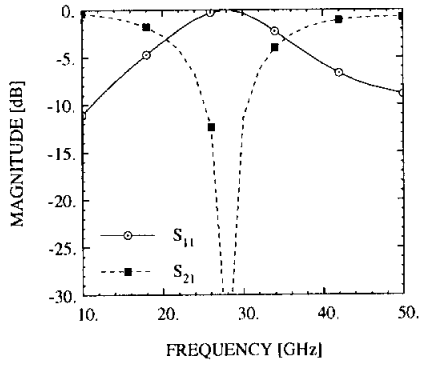

Figure 5.13: Performance of stub S-C.

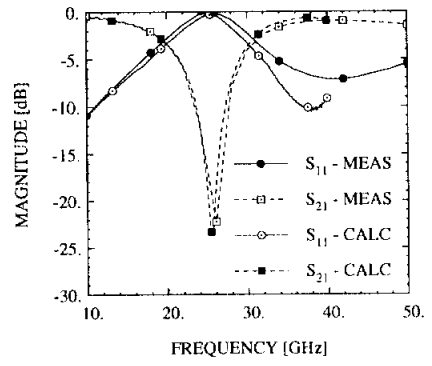

Figure 5.14: Performance of stub S-D.

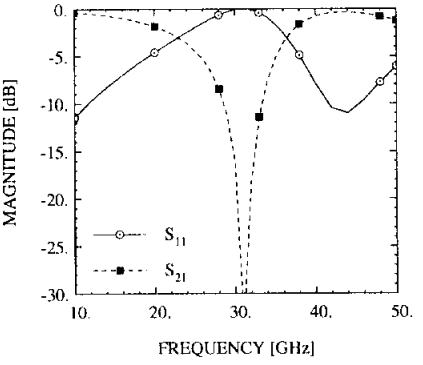

Figure 5.15: Performance of stub S-E.

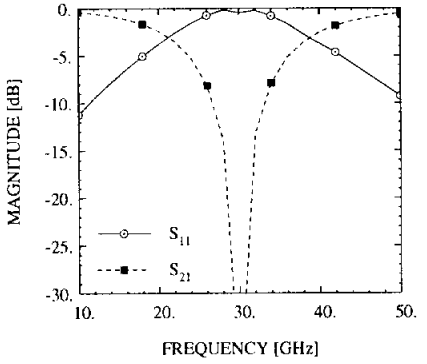

Figure 5.16: Performance of stub S-F1.

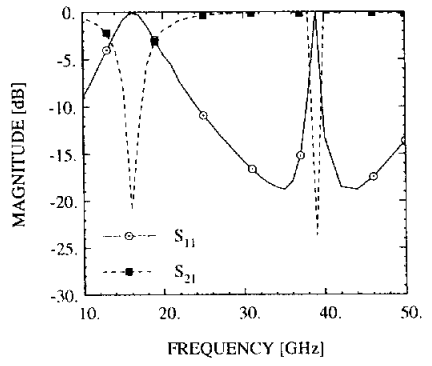

Figure 5.17: Performance of stub S-F2.

Folded Open-End Stubs

Along with the work on the short-end stubs, an investigation has been made into different possibilities for folded open-end stubs. In this case there is only one way of interleaving the fingers in a single-folded approach, and two ways for the double-folded geometry. These three configurations are illustrated along with the conventional design in Figure 5.18.

As shown by the examples provided in Table 5.2 and the corresponding plots in Figures 5.19-5.24, each pattern exhibits a different frequency response. It can be seen from the last column of the table that the performance of the conventional design (O-A) is achieved using a stub with a total length of around $\lambda_r/10$ (O-D1 through O-D3). It is also observed that the implementations which are essentially interdigitated capacitors (O-B1, O-B2, O-C) have characteristics that are distinctly different than the conventional stub. In all cases, the radiation loss is similar to that seen in Figure 5.9. Finally, as with the short-end stubs, a lower shielding cavity of dimensions 800 μm by 500 μm has been included in the designs on the high permittivity substrate.

The last row in Table 5.2 represents a circuit designed to resonate at approximately 330 GHz. The results, shown in Figure 5.24, do not include the effects of a lower shielding cavity and yet the radiation loss is still low enough that the performance is maintained through the first resonance. Using the approximation that the total ground plane separation should be less than $\lambda/10$, this design has an upper frequency for quasi-TEM operation of around 300 GHz. Assuming the minimum line width to be 5 μm, this represents the practical limit for the microshield, double-folded stub geometry.

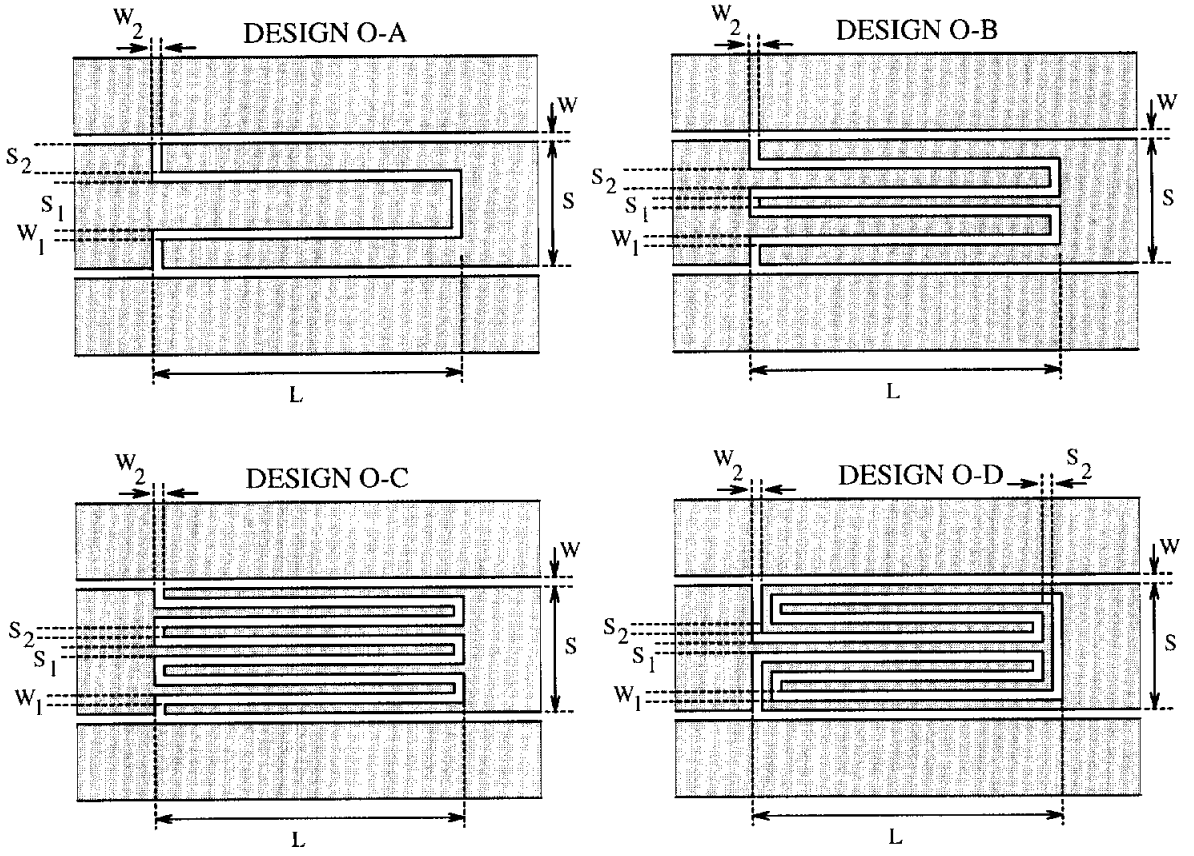

Figure 5.18: Conventional and compact open-end series stub configurations. S_1 refers to the center finger width and S_2 refers to the width of all outer fingers.

Design	S	W	S_1	S_2	W_1	W_2	L	ϵ_r	λ_r/L
O-A	260	20	70	75	20	20	2720	1.4	4.2
O-B1	260	20	36	36	20	20	2320	1.4	5.2
O-B2	90	60	10	10	10	10	900	13.1	4.9
O-C	260	20	20	20	20	20	1140	1.4	6.0
O-D1	260	20	20	20	20	20	1140	1.4	10.0
O-D2	130	80	10	10	10	10	550	13.1	10.0
O-D3	65	20	5	5	5	5	86	1.4	9.6

Table 5.2: Parameters for conventional (O-A) and folded open-end stub designs, where λ_r is the guide wavelength at the first band-pass resonance. All dimensions are in μm.

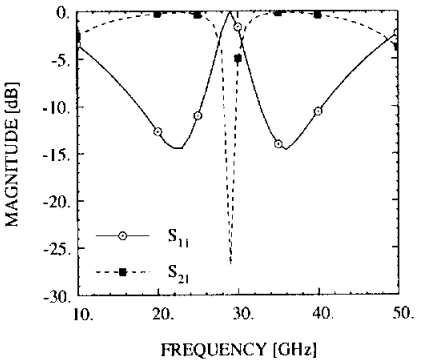

Figure 5.19: Performance of stub O-B1.

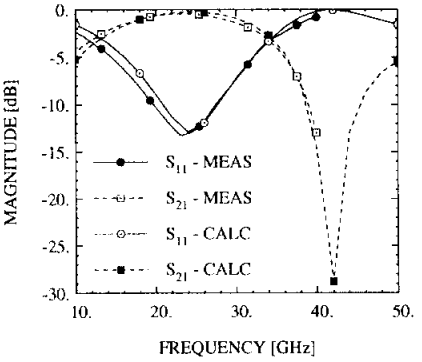

Figure 5.22: Performance of stub O-D1.

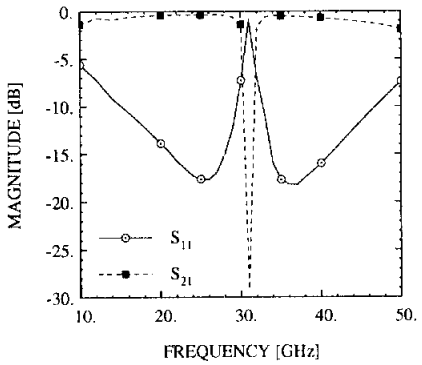

Figure 5.20: Performance of stub O-B2.

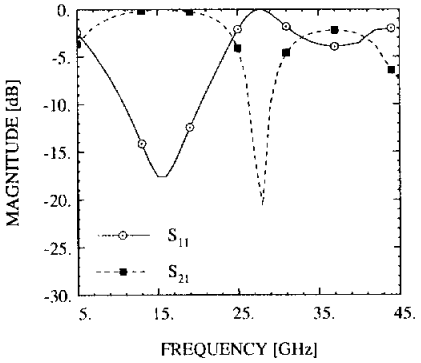

Figure 5.23: Performance of stub O-D2.

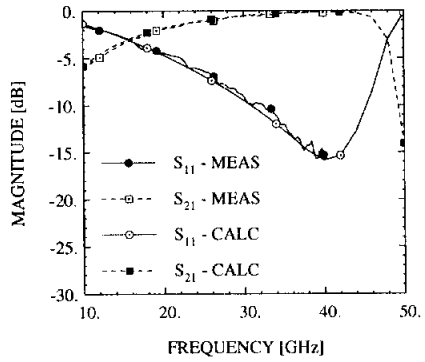

Figure 5.21: Performance of stub O-C.

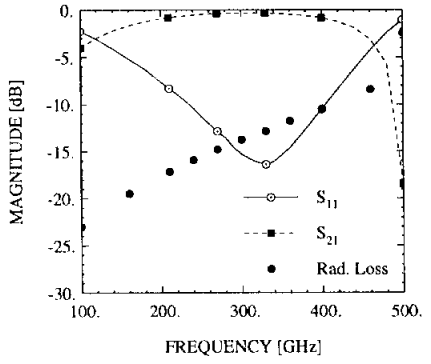

Figure 5.24: Performance of stub O-D3.

5.3.3 Hybrid Designs

In addition to the folded stub configurations, an alternative design approach has been developed which emphasizes bandwidth reduction along with circuit miniaturization. The target applications are those in which the quarter-wavelength resonance of the series stubs are utilized for frequency separation, as in the use of the open-end stub as a band-pass filter. With conventional or folded series open-end stubs, the 3-dB bandwidth typically ranges between 70% to over 100%, depending on the substrate and the stub geometry. This may force the circuit designer to cascade multiple stubs in series in order to achieve a smaller passband, leading to circuit dimensions around 0.5 λ_g or greater. An inherent property of the open-end stub, however, is that the bandwidth can be decreased by increasing the shunt capacitance. This fact motivated the implementation of the "hybrid" stub geometry, in which lumped element capacitors are integrated with the distributed element stub.

The basic configuration consists of two cascaded stubs, with the second stub reversed relative to the first (Figure 5.25). Along the length of the stubs, MIM (metal-insulator-metal) overlay capacitors are deposited in shunt with the outer stub arms and the upper ground planes. This is believed to be a unique approach for combining lumped and distributed elements for filter applications, although variations of the technique have been presented by previous authors (e.g. [71, 72]). In this research, the capacitor dielectric was a silicon monoxide (SiO) layer which was approximately 1 μm thick.

The particular geometry illustrated in Figure 5.25 is useful as a compact LO (local oscillator) block with good low frequency rejection, as demonstrated by the circuits described in Table 5.3. The performance of these designs is presented in Figures 5.26-5.31, and consists of measured data and theoretical data obtained using

the coupled line analysis. For the purpose of comparison, the performance of a design which has no capacitors (H-O1) is shown in Figure 5.26. The center frequency is 60 GHz, corresponding to the quarter-wavelength frequency of each of the open-end stubs. In design H-O2, 17.5 pF capacitors have been integrated 410 μm from the ends of each stub, resulting in a pass-band resonance at 37 GHz and a 3-dB bandwidth of 26% (Figure 5.27). By moving the capacitors closer to the ends of the stubs, the passband is shifted down to 32 GHz, as demonstrated by design H-O3 (Figure 5.28). This trend indicates that the lowest resonant frequency, for a given stub length and capacitor size, is obtained by positioning the capacitors at the stub ends. An explanation for this can be found by breaking down the circuit into simple resonators, each one formed by a series capacitance (the stub section) combined with a shunt capacitance (the overlay capacitors). Placing the capacitors at the end of each stub maximizes the distance between resonators, thus reducing the resonant frequency. By examining the curves in Figure 5.29, it is observed that the resonant frequency can also be decreased by utilizing larger capacitors. This is accompanied by a significant reduction in the bandwidth, however, and the insertion loss naturally tends to increase.

A method to lower the resonant frequency and keep the insertion loss down is to use stubs with a higher characteristic impedance, as in designs H-O5 and H-O6. These stubs have broader 3-dB bandwidths than stubs with lower characteristic impedance, since the shunt capacitance is smaller. Thus, the same size overlay capacitor yields a wider bandwidth and lower insertion loss; this is seen by comparing the characteristics of designs H-O3 and H-O5. The last design in the table (H-O6) shows that a resonant frequency at 25.5 GHz can be achieved with 1 dB insertion loss and 30 dB rejection at 5 GHz. An open-end series stub of approximately the

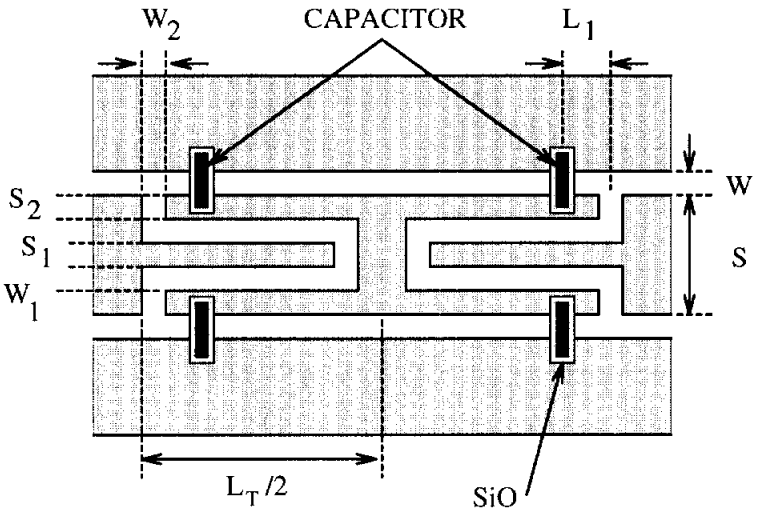

Figure 5.25: Hybrid open-end stub configuration.

the same length exhibits 0.25 dB loss at 27 GHz and only 7-9 dB rejection at 5 GHz.

Design	S	W	S_1	S_2	W_1	W_2	L_1	C, fF	ϵ_r	λ_r/L_T	$S_{21,max}$	%BW
H-O1	260	20	40	85	25	100	-	0.0	1.4	2.28	-	76
H-O2	260	20	40	85	25	100	410	17.5	1.4	2.98	-0.83	26
H-O3	260	20	40	85	25	100	170	17.5	1.4	3.15	-0.90	24
H-O4	260	20	40	85	25	100	170	35.0	1.4	3.83	-1.80	10.5
H-O5	260	70	40	85	25	100	170	17.5	1.1	3.70	-0.50	28
H-O6	260	70	40	85	25	100	170	25.8	1.1	4.45	-1.00	18

Table 5.3: Parameters for hybrid open-end stub configurations, all of which have a total length of L_T=2500 (refer to Figure 5.25). The passband insertion loss, $S_{21,max}$ (dB), is included for designs which have been characterized experimentally. All dimensions are in μm.

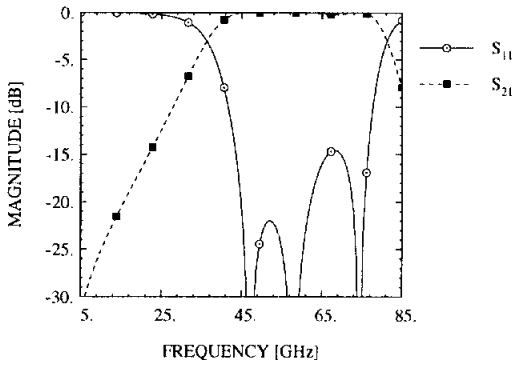

Figure 5.26: Performance of stub H-O1.

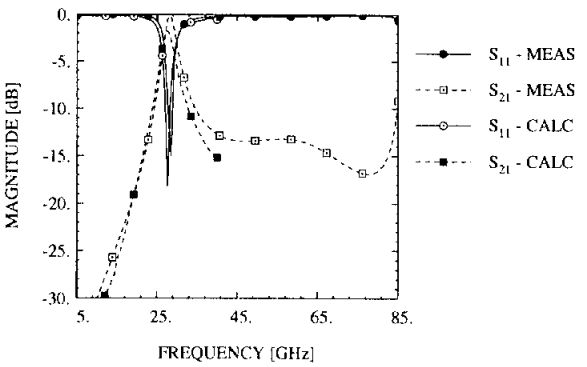

Figure 5.29: Performance of stub H-O4.

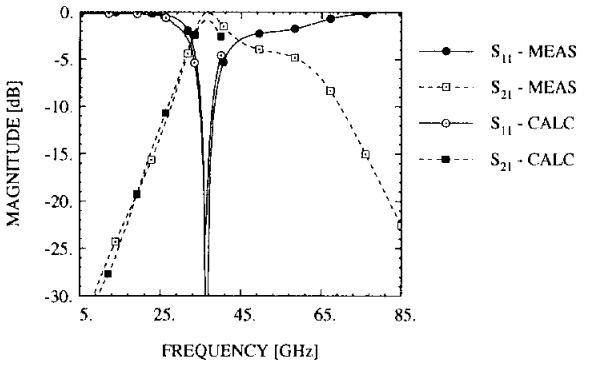

Figure 5.27: Performance of stub H-O2.

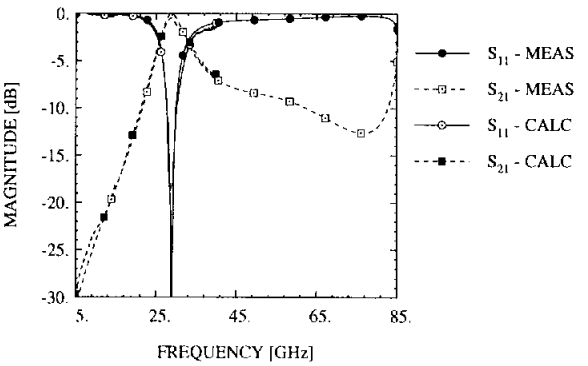

Figure 5.30: Performance of stub H-O5.

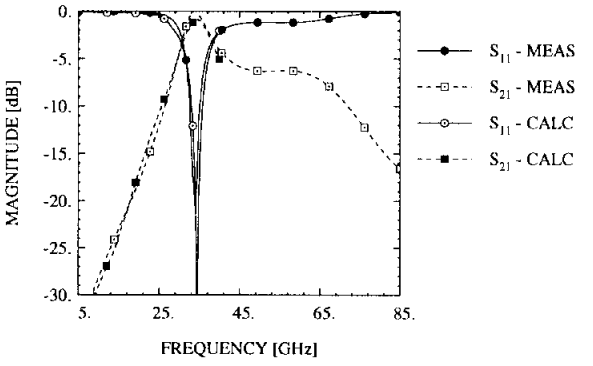

Figure 5.28: Performance of stub H-O3.

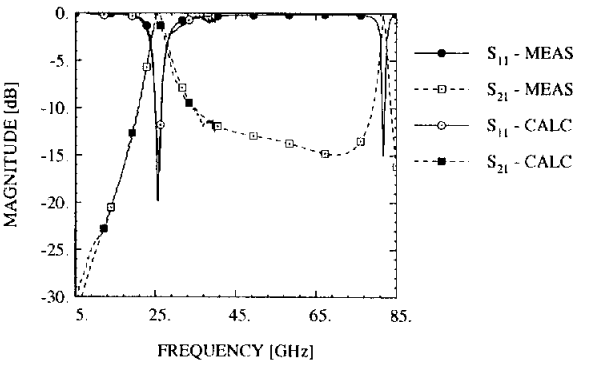

Figure 5.31: Performance of stub H-O6.

5.4 Low-Pass Filters

One of the first demonstrations of the microshield geometry was in implementing a stepped-impedance low-pass filter [73]. The stepped-impedance approach is a relatively easy technique to use, and it is well suited for applications which do not require a sharp roll-off in the insertion loss. An advantage of utilizing microshield for this application is that the absence of dielectric-related loss, both attenuation and parasitic radiation, results in low pass-band attenuation. Furthermore, the broad single mode bandwidth of microshield ensures that the high frequency rejection will not deteriorate due to the presence of higher-order modes.

In order to verify these expectations, stepped-impedance filters using 5-, 7-, and 9-sections were designed and tested. As presented in [73], the measured performance compared very well with ideal transmission line theory, as a result of the TEM nature of the microshield propagating mode. The transmission line model compensated for the step change in the center conductor width using standard expressions derived for microstrip [74]. As shown in [5], however, these approximations are not accurate at higher frequencies. In Figure 5.32, the measured data for a 5-section, 0.5 dB ripple Chebyshev filter is compared with results from the full-wave analysis described in Chapter III. The rejection is greater than 20 dB up to 75 GHz, which is about 1.5 octaves above the 3-dB point at 26 GHz. Also, the measured S_{21} is between 0.25 and 0.9 dB from 10-23 GHz; this is very close to the 0.5 dB ripple design specification, and indicates that the attenuation is approximately 0.3 dB. The discrepancy between the measured and calculated data may be explained by calibration errors, and the necessity to model the circuit with a single effective dielectric constant (refer to Chapter II.) In reality, the low- and high-impedance sections have different values

for ϵ_{re}, due to the large variation in the slot and center conductor widths.

The band-stop response of the short-end series stub discussed in Section 5.3.1 can also be useful for low-pass filter designs. One example is the addition of a short-end stub onto the end of the stepped-impedance low-pass filter described above. The stub has a length of 940μm, with other dimensions identical to those listed in Figure 5.4, and resonates around 90 GHz. A significant improvement in the stop-band is obtained, as can be seen by comparing the theoretical performance of this new filter (Figure 5.33) to the performance without the stub (Figure 5.32). Another example is a very compact (1.98 mm) low-pass/band-stop filter which consists of two of the short-end stubs positioned back-to-back. The filter has a corner frequency of 32 GHz, approximately 0.5 dB pass-band ripple, and very high rejection from 80 to 90 GHz (Figure 5.34). This type of performance could be useful in applications such as sub-harmonic mixing.

5.5 Band-Pass Filters

A variety of methodologies exists for the implementation of planar bandpass filters. In microstrip or stripline form it is common to utilize a configuration of edge-coupled strips, as with the filters presented by Chi and Robertson [4, 75]. For coplanar waveguide applications, filters using a combination of series and shunt tuning stubs, such as those presented in Section 5.3.1, have received considerable attention (e.g. [69, 76, 77]). In a slightly different manner, electrically-short series open-end stubs have been utilized as admittance inverters between $\lambda_g/2$ resonators in end-coupled designs [70]. The main objectives of this research, however, were to develop filters with minimal lateral width to keep the cavity dimensions small, and to achieve reasonably short longitudinal dimensions. Designs ranging in length between

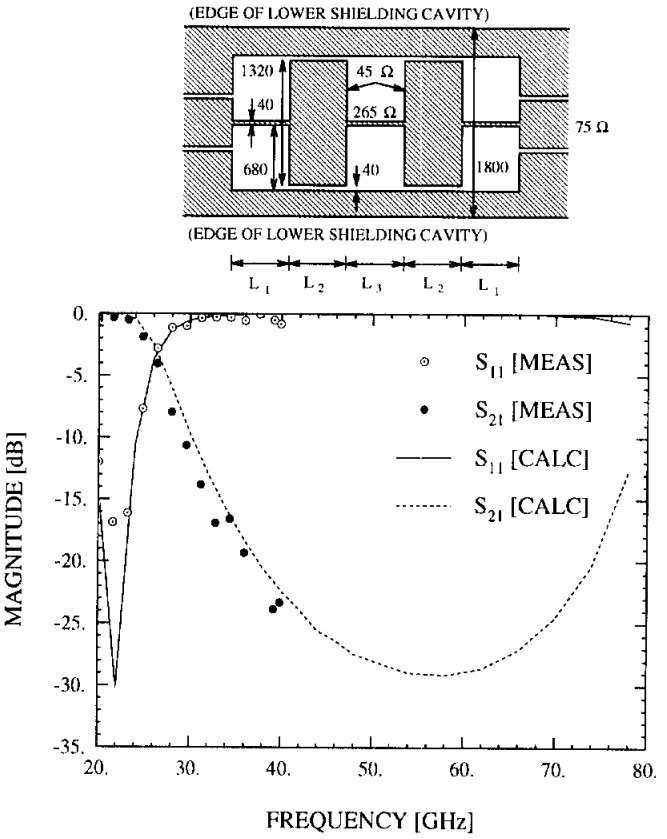

Figure 5.32: Measured and calculated S-parameters of a microshield low-pass filter. The lengths of the sections are L_1=745, L_2=1200, and L_3=1189 microns. The cavity height is 350 μm.

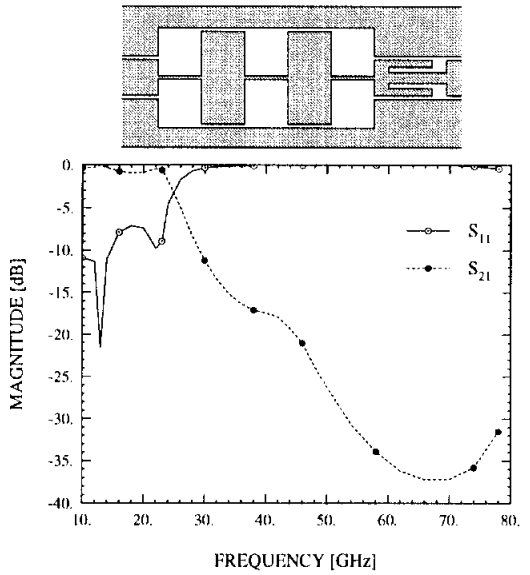

Figure 5.33: Theoretical performance of the filter shown in Figure 5.32 with a 90 GHz short-end series stub attached.

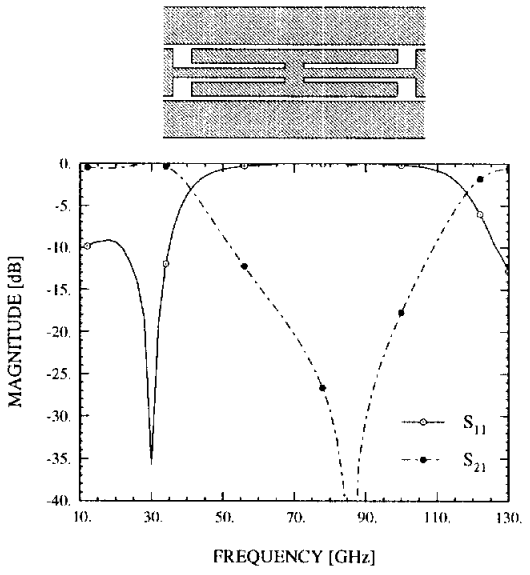

Figure 5.34: Theoretical performance of two 90 GHz short-end series stubs.

0.5-0.8 λ_g, and with bandwidths between 15 and 60%, will be presented herein. In all cases the measured pass-band attenuation, which includes radiation and conductor loss, has an uncertainty of less than $\pm$ 0.1 dB.

The different band-pass filter implementations are illustrated in Figure 5.35 and some of the performance characteristics are listed in Table 5.4. The first design consists of three open-end stubs which are cascaded in series, with each stub being approximately $\lambda_g/4$ in length at the center frequency. The measured response (Figure 5.36) shows an insertion loss of only 1.0 dB from 22-32 GHz, which is competitive with the best waveguide bandpass filters using suspended stripline [78]. The attenuation of this filter could be reduced by using thicker metalization[1] or larger slot widths to minimize the conductor loss. In order to predict the performance, the filter was treated as three non-coupled elements and the scattering parameters found from the full-wave analysis of a single stub were used. The agreement between the measured and calculated results is nearly exact at the high end of the band, and the shift of approximately 1 GHz at the low end of the band is consistent with the single stub comparison (Figure 5.9). This indicates that there is very little electromagnetic coupling between the stubs, even though the separation between them is only 150 μm. The response of the filter can also be modeled almost exactly, including the 1 dB insertion loss, by cascading the *measured* results for a single stub.

The next two designs in Table 5.4 are based on the folded open-end stub geometry, and their performance is illustrated in Figures 5.37 and 5.38. It is immediately apparent that these 5-section filters provide greater out-of-band rejection than the previous 3-section design, and yet they are only 65% as long due to the use of the compact stub. Design 2 has a measured 3-dB bandwidth of 32% and a pass-band loss

[1] All circuits fabricated in this study had a metalization thickness of 1 μm.

Design	Type	f_o	L_T at f_o, λ_g	%BW	$S_{21,max}$	S_{21} @ $0.5f_o$	S_{21} @ $1.5f_o$
1	O-A	29	0.80	58/55	-1.0	-17	-17
2	O-D	24	0.51	32/27	-2.0	-29	-32
3	O-D	25	0.53	44/38	-1.0	-20	-21
4	H-O	28	0.56	17/15	-0.9	-36	-18
5	H-O	29	0.47	17	-	-40	-21

Table 5.4: Parameters for microshield band-pass filter designs (refer to Figure 5.35). The passband insertion loss, $S_{21,max}$ (dB), is included for designs which have been characterized experimentally. In the %BW column, the first number is the measured 3-dB bandwidth and the second is the predicted value.

of 2 dB, while design 3 has a bandwidth of 40% and only 1 dB insertion loss. The single difference between the filters is the outer slot width, which is 20 μm and 70 μm for designs 2 and 3, respectively. This slot-width effect is characteristic of all the series stub-based designs, and while some decrease in loss is expected as the bandwidth increases, a substantial part of the improvement is due to the lower conductor loss of the higher impedance line. In comparing the measured and predicted results, it is seen that the center frequencies are within 0.5-1 GHz, but that a discrepancy of 5% in the bandwidth exists in both cases. This is believed to result from modeling the filters as non-coupled resonators, as explained for the previous case. A complete model of the entire filter would certainly be a more accurate comparison, however the size of the system becomes impractical to solve using the formulation presented in Chapter III.

The last two designs in Table 5.4 consist of a series combination of the hybrid open-end stub configuration. In comparison to the previous geometries, this type

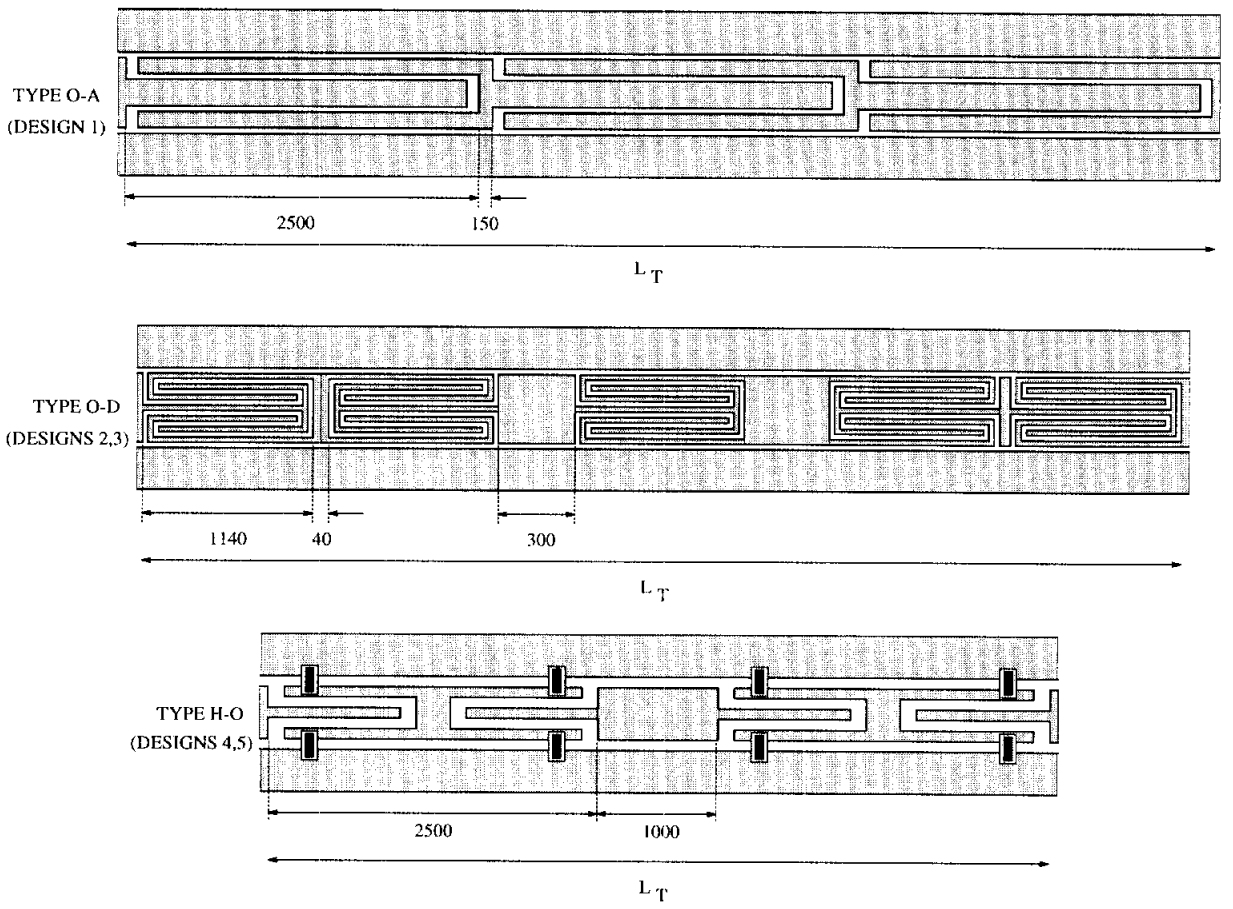

Figure 5.35: Band-pass filter configurations studied in this research. Element lengths and separations are specified in microns.

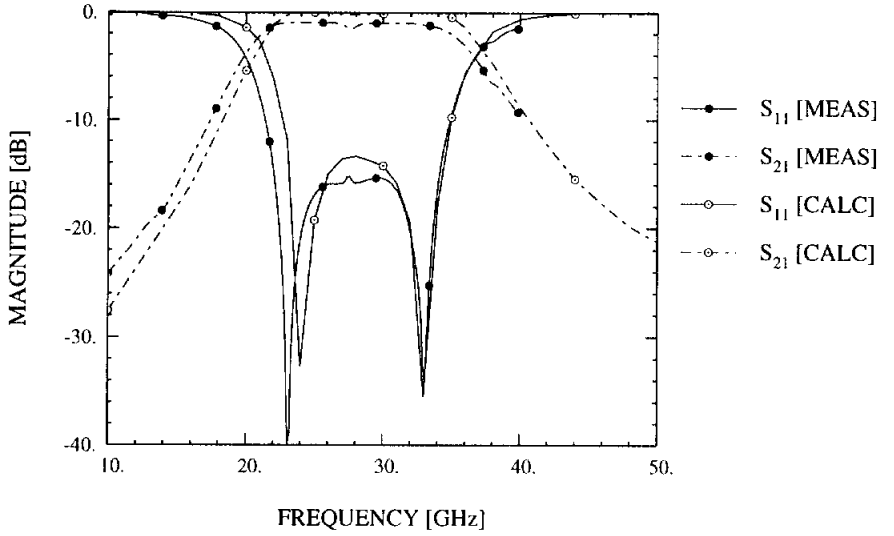

Figure 5.36: S-parameters for bandpass filter design 1 in Table 5.4. The open-end stub dimensions are the same as those in Figure 5.9.

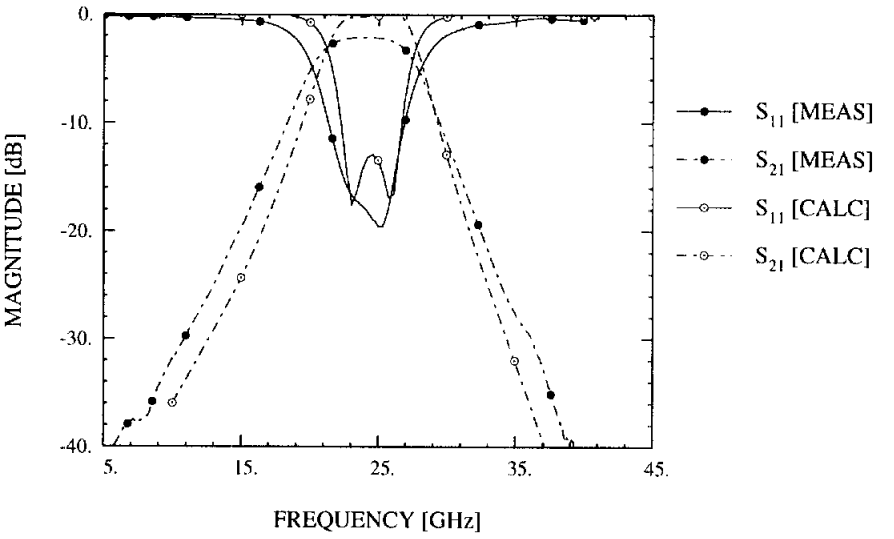

Figure 5.37: S-parameters for bandpass filter design 2 in Table 5.4. The folded open-end stub dimensions are the same as those of design O-D1 in Table 5.2.

of filter is more appropriate for achieving narrow bandwidths and fast roll-off in the rejection at the low end of the band. These advantages come at the expense of the high-end rejection, as seen in Figures 5.39 and 5.40. Design 4, which was developed without the aid of the coupled line analysis, has a bandwidth of 17% and a pass-band loss of 0.9 dB. Upon re-examining the design, it was found that the 1000 μm separation between the elements (see Figure 5.35) caused the second pass-band to shift down in frequency and degraded the out-of-band response. In design 5 the separation was reduced to 40 μm, resulting in improved high-end rejection and similar low-end and pass-band performance. The predicted response from the coupled line analysis of this filter is shown in Figure 5.40. Compared to design 1, the filter exhibits 23 dB more rejection at $0.5f_o$ and 4 dB more rejection at $1.5f_o$, although the overall length is 60% shorter.

5.6 Conclusions

The objective of this chapter has been to demonstrate that the low loss properties of the microshield line can be effectively utilized in practical applications. In this sense, the ability to design compact transitions between a standard substrate-supported line and a microshield line allows the advantages of each geometry to be exploited in a single circuit. The primary stub and filter designs which were investigated are series implementations with minimum lateral width and no upper shielding cavities. There is also negligible dependence on the height of the lower shielding cavity, since the fields are well-confined to the slots in the upper metalization. (In fact, many designs were tested which had no back-side metalization, and no noticeable effect on the performance was observed.) These characteristics enable relatively straight-forward integration of microshield components into con-

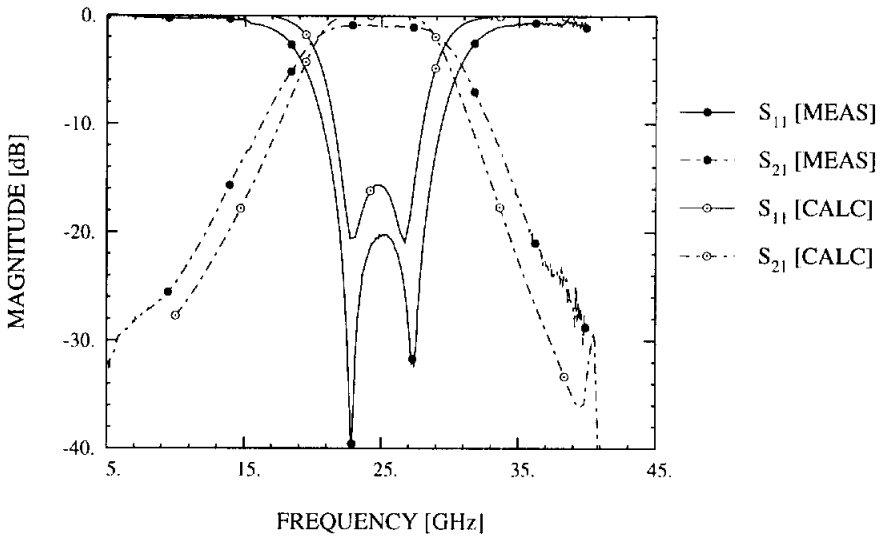

Figure 5.38: S-parameters for bandpass filter design 3 in Table 5.4. The folded open-end stub dimensions are the same as those of design O-D1 in Table 5.2, except that W=70 μm.

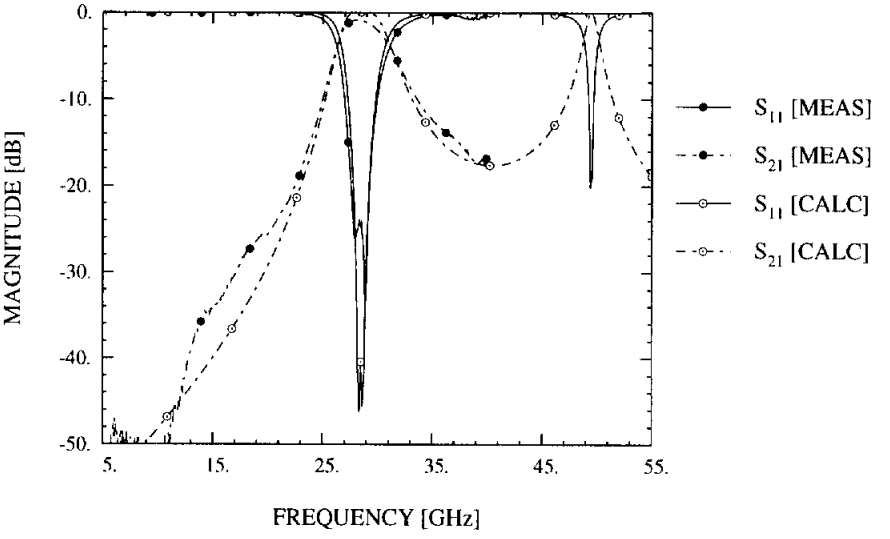

Figure 5.39: S-parameters for bandpass filter design 4 in Table 5.4. The hybrid stub design is the same as design H-O5 in Table 5.3.

ventional MMIC configurations. In addition, the folded and hybrid stub approaches address the need for miniaturization, yielding circuit dimensions equivalent to those of conventional geometries printed on high permittivity substrates.

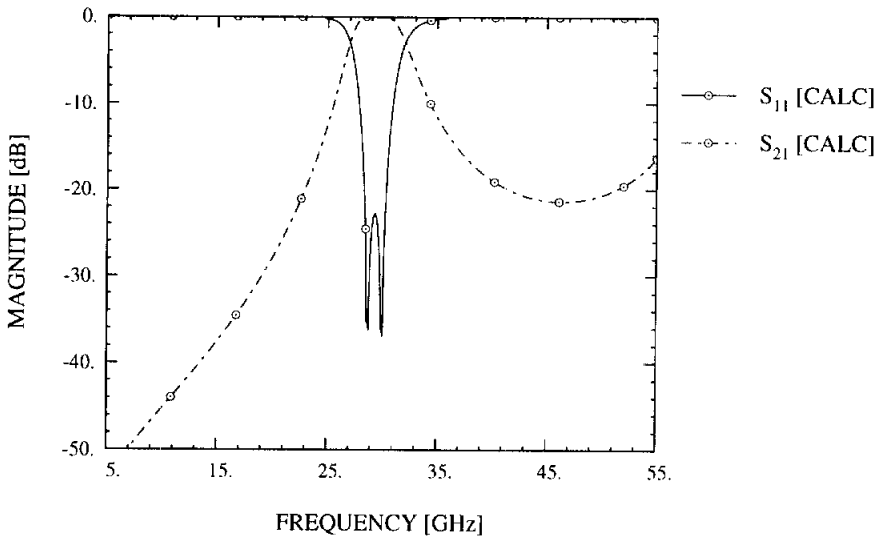

Figure 5.40: S-parameters for bandpass filter design 5 in Table 5.4, which is identical to design 4 except that all elements are separated by 40 μm.

CHAPTER VI

A 250 GHz MICROSHIELD BAND-PASS FILTER

6.1 Introduction

As discussed in Chapter II, the potential for high performance planar circuits which are implemented in conventional substrate-supported microstrip or coplanar waveguide is severely limited at submillimeter-wave frequencies. This shortcoming is primarily due to dielectric and radiation losses, and the most common solution is to utilize waveguide-based designs [79]. The machining tolerances on the waveguide parts become increasingly tight as the operating frequency increases, however, and the manufacturing costs rise accordingly. These arguments lead back to one of the primary motivating factors in developing the microshield line, which was to achieve low cost and high performance components for submillimeter-wave applications.

In order to demonstrate that these goals can be met, this chapter describes the use of the microshield line to implement the first planar band-pass filter at 250 GHz. The fabrication technique embodied the same low cost approach that is utilized for Ka-band components, and the filter exhibited less than 1.5 dB insertion loss with a 58% relative bandwidth. Also included in this chapter is a description of a quasi-optical measurement technique which was developed in order to determine the filter

S-parameters in the presence of reflections at the filter input and output ports. These reflections resulted from the integrated double folded-slot antenna which was used to couple in the RF power, and from the bismuth microbolometer that was used for power detection at the output of the filter.

6.2 Circuit Description

The new S-parameter extraction technique follows a semi-empirical/semi-analytical approach to model the filter, since very few direct methods are currently available for circuit characterization above 115 GHz. Electro-optic sampling and waveguide-based approaches could potentially be used, but were not available for this project. Therefore, the alternative technique employed here was based on quasi-optical methods, as illustrated in Figure 6.1. In addition to the band-pass filter itself, the block diagram contains a double folded-slot antenna, a bismuth microbolometer, and an RF short. It is noted in the figure that the device under test (DUT) can also be a length of microshield transmission line; as described in Section 6.4, this line is used for calibration purposes. With regard to the actual fabrication layout, both the filter and transmission line circuits were realized on a single membrane, as shown in Figure 6.2. The design of the filter and the antenna are discussed in the following two sections.

6.2.1 Band-pass Filter

The band-pass filter consists of a compact configuration of open-end series stubs which provides both low loss and longitudinal symmetry (Figure 6.3). As discussed in Chapter V, the location of the stub within the center conductor leads to greater field confinement and thus lower radiation loss than is characteristic of straight gap-

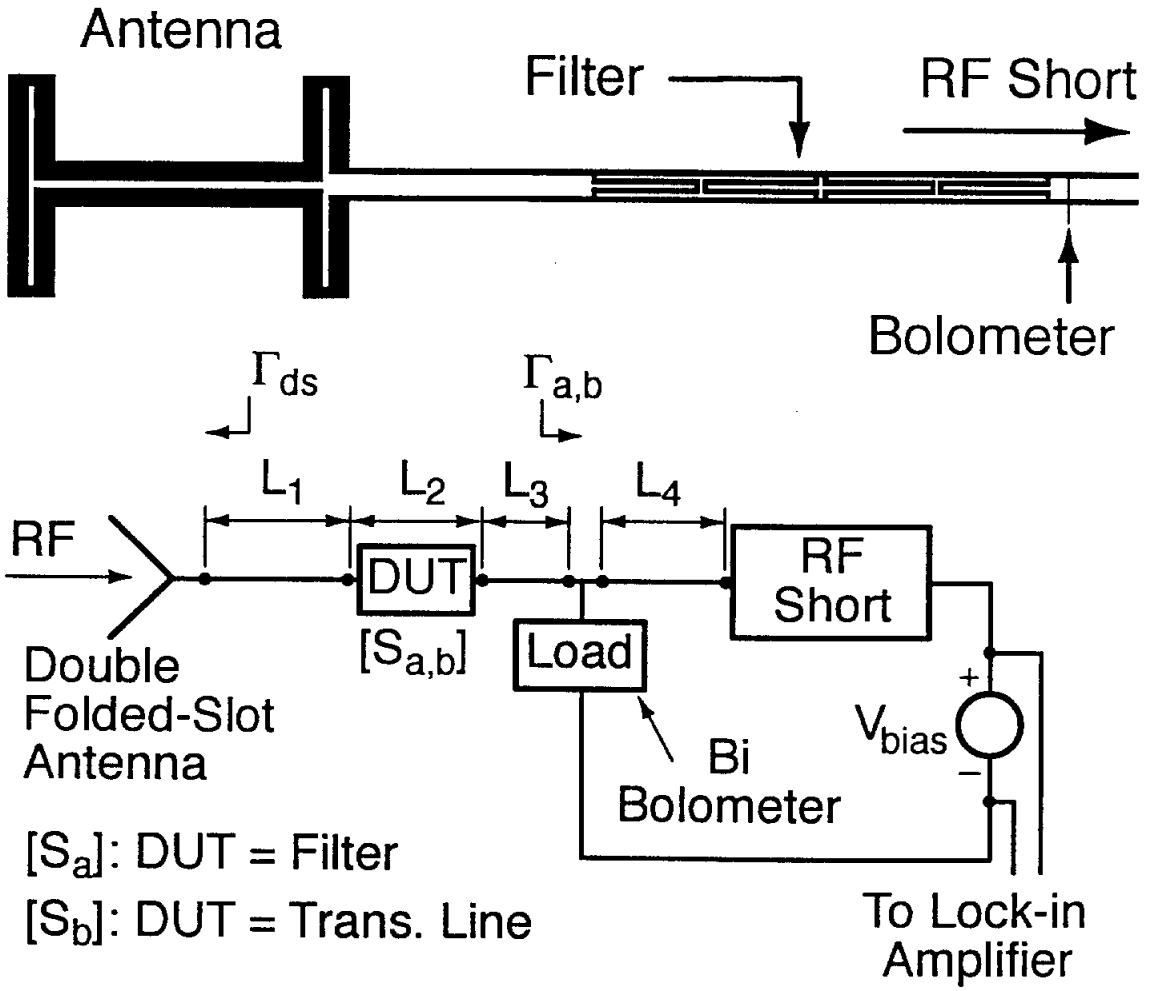

Figure 6.1: Diagram of the circuit used in the quasi-optical measurement, where DUT stands for device under test. The upper illustration shows a circuit which has a band-pass filter as the DUT. The reflection coefficients Γ_a and Γ_b may be different, in general, to allow for fabrication tolerances between the bolometers of the filter circuit and the transmission line circuit.

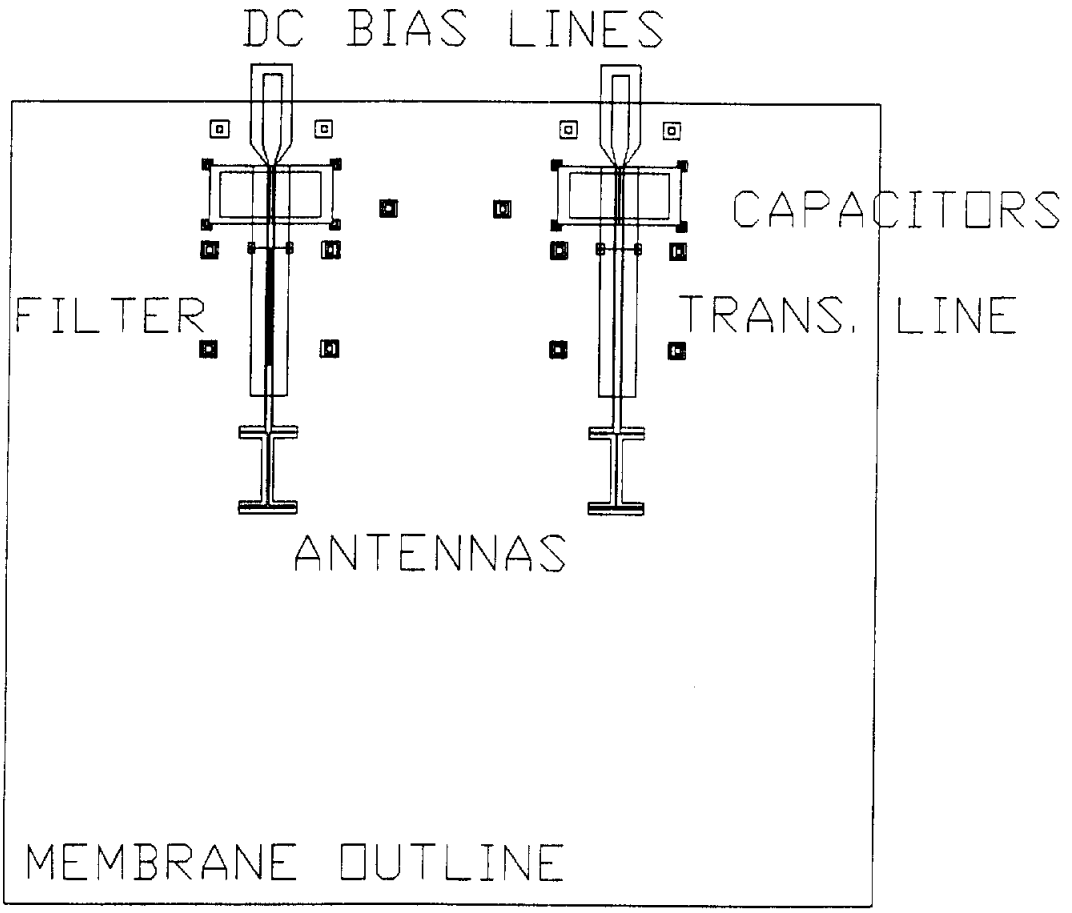

Figure 6.2: Layout of the actual circuit design, showing the side-by-side configuration of a band-pass filter and a straight length of microshield line used for calibration purposes.

coupled resonators or stubs with lateral extension [70, 80]. The design applied here utilizes four quarter-wavelength stubs which are resonant at 250 GHz, with the second and fourth stubs reversed relative to the first and third. The effective dielectric constant was predicted to be approximately 1.36 using the technique described in Chapter II, and the stub lengths were sized accordingly.

It can be observed from Figure 6.3 that the microshield configuration is slightly modified with respect to the standard approach outlined in Chapter I. Instead of using the membrane on the lower shielding cavity wafer to support the conducting lines, a third wafer is utilized on top to provide the membrane, and the shielding cavity sidewalls are formed using a separate wafer. The top wafer is essentially turned upside down and direct DC contact is made between the ground planes on the membrane and the sidewalls of the cavity wafer. This modification is convenient since it allows the wide opening of the lower cavity to be near the signal line and upper ground planes. The sidewalls thus have less influence on the propagation characteristics than if the much narrower opening of the cavity were near the top. Furthermore, at these very high frequencies the possibility of a cavity mode being excited is of concern. The assembly technique applied here allows a thicker cavity wafer to be used, which simplifies the fabrication and at the same time optimizes the tradeoff between keeping the sidewalls removed from the center conductor and keeping the waveguide-mode cutoff frequency high. For the dimensions given in Figure 6.3 the dominant mode cutoff frequency is greater than 500 GHz.

6.2.2 Double Folded-Slot Antenna

The double folded-slot antenna was chosen for coupling in the RF power because of its broad impedance bandwidth and its reduced beamwidth with respect to a single

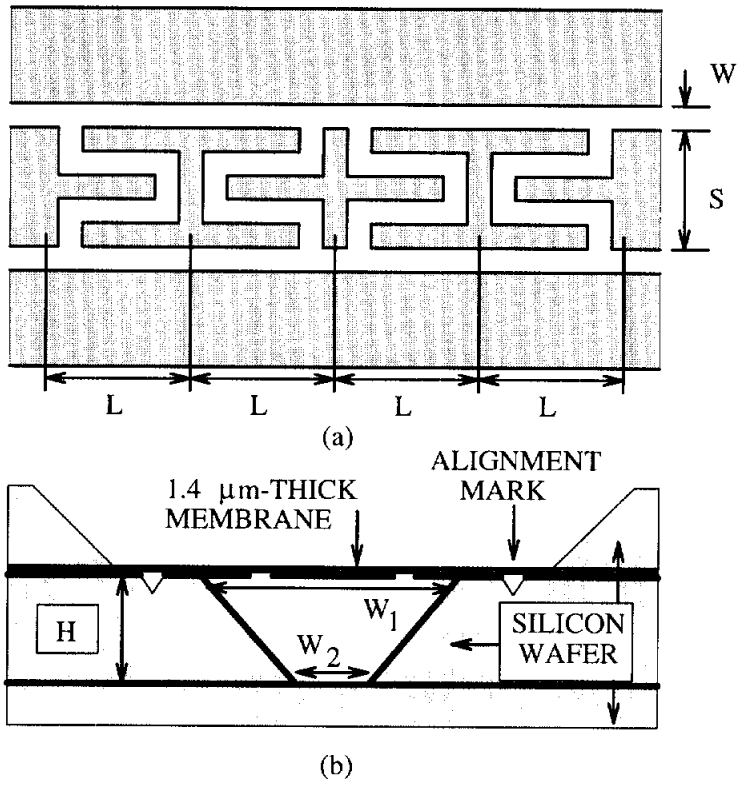

Figure 6.3: The four-section microshield band-pass filter (not to scale). The metalization pattern is shown in (a), where L=250, S=50 and W=10. A cross-sectional view is shown in (b), where H=200, W_1=320 and W_2=40. The geometry is comprised of three silicon wafers which are used to support the membrane and filter metalization, form the cavity sidewalls, and complete the lower ground plane, respectively. In (b), metalization is indicated by the dark lines. All dimensions are in microns.

Design	ϵ_r	W_f / S_f	W_{a1} / W_{a2} / S_a / L_a	W_c / S_c / L_{c1} / L_{c2} / L_{c3}	f_c
A	1.0	.010/.050	.020/.040/.020/.754	.040/.020/.407/0.00/0.00	170
A	1.0	.010/.050	.020/.040/.020/.494	.040/.020/.277/0.00/0.00	250
A	1.0	.010/.050	.015/.030/.015/.352	.030/.015/.199/0.00/0.00	340

Table 6.1: Parameters for the double folded-slot antenna designs used in characterizing the 250 GHz band-pass filter (refer to Figure 8.11). All dimensions are in millimeters and the center frequency, f_c, is in GHz.

folded-slot or slot design (see Chapter VIII). Since large reflections at the antenna input were undesirable in relation to the S-parameter extraction technique, the fact that a single antenna could be well-matched to the feedline over a wide frequency range simplified the experimental procedure. The reason for this is that only three antenna-filter circuit pairs were required for measurements over the 100-400 GHz span. Furthermore, the low sidelobe levels in the E- and H-plane patterns made the antenna performance less susceptible to finite ground plane effects. This helped to ensure that the patterns of the adjacent filter and transmission line circuits were not modified by the presence of unwanted ripples. Design parameters for the three antennas used for this work are given in Table 6.1 in accordance with the notation in Chapter VIII. Each design had an input impedance of approximately 80 Ω.

6.3 Fabrication

The fabrication methodology utilized here is essentially the same as that outlined in Appendix C. Some steps are unique to this project, however, and are described in the following:

1. It is critical that the silicon micromachining be done *before* the metal deposition phase. If this procedure is not adhered to, the under-cutting of the metalization due to the finite etch rate of SiO_2 in EDP, which is approximately 3-5Å/min., will prevent successful integration of the bismuth microbolometers. When etching completely through a 500 μm-thick wafer, up to 1000Å of oxide can be removed and continuous step coverage of the thin bismuth layer cannot be achieved.

2. Thin-film overlay capacitors are utilized as the RF shorts, and are fabricated by depositing a Ti-Pt-Au layer over a 3500Å-thick layer of evaporated silicon oxide (SiO). These capacitors have a very high yield and no pin-hole related shorts were encountered. The dielectric constant of SiO is 6.

3. The thin-film bismuth microbolometer detectors [81] are made by evaporating a 5 μm-wide layer of bismuth that is approximately 750Å-thick, and runs between the two upper ground planes and over the center conductor (effectively two resistors in parallel). This thickness results in a resistance of about 70 $\Omega/\square$. The deposition should be done in the final phase of fabrication since bismuth material does not hold up well to subsequent processing.

4. The lower shielding cavity sections were etched into a separate 200 μm-thick wafer and separated using a dicing saw. Small square patterns were also etched into the wafer and used to align the cavities to the circuits, through openings in the ground plane metalization (see Figure 6.3).

6.4 Quasi-Optical Measurement Technique

The objective of the quasi-optical measurement is to determine the amount of power transmitted through the filter as a function of frequency, using the circuit shown in Figure 6.1. In this figure, RF power is supplied from a Gunn diode/tripler pair and coupled into the circuit through the CPW-fed, double folded-slot antenna. The overlay capacitor is positioned approximately a quarter-wavelength away from the filter output (L_4) in order to allow DC biasing of the bismuth microbolometer, and at the same time ensure that maximum power is delivered to the bolometer by presenting an open circuit at the filter output[1]. The measurement is made by modulating the RF signal with a 1 KHz square wave and using a lock-in amplifier to detect the resulting 1 KHz voltage across the bolometer. As a means of calibration, measurements are taken on the circuit in which the filter is replaced by the length of microshield transmission line. Using the measured absolute responsivity (in Volts/Watt) of the bolometers in each circuit, one can determine the ratio of the power received through the filter (P_{filt}) to that received through the transmission line (P_{TL}).

6.5 Data Extraction

The remaining step involved in characterizing the filter is to extract its S-parameters using the experimental values for P_{filt}/P_{TL}. An equation which relates the scalar power measurement data and all the pertinent vector quantities in the system is derived from the circuit model in Figure 6.1:

$$P_{filt}/P_{TL} = |S_{21,a}|^2 \left|1 - \Gamma_{ds}\Gamma_b e^{-2\gamma(L_1+L_2+L_3)}\right|^2 \left(\frac{1-|\Gamma_a|^2}{1-|\Gamma_b|^2}\right) \times$$

[1]The capacitor was designed to have an impedance of approximately -j55 MΩ at 1 KHz and -j0.5 Ω at 100 GHz.

$$\left|1+\left(S_{11,a}^2-S_{21,a}^2\right)\Gamma_{ds}\Gamma_a e^{-2\gamma(L_1+L_3)}-\right.$$
$$\left.S_{11,a}\left(\Gamma_{ds}e^{-2\gamma L_1}+\Gamma_a e^{-2\gamma L_3}\right)\right|^{-2} \qquad (6.1)$$

where γ is the propagation constant of the microshield line. In order to resolve the unknowns in Eqn. 6.1, a Monte Carlo routine (MCr) has been implemented which uses a combination of empirical and analytical data for initial values. Estimates for Γ_a and Γ_b are computed using measured values for the bolometer DC resistance and values for γ extrapolated from 10-40 GHz measurements. Initial values for the antenna reflection coefficient (Γ_{ds}), on the other hand, have been determined using the full-wave analysis described in Chapter III. After specifying upper and lower limits for all the parameters in Eqn. 6.1, the MCr is then used to fit them to the model. The algorithm works by generating random values for all the variables, computing the associated P_{filt}/P_{TL} ratio, and determining the error with respect to the measured power ratio. After compiling approximately 1000 data sets, the range for each variable is divided into 8-10 separate "bins", and the number of data points within each bin that are associated with an error below the overall average is computed; this determines a success rate for each bin. The distribution across all bins is then analyzed to determine whether or not a single grouping of bins has a success rate greater than 50%. If this maxima is found, the allowable range for the given variable is appropriately reduced. An important point is that the initial range for the magnitude of the filter S-parameters is between 0 and 1, i.e. they are unconstrained. However, the quantity $|S_{11,a}|^2+|S_{21,a}|^2$ is restricted to a range which encompasses the expected overall filter loss. Also, the range for the phase is 80° about the values predicted by a full-wave analysis of the filter.

In order to investigate this method of solution, the filter S-parameters from the full-wave analysis were used along with randomly generated values for the remaining

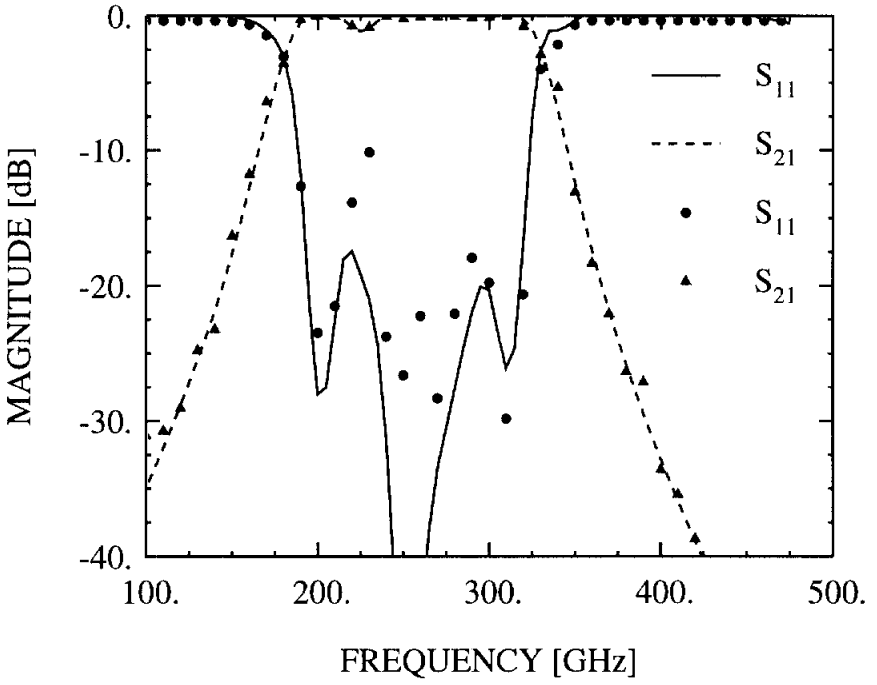

Figure 6.4: Comparison between the MCr-extracted values (markers) and the "exact" predicted filter response from a full-wave analysis (lines), using a hypothetical set of system parameters to compute P_{filt}/P_{TL}.

unknowns to compute exact values for P_{filt}/P_{TL}. The MCr was then applied to this hypothetical data set and the accuracy proved to be very good. As shown in Figure 6.4, the MCr-extracted $|S_{21,a}|$ follows the true distribution almost exactly and the maximum passband error is about 0.45 dB. As a consequence of the weaker dependence of Eqn. 6.1 on $|S_{11,a}|$ it is more difficult to resolve this parameter. Likewise, it is only possible to determine the phase of the S-parameters when the magnitude of the respective unknown is quite large. Even then, due to the rapid phase variation in the 4-element filter, the results can only approximate the overall distribution.

6.6 Results and Conclusion

Using the measurement technique described in Section 6.4 and the S-parameter extraction technique described in Section 6.5, the performance of the filter was measured at eight frequencies from 130-360 GHz. Due to the limited RF power and the low responsivity of the bolometers (around 2 Volts/Watt), the dynamic range is limited to approximately 20 dB. As shown in Figure 6.5, the S-parameters extracted from the raw measured data are very close to the predicted response from the full-wave analysis, which takes only radiation loss into account. The measured pass-band insertion loss for this four-section filter is around 1.5 dB and the relative bandwidth is 58%. It is also seen that the low frequency stop-band provides excellent rejection. These results confirm that high-performance, planar circuits are realizable at millimeter- and submillimeter-wave frequencies using the microshield line configuration.

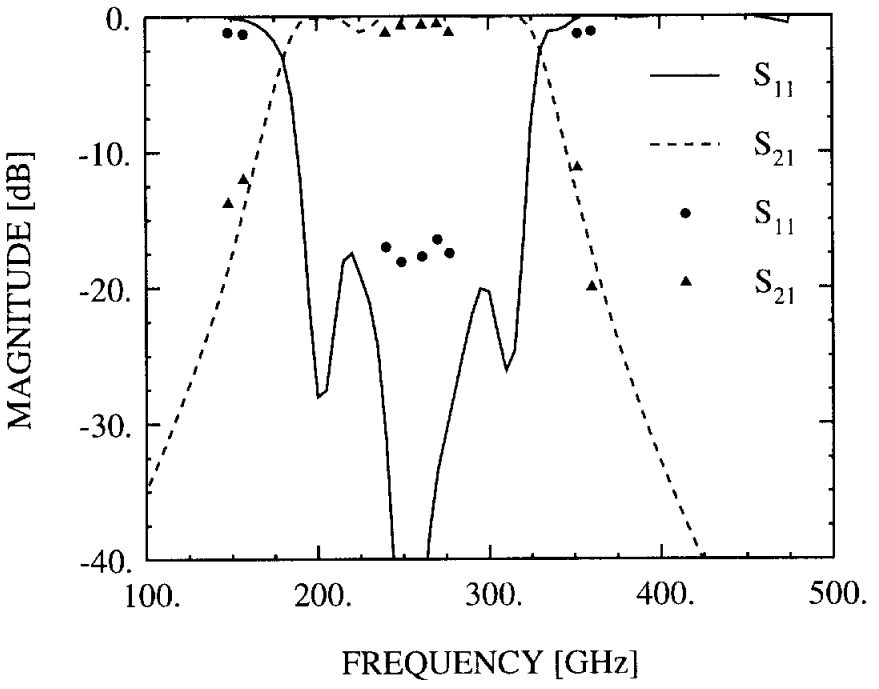

Figure 6.5: Comparison between the results extracted from raw measured data (markers) and the predicted filter response from the full-wave analysis (lines).

CHAPTER VII

MEMBRANE-SUPPORTED MICROSTRIP LINE

7.1 Introduction

The use of silicon micromachining and multiple-wafer configurations makes the design of a variety of transmission line geometries possible. One of the alternatives to the coplanar waveguide-like microshield line is a membrane-supported microstrip, shown in Figure 7.1. In order to demonstrate the characteristics of this air microstrip, the development of a circuit used in the power distribution stages of a Ka-band solid state power amplifier (SSPA) is described herein. This project constituted the first effort toward integrating micromachined, membrane-supported components with an amplifier stage. A hybrid approach was adopted for this initial work, and important lessons were learned pertaining to intelligent implementation of these new architectures.

As with microshield, the air microstrip has many advantages over a standard substrate-supported configuration. Obviously, there is no concern for dielectric loss, and the homogeneous medium also results in an extremely wide single-mode bandwidth. For example, a membrane line with a 500 μm wide signal line and a 350 μm thick substrate sustains a pure TEM mode from DC to at least 320 GHz [82], whereas

the same size line on silicon will propagate a higher order mode at 62 GHz [83]. This means that it is not necessary to use very thin substrates for millimeter-wave applications, which simplifies the handling during and after fabrication. Another advantage of the low permittivity substrate is that the parasitic capacitance associated with discontinuities is minimized. Finally, the advantages of the uniform air dielectric are combined with conductor loss which is, in general, lower than that of uniplanar geometries (e.g. coplanar waveguide).

The following sections contain descriptions of the power division circuitry and the SSPA which were mentioned above. The first topic is the quarter-wavelength impedance transformers that were used to transition between the silicon and the membrane-supported microstrip. Following this, the design and performance of a Ka-band Wilkinson power divider are presented. Except as noted, the fabrication of the micromachined circuits followed the procedures outlined in Appendix C, however the back-side metalization was not required. The chapter concludes with a description of the assembly and performance of the SSPA.

7.2 Silicon-to-Membrane Transitions

One of the important design issues associated with membrane-supported microstrip is obtaining a low loss transition between the silicon and membrane substrates. For the power divider application considered here, the required input and output impedances were 50 Ω. A transition based on simple impedance matching was impractical since a 50 Ω membrane line would occupy too much circuit area; assuming a substrate height of 350 μm, a 50 Ω membrane line is nearly 2 mm wide, compared to 0.32 mm for a line on silicon. The alternative approach was to utilize quarter-wavelength transformers to increase the impedance level of the membrane

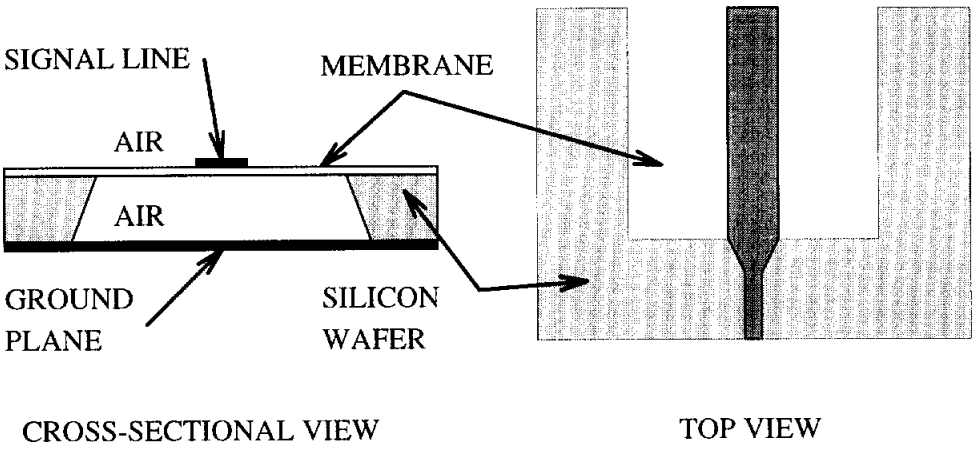

Figure 7.1: Illustration of the membrane-supported microstrip line. The top view is a transition from a silicon substrate to the membrane and shows the finite width of the membrane cavity.

circuits. Bandwidth limitations were not a concern since the SSPA specification called for single frequency operation.

A number of different transition designs were fabricated and measured in order to investigate the effects of the silicon-air interface. The situation is complicated by the angled profile which results from the anisotropy of the silicon etchant. The varying thickness of the silicon not only causes the characteristic impedance to change, but it also makes it difficult to account for the effects of step changes in the line width. One of the transitions which was tested is illustrated in Figure 7.2, along with parameters obtained from the Linecalc [84] program. This transition was designed to operate at 32 GHz, and the length of 73 Ω line was adjusted to compensate for the step width changes at each end [85]. These adjustments included an additional 66 μm due to the discontinuity at the 50 Ω line, and an additional 100 μm due to the discontinuity at the 106 Ω line. The latter value was an estimate chosen to lie between the compensation that would be necessary assuming dielectric constants of

1.0 and 11.7. Also, in order to maintain a relatively constant impedance, the line width was tapered over the distance that the silicon thickness changes.

The measured performance of the transition is shown in Figure 7.3. The insertion loss between the 50 Ω lines is approximately 0.25 dB, with a return loss of greater than 32 dB at resonance. Using a circuit simulator, it is easily determined that the resonance at 34 GHz corresponds to the performance of a single transition, while the 29 GHz resonance results from the back-to-back configuration, and is dependent upon the length of the 106 Ω membrane line. Since the design frequency was 32 GHz, the results indicate that the 73 Ω line was approximately 6% too short. These errors could derive from incorrect values for the step width corrections and/or the effective dielectric constant. Similar performance was found using transitions to 141 Ω and 177 Ω membrane lines.

Another design consideration was the separation between the membrane line and the silicon cavity sidewalls. In general, it would be desirable to use relatively narrow cavities without disturbing the circuit performance. In Figure 7.4, the scattering parameters for 50→106Ω transitions with sidewall separations of 1.5h and 3h are compared, where h is the height of the signal line above the ground plane. Except for the dip near 38 GHz, the differences in S_{21} for the two sidewall separations are less than 0.25 dB from 10-40 GHz. The discrepancies in S_{11} near resonance are partially due to measurement error, since there was some difficulty in obtaining an accurate calibration on the silicon substrates. These results demonstrate that compact geometries can be used without strong interference from the silicon substrate. Also note that the transitions used here did not have a taper at the impedance discontinuity, and the performance was nearly the same as the design shown in Figure 7.3.

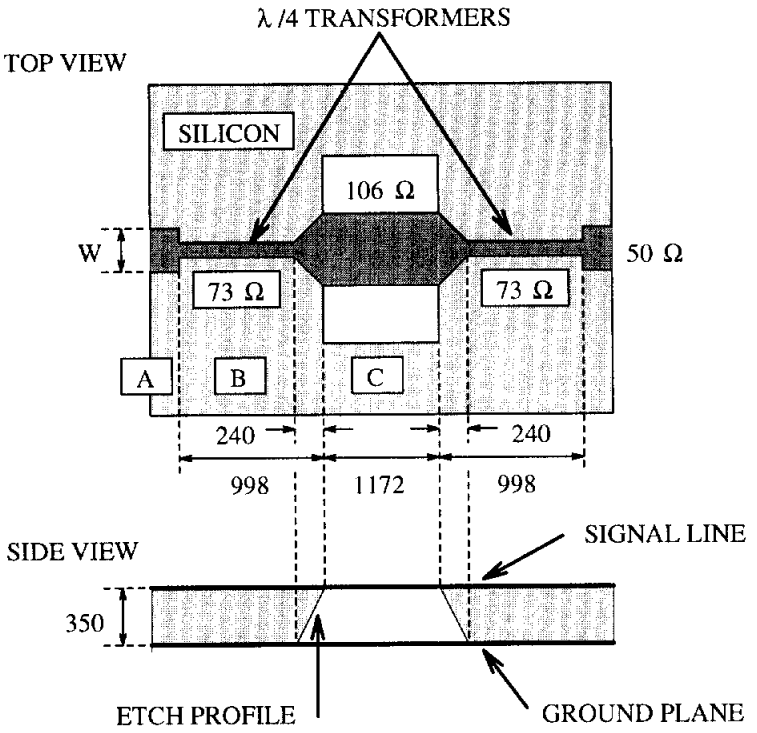

Line Section	Line width, μm	ϵ_{re}	Z_o, Ω
A	322	8.66	50
B	122	7.94	73
C	513	1.0	106

Figure 7.2: Top and side views of a 50-73-106 Ω transition, in which the 106 Ω section is a membrane-supported microstrip line. The parameters listed in the table pertain to 30 GHz operation [84]. All dimensions are in microns.

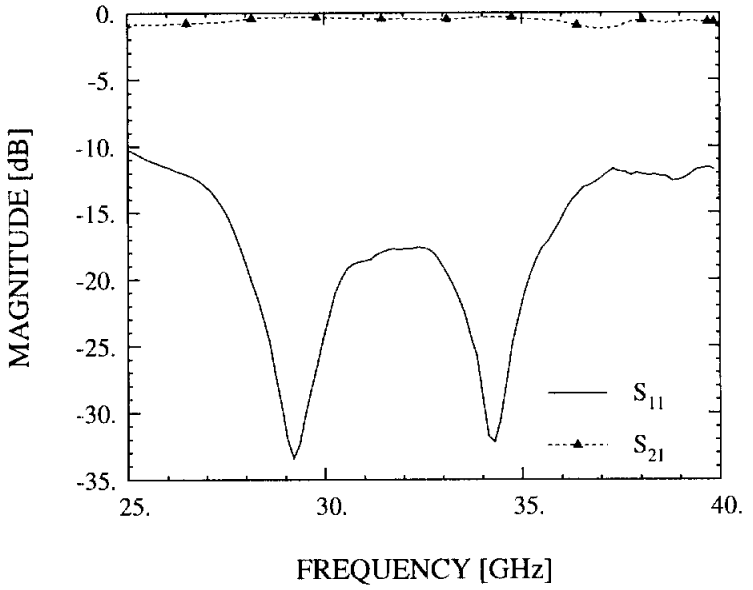

Figure 7.3: Measured S_{11} and S_{21} for the transition shown in Figure 7.2.

7.3 Wilkinson Power Divider

After the silicon-to-membrane transitions had been investigated, the Wilkinson power divider/combiner shown in Figure 7.5 was built and tested[1]. The layout utilized an 8x8 mm^2 membrane, which proved to be quite robust as only one circuit, out of more than fifty, failed during processing. The fabrication sequence began with the deposition of the 212 Ω thin-film resistors which were 324 μm long and 30 μm wide, using 400 Å-thick titanium (20 Ω/□). The front-side metalization and back-side masking layer removal then proceeded as described in Appendix C. Before the wet-etching, a dicing saw was used to separate the wafer into single rows of 2-4 circuits, cutting perpendicularly to the input and output 50 Ω lines. The micromachining was then performed to obtain the free-standing membrane, and scribe lines were simultaneously etched such that the circuits were connected by only

[1]As the power divider design evolved, the quarter-wavelength impedance transformers were eventually moved off the silicon and onto the membrane.

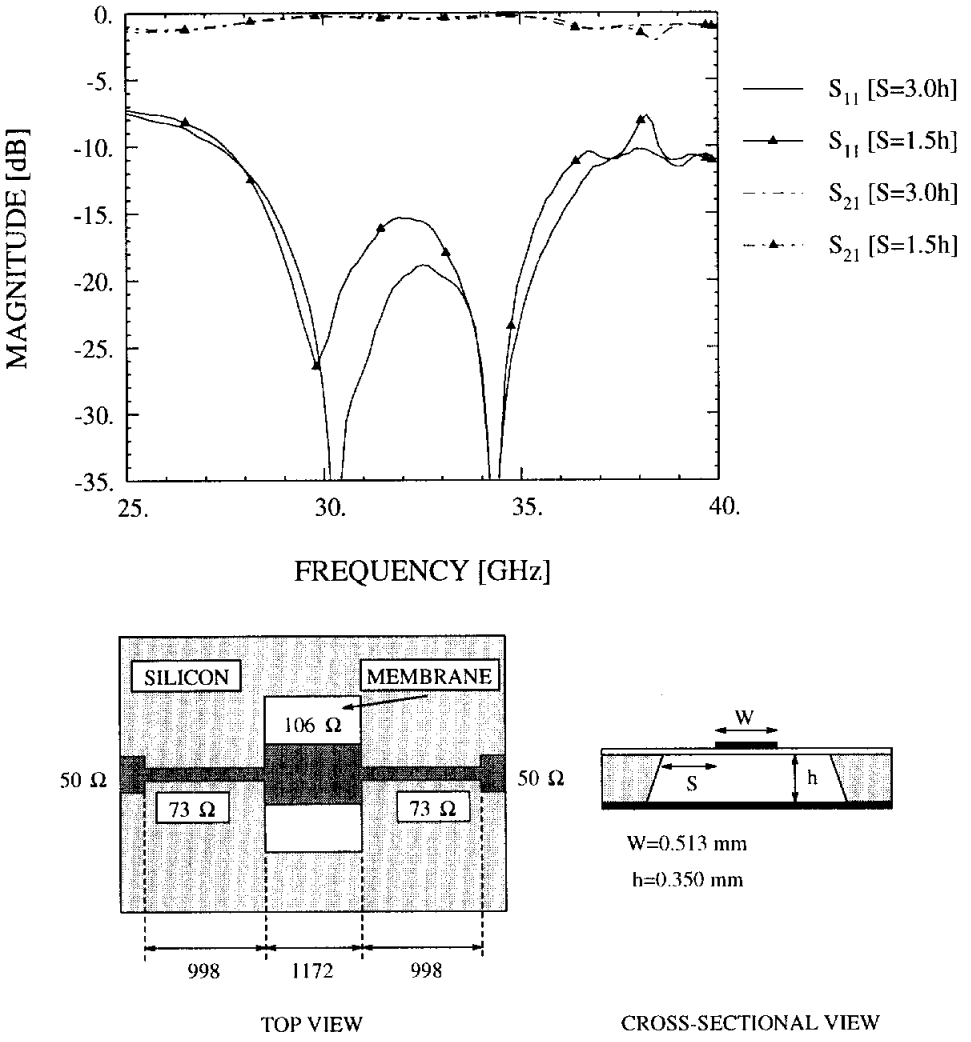

Figure 7.4: Measured S_{11} and S_{21} for (non-tapered) back-to-back 50-73-106Ω quarter-wave transitions. The spacing pertains to the 106Ω membrane-supported section.

100 μm-wide Si struts. This dicing/scribe line procedure provided a clean profile at the input and output lines, and at the same time minimized the number of pieces that had to be handled during etching. To complete the processing, the dividers were broken apart with a scalpel and an epoxy was then used to mount them to the test fixture (see Section 7.4). Finally, an aluminum plate was positioned above the circuits to protect the membranes during the measurement phase. By adjusting its height, the shield could also be used to tune the circuit performance.

The measured results for a back-to-back Wilkinson configuration with a shield height of 2.7 mm are given in Figure 7.6. This data demonstrates a return loss greater than 22 dB and an insertion loss of 1.2 dB at 33 GHz. Included in Figure 7.6 is the isolation between the two output ports, which was determined from an individual circuit by terminating the input port port with a 50 Ω thin-film resistor. The effects of varying the shield position on the insertion loss can be seen in Figure 7.7; the value of 2.7 mm was chosen as a compromise between minimizing the insertion loss and maximizing the return loss. A detailed breakdown of the performance is given in Table 7.1, which shows that the extracted insertion loss for a single divider with 50 Ω input/output impedance is 0.3 dB. After accounting for the quarter-wave transformers, the power divider itself contributes approximately 0.2 dB. Typical performance for Wilkinson-type designs at this frequency range, using conventional microstrip, is 0.4-0.5 dB [74].

7.4 Solid State Power Amplifier Demonstration

The SSPA module consisted of an amplifier power section with a membrane-based Wilkinson divider/combiner on the input and output ports (Figure 7.8). On either end of the module were 50 Ω microstrip lines on alumina, which were used to

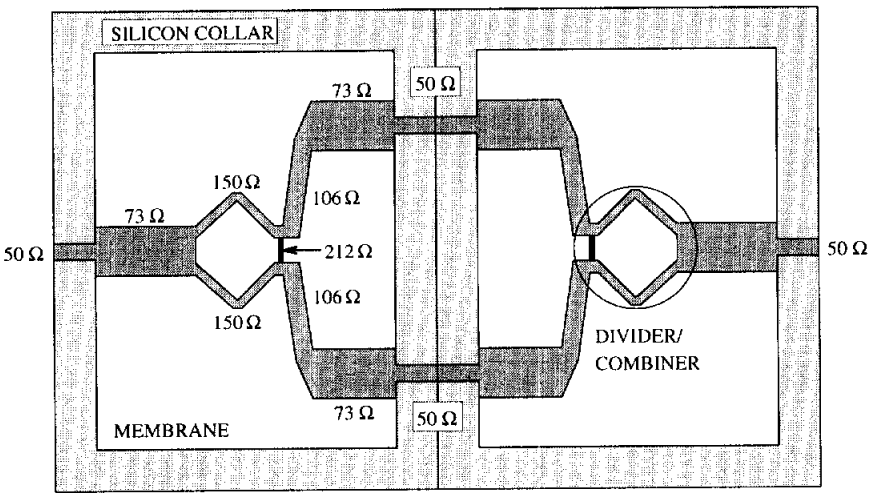

Figure 7.5: Layout of the membrane-supported Wilkinson power divider/combiner, shown in a back-to-back configuration.

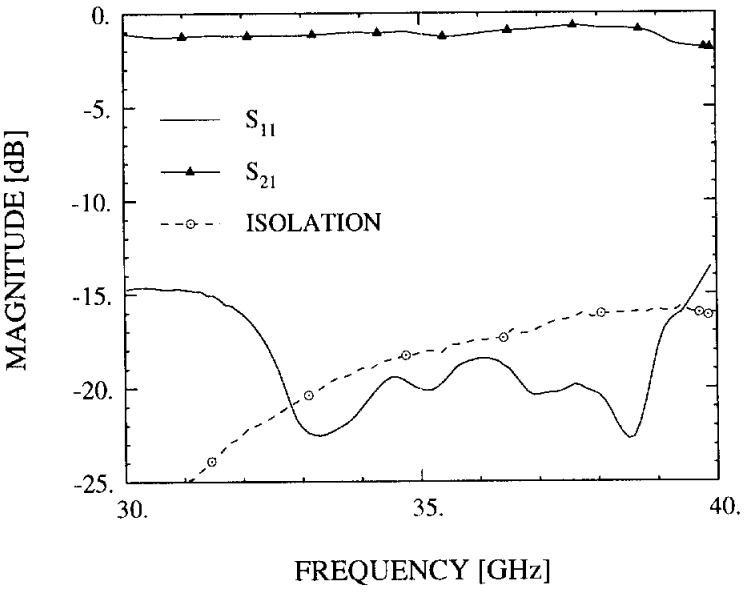

Figure 7.6: Measured scattering parameters for the back-to-back Wilkinson power divider shown in Figure 7.5, with a metal shield 2.7 mm above the membrane surface. The isolation was measured between the output ports of a single circuit.

Parameter	Units	Loss	Total
Wire-bond	dB	0.04	
50 Ω microstrip on 10 mil alumina	dB/mm	0.035-0.04	
50 Ω microstrip on 14 mil silicon	dB/mm	0.085	
106 Ω microstrip on membrane (14 mil)	dB/mm	0.025	
Insertion loss of back-to-back divider	dB		1.18
3 Wire-bonds	dB	-0.12	1.06
Loss per divider (divide by 2)	dB		0.53
Addtl. 50 Ω & 106 Ω line	dB	-0.23	0.30
Corrected loss per divider	dB		0.30
Input & Output $\lambda/4$ transformers	dB	-0.08	0.22
Loss per divider w/o transitions	dB		0.22

Table 7.1: Loss budget for the Wilkinson power divider shown in Figure 7.5. The entries at the top of the table are experimentally determined values at 30 GHz.

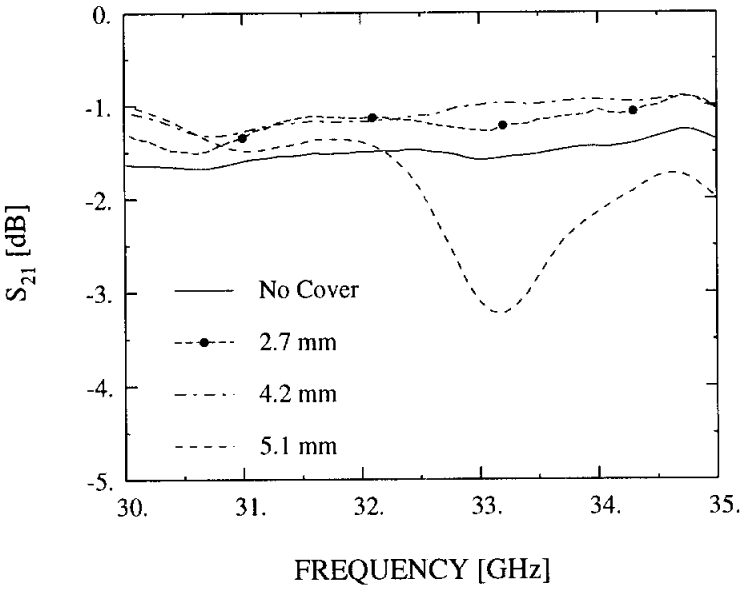

Figure 7.7: Measured insertion loss for the back-to-back Wilkinson power divider shown in Figure 7.5, for various shield heights.

interface with a Wiltron 3680K test fixture. The three sections (divider, power stage, combiner) were assembled using a gold plated, split-block test fixture with aluminum for the end pieces and Kovar for the center piece. The Kovar section was utilized in order to provide a good match to the thermal expansion of the GaAs MMIC chips. In hindsight, adhering the Wilkinson dividers directly to the aluminum blocks was not the optimum method, since thermal expansion mismatches caused some torsion of the silicon collar which surrounds the membrane. Future designs could be improved by first attaching the divider to a larger, Au-plated silicon piece, and/or by using a block material which has a better thermal match to silicon (e.g. Wolfmet TC [86]). After assembly, wire bonds were used to electrically connect the signal lines on the three pieces, and also to contact the output alumina pads.

The Ka-band amplifier module section was a simple combination of two commercially available 0.5W Alpha MESFET-based MMIC chips (SN AA035P2-00). Since

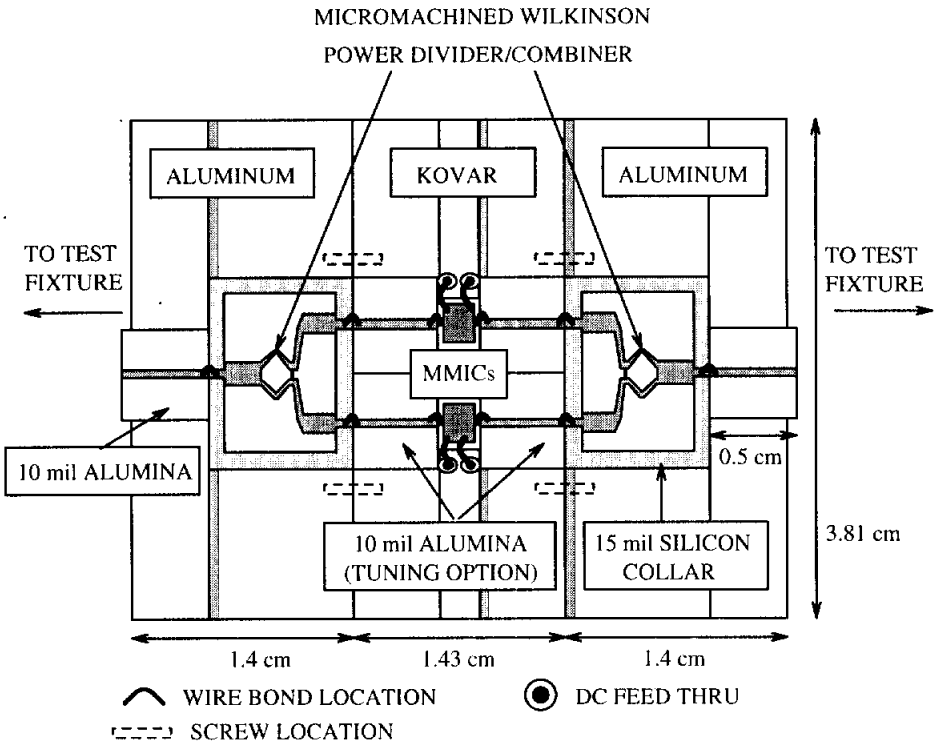

Figure 7.8: Ka-band 0.8W MMIC power amplifier.

large signal data was not available to pick two matched chips, 50 Ω alumina lines were placed at the input and output of the devices (0.51 cm long) to allow for tuning (Figure 7.8). The bias lines for both chips were tied together as in an actual application; therefore, only one gate- and one drain-power supply were required.

Performance data on the SSPA module was taken at several frequencies between 30-35 GHz, and it was found that no tuning was required on either the input or output. For a constant input power drive the circuit gain varied from 4 to 6.5 dB, with a constant output power of around 800 mW (Figure 7.9). As shown in Figure 7.10, the amplifier exhibited 5.2 dB gain with an output power of 0.85W and 17% power added efficiency at 33 GHz. This data includes the removal of the alumina lines whose loss is approximately 0.35 dB/cm, but not the extra wirebond interconnects. If we employed a traditional alumina power divider, the output power would have been reduced by approximately 130 mW with a 2.5% loss in efficiency. Attempts to tune the input/output of the circuit showed no appreciable improvement of the circuit performance.

7.5 Conclusion

The RF performance of a membrane-supported microstrip circuit has proven to be much better than that of circuits which are fabricated using traditional planar lines. The advantage is easily lost, however, if circuit functions are not efficiently implemented. As an example, the compatibility of line geometries going from essentially air to a substrate whose relative permittivity ranges from 2 to 13 becomes a challenge. In this initial work on the Wilkinson divider, it was necessary to step up the impedances and therefore contend with increased circuit dimensions and additional line losses. The obvious solution is to plan the circuit architecture in such a way as

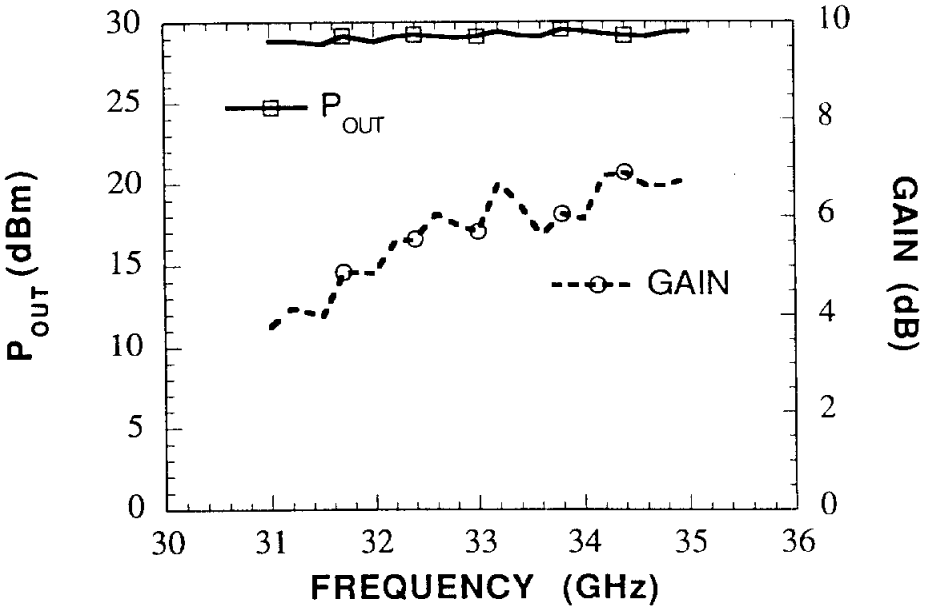

Figure 7.9: Frequency response of the Ka-band amplifier with constant input power.

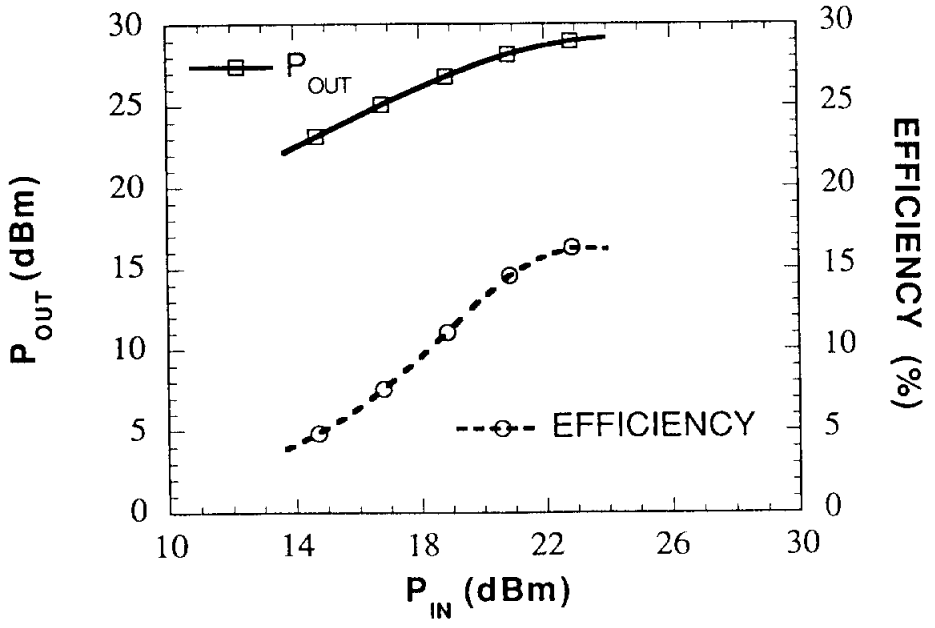

Figure 7.10: Gain and power added efficiency of Ka-band amplifier as a function of input drive level.

to take maximum advantage of the low loss media. In particular to communication systems, this line of thought leads naturally to the implementation of traditional circuit functions such as preselect filters, low noise amplifiers, phase shifters and couplers on a single membrane which can have superior performance without the need to "create" new active device technologies.

7.6 Acknowledgments

This project was conducted in cooperation with Dr. Martin Herman, Rob Staehle, Stacy Weinstein and Hoppy Price of the Jet Propulsion Laboratory, in association with the Pluto Fast Flyby Pre-Project Advanced Technology Insertion effort. Assistance with the test fixture design was contributed by Steve Robertson of the University of Michigan. All measurements of the SSPA were performed at the Jet Propulsion Laboratory.

CHAPTER VIII

SINGLE AND DOUBLE FOLDED-SLOT ANTENNAS ON SEMI-INFINITE SUBSTRATES

8.1 Introduction

The subject matter contained in this chapter diverges somewhat from the main theme of the thesis to discuss the characteristics of two planar antennas. One of these designs, the double folded-slot antenna, was utilized in the measurement of the 250 GHz bandpass filter presented in Chapter VI. To the best of the author's knowledge, the work presented here is the first in depth study of the folded-slot geometries on semi-infinite substrates.

As is well known, planar antennas consisting of patches, dipoles or slots, fed by a microstrip transmission line, are extremely useful due to their low cost, light weight, and flexibility of design. They have been extensively analyzed (e.g. [87]) and are used in applications which range from complex conformal arrays for radars to quasi-optical spatial power combiners [88]. As the popularity of the coplanar waveguide transmission line has increased significantly in recent years, antenna elements which are suitable for a CPW-feed configuration have also become important [89, 90, 91]. In light of this, design guidelines for CPW-fed, single and double folded-slot (DFS)

antennas on a dielectric half-space are presented herein. The DFS antenna consists of two planar, folded-slot elements which are displaced along a CPW line by a half-wavelength, yielding a compact geometry with a modest amount of beam-shaping.

The calculated and experimental results included here are intended to provide a relatively thorough introduction to the characteristics of these two antennas. The data primarily pertain to air (ϵ_r=1), quartz (ϵ_r=4) and silicon (ϵ_r=11.7) substrates. In Section 8.2, the resonant circumference, self impedance, and mutual impedance of the folded-slot are examined. This is followed by an analysis of the input impedance (Z_{in}), directivity and far-field patterns of several double folded-slot designs in Section 8.3. Theoretical results have been obtained using the full-wave analysis described in Chapter III.

8.2 Single Folded-Slot Antennas

The geometries of the single folded-slot antenna and the slot antenna are illustrated in Figures 8.1 and 8.2, respectively. Both antennas have radiation patterns which are identical to that of a magnetic dipole, and radiate power into the substrate proportional to $\epsilon_r^{1.43}$ at the first resonance. (The factor for an elementary slot is $\epsilon_r^{1.5}$.) The impedance characteristics of the two geometries, however, are quite dissimilar. The frequency behavior of the self impedances for the folded-slot designs described in Table 8.1 are given in Figure 8.3. It is seen that the first useful resonance coincides with the peak in the real part of the self impedance, since the first zero crossing of the imaginary part is associated with a near short-circuit impedance. The dependence of this first resonance on the dielectric constant of the substrate material, ϵ_r, is examined in Figure 8.4. This data shows the circumference of the antenna normalized to the free-space wavelength at the resonant frequency, where the circumference is

given by $C = 2(L_a + S_a + W_{a2} - W_{a1})$. The curves can be approximated using a quasi-static expression for the effective dielectric constant:

$$C/\lambda_o \approx \frac{C_o}{\sqrt{(\epsilon_r + 1)/2}} \tag{8.1}$$

where C_o is the value of C/λ_o for $\epsilon_r = 1.0$. For the designs considered in Figure 8.4, this constant is equal to 0.97 and 0.99 for $S_a/L_a = 0.01$ and 0.04, respectively. Equation 8.1 slightly underestimates the full-wave result, which may be partially due to the fact that the results in Figures 8.3 and 8.4 take into account the effects of the CPW feedline; this will slightly reduce the effective slot circumference, thereby increasing the resonant frequency. As a comparison, the plots in Figure 8.5 show Z_{self} for a folded-slot (design C) and a comparable slot antenna. The peak in $\mathrm{Re}(Z_{self})$ at the first resonance for the folded-slot is four times smaller than for the slot, which is the dual of the relationship between folded-dipoles and standard dipole antennas [32]. The self impedance of each antenna at its respective second resonance, however, is 16 Ω.

For purposes of array design, it is also useful to investigate the mutual coupling between two antenna elements. Shown in Figures 8.6-8.8 is the mutual impedance, Z_{12}, between two folded-slots of designs A-C, respectively, at the first resonance. The antennas are in the broadside configuration with each input port positioned as shown in Figure 8.1, and the separation distance S is measured between the center of the folded slots. In contrast to the self impedance data, these calculations do not include the CPW feedlines. Since the CPW lines radiate little or no power, however, negligible differences are incurred by their omission. By comparing the plots in Figure 8.8 to those in Figure 8.9 for the comparable slot antenna pair, it is clear that the impedance coupling between the slots is four times as strong as the coupling between the folded-slots, as found above for Z_{self}. The impedance coupling between

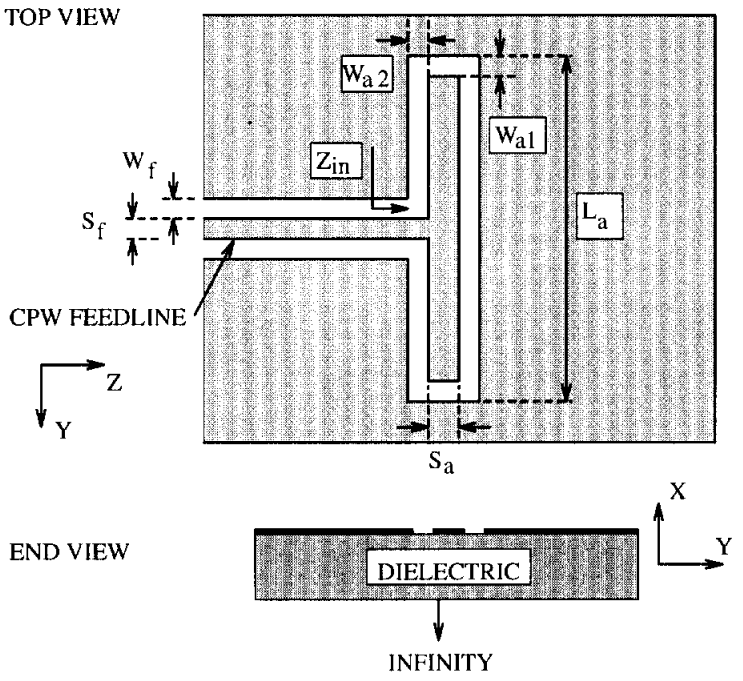

Figure 8.1: Single folded-slot antenna on a dielectric half-space (not to scale).

two folded-slots of design C at the second resonance (Circumference = $0.47\lambda_o$) is shown in Figure 8.10, and in this case the coupling is nearly the same as for the slot antennas at the second resonance ($L_a = 0.33\lambda_o$).

The mutual coupling values given here were determined by inverting the admittance matrix (Eqn. 3.34) and extracting the (i,j) element of the resultant impedance matrix, where i refers to the subsection at the input port of the first antenna and j refers to the subsection at the input of the second antenna. This element, Z_{ij}, relates the voltage at port i due to a source current at port j.

8.3 Double Folded-Slot Antennas

The design of the double folded-slot antenna is primarily based on two parameters: the folded-slot elements and the connecting line between them. General guidelines

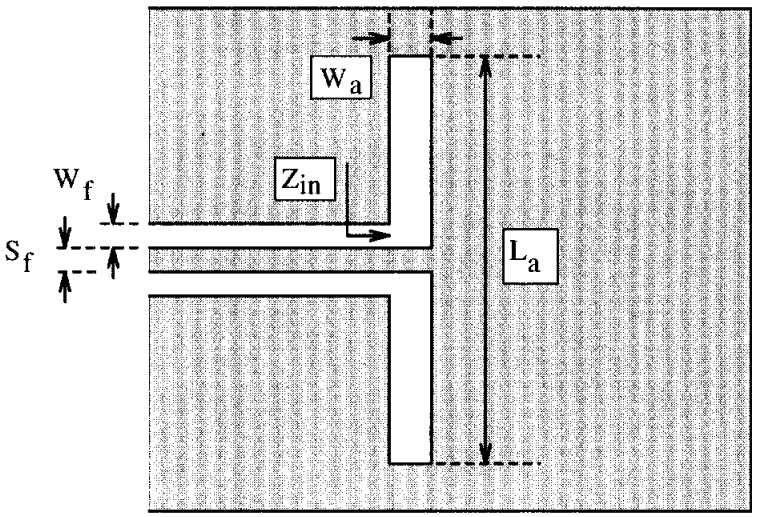

Figure 8.2: CPW-fed slot antenna (not to scale).

Design	ϵ_r	W_f / S_f	W_{a1} / W_{a2} / S_a / L_a
A	1.0	.10/.40	.10/.20/.10/10.0
B	4.0	.10/.40	.10/.20/.10/10.0
C	11.7	.10/.40	.10/.20/.10/10.0

Table 8.1: Parameters for different folded-slot antenna designs (refer to Figure 8.1). ϵ_r refers to the dielectric constant of the lower half-space and all dimensions are in millimeters.

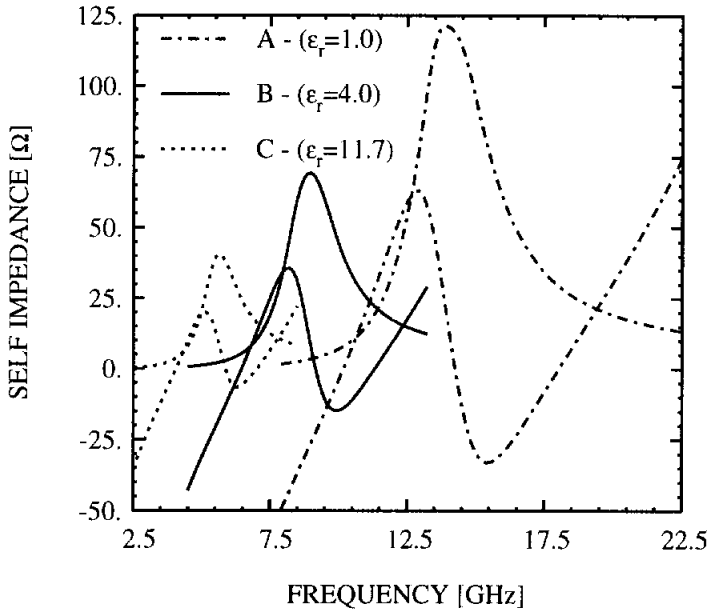

Figure 8.3: Calculated self impedances for folded-slot designs A, B, and C from Table 8.1.

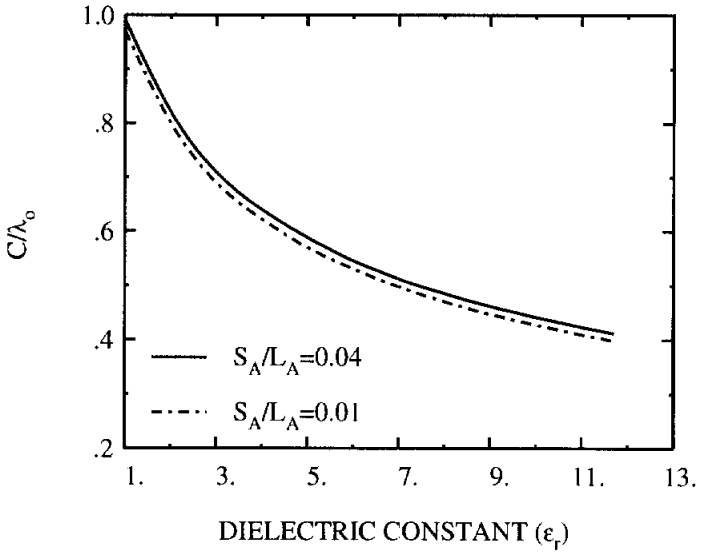

Figure 8.4: Resonant circumference of a folded-slot antenna versus the dielectric constant of the semi-infinite substrate. The antenna dimensions are $W_{a1}/L_a = 0.01$, $W_{a2}/L_a = 0.02$, $L_a = 10$ mm, and S_a is given in the figure. The results include the effects of the CPW feedline with dimensions $W_f = 0.1$ mm and $S_f = 0.4$ mm.

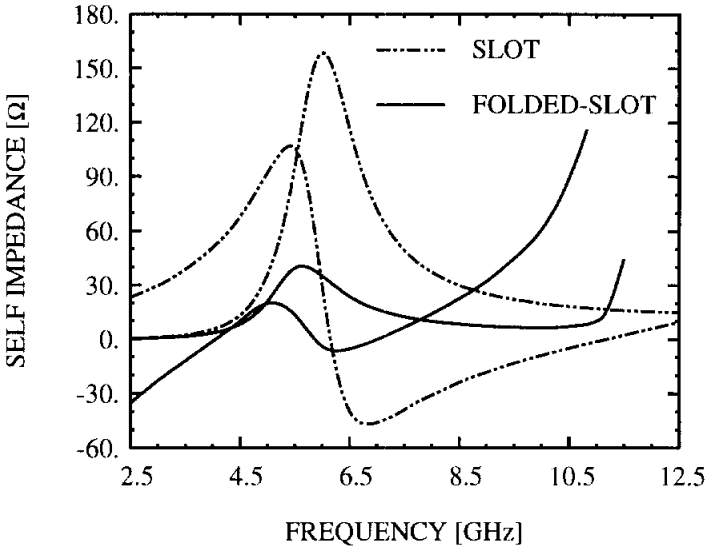

Figure 8.5: Calculated self impedances for folded-slot design C ($\epsilon_r = 11.7$) from Table 8.1 and a comparable slot antenna. The dimensions of the slot are $W_a/L_a = 0.02$ and $L_a = 10$ mm.

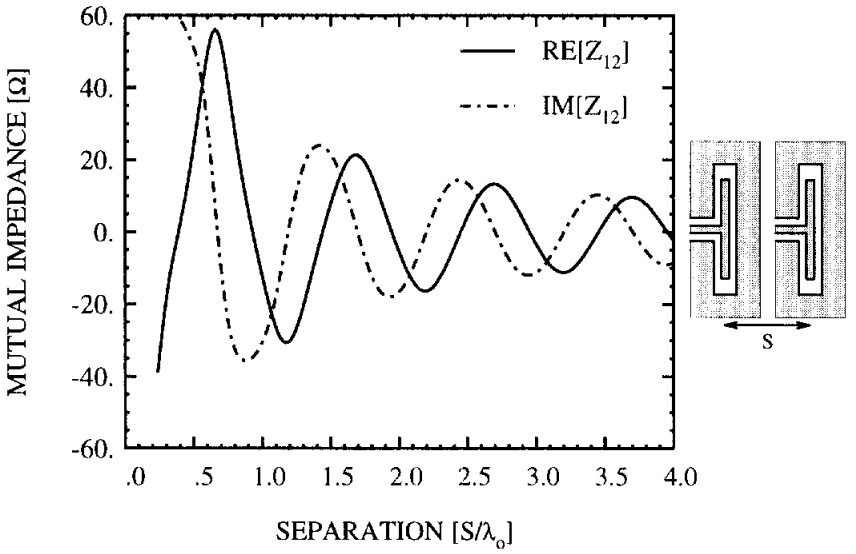

Figure 8.6: Calculated mutual impedance for two folded-slot antennas of design A ($\epsilon_r = 1.0$) from Table 8.1 versus separation distance. The antennas are aligned in a broadside configuration, and the computations are performed at the first resonance of a single folded-slot (Circumference = $0.97\lambda_o$).

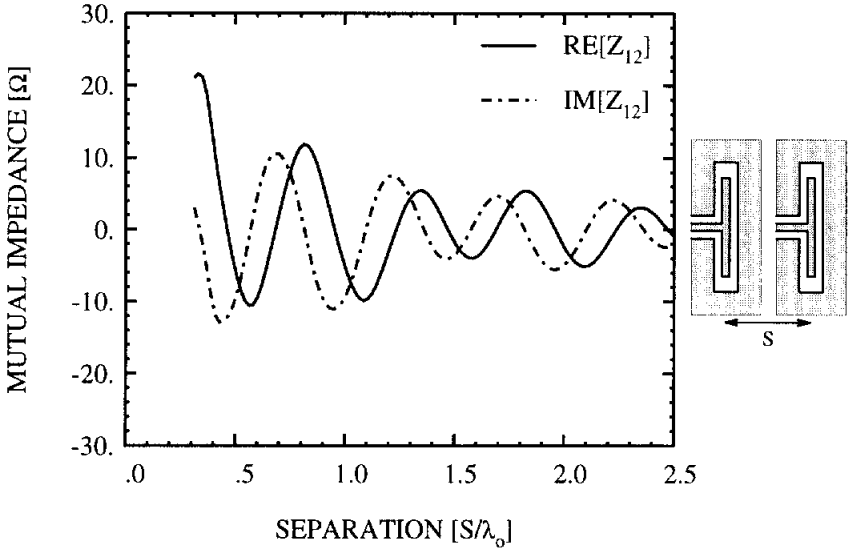

Figure 8.7: Calculated mutual impedance for two folded-slot antennas of design B ($\epsilon_r = 4.0$) from Table 8.1 versus separation distance (broadside configuration). The computations are performed at the first resonance of a single folded-slot (Circumference = $0.62\lambda_o$).

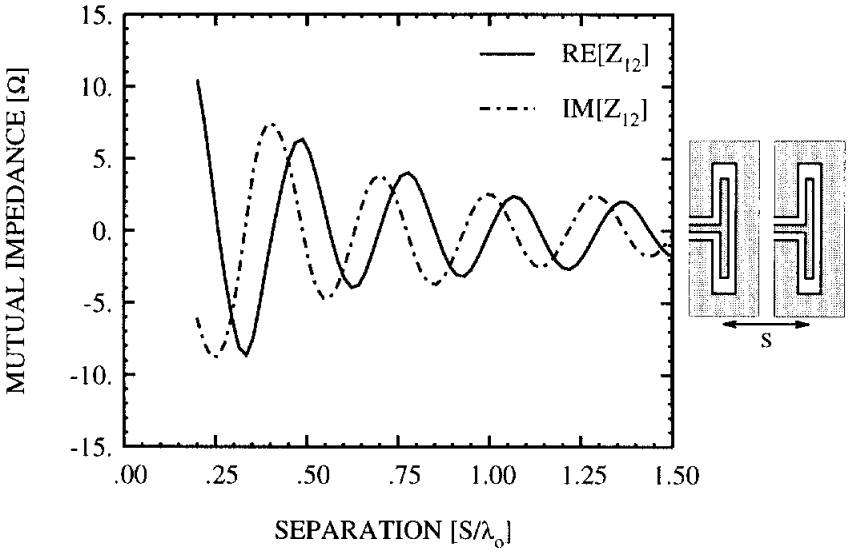

Figure 8.8: Calculated mutual impedance for two folded-slot antennas of design C ($\epsilon_r = 11.7$) from Table 8.1 versus separation distance (broadside configuration). The computations are performed at the first resonance of a single folded-slot (Circumference = $0.40\lambda_o$).

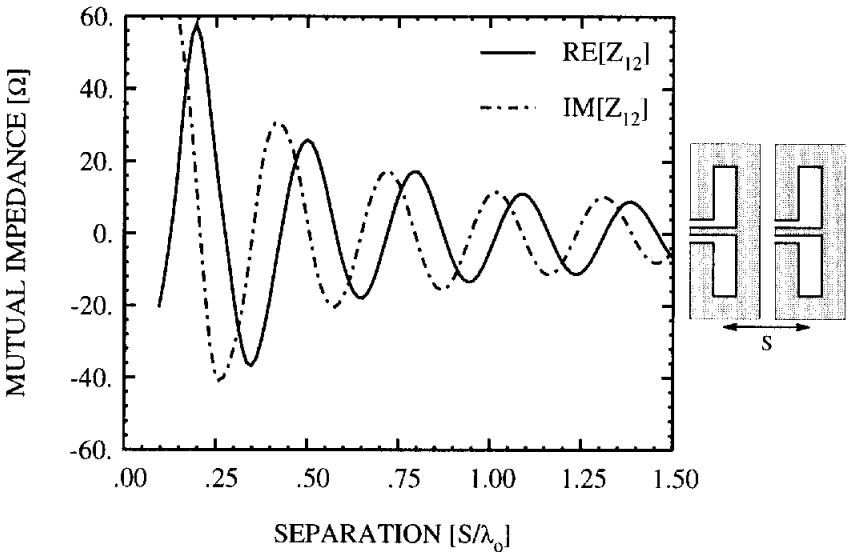

Figure 8.9: Calculated mutual impedance for two slot antennas on a silicon substrate ($\epsilon_r = 11.7$) versus separation distance, where the antenna dimensions are $W_a/L_a = 0.02$ and $L_a = 10$ mm. The antennas are aligned in a broadside configuration, and the computations are performed at the first resonance of a single slot ($L_a = 0.19\lambda_o$).

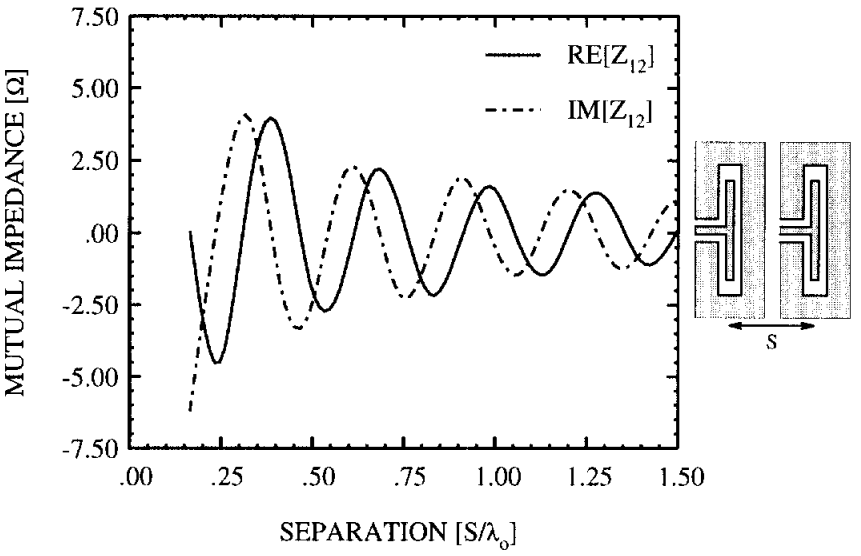

Figure 8.10: Calculated mutual impedance for two folded-slot antennas of design C ($\epsilon_r = 11.7$) from Table 8.1 versus separation distance (broadside configuration). The computations are performed at the second resonance of a single folded-slot (Circumference = $0.47\lambda_o$).

for each of these are given below, and typical performance characteristics of the designs given in Table 8.2 are discussed in the following sections. In what follows, the frequency at which the E- and H-plane patterns are peaked at broadside and the two sidelobes in the E-plane are symmetric is defined as the center frequency, f_o.

8.3.1 Design Guidelines

- *Folded-Slot Element* - The total circumference, measured through the center of the slots, should be approximately equal to 1.0-1.04 λ_g, where λ_g is the guided wavelength of the propagating CPW mode at f_o. In computing this wavelength, the same quasi-static approximation used in Eqn. 8.1 has been applied. Widening the slot width W_{a2} decreases the center frequency and also tends to reduce the variation in the input impedance (Z_{in}) versus frequency.

Values for W_{a2} around $\lambda_g/60$ generally provide the best impedance bandwidth performance. Finally, the slot separation S_a should be minimized in order to maintain low cross-polarization levels.

- *Connecting Line* - In order to feed each folded-slot antenna in phase and maximize the main beam efficiency, the feeding line between the two elements must provide a 180° phase shift for the guided CPW mode and the radiating space wave. For the typical configuration where the substrate and superstrate have different permittivities, proper feeding can be accomplished using a meander line such as that shown in Figure 8.11. Ideally, the path length through the connecting line ($L_{ct} = 2L_{c1} + L_{c2} + 2L_{c3}$) should be approximately equal to 0.5 λ_g and the physical distance ($L_{ph} = 2L_{c1} + L_{c2}$) should be approximately equal to 0.5 λ_{ant}. Here λ_{ant} refers to the wavelength in the dielectric half-space. Results derived from the full-wave analysis, for the designs in Table 8.2, confirmed that the optimum separations for the guided wave and the space wave were within 2% of 180°. As the slot width W_{a2} becomes more narrow and the element spacing shifts, the optimum L_{ct} and L_{ph} values tend to increase. Another important feature of the connecting line is that the meander section is relatively short and does not cause significant slot-line mode excitation, since each bend is complimentary to a bend in the opposite direction. In comparison, a similar twin-slot antenna that is fed from one side requires a 1.0 λ_g element separation in order to feed each antenna in phase. The necessary meander line is thus twice as long as that used with the DFS, and has been found to degrade the overall antenna performance.

8.3.2 Radiation Patterns

Since each of the slots is equivalent to a magnetic dipole, the E-plane for the double folded-slot antenna is parallel to the feedline and normal to the plane of the antenna. With the correct phasing between the elements, the main beam points at $\Theta = 90°$, i. e. broadside. The H-plane is parallel to the slots and has one lobe that is symmetric about $\Phi = 90°$, which is simply the pattern for a single magnetic dipole. In order to demonstrate typical characteristics, the E- and H-plane patterns for design B are shown in Figures 8.12 and 8.13. Due to limitations in the experimental setup, the measured patterns are only strictly valid from about 30° to 150°. It can be observed that the sidelobe facing the feedline ($\Theta = 180°$) rises quickly as the frequency increases.

Without the additional beam shaping which is provided by a dielectric lens, the half-power beamwidths of the DFS antenna are approximately 50° in the E-plane and 76° in the H-plane. For the air substrate geometry, standard approximations (e.g. [32], pg. 32) predict a directivity around 6.3-7 dB from these beam sizes, and the moment method results fall into the range of 6.3-6.5 dB. On the quartz and silicon substrates, the directivity is greater since there is preferential radiation into the higher dielectric constant material [87]. For the quartz design (C), the power radiated into air accounts for approximately 24% of the total, and on silicon (designs D and E) the percentage drops to about 8%. Typically, patterns with the main lobe near broadside and sidelobes below -12 dB are possible over 8-10% bandwidths.

8.3.3 Input Impedance

The input impedances for the five geometries given in Table 8.2 are presented in Figures 8.14-8.17. By comparing these results to the impedance of a single slot

or a single folded-slot, it is seen that the general characteristics around the first resonance are similar. For the DFS, however, the first resonance occurs at a lower frequency when the slot circumference is only around 0.8 λ_g, as opposed 1.0 λ_g for the single folded-slot antenna. At the design frequency, when the two DFS elements are being fed in phase, the input impedance tends to flatten out, resulting in a second, broad resonant region on either side of f_o. The impedance bandwidth which can be obtained is larger than that provided by similar twin-slot antenna arrays.

The results for the air-substrate designs A and B are shown in Figures 8.14 and 8.15, respectively. The impedance is between 55-75 Ω, with an imaginary part less than $\pm$j10 Ω, over a 20-25% bandwidth. The discrepancy between the experimental and calculated values is primarily due to interference from the (large) flange mount coaxial connector which is 2 cm from the antenna. Low sidelobe levels exist at the same frequencies at which the agreement is very good, but the sidelobes illuminate the connector outside the center frequency band (see Figure 8.12). In Figure 8.16, calculated values for the low frequency designs on quartz and silicon are shown. As expected, the impedance is scaled down by approximately $(\epsilon_{re})^{\frac{1}{2}}$ relative to the levels for the air substrate, where ϵ_{re} is the effective dielectric constant for the propagating CPW mode. Finally, the characteristics of a higher frequency design on silicon are given in Figure 8.17, in order to validate the full-wave analysis when the meander line is included. Although the parameters for this geometry differ from the design rules stated in Section 8.3.1, this was the only measured data available at the time [92]. The predicted and experimental values for the first and second resonant frequencies agree to within 3.5%, however these is some additional ripple in the measured data. In this case, the discrepancies can be partially explained by reflections at the interface between free-space and the Stycast lens ($\epsilon_r = 12$) that was attached to the substrate

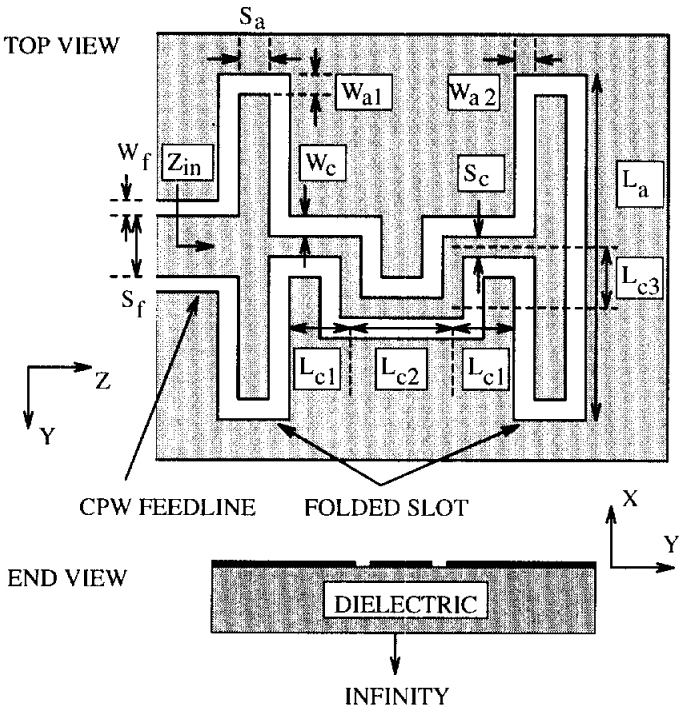

Figure 8.11: Double folded-slot antenna on a dielectric half-space (not to scale). The E-plane pattern is in a plane parallel with the feedline and normal to the page, at $\Phi = 90°$ and $\Theta = 0$-$180°$; the feedline is at $\Theta = 180°$.

in order to simulate the semi-infinite dielectric half-space. A matching layer could be used to minimize this interference.

8.4 Conclusion

This chapter has presented an investigation into the characteristics of single and double folded-slot antennas on semi-infinite substrates. These antennas are naturally suited for coplanar waveguide feedline configurations and are therefore easily integrated with active devices. The double folded-slot antenna is a compact planar geometry which measures approximately one half of a guided wavelength on each side. It provides a broad band input impedance of up to 25%, and a directivity of at least 6.5 dB, depending on the substrate. Furthermore, the DFS antenna requires ap-

Design	ϵ_r	W_f / S_f	W_{a1} / W_{a2} / S_a / L_a	W_c / S_c / L_{c1} / L_{c2} / L_{c3}	f_o
A	1.0	.100/3.30	.415/.415/.415/25.0	.415/.415/12.6/0.00/0.00	6.06
B	1.0	.100/3.30	.415/1.66/.415/25.0	.415/.415/12.6/0.00/0.00	5.68
C	4.0	.264/1.58	.264/.528/.264/15.8	.264/.264/4.17/4.17/1.65	6.05
D	11.7	.165/.495	.165/.330/.165/9.92	.165/.165/2.44/2.44/1.30	6.05
E	11.7	.060/.030	.040/.040/.150/2.55	.040/.070/.455/.700/.545	23.8

Table 8.2: Parameters for several double folded-slot antenna designs (refer to Figure 8.11). ϵ_r refers to the dielectric constant of the lower half-space. All dimensions are in millimeters and the center frequency, f_o, is in GHz.

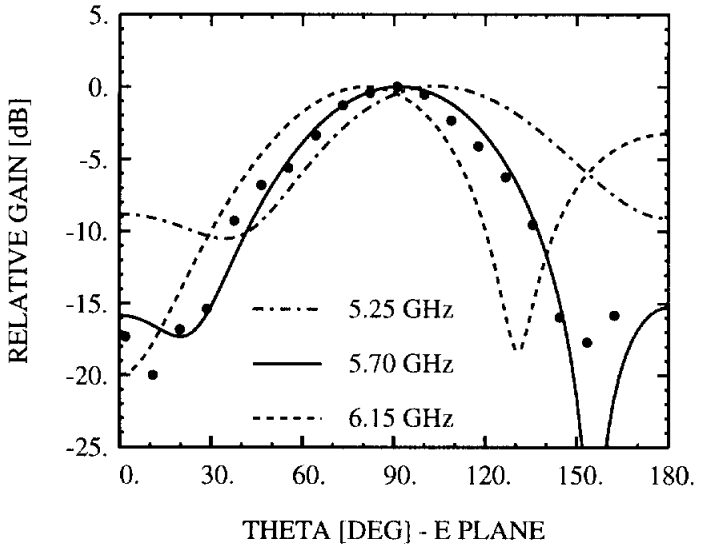

Figure 8.12: E-plane patterns for the double folded-slot antenna design B, at three different frequencies. The markers represent measured data at 5.70 GHz.

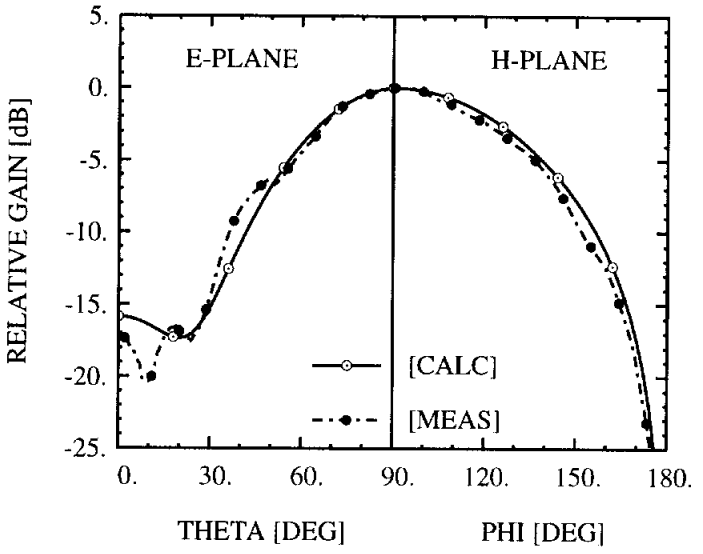

Figure 8.13: E- and H-plane patterns for the double folded-slot antenna design B at 5.7 GHz.

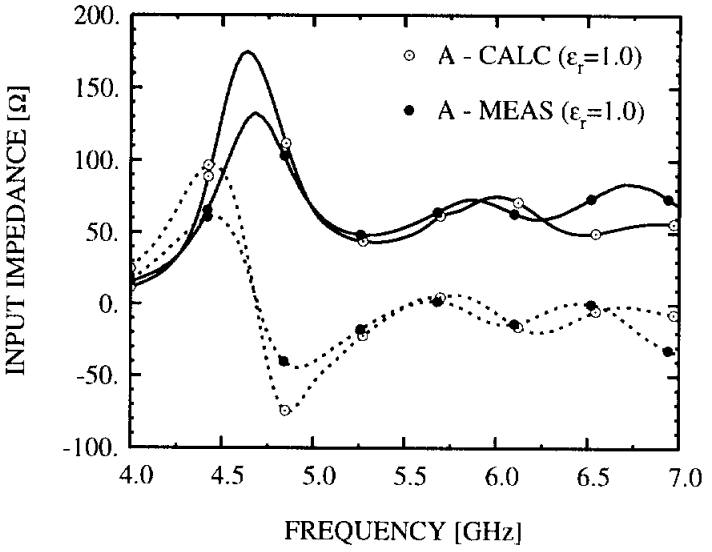

Figure 8.14: Calculated and measured input impedance for design A from Table 8.2.

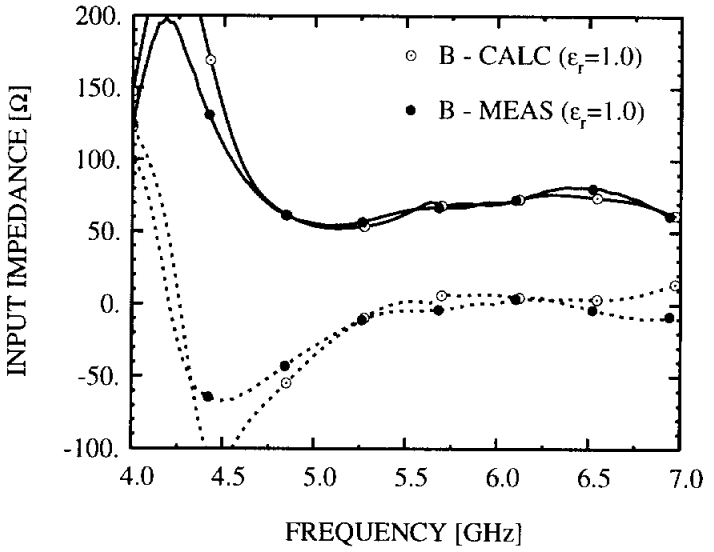

Figure 8.15: Calculated and measured input impedance for design B from Table 8.2.

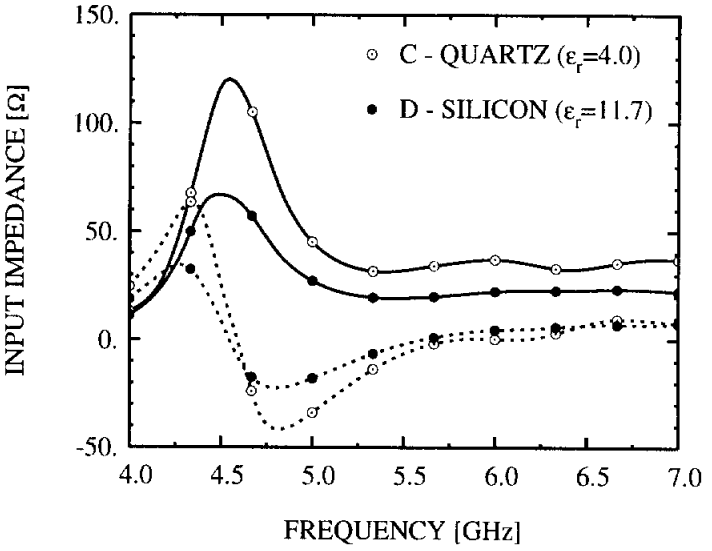

Figure 8.16: Calculated input impedance for designs C and D from Table 8.2.

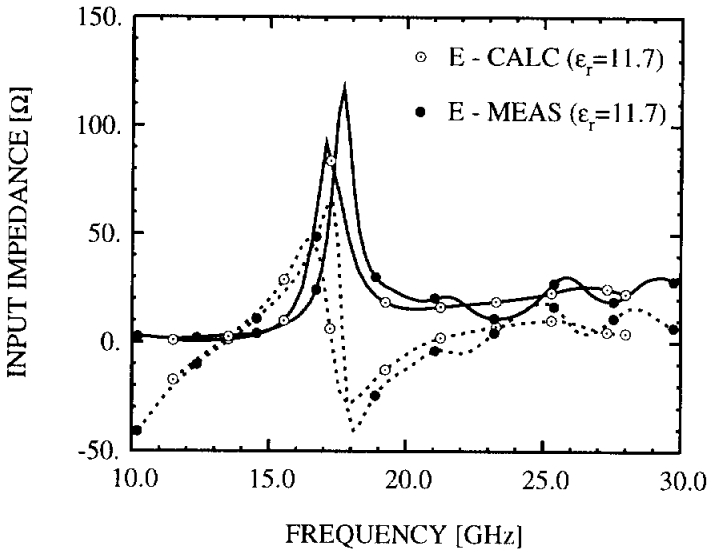

Figure 8.17: Calculated and measured input impedance for design E from Table 8.2. The measured data is from [92].

proximately half the area of a double slot antenna, since the latter must be operated at its second resonance to obtain a reasonably broad band input impedance.

CHAPTER IX

SUMMARY AND RECOMMENDATIONS FOR FUTURE WORK

In order to coalesce the concepts and results presented in this work, the main topics which have been examined are recapitulated herein. The use of the thin dielectric membranes to support conducting lines is a specific area in the overall field of micromachined, microwave circuitry. As a whole, this field appears to present a very promising new direction, and the potential areas of improvement over conventional transmission lines seem numerous. A thorough investigation into these possibilities is not attempted here, however specific suggestions for expanding and improving upon aspects of this particular research are included.

9.1 Summary

A detailed study of membrane-supported, high frequency transmission lines has been presented in this thesis. The material has focused on the microshield configuration, which is a quasi-planar geometry with coplanar conducting lines and an air-filled lower shielding cavity. A comparison with conventional substrate-supported coplanar waveguide demonstrated the advantages of microshield in terms of attenuation, broad-band TEM operation, low parasitic radiation, and the improved performance of discontinuities.

Considerable attention has been devoted to the theoretical characterization of general coplanar waveguide-type discontinuities, of which microshield is a particular class. The analysis of open, partially shielded and completely enclosed circuits was performed using a full-wave integral equation technique. This algorithm utilizes variable mesh subdivision and flexible geometric definition to allow a wide range of coplanar-type discontinuities to be easily characterized. In addition, a computationally efficient approach was developed specifically for the analysis of various tuning stub designs. The method combines a 2-D spectral domain approach with a coupled line analysis to provide an order of magnitude improvement over the full-wave technique in terms of speed. The recommended guidelines to ensure its accuracy are non-restrictive, and it provides a useful means of studying circuits with integrated lumped elements.

To complement the theoretical work, an extensive investigation has been made into the fabrication and experimental characterization of membrane-supported circuits. Part of this effort concerned microshield components designed to operate in the 5-40 GHz frequency range. It was demonstrated that broad band, low loss transitions between microshield and coplanar waveguide printed on a high permittivity substrate can be achieved by properly matching the characteristic impedances. For filter applications, new compact tuning stub geometries were presented which are up to 60% shorter than conventional configurations, yet exhibit nearly the same electrical characteristics. Another new approach was developed that combines integrated thin-film capacitors with standard distributed-element stubs. For a circuit length of $\lambda/4$, these designs provide at least 20 dB more low frequency rejection than a simple tuning stub. A number of band-pass filter implementations were also pursued which employed the different types of series stubs as end-to-end resonators. These designs

achieve minimum lateral width (typically around 300 μm) and lengths ranging between 0.5-0.8 λ, with bandwidths between 15-60%. An accomplishment in the area of submillimeter wave circuits was the first experimental validation of a 250 GHz planar band-pass filter. This project required a novel approach to extract the S-parameters from data which was measured using a quasi-optical setup, as well as a new double folded-slot antenna for coupling power into the filter. In support of this research, studies were conducted on the characteristics of single and double-folded slot antennas on semi-infinite substrates. Finally, as an alternative to the microshield line, a membrane-supported microstrip geometry was presented. Its use was illustrated in the power distribution stages of a Ka-band solid state power amplifier, where a single Wilkinson power divider/combiner exhibited approximately half the loss which is characteristic of conventional microstrip implementations.

9.2 Recommendations

With regard to the theoretical characterization of coplanar waveguide-type discontinuities, one subject which deserves more consideration is the coupled line analysis. Although only three center conductor (or four slot) geometries have been studied here, the technique can be extended to handle the compact, folded stub geometries presented in Chapter V. Furthermore, in its present form, the analysis can be applied to the bent stubs which are printed in the ground conductor. The efficiency and accuracy of this technique will allow each stub configuration to be evaluated over a wide range of parameters, leading to equivalent circuit models for design-based applications. One obvious extension of the work is to combine the thin-film capacitors with the folded tuning stubs, to realize an essentially lumped element approach.

There is also important research which remains to be done regarding the actual

implementation of the microshield transmission line, specifically related to the lower shielding cavity. In this work, the cavities were typically 1200-1800 μm wide at the top, which was necessary for two reasons: first, in order to ensure that the back-side metalization was not deposited beneath the slots in the upper CPW line, the resolution of the shadow evaporation technique required at least a 100 μm tolerance on either side of the slots; second, to achieve a good RF short between the upper and lower ground planes through the membrane, a 250-300 μm overlap was used. Assuming the transmission line has a width of 300 μm, this leads to a minimum cavity dimension of around 1100 μm. While this limit may be reduced through improvement of the existing techniques, the effectiveness of the RF short and the shielding cavity in replacing the conventional air-bridge is still in question. Since the cavity dimensions increase at the bottom due to the anisotropy of the etch, the total path length between the edges of the upper ground planes can easily reach 3500 μm, allowing the RF potential to float. One means of overcoming this problem is to shield the circuits from above, as was done with the sub-mm wave filter described in Chapter VI. With this approach the back-side metalization is avoided and direct DC contact can be made between the shielding cavity and the upper ground conductors. Furthermore, the cavity depth can be made less than the wafer thickness in order to reduce the path length between the ground planes. An alternative solution, which in some cases may simplify the fabrication, is to use the back-side shielding approach augmented with air-bridges where necessary. In any case, these concerns will have to be addressed to proceed with circuits utilizing complex and high density layouts.

Perhaps most important is the need to consider what requirements should be met in order to help membrane-supported transmission lines find wide use. First among these is certainly reliability, a subject which is currently under study at the

California Institute of Technology's Jet Propulsion Laboratory. This work will help to determine if the membrane lines can be space-qualified, and therefore suitable for use in satellite-based communications and radio astronomy platforms. As touched upon in Chapter VII, realizing the full potential of the micromachined architectures will also be aided by the integration of multiple circuit functions into a single chip. For example, the 0.2 dB improvement in the insertion loss of the air-microstrip Wilkinson power divider/combiner becomes much more significant when placed in the context of 1-4 or 1-8 power distribution arrangements. Particularly at higher frequencies, chip-to-chip interconnects will partially erase the performance margins gained by the membrane-supported components. This also leads to another critical area, which is that of low loss interconnection schemes, whether with other planar lines, waveguide or active devices. At the individual circuit level it is difficult to argue against the intrinsic advantages of the micromachined, membrane-supported transmission lines for millimeter and submillimeter wave applications. These other issues need attention, however, to increase the acceptance of the technology.

APPENDICES

APPENDIX A

MULTI-PORT NETWORK Z-PARAMETERS

This appendix contains expressions for the Z-parameters of multi-port networks under various transformations. The relations are associated with the quasi-TEM analysis of the three center conductor CPW circuits presented in Chapter IV.

A.1 Extending One Port of a 4x4 Z Matrix

In this section, expressions are given for the Z-matrix which results when port 3 of a 4-port network has an additional section of line added to it, as shown in Figure A.1. The derivation is based on the following two conditions:

$$\begin{aligned} I_{a3} &= -I_{b1} \\ V_{a3} &= V_{b1} \end{aligned} \tag{A.1}$$

The Z-parameters for the transmission line section are:

$$\begin{aligned} Z_{b,11} = Z_{b,22} &= -jZ_0 cot(\beta L) \\ Z_{b,12} = Z_{b,21} &= -jZ_0 csc(\beta L) \end{aligned} \tag{A.2}$$

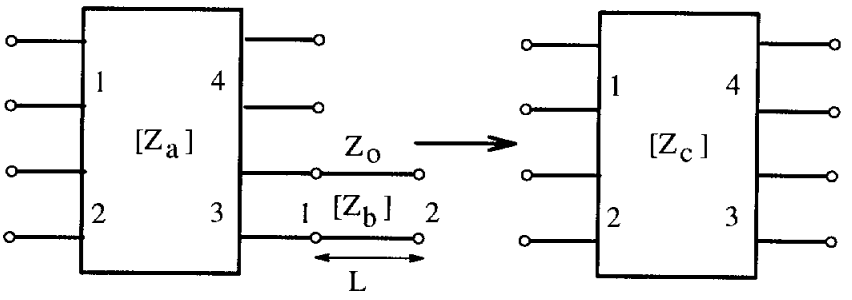

Figure A.1: A 4-port Z-matrix with an additional section of transmission line added to port 3_a.

where Z_0 is the characteristic impedance and L is the length. The elements of the resulting impedance matrix are given by:

$$\begin{aligned}
Z_{c,ij} &= Z_{a,ij} - Z_{a,i3}Z_{a,3j}/(Z_{a,33} + Z_{b,11}) && \text{i=1,2,4; j=1,2,4} \\
Z_{c,i3} &= Z_{a,i3}Z_{b,12}/(Z_{a,33} + Z_{b,11}) && \text{i=1,2,4; j=3} \\
Z_{c,3j} &= Z_{b,12}Z_{a,3j}/(Z_{a,33} + Z_{b,11}) && \text{i=3; j=1,2,4} \\
Z_{c,33} &= Z_{b,22} - Z_{b,12}Z_{b,21}/(Z_{a,33} + Z_{b,11}) && \text{i=3; j=3}
\end{aligned} \tag{A.3}$$

If the extension is connected instead to port x, simply interchange $i, j = x$ with $i, j = 3$ for the $[Z_a]$ components.

A.2 Terminating One Port of a 4x4 Z Matrix

In this section, expressions are given for the Z-matrix which results when port 3 of a 4-port network is terminated in either a short- or open-circuit, as shown in Figure A.2. If the termination is a short-circuit, then $V_{a3} = 0$ and the following 3x3 matrix is derived:

$$\begin{aligned}
Z_{b,ij} &= Z_{a,ij} - Z_{a,i3}Z_{a,3j}/Z_{a,33} && \text{i=1,2; j=1,2} \\
Z_{b,i3} &= Z_{a,i4} - Z_{a,i3}Z_{a,34}/Z_{a,33} && \text{i=1,2; j=3} \\
Z_{b,3j} &= Z_{a,4j} - Z_{a,43}Z_{a,3j}/Z_{a,33} && \text{i=3; j=1,2} \\
Z_{b,33} &= Z_{a,44} - Z_{a,43}Z_{a,34}/Z_{a,33} && \text{i=3; j=3}
\end{aligned} \tag{A.4}$$

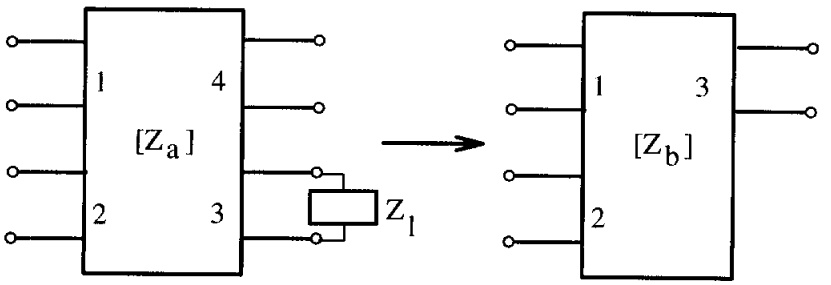

Figure A.2: A 4-port Z-matrix with a termination connected to port 3_a.

If the termination is an open-circuit, then $I_{a3} = 0$ and the following 3x3 matrix is derived:

$$\begin{aligned} Z_{b,ij} &= Z_{a,ij} \quad \text{i=1,2; j=1,2} \\ Z_{b,i3} &= Z_{a,i4} \quad \text{i=1,2; j=3} \\ Z_{b,3j} &= Z_{a,4j} \quad \text{i=3; j=1,2} \\ Z_{b,33} &= Z_{a,44} \quad \text{i=3; j=3} \end{aligned} \tag{A.5}$$

A.3 Common-Port Conversion of a 3x3 Z Matrix

In this section, expressions are given for the Z-matrix which results when ports 1 and 2 of a 3-port network are connected together. If the ports are connected in series as shown in the top of Figure A.3, the following boundary conditions exist:

$$\begin{aligned} I_{b1} &= I_{a1} = I_{a2} \\ V_{b1} &= V_{a1} + V_{a2} \end{aligned} \tag{A.6}$$

and the expressions for the 2-port network are:

$$\begin{aligned} Z_{b,11} &= Z_{a,11} + Z_{a,22} + Z_{a,12} + Z_{a,21} \\ Z_{b,12} &= Z_{a,13} + Z_{a,23} \\ Z_{b,21} &= Z_{b,12} \end{aligned}$$

$$Z_{b,22} = Z_{a,33} \tag{A.7}$$

If the ports are connected in shunt as shown in the bottom of Figure A.3b, the dual boundary conditions result:

$$\begin{aligned} I_{b1} &= I_{a1} + I_{a2} \\ V_{b1} &= V_{a1} = V_{a2} \end{aligned} \tag{A.8}$$

and the expressions for the resulting 2-port network are:

$$\begin{aligned} Z_{b,11} &= (Z_{a,11}Z_{a,22} - Z_{a,12}Z_{a,21})/\Delta \\ Z_{b,12} &= (Z_{a,23}(Z_{a,11} - Z_{a,12}) + Z_{a,13}(Z_{a,22} - Z_{a,21}))/\Delta \\ Z_{b,21} &= Z_{b,12} \\ Z_{b,22} &= (Z_{a,31}(Z_{a,23} - Z_{a,13}) + Z_{a,32}(Z_{a,13} - Z_{a,23}))/\Delta + Z_{a,33} \\ \Delta &= Z_{a,11} + Z_{a,22} - 2Z_{a,12} \end{aligned} \tag{A.9}$$

Reciprocal networks are assumed.

A.4 Cascade of Two 4-Port Z Matrices

In this section, expressions are given for the overall Z-matrix which results when two 4-port networks are connected as shown in Figure A.4. The derivation is based on the following four conditions:

$$\begin{aligned} I_{a4} &= -I_{b1} \\ I_{a3} &= -I_{b2} \\ V_{a4} &= V_{b1} \\ V_{a3} &= V_{b2} \end{aligned} \tag{A.10}$$

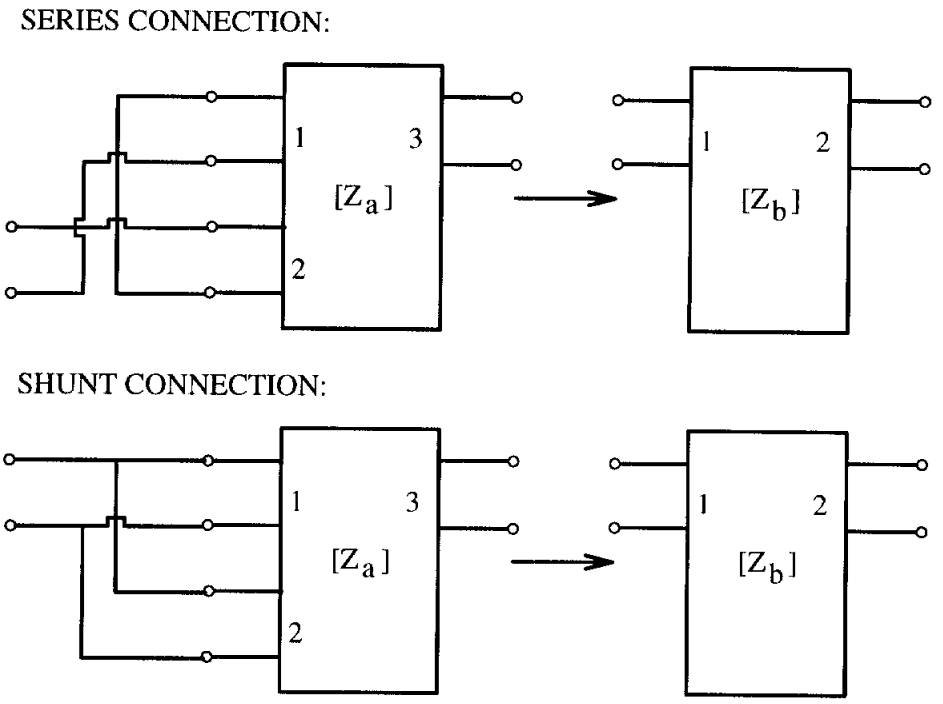

Figure A.3: A 3-port Z-matrix with ports 1_a and 2_a connected in series and in shunt.

The following terms are first defined:

$$
\begin{aligned}
A_{31} &= (Z_{a,31}(Z_{a,44}+Z_{b,11}) - Z_{a,41}(Z_{a,43}+Z_{b,12}))/\Delta \\
A_{32} &= (Z_{a,32}(Z_{a,44}+Z_{b,11}) - Z_{a,42}(Z_{a,43}+Z_{b,12}))/\Delta \\
A_{33} &= (Z_{b,13}(Z_{a,43}+Z_{b,12}) - Z_{b,23}(Z_{a,44}+Z_{b,11}))/\Delta \\
A_{34} &= (Z_{b,14}(Z_{a,43}+Z_{b,12}) - Z_{b,24}(Z_{a,44}+Z_{b,11}))/\Delta \\
A_{41} &= (Z_{a,41}(Z_{a,33}+Z_{b,22}) - Z_{a,31}(Z_{a,43}+Z_{b,12}))/\Delta \\
A_{42} &= (Z_{a,42}(Z_{a,33}+Z_{b,22}) - Z_{a,32}(Z_{a,43}+Z_{b,12}))/\Delta \\
A_{43} &= (Z_{b,23}(Z_{a,43}+Z_{b,12}) - Z_{b,13}(Z_{a,33}+Z_{b,22}))/\Delta \\
A_{44} &= (Z_{b,24}(Z_{a,43}+Z_{b,12}) - Z_{b,14}(Z_{a,33}+Z_{b,22}))/\Delta \\
\Delta &= (Z_{a,34}+Z_{b,21})(Z_{a,43}+Z_{b,12}) - (Z_{a,44}+Z_{b,11})(Z_{a,33}+Z_{b,22}) \qquad \text{(A.11)}
\end{aligned}
$$

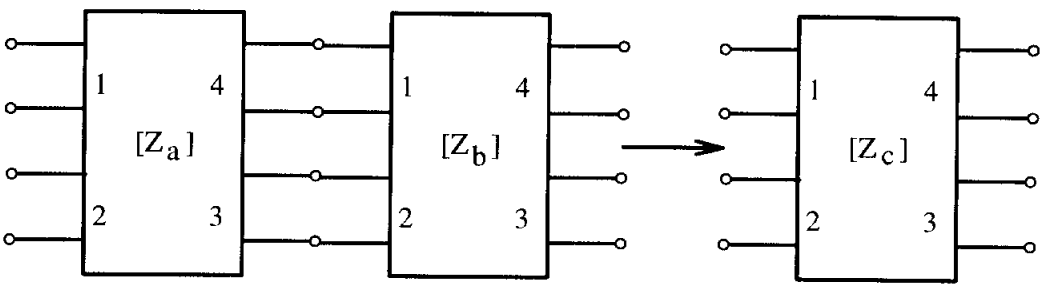

Figure A.4: Series connection of two 4-port Z matrices, where ports 3_a and 4_a are connected to ports 2_b and 1_b, respectively.

For i=1,2 the results are:

$$\begin{aligned} Z_{c,i1} &= Z_{a,i3}A_{31} + Z_{a,i4}A_{41} + Z_{a,i1} \\ Z_{c,i2} &= Z_{a,i3}A_{32} + Z_{a,i4}A_{42} + Z_{a,i2} \\ Z_{c,i3} &= Z_{a,i3}A_{33} + Z_{a,i4}A_{43} \\ Z_{c,i4} &= Z_{a,i3}A_{34} + Z_{a,i4}A_{44} \end{aligned} \tag{A.12}$$

For i=3,4 the results are:

$$\begin{aligned} Z_{c,i1} &= -Z_{b,i1}A_{41} - Z_{b,i2}A_{31} \\ Z_{c,i2} &= -Z_{b,i1}A_{42} - Z_{b,i2}A_{32} \\ Z_{c,i3} &= -Z_{b,i1}A_{43} - Z_{b,i2}A_{33} + Z_{b,i3} \\ Z_{c,i4} &= -Z_{b,i1}A_{44} - Z_{b,i2}A_{34} + Z_{b,i4} \end{aligned} \tag{A.13}$$

APPENDIX B

SPECTRAL DOMAIN APPROACH

B.1 Fourier Transformation of Basis Functions

The Fourier transform is defined as:

$$\tilde{\Phi}(\alpha_f) = \int_{-\infty}^{\infty} \Phi(x)\, e^{j\alpha_f x}\, dx \tag{B.1}$$

In order to compute the Fourier transform of the basis functions in Eqn. 4.3, the following integral relation is useful:

$$\int_{-a}^{a} \frac{1}{\sqrt{a^2 - x^2}} e^{j\delta x} dx = \pi J_o(a|\delta|) \tag{B.2}$$

where J_o is the zeroth-order Bessel function of the first kind. Using these two equations, the Fourier-transformed basis functions are found to be (for $i = 1, 2$):

$$\tilde{E}_{xm,i} = \begin{cases} \frac{-j\pi w_i}{2} sin(\alpha_f b_i) \left[J_o\left(\frac{|w_i\alpha_f + (m-1)\pi|}{2}\right) + J_o\left(\frac{|w_i\alpha_f - (m-1)\pi|}{2}\right)\right], & \text{m=1,3,...} \\ \frac{-j\pi w_i}{2} cos(\alpha_f b_i) \left[J_o\left(\frac{|w_i\alpha_f + (m-1)\pi|}{2}\right) - J_o\left(\frac{|w_i\alpha_f - (m-1)\pi|}{2}\right)\right], & \text{m=2,4,...} \end{cases}$$

$$\tilde{E}_{zn,i} = \begin{cases} \frac{\pi w_i}{2} cos(\alpha_f b_i) \left[J_o\left(\frac{|w_i\alpha_f + m\pi|}{2}\right) + J_o\left(\frac{|w_i\alpha_f - m\pi|}{2}\right)\right], & \text{n=1,3,...} \\ \frac{-\pi w_i}{2} sin(\alpha_f b_i) \left[J_o\left(\frac{|w_i\alpha_f + m\pi|}{2}\right) - J_o\left(\frac{|w_i\alpha_f - m\pi|}{2}\right)\right], & \text{n=2,4,...} \end{cases} \tag{B.3}$$

The geometrical parameters are defined in Figure 4.2.

To compute the characteristic impedance, the basis functions for an individual slot may also be utilized. In the space domain, the necessary functions are equal to

the first terms on the right-hand side of Eqns. 4.3. The Fourier transform of these terms are:

$$\tilde{E}_{xm,i^-} = \begin{cases} \frac{\pi w_i}{4} e^{-j\alpha_f b_i} \left[J_o\left(\frac{|w_i\alpha_f+(m-1)\pi|}{2}\right) + J_o\left(\frac{|w_i\alpha_f-(m-1)\pi|}{2}\right)\right], & \text{m=1,3,...} \\ \frac{-j\pi w_i}{4} e^{-j\alpha_f b_i} \left[J_o\left(\frac{|w_i\alpha_f+(m-1)\pi|}{2}\right) - J_o\left(\frac{|w_i\alpha_f-(m-1)\pi|}{2}\right)\right], & \text{m=2,4,...} \end{cases}$$

$$\tilde{E}_{zn,i^-} = \begin{cases} \frac{\pi w_i}{4} e^{-j\alpha_f b_i} \left[J_o\left(\frac{|w_i\alpha_f+n\pi|}{2}\right) + J_o\left(\frac{|w_i\alpha_f-n\pi|}{2}\right)\right], & \text{n=1,3,...} \\ \frac{-j\pi w_i}{4} e^{-j\alpha_f b_i} \left[J_o\left(\frac{|w_i\alpha_f+n\pi|}{2}\right) - J_o\left(\frac{|w_i\alpha_f-n\pi|}{2}\right)\right], & \text{n=2,4,...} \end{cases} \tag{B.4}$$

B.2 Determination of Unknown Coefficients

Once the true propagation constant, β, has been found, Eqn. 4.5 is manipulated to determine the unknown coefficients of the E-field basis functions. These coefficients are proportional to one another, and so by normalizing to $c_{1,1} = 1$, Eqn. 4.5 can be rewritten as:

$$\begin{bmatrix} K_{1,2} & \cdots & K_{1,M+N} \\ \vdots & & \\ K_{M+N,2} & \cdots & \cdots \end{bmatrix} \begin{bmatrix} c_{1,2} \\ \vdots \\ d_{2,N} \end{bmatrix} = - \begin{bmatrix} K_{1,1} \\ \vdots \\ K_{M+N,1} \end{bmatrix} \tag{B.5}$$

The QR algorithm [93] can now be applied to the $(M+N) \times (M+N-1)$ matrix K to find the best approximation to the unknown coefficient vector.

B.3 Characteristic Impedance Calculation

The characteristic impedances of the slots shown in Figure 4.2 are found by evaluating the electric and magnetic fields in the cross-section. Subsequently, the associated power integrals in the y direction are computed analytically (see Eqn. 4.8). These two steps are outlined in the following sections.

B.3.1 Evaluating Electric and Magnetic Fields

Following the immittance approach described in [52], the field components in the dielectric regions of Figure 4.2 are treated as the superposition of inhomogeneous plane waves which propagate away from the z-axis at an angle θ. At *each* θ the plane waves are decomposed into TM-to-y and TE-to-y modes, for which all field components can be defined in terms of E_y and H_y, respectively. The expressions in each region as follows [31]:

$$\begin{array}{ll} \underline{\text{TM-to-y}} & \underline{\text{TE-to-y}} \\ \tilde{E}_x = -jR\frac{\partial \tilde{E}_y}{\partial y} & \tilde{E}_x = -j\hat{z}Q\tilde{H}_y \\ \tilde{E}_z = -jQ\frac{\partial \tilde{E}_y}{\partial y} & \tilde{E}_z = j\hat{z}R\tilde{H}_y \\ \tilde{H}_x = j\hat{y}Q\tilde{E}_y & \tilde{H}_x = -jR\frac{\partial \tilde{H}_y}{\partial y} \\ \tilde{H}_z = -j\hat{y}R\tilde{E}_y & \tilde{H}_z = -jQ\frac{\partial \tilde{H}_y}{\partial y} \end{array} \tag{B.6}$$

where

$$\begin{aligned} R &= \frac{\alpha_f}{\alpha_f^2 + \beta^2} \\ Q &= \frac{\beta}{\alpha_f^2 + \beta^2} \\ \hat{y} &= j\omega\epsilon \\ \hat{z} &= j\omega\mu \end{aligned} \tag{B.7}$$

Recall that α_f is the Fourier transform variable and β is the propagation constant. Accounting for the perfectly conducting boundary at y=0 and at y=b+g+t=c, the E_y and H_y components are defined as:

$$\begin{aligned} Region3: \quad -j\hat{y}_3\tilde{E}_{y3} &= A^e cosh(\gamma_3 y) \\ Region2: \quad -j\hat{y}_2\tilde{E}_{y2} &= B^e cosh(\gamma_2(y-b)) + C^e sinh(\gamma_2(y-b)) \\ Region1: \quad -j\hat{y}_1\tilde{E}_{y1} &= D^e cosh(\gamma_1(c-y)) \end{aligned} \tag{B.8}$$

$$
\begin{aligned}
Region3: \quad -j\hat{z}_3\tilde{H}_{y3} &= A^h sinh(\gamma_3 y) \\
Region2: \quad -j\hat{z}_2\tilde{H}_{y2} &= B^h sinh(\gamma_2(y-b)) + C^h cosh(\gamma_2(y-b)) \\
Region1: \quad -j\hat{z}_1\tilde{H}_{y1} &= D^h sinh(\gamma_1(c-y))
\end{aligned} \tag{B.9}
$$

where $\gamma_i = \sqrt{\alpha_f^2 + \beta^2 - \omega^2\mu\epsilon_i}$.

In order to determine the coefficients $A^{e,h}$-$D^{e,h}$, the boundary conditions on the tangential E- and H-fields are enforced at each regional interface. Since the TM-to-y and TE-to-y modes are orthogonal, the boundary conditions must be satisfied separately for each mode, which requires that the electric current $\vec{J}$ also be decomposed into parts associated with TM-to-y and TE-to-y fields. For this, we begin by observing the definition of the inverse Fourier transform:

$$
\Phi(x,y)e^{-j\beta z} = \frac{1}{2\pi}\int_{-\infty}^{\infty} \check{\Phi}(\alpha,y)\, e^{-j(\alpha_f x+\beta z)}\, d\alpha \tag{B.10}
$$

from which the interpretation of the field components as summations of plane waves can be understood. Note that this plane wave assimilation also holds for the electric current, $\vec{J}$. Next, the coordinate transformation shown in Figure B.1 is defined:

$$
\begin{aligned}
sin\theta &= \frac{\alpha_f}{\sqrt{\alpha_f^2+\beta^2}} \\
cos\theta &= \frac{\beta}{\sqrt{\alpha_f^2+\beta^2}} \\
u &= z\, sin\theta - x\, cos\theta \\
v &= z\, cos\theta + x\, sin\theta
\end{aligned} \tag{B.11}
$$

With this transformation, each plane wave is seen to be propagating in the v-direction and is constant in the u-direction. Thus, using standard expressions for the electric and magnetic fields in terms of the vector potentials for an electric current source [32], and taking $\partial/\partial u$ equal to zero, it is found that the current $\tilde{J}_v$ will produce only

the TM-to-y fields ($\tilde{E}_y$, $\tilde{H}_u$, $\tilde{E}_v$) and $\tilde{J}_u$ will produce only the TE-to-y fields ($\tilde{H}_y$, $\tilde{E}_u$, $\tilde{H}_v$). From Eqn. B.11, the decomposition for the current is then written as:

$$\begin{array}{cc} \underline{\text{TM-to-y Source}} & \underline{\text{TE-to-y Source}} \\ \tilde{J}_v = \frac{\beta \tilde{J}_z}{\sqrt{\alpha_f^2+\beta^2}} + \frac{\alpha_f \tilde{J}_x}{\sqrt{\alpha_f^2+\beta^2}} & \tilde{J}_u = \frac{\alpha_f \tilde{J}_z}{\sqrt{\alpha_f^2+\beta^2}} - \frac{\beta \tilde{J}_x}{\sqrt{\alpha_f^2+\beta^2}} \end{array} \tag{B.12}$$

With these transformations, the boundary condition on the tangential magnetic field at y=b+g,

$$\hat{y} \times (\tilde{H}_{t1} - \tilde{H}_{t2}) = \tilde{J}_t \tag{B.13}$$

is cast into the following form:

$$\begin{array}{cc} \underline{\text{TM-to-y}} & \underline{\text{TE-to-y}} \\ \tilde{H}_{u1} - \tilde{H}_{u2} = \tilde{J}_v & \tilde{H}_{v1} - \tilde{H}_{v2} = -\tilde{J}_u \end{array} \tag{B.14}$$

where

$$\begin{aligned} \tilde{H}_u &= \tilde{H}_z^{TM} sin\theta - \tilde{H}_x^{TM} cos\theta \\ \tilde{H}_v &= \tilde{H}_z^{TE} sin\theta + \tilde{H}_x^{TE} cos\theta \end{aligned} \tag{B.15}$$

The minus sign in Eqn. B.14 results from the fact that $\hat{y} \times \hat{u} = \hat{v}$ and $\hat{y} \times \hat{v} = -\hat{u}$. Since no other sources exist, the remaining boundary conditions are continuity of the tangential E-field at y=b+g, and continuity of both the E- and H-fields at y=b.

Upon substituting Eqns. B.6 into the appropriate boundary condition relations, a system of linear equations is generated involving the unknown coefficients. It is possible to use a series of back-substitutions to solve for each coefficient explicitly, yet this approach becomes increasingly tedious as the number of dielectric layers increases. A much more compact technique is to simply assemble the equations in matrix form, and solve for the coefficients numerically through a single matrix

inversion and vector multiplication. First, the following constants are defined:

$$\begin{aligned} S_i &= sinh(\gamma_i d_i) \\ C_i &= cosh(\gamma_i d_i) \\ Ct_i &= C_i/S_i \end{aligned} \tag{B.16}$$

where d_i is the thickness of the i^{th} dielectric layer. The matrix equation for the TM fields is then:

$$\begin{bmatrix} \frac{\gamma_3}{\hat{y}_3} & 0 & \frac{-\gamma_2}{\hat{y}_2 S_2} & 0 \\ Ct_3 & \frac{-1}{S_2} & 0 & 0 \\ 0 & \frac{\gamma_2}{\hat{y}_2} & \frac{\gamma_2 Ct_2}{\hat{y}_2} & \frac{\gamma_1}{\hat{y}_1} \\ 0 & -Ct_2 & -1 & Ct_1 \end{bmatrix} \begin{bmatrix} A^e S_3 \\ B^e S_2 \\ C^e S_2 \\ D^e S_1 \end{bmatrix} = \begin{bmatrix} 0 \\ 0 \\ 0 \\ \tilde{J}_u \sqrt{\alpha_f^2 + \beta^2} \end{bmatrix} \tag{B.17}$$

and for the TE fields:

$$\begin{bmatrix} 1 & 0 & \frac{-1}{S_2} & 0 \\ \frac{\gamma_3 Ct_3}{\hat{z}_3} & \frac{-\gamma_2}{\hat{z}_2 S_2} & 0 & 0 \\ 0 & 1 & Ct_2 & -1 \\ 0 & \frac{\gamma_2 Ct_2}{\hat{z}_2} & \frac{\gamma_2}{\hat{z}_2} & \frac{\gamma_1 Ct_1}{\hat{z}_1} \end{bmatrix} \begin{bmatrix} A^h S_3 \\ B^h S_2 \\ C^h S_2 \\ D^h S_1 \end{bmatrix} = \begin{bmatrix} 0 \\ 0 \\ 0 \\ \tilde{J}_u \sqrt{\alpha_f^2 + \beta^2} \end{bmatrix} \tag{B.18}$$

The purpose of scaling the coefficients by S_i is to increase the numerical stability of the solution.

It is apparent that after the matrix inversion in Eqns. B.17 and B.18 the coefficients for the total E- and H-fields (Eqn. B.6) are expressed in terms of the electric current $\tilde{J}$. Furthermore, using Eqn. 4.1, the total fields are also known as functions of the electric field in the *slots*. By superposition, furthermore, the E- and H-fields associated with an individual slot may be computed by utilizing only the relevant *slot* fields in Eqn. 4.1. This is the means by which $\vec{H}_{i-}^{*}$ in Eqn. 4.8 is calculated.

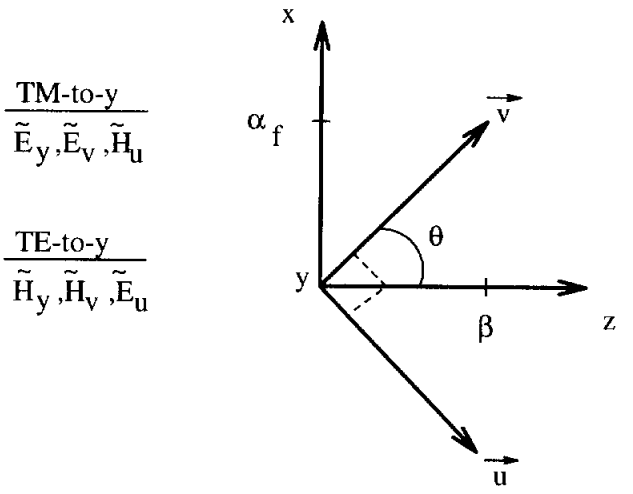

Figure B.1: Coordinate transformation for decomposition of fields into TM-to-y and TE-to-y components.

B.3.2 Evaluating the Power Integrals

In order to calculate the characteristic impedance, it is necessary to integrate the Poynting vector along y, as shown in Eqn. 4.8. The total power is a summation of the powers in each separate dielectric layer, which can be expressed as:

$$\begin{aligned} P_i &= \int_{y1}^{y2} \left(\tilde{E}_{xi,TM} + \tilde{E}_{xi,TE}\right)\left(\tilde{H}^*_{yi,TE}\right) - \left(\tilde{H}^*_{xi,TM} + \tilde{H}^*_{xi,TE}\right)\left(\tilde{E}_{yi,TM}\right) dy \\ P_i &= P_{i,TM-TE} + P_{i,TE-TE} + P_{i,TM-TM} + P_{i,TE-TM} \end{aligned} \tag{B.19}$$

where $i = 1, 2, 3$ for the three-layer dielectric (Figure 4.2) and $y1, y2$ denote the limits of the i^{th} region. These integrals are carried out analytically, and the results are as follows:

$$\begin{aligned} P_{1,TM-TE} &= \frac{\pm jRD^e_n D^{h*}_n}{2\hat{y}_1 \hat{z}^*_1}\left[\frac{S_1C_1 - \gamma_1 t}{|S_1|^2}\right] \\ P_{1,TE-TE} &= \frac{\mp jQD^h_n D^{h*}_n}{2\hat{z}^*_1 \gamma_1}\left[\frac{S_1C_1 - \gamma_1 t}{|S_1|^2}\right] \\ P_{1,TM-TM} &= \frac{jQD^e_n D^{e*}_n}{2\hat{y}_1 \gamma_1}\left[\frac{S_1C_1 + \gamma_1 t}{|S_1|^2}\right] \end{aligned}$$

$$
\begin{aligned}
P_{1,TE-TM} &= \frac{jRD_n^e D_n^{h*}\gamma_1^*}{2\hat{y}_1\hat{z}_1^*\gamma_1}\left[\frac{S_1C_1+\gamma_1 t}{|S_1|^2}\right] \\
P_{2,TM-TE} &= \frac{-jR}{2\hat{y}_2\hat{z}_2^*}\left(\pm B_n^e B_n^{h*}\left[\frac{S_2C_2-\gamma_2 g}{|S_2|^2}\right]+C_n^e C_n^{h*}\left[\frac{S_2C_2+\gamma_2 g}{|S_2|^2}\right]+\right. \\
&\quad \left. B_n^e C_n^{h*}\left[\frac{S_2S_2}{|S_2|^2}\right]\pm C_n^e B_n^{h*}\left[\frac{S_2S_2}{|S_2|^2}\right]\right) \\
P_{2,TE-TE} &= \frac{-jQ}{2\hat{z}_2^*\gamma_2}\left(\pm B_n^h B_n^{h*}\left[\frac{S_2C_2-\gamma_2 g}{|S_2|^2}\right]+C_n^h C_n^{h*}\left[\frac{S_2C_2+\gamma_2 g}{|S_2|^2}\right]+\right. \\
&\quad \left. B_n^h C_n^{h*}\left[\frac{S_2S_2}{|S_2|^2}\right]\pm C_n^h B_n^{h*}\left[\frac{S_2S_2}{|S_2|^2}\right]\right) \\
P_{2,TM-TM} &= \frac{jQ}{2\hat{y}_2\gamma_2}\left(B_n^e B_n^{e*}\left[\frac{S_2C_2+\gamma_2 g}{|S_2|^2}\right]\pm C_n^e C_n^{e*}\left[\frac{S_2C_2-\gamma_2 g}{|S_2|^2}\right]+\right. \\
&\quad \left. C_n^e B_n^{e*}\left[\frac{S_2S_2}{|S_2|^2}\right]\pm B_n^e C_n^{e*}\left[\frac{S_2S_2}{|S_2|^2}\right]\right) \\
P_{2,TE-TM} &= \frac{-jR\gamma_2^*}{2\hat{y}_2\hat{z}_2^*\gamma_2}\left(B_n^e B_n^{h*}\left[\frac{S_2C_2+\gamma_2 g}{|S_2|^2}\right]\pm C_n^e C_n^{h*}\left[\frac{S_2C_2-\gamma_2 g}{|S_2|^2}\right]+\right. \\
&\quad \left. C_n^e B_n^{h*}\left[\frac{S_2S_2}{|S_2|^2}\right]\pm B_n^e C_n^{h*}\left[\frac{S_2S_2}{|S_2|^2}\right]\right) \\
P_{3,TM-TE} &= \frac{\mp jRA_n^e A_n^{h*}}{2\hat{y}_3\hat{z}_3^*}\left[\frac{S_3C_3-\gamma_3 b}{|S_3|^2}\right] \\
P_{3,TE-TE} &= \frac{\mp jQA_n^h A_n^{h*}}{2\hat{z}_3^*\gamma_3}\left[\frac{S_3C_3-\gamma_3 b}{|S_3|^2}\right] \\
P_{3,TM-TM} &= \frac{jQA_n^e A_n^{e*}}{2\hat{y}_3\gamma_3}\left[\frac{S_3C_3+\gamma_3 b}{|S_3|^2}\right] \\
P_{3,TE-TM} &= \frac{-jRA_n^e A_n^{h*}\gamma_3^*}{2\hat{y}_3\hat{z}_3^*\gamma_3}\left[\frac{S_3C_3+\gamma_3 b}{|S_3|^2}\right]
\end{aligned}
\tag{B.20}
$$

The variables $\hat{y}_i$, $\hat{z}_i$, γ_i, R, Q, S_i and C_i are defined in Section B.3.1. The subscript n on the field coefficients $A^{e,h}$-$D^{e,h}$ indicates that each is scaled by S_i as in Eqns. B.17 and B.18. Finally, the upper sign on the $\pm$ or $\mp$ is used for real γ_i and the lower sign is for imaginary γ_i.

For convenience in computer implementation, the expressions in Eqn. B.20 have been written such that terms in brackets [] go to 1 as the arguments of the hyperbolic functions go to infinity. Also, the magnetic field coefficients are easily identified by the complex conjugate $*$. This makes it relatively simple to calculate the power

associated with a single slot, using the coefficients for the total E-field (due to all slots) and for the partial H-field (due to one slot), as is required by Eqn. 4.8. The coefficients are computed according to Section B.3.1.

B.4 Derivation of the Green's Function

The derivation of the Green's function which is presented here follows the immittance approach found in [52], and makes use of the (u, v) coordinate transformation described in Section B.3.1. It is based on the application of equivalent transmission line models for the TM-to-y and TE-to-y modes, where a separate transmission line is used for each mode, and the summation over all lines is used to model the arbitrary field in the cross-section of Figure 4.2 ([31], Ch. 8). The equivalent models are shown in Figure B.2.

For the TM-to-y modes, we have from Eqn. B.14,

$$\tilde{H}_{u1} - \tilde{H}_{u2} = \tilde{J}_v \tag{B.21}$$

Also, the transverse field components on either side of $y = b + g$, propagating away from the source, can be written in terms of the wave admittances as follows

$$\begin{aligned} \frac{-\tilde{H}_{u1}}{\tilde{E}_{v1}} &= Y_1^e \\ \frac{\tilde{H}_{u2}}{\tilde{E}_{v2}} &= Y_2^e \end{aligned} \tag{B.22}$$

where the admittances are those seen looking toward the directions shown in Figure B.2. Finally, since continuity conditions require that $\tilde{E}_{v1} = \tilde{E}_{v2}$, it is found that

$$(Y_1^e + Y_2^e)\tilde{E}_v = -\tilde{J}_v \tag{B.23}$$

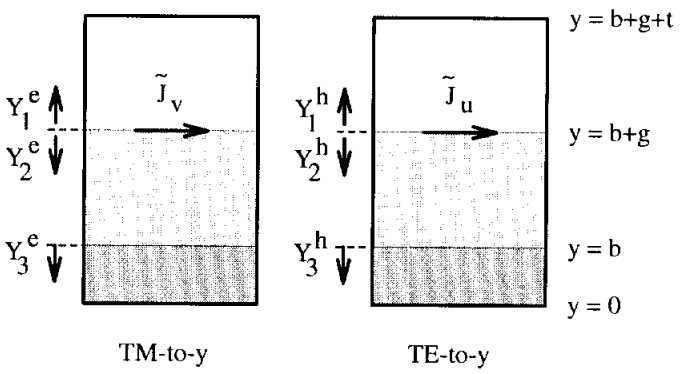

Figure B.2: Equivalent transmission line models for the TM-to-y and TE-to-y modes.

For the TE-to-y modes, similar arguments lead to the following:

$$(Y_1^h + Y_2^h)\tilde{E}_u = -\tilde{J}_u \tag{B.24}$$

These equations are now cast into the appropriate form for Eqn. 4.1 by mapping $\tilde{E}_{u,v}$ and $\tilde{J}_{u,v}$ back to the (x, z) coordinates, and solving for $\tilde{J}_x$ and $\tilde{J}_z$. The results are:

$$\begin{aligned}
\tilde{Y}_{xx} &= \frac{-1}{\alpha_f^2 + \beta^2}\left(\alpha_f^2(Y_1^e + Y_2^e) + \beta^2(Y_1^h + Y_2^h)\right) \\
\tilde{Y}_{xz} &= \frac{\alpha_f \beta}{\alpha_f^2 + \beta^2}\left((Y_1^e + Y_2^e) - (Y_1^h + Y_2^h)\right) \\
\tilde{Y}_{zx} &= \tilde{Y}_{xz} \\
\tilde{Y}_{zz} &= \frac{-1}{\alpha_f^2 + \beta^2}\left(\beta^2(Y_1^e + Y_2^e) + \alpha_f^2(Y_1^h + Y_2^h)\right)
\end{aligned} \tag{B.25}$$

The remaining step is to determine the values of the wave admittances, $Y^{e,h}$. This involves only the use of simple transmission theory to cascade the impedance at the upper and lower sidewall boundaries to the input impedance seen at the $y = b + g$ interface. For the three layer substrate, the procedure can be written as follows:

$$Y_i^{e,h} = \frac{1}{Z_{0,i}^{e,h}}\left(\frac{Z_{0,i}^{e,h} + jZ_{L,i}^{e,h}tan(\beta\, d_i)}{Z_{L,i}^{e,h} + jZ_{L,i}^{e,h}tan(\beta\, d_i)}\right) \tag{B.26}$$

where

$$\begin{aligned}
Z^{e}_{0,i} &= \tfrac{\gamma_i}{j\omega\epsilon_i} && \text{TM-to-y modes} \\
Z^{h}_{0,i} &= \tfrac{j\omega\mu_i}{\gamma_i} && \text{TE-to-y modes} \\
Z^{e,h}_{L,1} &= 0 && \text{Top sidewall at } y = b+g+t \\
Z^{e,h}_{L,2} &= \left(Y^{e,h}_{3}\right)^{-1} && \text{Interface between layers 2 and 3} \\
Z^{e,h}_{L,3} &= 0 && \text{Bottom sidewall at } y = 0
\end{aligned} \tag{B.27}$$

This assumes that the dielectric materials are lossless. Also, the variable d_i is the thickness of each layer and γ_i is the eigenvalue for the y-direction, as defined in Section B.3.1.

APPENDIX C

FABRICATION METHODOLOGY

C.1 Introduction

A detailed description of the processing steps involved in the fabrication of silicon micromachined circuits is presented in this appendix. The procedures are grouped into five primary categories, which are the growth of the tri-layer dielectric membrane, deposition of the circuit metalization, wet chemical etching (micromachining) of the silicon, backside metalization, and final circuit assembly. The membrane is mainly of importance in the realization of membrane-supported configurations, but is also useful as a temporary masking layer in general micromachining applications. Typically, however, a single oxide layer is more convenient when only the masking function is required. The silicon wafers must be at least single-side polished on the surface which will be patterned with circuit metalization, and double-side polished wafers are desirable when fine features are to be micromachined on the back side. If the etch patterns consist of relatively large openings and do not require great resolution, the additional expense of double-side polishing can be safely avoided. It is imperative, however, that silicon with a resistivity of at least 1500-2000 Ω-cm be used wherever silicon is exposed to the RF energy. This is done to avoid excessive dielectric loss, and necessitates the use of wafers which are grown using the float zone

(FZ) process [94]. For ground planes or RF shielding cavities, less expensive, low-resistivity (approximately 10 Ω-cm) wafers are utilized. These are typically grown using the Czochralski (CZ) method [95].

There are undoubtedly countless numbers of possible variations and extensions of the techniques included here. The intent of this writing is merely to describe a reasonably broad set of procedures which have been found to be reliable for fabrication of the micromachined circuits. For more extensive reviews of silicon processing and micromachining, the reader is referred to [96].

C.2 Dielectric Membrane Growth

The cornerstone of silicon micromachined, membrane-based transmission line architectures is the three-layer dielectric material on which the conducting lines are supported (Figure C.1). This membrane comprises a thermally grown oxide which is subsequently layered with a silicon nitride and another oxide, both of which are deposited using low pressure chemical vapor deposition (LPCVD). By properly balancing the thickness of each layer, a composite in slight tension is obtained which remains rigid when the silicon substrate is removed, and is robust enough to withstand subsequent processing such as photoresist application and metalization. Furthermore, membranes with dimensions up to 8×8 mm^2 have been fabricated successfully with yields exceeding 95% [97].

The critical issue in achieving flat, large area membranes is determining the correct thicknesses of the constituent layers. The thermal coefficients of expansion for Si and high-temperature CVD SiO_2 and Si_3N_4 are 2.6×10^{-6}/°C, 5×10^{-7}/°C and 4-7×10^{-6}/°C, respectively [98]. Therefore, by adjusting the thickness of each layer, a net tensile stress can be left in the membrane when the wafer is cooled to room

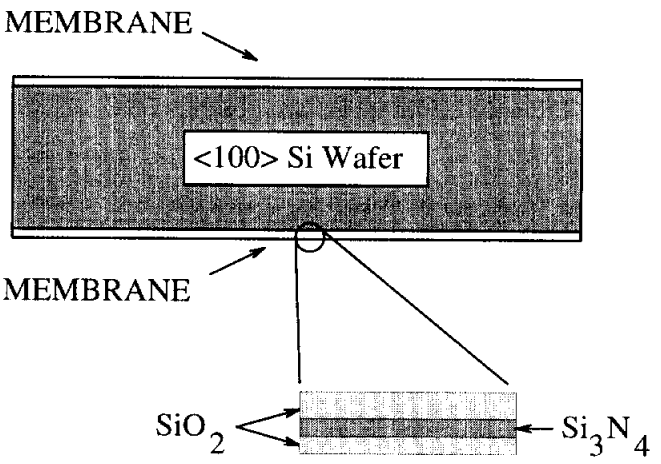

Figure C.1: The tri-layer dielectric membrane which is grown on both sides of a silicon wafer.

temperature from the 800-900°C temperatures in the LPCVD furnaces. High-yield membranes are obtained on 10 cm diameter, 500-550 μm-thick wafers using values of 7500Å/3500Å/4500Å for the thermal oxide, intermediate nitride, and top oxide layer thicknesses, respectively. A direct, experimental technique for determining the appropriate layer thicknesses is outlined in [99][1].

Procedures for membrane fabrication are outlined in the following:

1. Pre-Furnace Wafer Clean Prior to the thermal oxide growth, the wafers must be stripped and cleaned of all foreign materials to ensure a high-quality film and to prevent contamination of the furnace. The necessary steps are outlined in Table C.1.

2. Thermal SiO_2 Deposition The thermal oxide is grown using a dry-wet-dry sequence at a temperature of 1100°C and a pressure of 1 ATM, with the temperature held at 800°C while transferring the wafers in and out of the furnace. The

[1]The specific layer thicknesses given here have been slightly modified with respect to those given in [99].

Solution	Ratio	T°C	Time (Min.)
H_2O_2:NH_3OH:H_2O	1:1:5	90	10-20
H_2O quench		24	2
HF:H_2O	1:10 (Note 1)	24	1
H_2O quench		24	2
H_2O_2:HCL:H_2O	4:4:25	90	10-20
H_2O quench		24	5
H_2O rinse w/N_2 bubbling		24	Note 2

Table C.1: Prefurnace clean procedure. Note 1: When cleaning wafers with critical oxide layers, a 1:100 solution can be used instead. Note 2: The last rinse is continued until the bath resistivity exceeds 13-14 MΩ-cm.

first and last dry oxide layers are dense films which are grown to thicknesses of 5-10Å using an oxygen flow rate of 3 L/min. The intermediate wet layer is grown using flow rates of 1.7 L/min for O_2 and 2.5 L/min for H_2, yielding a faster growth rate but more porous film in comparison to the dry layers. The time required to grow a 7000Å-thick oxide is approximately 3-4 hours.

3. LPCVD Si_3N_4 and SiO_2 Deposition Following the thermal oxide growth, the wafers are moved to an LPCVD furnace for deposition of the intermediate nitride and the final oxide. The furnace temperature is approximately 900°C, and the growth rates are around 45-50 Å/min and 60-70 Å/min for the nitride and oxide, respectively. Specific parameters for this process are given in Table C.2.

Dielectric Layer	T°C	Ingredients	Flow Rates (sccm)
Si_3N_4	830	NH_3	160
		DCS	40
SiO_2	910	N_2 dilute	145
		N_2O	120
		DCS	60

Table C.2: LPCVD deposition parameters. DCS stands for dichlorosilane.

C.3 Circuit Metalization

This section outlines the procedure for depositing the thin-film metalization which constitutes the circuit pattern, onto the front side of the wafer (Figure C.2). The steps described here are primarily based on the image reversal photoresist technique. In this process, dark features on the circuit mask correspond to areas where metal will be deposited, which generally simplifies the alignment procedure since most of the mask is transparent (a clear-field mask). Also, in comparison to alternative methods such as the chlorobenzene process, the image reversal method has been found to yield more ideal metal profiles.[2]

Before starting the procedure, appropriately sized silicon pieces must be prepared. This involves dicing, or simply scribing, a whole wafer into smaller pieces, making sure that the edges follow straight lines along the ⟨110⟩ crystal directions (either parallel or perpendicular to the major flat). If this is not done it will be impossible to correctly align the etch patterns with the crystal structure. This type of misalignment

[2]Results with the chlorobenzene process demonstrated a phenomena known as "lift-off flags", referring to metal profiles which have sharp, up-turned spikes at the edges of the pattern.

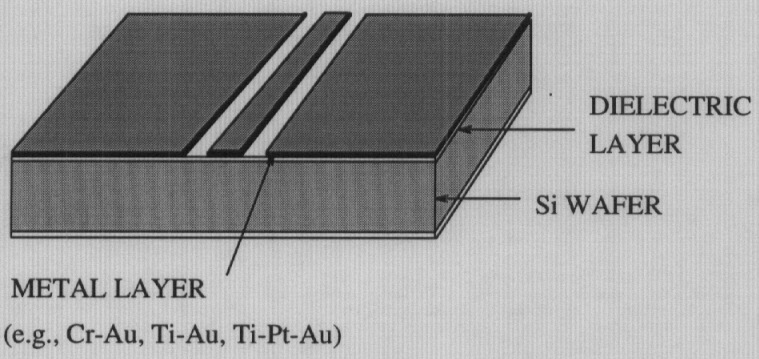

Figure C.2: Circuit pattern deposited onto the front side of a wafer using thin-film application techniques.

results in poor cavity definition and undercutting of the etch masking layers.

The circuit metalization sequence is as follows:

1. Wafer Preparation: For best results, the wafer should be thoroughly cleaned using a 1:1 "piranha" etch (a 1:1 ratio of H_2SO_4:H_2O_2). The duration of the clean should be about 10 minutes, which is the approximate lifetime of the reaction.

2. Image Reversal:

   (a) Clean the wafer with acetone and IPA (isopropyl alcohol). Dehydrate bake for 3 minutes on a hot-plate at 130°C. Keep the desired membrane surface face up and rest the wafer edge on a glass slide.

   (b) Spin-apply HMDS (hexamethyldisilazane) adhesion promoter and AZ 5214-E photoresist [100] at 2.5 KRPM. This yields a photoresist thickness of approximately 2 μm.

   (c) Soft-bake 1 minute at 105°C on a hot-plate.

   (d) Align and expose for 8 seconds at 20 mW/cm^2 ultraviolet light intensity

(λ = 405 nm). To achieve success in the subsequent micromachining steps, the mask must be aligned to a straight edge of the wafer, such that the patterns to be etched into the front or back side can be correctly positioned along the $\langle 110 \rangle$ crystal directions. This step is made easier if the mask incorporates long, straight alignment marks around the edge of the circuit area. These can be used to align the wafer via Θ-positioning, and, if necessary, the pattern can then be translated back to the center of the wafer using x and y positioning only.

(e) Post-bake 1 minute at 130°C on a hot-plate. This step causes the exposed photoresist to "cross-link", and leads to the formation of a thin crust on the upper surface.

(f) Flood expose for 120 seconds at 20 mW/cm^2 UV power density. This long exposure is needed to activate the photoresist which was not exposed previously.

(g) Develop in AZ 327 MIF [100] developer for 45-55 seconds. This removes the photoresist which was not exposed during the first alignment, and will also remove some of the photoresist beneath the edges of the cross-linked pattern. It is this undercutting that allows the evaporation and subsequent lift-off of the evaporated metal to succeed.

(h) Check pattern definition using a microscope.

3. Metal Deposition:

(a) Descum the wafer using a 36 second, 80 W O_2 plasma etch.

(b) Deposit metalization using evaporation techniques. Metal systems such as chrome-gold, titanium-gold, or titanium-platinum-gold are resistant to

wet etching using the EDP solution. Alternatively, if thicker layers are necessary to minimize attenuation, copper or silver may be used instead of gold to reduce fabrication costs. Most anisotropic silicon etchants attack aluminum at a substantial rate, and therefore Al should not be used in applications requiring long etch times.

(c) Soak in acetone for approximately 6 hours to dissolve the photoresist masking layer and complete the pattern lift-off.

The process described has been verified for line dimensions down to 10 μm, and evaporated metalization thicknesses up to 1.2 μm.

Due to the slow spin-rate for the photoresist deposition, beading will occur around the edges of the silicon piece, leaving up to 5 mm around the circumference which is non-usable. For 1-2 μm features, the beading should be removed using a technique such as that described in ([101], App. B). Also, for metalization thicknesses up to 0.6 μm, the AZ 5214-E can be spun on at 4.5 KRPM. This provides about 1.4 μm photoresist thickness and is better for feature sizes down to 3-5 μm. Using this method, the first expose and flood expose times should be reduced to 4 seconds and 90 seconds, respectively.

It is important to point out that free-standing membranes of the type described in Section C.2 can withstand the circuit metalization procedure. Therefore, the silicon micromachining can precede the metal deposition if necessary. In this case, photoresist application requires that the wafer first be attached to a support wafer, separated by small silicon standoffs (Figure C.3). The support/standoff/membrane wafer system can be temporarily assembled using a heavy photoresist "glue" such as S1400-37 [102], and baked on a hot-plate at 130°C for 1 minute. This assembly will easily survive the photoresist spin and alignment steps, and can be separated during

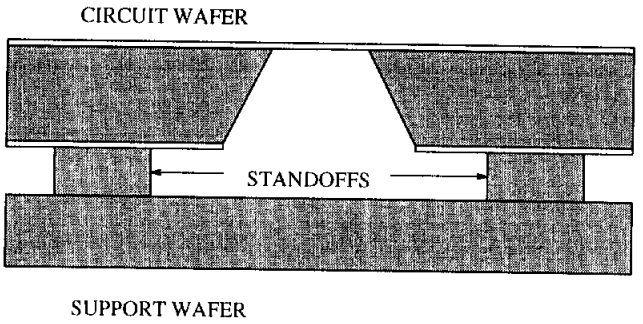

Figure C.3: Circuit-wafer/standoff/support-wafer assembly used for the photoresist process on free-standing membrane pieces.

the photoresist development stage to simplify drying. Alternatively, the circuit wafer can be separated during the second hot-plate bake by handling it instead of the support wafer. Some type of standoff arrangement is also necessary during the metal evaporation, to prevent the membrane from bursting due to evacuation of the lower cavity formed by the etched silicon.

For applications requiring thicker metalization layers, the evaporation technique can be supplemented with gold electro-plating. One method of implementing the plating process begins with the evaporation of Ti-Au-Ti or Cr-Au-Ti seed layers over the entire front (or back) wafer surface, using thicknesses of 500Å/1000Å/500Å, respectively. The photoresist is then applied and patterned using the image reversal technique. Alternatively, an S1400-37 positive photoresist process can be used to provide a thicker photoresist layer. This process requires a dark field mask, and is outlined in steps 1a-1h in Section C.4. The next step is to remove the exposed Ti in the pattern openings using a 10:1 H_2O:HF etch for 3-10 seconds. The metalization can then be built up using electro-plating, and the Ti layer which remains outside the pattern will help to prevent lateral spreading of the plated Au. Finally, the photoresist is removed with an acetone soak or hot PRS-1000 photoresist stripper.

Unwanted seed layer metals are removed using gold and chrome etchants, and 10:1 H_2O:HF for Ti.

C.4 Silicon Micromachining

The technologies related to silicon micromachining began to emerge in the 1960s [103], and continued to evolve into what is currently a wide array of techniques aimed at manipulating silicon for mechanical purposes. The development of complex micro electro mechanical systems (MEMS), sensors, and actuators has driven many of the significant advancements in this area, and a large volume of related work has been published in journals on solid state electronics and processing. The microwave community, in which the use of micromachining is relatively new, now has the advantage of drawing upon these established resources to solve problems and develop new concepts for microwave circuits.

The procedure which will be presented here is a very basic approach to bulk silicon micromachining using an anisotropic etchant. It relies on the use of a wet etchant such as KOH (potassium hydroxide) or EDP [104] (ethylenediamine pyrocatechol) to remove silicon preferentially along certain crystal directions, thereby allowing the formation of well-defined cavity regions. In the work considered here, wafers with a $\langle 100 \rangle$ orientation are typically used, and the etch rates are about 50:50:1 for the $\langle 100 \rangle$, $\langle 110 \rangle$, and $\langle 111 \rangle$ directions, respectively, using EDP at 100°C [105] (see Figure C.4). Similar ratios are achievable using KOH, however this is generally not the etchant of choice for dielectric membrane-related work since it etches silicon dioxide much faster than does EDP. The SiO_2 etch rate in EDP is approximately 5Å/minute, and in KOH the rate can be increased by an order of magnitude. Other masking films for EDP include Si_3N_4, Au, Cr, Ti, Ag, Cu, and Ta [106].

In order to describe the complete micromachining procedure, a typical process flow for single-side etching from the back of a wafer is outlined in the following. It is assumed that single-layer oxides or oxide/nitride/oxide layers are in place and will serve as the masking films for the etchant.

1. Wafer Preparation:

   (a) Clean wafer with acetone and IPA. Dehydrate bake for 3 minutes on a hot-plate at 130°C. Keep the desired membrane surface face up and rest the wafer edge on a glass slide.

   (b) Spin HMDS adhesion promoter and S1400-37 photoresist at 3.5 KRPM onto the front (desired) membrane surface. This provides a photoresist thickness of approximately 3.5 μm.

   (c) Hard-bake 30 minutes at 110°C in an oven. Alternatively, a 1 minute bake at 130°C on a hot-plate can be used. This photoresist serves to protect the front side of the wafer during the proceeding masking layer removal steps.

   (d) Spin HMDS adhesion promoter and S1400-37 photoresist at 3.5 KRPM onto the back side of the wafer.

   (e) Soft-bake 30 minutes at 90°C in an oven.

   (f) Align and expose the patterns to be etched into the silicon using a mask aligner and a dark-field photo mask, at an ultraviolet light power density of 20 mW/cm^2 for 15 seconds. The dark-field mask has openings in the emulsion or chrome which correspond to the areas where photoresist is to be removed, since S1400-37 is a positive resist. The etch pattern must

either be aligned to the ⟨110⟩ direction using the wafer edges, or to a pre-aligned front-side metalization layer using infra-red alignment techniques.

(g) Develop in MF351 developer [102] using a 1:5 MF351:H_2O (de-ionized) solution for 60 seconds.

(h) Hard bake 30 minutes at 110°C in an oven.

2. Masking Layer Removal

(a) Silicon dioxide masking layers can be removed using buffered hydrofluoric acid (BHF). The etch rate is approximately 1000 Å/minute.

(b) Silicon nitride masking layers are removed with a CF_4 plasma etch. In this process, the etching chamber is pumped down to 75 mTorr and CF_4 and O_2 are then flowed in at about 20 sccm and 0.5 sccm, respectively; the CF_4 flow rate is adjusted until the chamber pressure reaches 250 mTorr. After allowing the system pressure to stabilize, a 100 W RF plasma is ignited which will etch the nitride at a rate of approximately 700Å/minute. The photoresist masking layer described in the previous steps can safely withstand 11-12 minutes of the plasma etch, but etch durations should be closely monitored if thinner photoresist products (e.g. AZ 5214-E) are employed. When removing the middle nitride layer of the tri-layer composite membrane described in Section C.2, the integrity of the photoresist mask is critical for the final SiO_2 etch using BHF. The photoresist etch rate in the plasma can be as high as 1500 Å/minute.

3. Silicon Etching with EDP

(a) Prepare the EDP solution by combining the following ingredients in a

large Pyrex beaker, in the order listed: 96 mL of de-ionized H_2O, 96 gm of catechol, 1.8 gm of pyrazine, and 300 mL of ethylenediamine. (Different quantities of the solution can be mixed by proportionally adjusting the amount of each substance.) Cover the beaker tightly with heavy duty aluminum foil, place on a hot-plate, and heat the solution to 110-112°C. It is convenient to use a thermometer probe with feedback to maintain a constant temperature. All mixing, heating, and etching must be done inside a well-ventilated fume hood.

(b) While the EDP is warming up, the final masking layer removal steps should be completed to expose the bare silicon. For example, this might pertain to the BHF etch of the lower thermal oxide layer of the membrane described in Section C.2. Any native oxide growth will impede the etching process, and should be removed using a quick BHF dip. Photoresist can also be stripped off using acetone and IPA, since it will eventually come off in the EDP.

(c) Place the wafers in a Teflon holder and place the holder in the heated EDP solution. Be certain to keep the beaker covered. The etch rate is approximately 1.2-1.4 μm/minute, and therefore 6.5-7 hours are needed to etch completely through a 500 μm-thick wafer. These results pertain to fairly wide cavities (1-1.2 mm) and include the effects of "notching" [107], which refers to the slowing of the etch rate in the center of the lower cavity surface, with respect to the rate along the cavity edges. Narrower cavities, particularly those which come down to a point, tend to etch at somewhat higher rates.

(d) When the etching is complete, the samples should be rinsed in warm de-

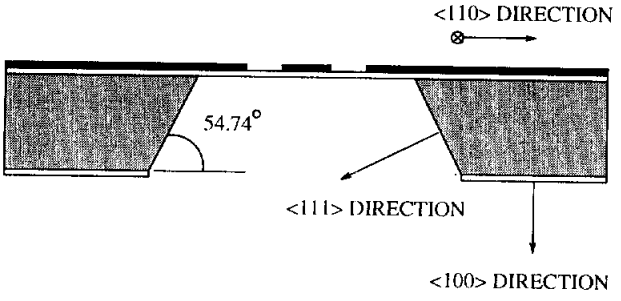

Figure C.4: Etch profile for a ⟨100⟩ oriented silicon wafer using an anisotropic etchant.

ionized water, acetone, and IPA for approximately 15 minutes apiece. The samples should then soak in methanol for 6-10 hours to completely remove any EDP residue.

In certain applications it is convenient to use a thin Cr-Au layer to mask the EDP. The metalization can be deposited using the image reversal and liftoff procedure outlined in Section C.3. Also, in situations where different parts of a sample need to be etched to different depths, a multi-step etching procedure can be employed [108]. In the first stage the masking layers are removed only from the areas which require the most etching, and the sample is placed in the EDP for a predetermined amount of time. The sample is then removed from the EDP, cleaned with the water/acetone/IPA/methanol sequence (using a shorter duration for the methanol soak), and the masking layer is then removed from the other desired etch regions. The sample is then placed back in the EDP solution to complete the etch.

C.5 Backside Metalization

With many of the micromachined circuit geometries, it is necessary to deposit metalization on the backside of the circuit wafer following the silicon etching proce-

dure. In some cases this may simply entail covering the entire back surface, which is easily accomplished using evaporation or electro-plating. The process is somewhat more complicated for the membrane-supported microshield line, since the metal must be selectively deposited inside the lower shielding cavity. It is necessary to cover the cavity sidewalls and some portion of the backside of the membrane, in order to provide an RF short between the upper ground planes and the cavity. To prevent a similar shorting of the transmission line itself, however, the region beneath the slots in the coplanar conducting lines must be shielded from the metalization. This selectivity is achieved with the use of the "shadow" mask illustrated in Figure C.5. The mask is a silicon wafer that is processed along with the circuit wafer, and has openings etched into it through which the evaporated metal is allowed to pass. The shadow mask is correctly positioned on the backside of the circuit wafer using small alignment cavities that have been etched into each wafer, and temporarily attached using the photoresist adhesion technique described in Section C.6. The achievable resolution with this method is approximately 50 μm. Following the metal evaporation, the shadow mask is removed by soaking the wafers in acetone.

C.6 Circuit Assembly

The final phase of the fabrication sequence generally involves the assembly of two to three stacked wafer pieces, such as the ground plane, circuit, and shielding cavity (Figure C.6). Accurate positioning of each level mandates the incorporation of alignment mechanisms such as patterns in the metalization, and micromachined cavities in the silicon which are etched completely or partially through the wafer. These alignment marks should be considered in the first phase of the circuit design.

Two convenient adhesives for bonding the wafers together are photoresist and

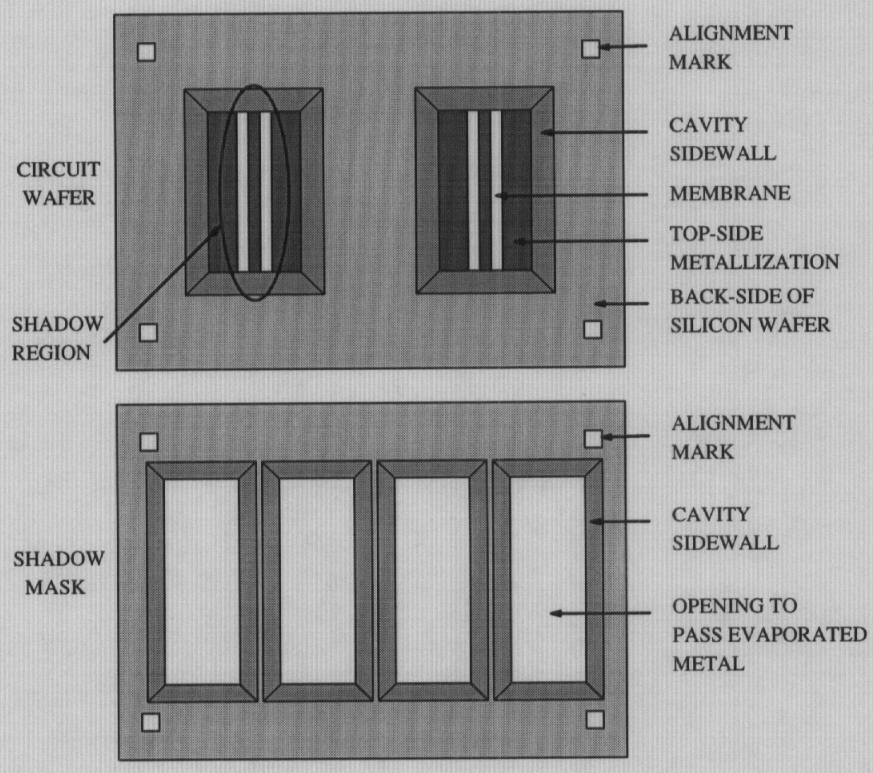

Figure C.5: The etched shadow mask used for backside metalization of the wafer.

APPENDIX D

MEASUREMENT TECHNIQUE

D.1 Introduction

The purpose of this appendix is to describe the transitions and calibration standards which are used in the experimental characterization of microshield circuits. The content is specifically aimed at measurements made using a microwave probe station and a vector network analyzer (HP 8510B). A critical element in this setup is the transition from the ground-signal-ground (CPW) microwave probes to the microshield line, and this is the subject of the first section. The second section describes the thru-reflect-line (TRL) technique [109] which is utilized to calibrate the measurement system.

D.2 Probe-to-Microshield Transition

The accuracy of the system calibration is strongly tied to the performance of the transition from the measurement probes to the microshield line. In designing the transition, it is necessary to print the probe contact pads on a short section of grounded coplanar waveguide (GCPW) on the silicon substrate, and use a short section of line to connect to the microshield. This approach must be taken since the membranes cannot directly withstand the force of repeated probe contact. The

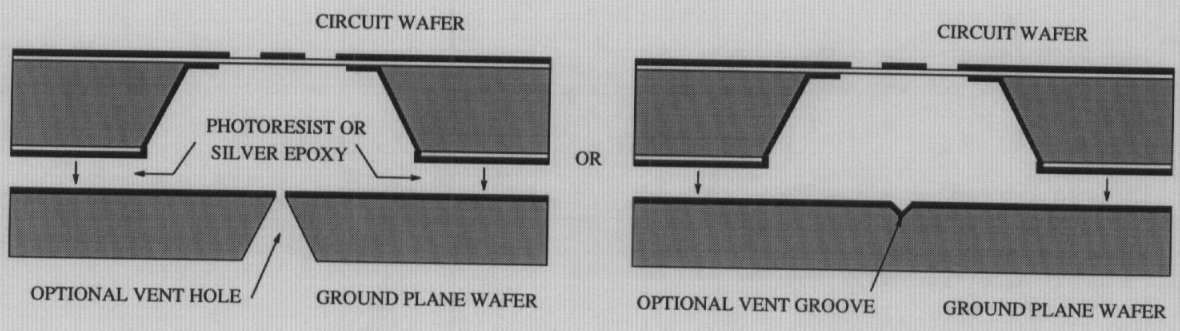

Figure C.6: Final circuit assembly.

silver epoxy. The photoresist technique is very useful for temporary assembly, and is common laboratory practice for the purpose of making electrical performance measurements. Using this approach, small drops of a photoresist such as AZ 5214-E are applied to a wafer, and then two pieces are aligned under a microscope or mask-aligner. The assembled wafers are then baked on a hot-plate at 130°C for approximately 60 seconds to cure the photoresist. The wafers are easily separated by soaking them in acetone. The silver epoxy technique follows the same basic steps and will also provide electrical contact if necessary. After applying the epoxy, the wafers are aligned and then baked in an oven at 120°C for approximately 1 hour, forming an essentially permanent bond between the wafers. The elevated cure temperature results in a high-conductivity contact.

In some cases it is desirable to provide a path for the release of gases when completely enclosing a cavity. For example, when the lower shielding cavity of a membrane-supported geometry is sealed, the membrane may be slightly deformed during the cure of the adhesive. Gases can be allowed to escape either by leaving some part of the contacting wafer surfaces free from photoresist or silver epoxy, or by putting scribe lines in the ground plane which lead out from the inside of the cavity. Alternatively, small air-holes may be etched into the ground plane wafer.

initial design that was used consisted of 55Ω GCPW contact pads followed by a 735 μm-long GCPW impedance matching section (Figure D.1). This configuration was intended to act as a low-loss transition to a 73Ω microshield line. Unfortunately, the performance of this design was rather poor and repeatability was difficult to achieve; typical results for the calibrated insertion loss of a microshield delay line are also shown in Figure D.1.

The cause of the erratic performance of this first transition was the leakage of power into undesired substrate modes along the length of grounded CPW line. The discontinuities at the probe contact pads, impedance steps, and the end of the microshield cavity are all possible sources of excitation for undesired parallel plate modes and TM_n and TE_n surface waves. Also, the finite lateral extent of the ground planes can result in predictable resonances in the GCPW line. As discussed in Chapter II, the ground plane spacing (S+2W) must be kept small compared to the ground plane width and the substrate height in order to maintain propagation in the CPW-like mode [10, 17, 110]. A shorter length of GCPW between the probe contact pads and the microshield line could also improve the performance since the power leakage increases with distance. Finally, leaky modes may be eliminated by integrating metallic cavities in the back of the substrate near the probe contact points.

These three modifications were implemented into the transition design shown in Figure D.2, and the significant improvement in the calibration is demonstrated in the same figure. In a later design, the ripple near 36 GHz was reduced by completely eliminating the 300 μm-long GCPW line.

As a final note, the probe contact pads shown here were intended for use with 150 μm-pitch probes. The designs proved to work well for probe sizes as large as 250 μm.

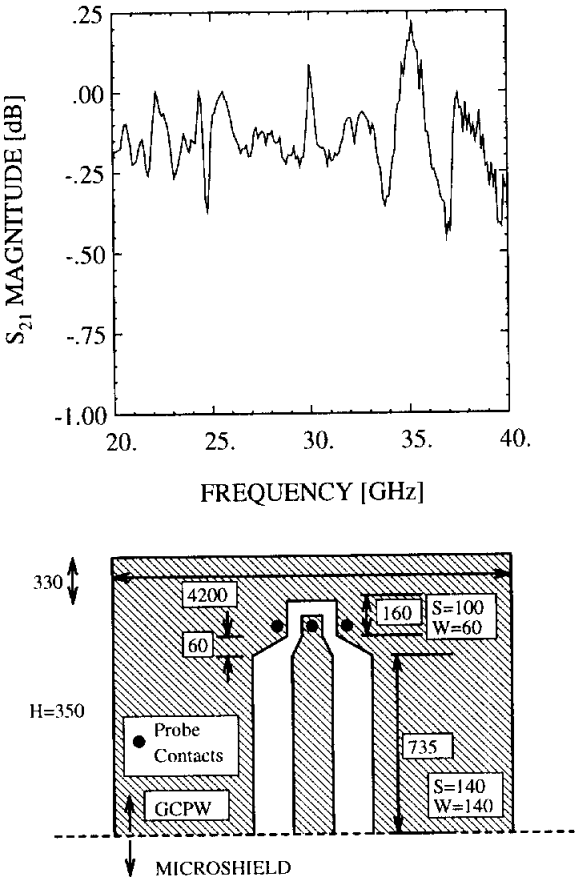

Figure D.1: A transition from the CPW microwave probes to the microshield line, and the measured S_{21} of a microshield delay line using this design. All dimensions are in microns.

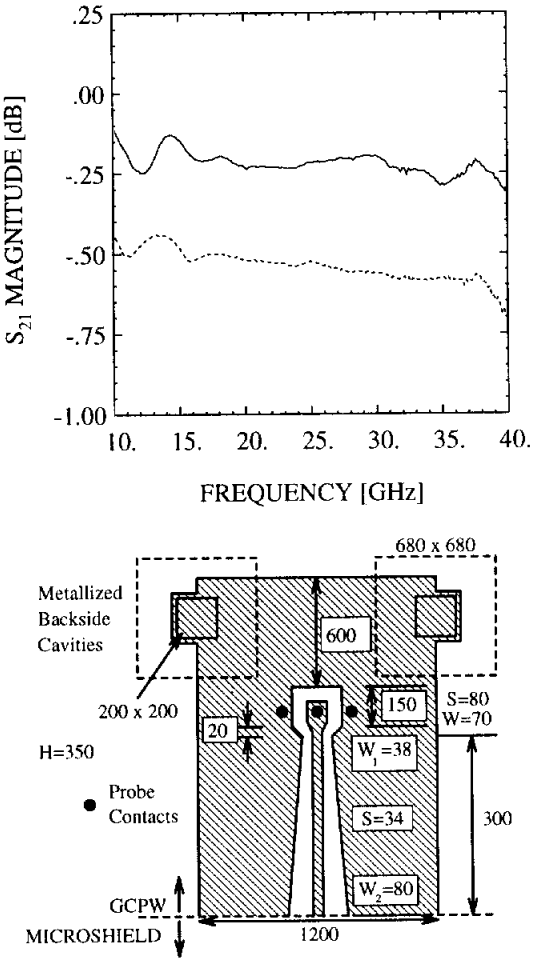

Figure D.2: Measured S_{21} of two microshield delay lines of different length, using the modified transition from the CPW probes. The cavities are etched from the backside of the wafer and are pyramidal in shape; the dotted line is the cavity size at the bottom of the wafer. All dimensions are in microns.

D.3 TRL Calibration Technique

One of the simplest and most accurate methods for calibrating on-wafer measurement setups is the thru-reflect-line (TRL) technique [109, 111]. This approach requires one straight line (the thru), one line that is either open- or short-circuited (the reflect), and one or more lines which have known electrical delays with respect to the thru (the line(s)). One significant advantage of the TRL method is that the reflects do not have to be ideal; a reflection coefficient which is close to ± 1 is sufficient. The number of necessary delay lines depends on the bandwidth over which the measurements are made, and generally a given line should have a delay between 20° and 160° [112]. Thus, for broad-band measurements, two or more delay lines may be needed. It is worth noting that the TRL software which is currently provided with the HP 8510-series of network analyzers employs a "split-band" approach for calibration. Using this method, a non-overlapping frequency band is associated with each delay line, resulting in discontinuities at each segmentation. In contrast, software from NIST (National Institute of Standards and Technology) uses redundant data from the multiple standards and can thus provide a more accurate, uniform calibration across the band [113].

A sample of the calibration standards which have been used in this research are shown in Figure D.3, and the corresponding dimensions are given in Table D.1. These illustrations pertain to the microshield line sections only, and do not include the probe-to-microshield transitions which are connected at each end. In these designs, the length L is chosen to be at least $\lambda/20$ at the lowest frequency to prevent higher-order mode coupling between the probe transitions. The delay length shown in the table, ΔL, proved to be adequate for calibration from 5-40 GHz, although additional

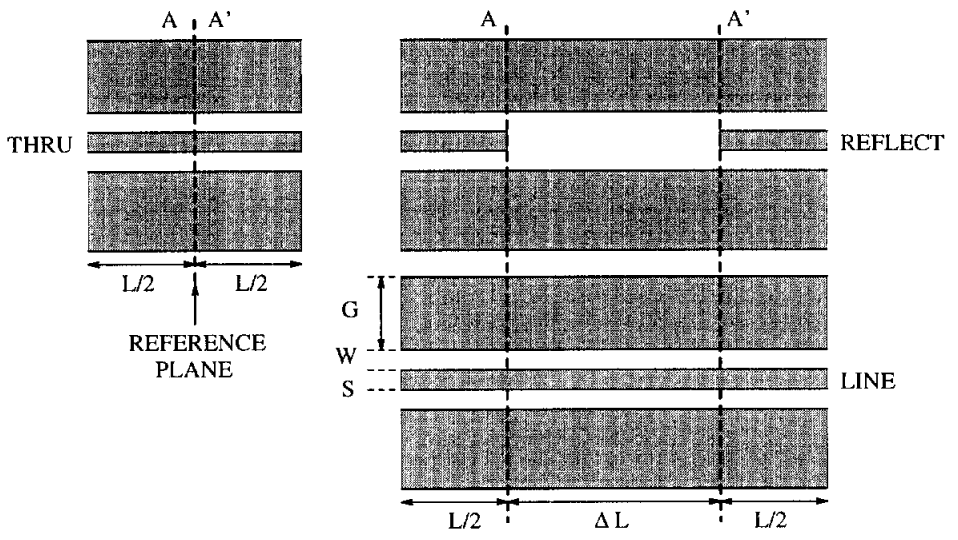

Figure D.3: Microshield line sections of the TRL calibration standards.

lines were also used with the NIST routines for the reasons mentioned above. In order to have a negligible effect on the characteristic impedance, the ground plane width, G, should be greater than (S/2+W) [9]. This requirement was easily met for all the circuits involved in this research, since the ground planes must extend past the cavity sidewalls, and the cavity widths used here ranged from 1.4-1.8 mm. Finally, since the accuracy of the calibration depends on how well-matched the system is to begin with, microshield standards with characteristic impedances closer to 50 Ω provided the best results. Adequate performance was obtained using the 99 Ω standards (designs C and D in the table), but some form of impedance transformer is suggested for systems at or above this impedance level. At lower frequencies, the transformers will most likely need to be printed on the silicon substrate in order to keep the line dimensions reasonable.

Design	L	ΔL	S	W	G	Z_o, Ω
A	2500	3000	250	25	950	73
B	2500	3000	190	55	950	99
C	2500	3000	260	20	850	67
D	2500	3000	260	70	850	99

Table D.1: Line dimensions (in μm) used for four microshield calibration sets of the type shown in Figure D.3.

BIBLIOGRAPHY

BIBLIOGRAPHY

[1] G. M. Rebeiz, Y. Guo, D. B. Rutledge and D. P. Kasilingam, "Two-Dimensional Horn Imaging Arrays, " *IRMM*, 1987, Orlando, pp. 224-225.

[2] G. M. Rebeiz, D. P. Kasilingam, Y. Guo, P. A. Stimson and D. B. Rutledge, "Monolithic Millimeter-Wave Two-Dimensional Horn Imaging Arrays, " *IEEE Trans. Antennas Propagat.*, vol. 38, pp. 1473-1482, September 1990.

[3] N. I. Dib, W. P. Harokopus, L. P. Katehi, C. C. Ling, and G. M. Rebeiz, "Study of a Novel Planar Transmission Line," *1991 IEEE MTT-S Digest*, Boston, vol. 2, pp. 623-626.

[4] C. Y. Chi and G. M. Rebeiz, "Planar Microwave Millimeter-Wave Lumped Elements and Coupled-Line Filters Using Micro-machining Techniques," *IEEE Trans. MTT*, vol. 43, no. 4, pp. 730-738, April 1995.

[5] S. V. Robertson, L. P. Katehi, and G. M. Rebeiz, "W-Band Microshield Low-Pass Filters," *1994 IEEE MTT-S Digest*, San Diego, vol. 2. pp. 625-628.

[6] R. F. Drayton and L. P. Katehi, "Development of Miniature Microwave Circuit Components Using Micromachining Techniques," *1994 IEEE MTT-S Digest*, San Diego, vol. 1, pp. 225-228.

[7] M. Yap, Y-C Tai, W. R. McGrath, and C. Walker, "Silicon Micromachined Waveguides for Millimeter and Submillimeter Wavelengths, " *Proceedings of the Third International Symposium on Space Terahertz Technology*, pp. 316-323, 1992.

[8] G. Ghione and C. Naldi, "Analytical Formulas for Coplanar Lines in Hybrid and Monolithic MICs," *Electron. Lett.*, vol. 20, no. 4, pp. 179-181, Feb. 1984.

[9] N. I. Dib, "Theoretical Characterization of Coplanar Waveguide Transmission Lines and Discontinuities," Ph.D. Thesis, Radiation Laboratory, University of Michigan, 1992.

[10] W. H. Haydl, W. Heinrich, R. Bosch, M. Schlechtweg, P. Tasker, and J. Braunstein, "Design data for millimeter wave coplanar circuits," *1993 European Microwave Conference Proceedings*, pp. 223-228.

[11] T. M. Weller, L. P. Katehi, and G. M. Rebeiz, "High Performance Microshield Line Components," *IEEE Trans. MTT*, vol. 43, no. 3, pp. 534-543.

[12] M. Zhang, C. Wu, K. Wu, and J. Litva, "Losses in GaAs Microstrip and Coplanar Waveguide," *1992 IEEE MTT-S Digest*, Albuquerque, vol. 2, pp. 971-974.

[13] W. H. Haydl, J. Braunstein, T. Kitazawa, M. Schlechtweg, P. Tasker, and L. F. Eastman, "Attenuation of Millimeter Wave Coplanar Lines on Gallium Arsenide and Indium Phosphide Over the Range 1-60 GHz," *1992 IEEE MTT-S Digest*, Albuquerque, vol. 1, pp. 349-352.

[14] H. J. Cheng, J. F. Whitaker, T. M. Weller, and L. P. Katehi, "Terahertz-Bandwidth Characterization of Coplanar Waveguide on Dielectric Membrane via Time-Domain Electro-Optic Sampling," *1994 IEEE MTT-S Digest*, San Diego, vol. 1, pp. 477-480.

[15] R. W. Jackson, "Considerations in the Use of Coplanar Waveguide For Millimeter-Wave Integrated Circuits," *IEEE Trans. MTT*, Vol. 34, No. 12, December, 1986, pp. 1450-1456.

[16] J. B. Knorr and K-D Kuchler, "Analysis of Coupled Slots and Coplanar Strips on Dielectric Substrate," *IEEE Trans. MTT*, vol. MTT-23, No. 7, pp. 541-548, July 1975.

[17] M. Riaziat, I. J. Feng, R. Majidi-Ahy, and B. A. Auld, "Single-Mode Operation of Coplanar Waveguides," *Electronics Letters*, 19th November, 1987, Vol. 23, No. 24, pp. 1281-1283.

[18] M. Riaziat, I. J. Feng, and R. Majidi-Ahy, "Propagation Modes and Dispersion Characteristics of Coplanar Waveguides," *IEEE Trans. MTT*, Vol. 38, No. 3, March, 1990, pp. 245-251.

[19] W-T Lo, C-K C. Tzuang, S-T Peng, C-C Chang, J-W Huang, and C-C Tien, "Resonant Phenomena in Conductor-Backed Coplanar Waveguide (CBCPW) ," *1993 IEEE MTT-S Digest*, Atlanta, vol. 3, pp. 1199-1202.

[20] M. A. Magerko, L. Fan, and K. Chang, "Multiple Dielectric Structures to Eliminate Moding Problems in Conductor-Backed Coplanar Waveguide MICs," *IEEE Microwave and Guided Letters*, Vol. 2, No. 6, June, 1992, pp. 257-259.

[21] M. Tsuji, H. Shigesawa, and A. A. Oliner, "New Interesting Leakage Behavior on Coplanar Waveguides of Finite and Infinite Widths," *1991 IEEE MTT-S Digest*, Boston, vol. 2, pp. 563-566.

[22] H. Shigesawa, M. Tsuji, and A. A. Oliner, "Conductor-Backed Slot Line and Coplanar Waveguide: Dangers and Full-Wave Analyses," *1988 IEEE MTT-S Digest*, New York, vol. 1, pp. 199-202.

[23] H. Shigesawa, M. Tsuji, and A. A. Oliner, "A New Mode-Coupling Effect on Coplanar Waveguides of Finite Width," *1990 IEEE MTT-S Digest*, Dallas, vol. 3, pp. 1063-1066.

[24] W. J. Getsinger, "End-Effects in Quasi-TEM Transmission Lines," *IEEE Trans. MTT*, Vol. 41, No. 4, April, 1993, pp. 666-672.

[25] K. Beilenhoff, H. Klingbeil, W. Heinrich, and H. Hartnagel, "Open and Short Circuits in Coplanar MMIC's," *IEEE Trans. MTT*, Vol. 41, No. 9, September, 1993, pp. 1534-1537.

[26] R. Chadha and K. C. Gupta, "Compensation of Discontinuities in Planar Transmission Lines," *IEEE Trans. MTT*, Vol. 30, No. 12, December, 1982, pp. 2151-2156.

[27] Amjad A. Q. Omar, "An Accurate Solution of 3-D Coplanar Waveguide Circuits," Ph.D. Thesis, University of Waterloo, Waterloo, Ontario, Canada, 1993.

[28] R. N. Simons and G. E. Ponchak, "Modeling of Some Coplanar Waveguide Discontinuities," *IEEE Trans. MTT,* Vol. 36, December, 1988, pp. 1796-1803.

[29] W. P. Harokopus, Jr., "High Frequency Characterization of Open Microstrip Discontinuities," Ph.D. Thesis, Radiation Laboratory, University of Michigan, 1991.

[30] K. Koshiji, E. Shu, and S. Miki, "An Analysis of Coplanar Waveguide with Finite Conductor Thickness - Computation and Measurement of Characteristic Impedance," *Electronics and Communications in Japan*, vol. 64-B, no. 8, pp. 69-78, 1981.

[31] R. F. Harrington, **Time Harmonic Electromagnetic Fields**, McGraw-Hill, 1987.

[32] C. A. Balanis, **Antenna Theory - Analysis and Design**, New York: John Wiley & Sons, Inc., ch. 2-3 and 8, 1982.

[33] R. E. Collin, **Field Theory of Guided Waves**, New York: IEEE Press, 1991.

[34] N. L. VandenBerg, "Full Wave Analysis of Microstrip Slot Antennas and Couplers," Ph.D. Thesis, Radiation Laboratory, University of Michigan, 1991.

[35] R. F. Harrington, **Field Computation by Moment Methods**, Macmillan, New York, 1968.

[36] J. C. Rautio, "A Time-Harmonic Electromagnetic Analysis of Shielded Microstrip Circuits," Ph. D. Thesis, Syracuse University, 1986.

[37] K. Barkleshli and J. L. Volakis, "Electromagnetic Scattering from an Aperture Formed by a Rectangular Cavity Recessed in a Ground Plane, " *Journal of Electromagnetic Waves and Applications*, vol. 5, no. 7, pp. 715-734, 1991.

[38] J. R. Mautz and R. F. Harrington, "Electromagnetic transmission through a rectangular aperture in a perfectly conducting plane," *Scientific Report*, no. 10, prepared under contract F9268-73-C-0047 with the A. F. Cambridge Labs, Hanscom AFB, Feb. 1976.

[39] K. Barkeshli and J. L. Volakis, "On the Implementation of the Conjugate Gradient Fourier Transform Method for Scattering by Planar Plates," *IEEE AP Society Magazine*, April 1990, pp. 20-26.

[40] S-W Lee, J. Boersma, C-L Law, and G. A. Deschamps, "Singularity in Green's Function and Its Numerical Evaluation," *IEEE Trans. AP*, vol. AP-28, no. 3, May 1980, pp. 311-317.

[41] I. S. Gradshteyn and I. M. Ryzhik, **Table of Integrals, Series, and Products**, San Diego, CA: Academic Press, Inc., 1965.

[42] S. Couture, J. Beal and Y. Antar, "The Cubic Spline Interpolation of a Standing Wave Envelope," *1992 IEEE AP-S Symposium Digest*, vol. 1, pp. 196-199.

[43] D. M. Pozar, **Microwave Engineering**, Addison Wesley Publishing, 1990.

[44] P. B. Katehi, "A Generalized Method for the Evaluation of Mutual Coupling in Microstrip Arrays," *IEEE Trans. AP*, vol. AP-35, no. 2, Feb. 1987, pp. 125-133.

[45] L. P. Dunleavy, "Discontinuity Characterization in Shielded Microstrip: A Theoretical and Experimental Study," Ph. D. Thesis, University of Michigan, 1988.

[46] C. P. Wen, "Coplanar Waveguide: A Surface Strip Transmission Line Suitable for Nonreciprocal Gyromagnetic Device Applications," *IEEE Trans. MTT*, vol. MTT-17, no. 12, pp. 1087-1090, Dec. 1969.

[47] C. P. Wen, "Coplanar-Waveguide Directional Couplers," *IEEE Trans. MTT*, vol. MTT-18, no. 6, pp. 318-322, June 1970.

[48] G. Ghione and C. U. Naldi, "Coplanar Waveguides for MMIC Applications: Effect of Upper Shielding, Conductor Backing, Finite-Extent Ground Planes, and Line-to-Line Coupling," *IEEE Trans. MTT*, vol. MTT-35, no. 3, pp. 260-267, March 1987.

[49] V. F. Hanna and D. Thebault, "Analysis of Asymmetrical Coplanar Waveguides," *Int. J. Electronics*, vol. 50, no. 3, pp. 221-224, 1981.

[50] W. J. Getsinger, "A Solution to the 3-Conductor Mapping Problem with Application to Planar Lines and Couplers," Proceedings of the 17^{th} European Microwave Conference, Rome, pp. 1009-1014.

[51] D. Marcuse, "Electrostatic Field of Coplanar Lines Computed with the Point Matching Method," *IEEE J. Quantum Electronics*, vol. 25, no. 5, pp. 939-947, May 1989.

[52] T. Itoh, Editor, "Numerical Techniques for Microwave and Millimeter-Wave Passive Structures," New York: Wiley Interscience, 1989.

[53] T. E. van Deventer, "Characterization of Two-Dimensional High Frequency Microstrip and Dielectric Interconnects," Ph.D. Thesis, Radiation Laboratory, University of Michigan, 1992.

[54] G. Kibuuka, R. Bertenburg, M. Naghed and I. Wolff, "Coplanar Lumped Elements and Their Application in Filters on Ceramic and Gallium Arsenide Substrates," *Proceedings of the 19^{th} European Microwave Conference*, London, pp. 656-661.

[55] R. H. Jansen, "Unified User-Oriented Computation of Shielded, Covered, and Open Planar Microwave and Millimeter-wave Transmission-line Characteristics," *IEE Journal of Microwaves, Opt. and Acoust.*, vol. 3, pp. 14-22, January 1979.

[56] E. M. T. Jones and J. T. Bolljahn, "Coupled-Strip-Transmission-Line Filters and Directional Couplers," *IRE Trans. MTT*, vol. MTT-4, pp. 75-81, April 1956.

[57] H. Ozaki and J. Ishii, "Synthesis of a Class of Strip-Line Filters," *IRE Trans. Circuit Theory*, vol. CT-6, pp. 104-109, June 1957.

[58] V. K. Tripathi, "Asymmetric Coupled Transmission Lines in an Inhomogeneous Medium," *IEEE Trans. MTT*, vol. MTT-23, pp. 734-739, Sept. 1975.

[59] V. K. Tripathi, "On the Analysis of Symmetrical Three-Line Microstrip Circuits," *IEEE Trans. MTT*, vol. MTT-25, pp. 726-729, Sept. 1977.

[60] D. Pavlidis and H. L. Hartnagel, "The Design and Performance of Three-Line Microstrip Couplers," *IEEE Trans. MTT*, vol. MTT-24, pp. 631-640, Oct. 1976.

[61] J. L. Allen, "Non-symmetrical Coupled Lines in an Inhomogeneous Dielectric Medium," *Int. J. Electronics*, vol. 38, no. 3, pp. 337-347, 1975.

[62] K. D. Marx, "Propagation Modes, Equivalent Circuits, and Characteristic Terminations for Multiconductor Transmission Lines with Inhomogeneous Dielectrics," *IEEE Trans. MTT*, vol. MTT-21, pp. 450-457, July 1973.

[63] W. J. Getsinger, "Circuit Duals on Planar Transmission Media," *1983 IEEE MTT-S Digest*, pp. 154-156.

[64] K. Iguchi, M. Tsuji and H. Shigesawa, "Negative Coupling Between TE_{10} and TE_{20} Modes for use in Evanescent-Mode Bandpass Filters and Their Field-Theoretic CAD, " *1994 IEEE MTT-S Digest*, San Diego, vol. 2, pp. 727-730.

[65] J. Machac and W. Menzel, "On the design of waveguide-to-microstrip and waveguide-to-coplanar line transitions," *Proceedings of the 23nd European Microwave Conference*, Madrid, vol. 1, pp. 615-616.

[66] N. I. Dib, L. P. Katehi, G. E. Ponchak, and R. N. Simons, "Theoretical and Experimental Characterization of Coplanar Waveguide Discontinuities for Filter Applications," *IEEE Trans. MTT*, vol. 39 , No. 5, May, 1991, pp. 873-882.

[67] A. K. Sharma and H. Wang, "Experimental Models of Series and Shunt Elements in Coplanar MMICs," *1992 IEEE MTT-S Digest*, Albuquerque, vol. 3, pp. 1349-1352.

[68] P. A. R. Holder, "X-band microwave integrated circuits using slotline and coplanar waveguide," *The Radio and Electronic Engineer*, Vol. 48, No. 1/2, January/February, 1978, pp. 38-42.

[69] K. Hettak, J.Ph. Coupez, E. Rius and S. Toutain, "A New Uniplanar Bandpass Filter Using $\lambda_g/2$ Slotline and $\lambda_g/4$ Coplanar Waveguide Resonators, " *Proceedings of the 1994 EuMC*, Cannes, vol. 2, pp. 1360-1366.

[70] D. F. Williams and S. E. Schwarz, "Design and Performance of Coplanar Waveguide Bandpass Filters," *IEEE Trans. MTT*, vol. MTT-31, no. 7, July, 1983, pp. 558-566.

[71] T. Ishizaki, M. Fujita, H. Kagata, T. Owans, and H. Miyake, "A Very Small Dielectric Planar Filter for Portable Telephones, " *IEEE Trans. MTT*, vol. MTT-42, pp. 2017-2022, November 1994.

[72] R. Pregla, "Microwave Filters of Coupled Lines and Lumped Capacitances, " *IEEE Trans. MTT*, vol. MTT-18, pp. 278-280, May 1970.

[73] T. M. Weller, G. M. Rebeiz, and L. P. Katehi, "Experimental Results on Microshield Line Circuits," *1993 IEEE MTT-S Digest*, Atlanta, vol. 2, pp. 827-830.

[74] M. Hamadallah, "Microstrip Power Dividers at mm-Wave Frequencies," *Microwave Journal*, July 1988, pp. 116-127.

[75] S. V. Robertson, L. P. Katehi, and G. M. Rebeiz, "Micromachined Self-Packaged W-Band Bandpass Filters, " *1995 IEEE MTT-S International Microwave Symposium Digest.*

[76] K. Hettak, T. Le Gouguec, J. Ph. Coupez, S. Toutain, S. Meyer and E. Penard, "Very Compact Low Pass and Bandpass Filters using Uniplanar Structures, " *Proceedings of the 1993 EuMC*, Madrid, vol. 1, pp. 238-239.

[77] Y. Noguchi, S. Kitazawa, T. Wada, T. Ohmiyama and N. Okamoto, "A New Compact $\lambda_g/4$ Coplanar Waveguide Resonator Bandpass Filter, " *Proceedings of the 1993 EuMC*, Madrid, vol. 1, pp. 631-633.

[78] W. Menzel, "Broadband Filter Circuits Using an Extended Suspended Substrate Transmission Line Configuration," *Proceedings of the 22nd EuMC*, Helsinki, vol. 1, 1992, pp. 459-463.

[79] L. Q. Bui, D. Ball, and T. Itoh, "Broad-Band Millimeter-Wave E-Plane Bandpass Filters, " *IEEE Trans. MTT*, pp. 1655-1658, December 1984.

[80] N. I. Dib and L. P. Katehi, "Impedance Calculation for the Microshield Line," *Microwave and Guided Wave Letters*, Vol. 2, No. 10, Oct., 1992, pp. 406-408.

[81] D. P. Neikirk, W. W. Lam and D. B. Rutledge, "Far-Infrared Microbolometer Detectors," *International Journal of Infrared and Millimeter Waves*, vol. 5, no. 3, pp. 245-278, 1984.

[82] Personal communication from Dr. Kazem Sabetfakhri.

[83] Brian C. Wadell, **Transmission Line Design Handbook**, Artech House, Boston, 1991, pp. 95-97.

[84] A product of Hewlett-Packard/EEsof, Westlake Village, CA.

[85] E. O. Hammerstad and F. Bekkadal, "A Microstrip Handbook, " ELAB Report, STF 44 A74169, N7034, University of Trondheim, Norway, 1975.

[86] M & I Materials LTD, P. O. Box 136, Manchester M60 1AN, England.

[87] M. Kominami, D. M. Pozar and D. H. Schaubert, "Dipole and Slot Elements and Arrays on Semi-Infinite Substrate," *IEEE Trans. Antennas Propagat.*, vol. AP-33, no. 6, June 1985, pp. 600-607.

[88] S. Kawasaki and T. Itoh, "40 GHz Quasi-Optical Second Harmonic Spatial Power Combiner Using FETs and Slots," *1992 IEEE MTT-S Digest*, Albuquerque, vol. 3, pp. 1543-1546.

[89] S. V. Robertson, N. I. Dib, G. Yang, and L. P. Katehi, "A Folded-Slot Antenna for Planar Quasi-Optical Mixer Applications," *1993 IEEE AP-S Digest*, Ann Arbor, vol. 2, pp. 600-603.

[90] H. S. Tsai, M. J. W. Rodwell and R. A. York, "Planar Amplifier Array with Improved Bandwidth Using Folded-Slots," *IEEE Microwave and Guided Wave Letters* , vol. 4, no. 4, April 1994, pp. 112-114.

[91] X. H. Yang and W. X. Zhang, "Coplanar Waveguide Antenna Arrays for MIC/MMIC at Millimeter Wave Frequencies," *Electronics Letters*, vol. 26, no. 18, Aug. 1990, pp. 1464-1465.

[92] S. M. Mollenkopf, Radiation Laboratory, University of Michigan, personal communication, May 1994.

[93] P. G. Ciarlet, "Introduction to Numerical Linear Algebra and Optimization," Cambridge: Cambridge University Press, 1989.

[94] H. G. Kramer, "Float-Zoning of Semiconductor Silicon: A Perspective, " *Solid State Technol.*, p. 137, January 1983.

[95] R. A. Laudise, **The Growth of Single Crystals**, Prentice-Hall, Englewood Cliffs, N. J., 1970.

[96] S. Wolf and R. N. Tauber, **Silicon Processing for the VLSI Era**, Volume 1: Process Technology, Sunset Beach, California: Lattice Press, 1986.

[97] T. Weller, L. Katehi, M. Herman, and P. Wamhof, "Membrane Technology Applied to Microstrip: A 33 GHz Wilkinson Power Divider," *1994 IEEE MTT-S Digest*, San Diego, vol. 2, pp. 911-914.

[98] L. I. Maissel and R. Glang, **Handbook of Thin Film Technology**, ch. 6, pp. 29-30, New York: McGraw Hill, 1970.

[99] Curtis S. Ling, "An Integrated 94 GHz Monopulse Tracking Receiver," Ph.D. Thesis, Radiation Laboratory, University of Michigan, 1993.

[100] AZ Photoresist Products, Sunnyvale, CA.

[101] Steven Scott Gearhart, "Integrated Millimeter-Wave and Submillimeter-Wave Antennas and Schottky-Diode Receivers," Ph.D. Thesis, Radiation Laboratory, University of Michigan, 1994.

[102] The Shipley Company, 1457 MacArthur Rd., Whitehall, PA.

[103] M. P. Lepselter, "Beam-Lead Technology, " *Bell System Technical Journal*, pp. 233-254, February 1966.

[104] R. M. Finne and D. L. Klein, "A Water-Amine-Complexing Agent System for Etching Silicon, " *J. Electrochem. Soc.*, pp. 965-970, September 1967.

[105] H. Seidel, L. Csepregi, A. Heuberger, and H. Bauingartel, "Anisotropic Etching of Crystalline Silicon in Alkaline Solutions: Orientation Dependence and Behavior of Passivation Layers, " *J. Electrochem. Soc.*, pp. 3612-3626, November 1990.

[106] K. E. Petersen, "Silicon as a Mechanical Material, " *Proceedings of the IEEE*, vol. 70, no. 5, May 1982.

[107] G. Findler, J. Muchrow, M. Koch, and H. Munzel, "Temporal Evolution of Silicon Surface Roughness During Anisotropic Etching Processes," *Micro Electro Mechanical Systems 1992*, pp. 62-66, February 1992.

[108] R. F. Drayton, T. M. Weller, and L. P. Katehi, "Development of Miniaturized Circuits for High-Frequency Applications using Micromachining Techniques," *International Journal of Microcircuits and Electronic Packaging*, Third Quarter, 1995.

[109] G. F. Engen and C. A. Hoer, "Thru-Reflect-Line: An Improved Technique for Calibrating the Dual Six-Port Automatic Network Analyzer," *IEEE Trans. MTT*, Vol. MTT-27, No. 12, December, 1979, pp. 987-993.

[110] E. M. Godshalk, "Generation and Observation of Surface Waves on Dielectric Slabs and Coplanar Structures," *1993 IEEE MTT-S Digest*, Atlanta, vol. 2, pp. 923-926.

[111] D. Rubin, "De-Embedding mm-Wave MICs with TRL, " *Microwave Journal*, June 1990, pp. 141-150.

[112] C. A. Hoer, "Choosing Line Lengths for Calibrating Network Analyzers, " *IEEE Trans. MTT*, vol. 31, no. 1, Jan. 1983, pp. 76-78.

[113] R. B. Marks, "A Multiline Method of Network Analyzer Calibration, " *IEEE Trans. MTT*, vol. 39, no. 7, July 1991, pp. 1205-1215.